DISSECTING PROTEIN INTERACTIONS, LIGAND BINDING, AND CONFORMATIONAL REGULATION USING HYDROGEN-DEUTERIUM EXCHANGE MASS SPECTROMETRY

VIMANDA CHOW

A Dissertation submitted to the Faculty of Graduate Studies in Partial Fulfillment of the
Requirements for the Degree of Doctor of Philosophy

Chemistry, York University, Toronto, Ontario

August 2025

Abstract

Understanding protein interactions and structural dynamics is fundamental to elucidating biological function, disease mechanisms, and therapeutic design. Proteins rarely act in isolation; their activities are mediated through transient or stable interactions with ligands, other proteins, nucleic acids, and membranes. Capturing these dynamic events requires biophysical tools capable of resolving structural changes at high temporal and spatial resolution. Among these, hydrogen-deuterium exchange mass spectrometry (HDX-MS) has emerged as a powerful technique for probing conformational flexibility and interaction interfaces under near-physiological conditions. In this work, we employed HDX-MS, including millisecond-to-second timescales, as a structural biology tool to investigate conformational dynamics and interaction landscapes across a diverse range of protein systems. HDX-MS enabled detailed characterization of cytochrome c (cyt c) binding to phospholipid membranes, revealing that cardiolipin (CL) and the model lipid, 1-palmitoyl-2-oleoyl-sn-glycero-3-phospho-(1'-rac-glycerol) (POPG) both induce similar protection in specific interaction sites, particularly the adjacent "L" and "A" regions, while leaving others unperturbed. Expanding to nuclear receptors, HDX-MS provided mechanistic insights into the ligand-induced conformational plasticity of Constitutive Androstane Receptor (CAR) and Pregnane X Receptor (PXR). In CAR, transcriptional activation correlated with stabilization of helix 11 (H11) and can be independent of helix 12 (H12), and distinct structural responses were observed between full agonist and partial agonist. In the CAR: Retinoid X Receptor alpha (RXRα) heterodimer, we uncovered ligand-driven allosteric communication across the dimer interface, with dual ligands producing cooperative stabilization of the CAR ligand-binding domain. In PXR, cooperative binding of furanodienone (FDN) with estrogenic steroids (E2 and EE2) led to enhanced stabilization of helices H3 and H12, promoting full agonist-like activity. Finally, in the lipid hydrolase (ABHD2), HDX-MS enabled mapping of binding interfaces for inhibitors 191R and 192. Dynamic comparison with the catalytically inactive S207A mutant revealed mutation-induced stabilization and altered ligand responsiveness in the absence of crystallographic data. Together, these findings highlight HDX-MS as an effective and versatile technique for elucidating protein-ligand and protein-lipid interactions and highlighting its growing utility in guiding therapeutic development across diverse biological systems.

Acknowledgements

I want to express my deepest gratitude to Dr. Derek Wilson and Dr. Andrew James for their invaluable guidance, encouragement, and patience throughout my PhD journey. I am also grateful to Dr. Gerald Audette and Dr. Philip Johnson for their insightful feedback and advice, which significantly improved the quality of this dissertation. I would also like to acknowledge Dr. David Schriemer and Dr. Dasantila Golemi-Kotra for serving as my external and internal committees.

I acknowledge the support of York University and NSERC, whose resources and financial assistance made this research possible. Special thanks go to Dr. Jiabao Liu (from the University of Toronto) for your endless supplies of protein samples and cell-based results that significantly contributed to my Chapters 3 and 4 in this thesis. I have greatly enjoyed our scientific exchanges throughout the years. Thank you to the Wilson Lab members (Cristina, Ventia, Irina, Esther, Joe, Ayesha, Alex, Alice and Iqra), present and past, whose personalities and outlook on different matters provided insight into many aspects of my research.

On a personal note, I am deeply thankful to my family and friends; you mean the world to me. Your endless support has gotten me through these five years. Himanshu, my husband, you have been my biggest support throughout this whole journey. When I wonder if all this is worth it, you constantly remind me to keep going, that I can do it, and I'm very close to the end. Also, patiently waiting every day to drive me home, or spontaneous trips back to school because the robot stopped responding. Vianna, my baby sister, who's not a baby anymore. Thank you for all the necessary hangouts that help my brain take the break it needed and prevent me from burning out weekly. I must shout out my science girlies, for their unwavering support and understanding of the struggle of a PhD student, Christina, Carmen and Viktoria. Thank you for providing insight during the more challenging moments of this journey. Angela, Brianne, Jessica, and Brittany, for all those days, I escaped the reality and struggles of my research and just breath. Also, for asking me how my work has been going, me ranting, and you just sit and listen. Lastly, Yoon, Lina, Dirosan, Devang, and Fabod, thank you for all the meals shared and the endless support over the past 5 years! I appreciate you guys and can't wait to celebrate all the upcoming milestones with you guys. Lastly, Craig, Lesley and Noveah for endless nights of reading my thesis, providing feedback and listening to my presentation maybe a million times. You guys make me feel like the luckiest person in the world to have such a great and supportive family.

Finally, I extend my heartfelt appreciation to all those whose names may not appear here, but whose contributions were no less important.

Table of Contents

List of Figures

List of Abbreviations

HDX – Hydrogen Deuterium eXchange
MS – Mass spectrometry
Cyt c – Cytochrome C
ETC – Electron Transport Chain
CL – Cardiolipin
POPG – 1-palmitoyl-2-oleoyl-sn-glycero-3-phospho-(1’-rac-glycerol)
DMPC – 1,2-dimyristoyl-*sn*-glycero-3-phosphocholine
CAR – Constitutive Androstane Receptor
PXR – Pregnane X Receptor
H# – Helix number
RXRα – Retinoid X Receptor Alpha
FDN – Furanodienone
E2 – Estradiol
EE2 – 17α-ethinylestradiol
ABHD2 – α/βHydrolase Domain containing 2
NMR – Nuclear Magnetic Resonance
XL – Cross-Linking
LC – Liquid Chromatography
GC – Gas Chromatography
CE – Capillary Electrophoresis
ESI – ElectroSpray Ionization
MALDI – Matrix-Assisted Laser Desorption/Ionization
IEM – Ion Evaporation Model
CRM – Charged Residue Model
CEM – Chain Ejection Model
m/z – Mass-to-Charge
Q – Quadrupole
TOF – Time-of-Flight
DC – Direct current
RF -Radio Frequency
FWHM – Full-Width at Half Maximum
IMS – Ion Mobility Spectrometry
cIM – Cyclic Ion Mobility
CCS – Collisional Cross Section
DTIMS -Drift Tube IMS
TWIMS – Travelling Wave IMS
CID – Collision-Induced Dissociation
QET – Quasi-Equilibrium Theory
RRKM – Rice-Ramsperger-Kassel-Marcus
amu – Atomic Mass Unit
PDLA – Poly-DL-Alanine
HX – Hydrogen eXchange
PF – Protection Factor
TCEP – Tris 2-CarboxyEthyl Phosphine
ERC – Electrochemical Reducing Cells

nepII – Nepenthesis II
IDP – Intrinsically disordered proteins
IDR – Intrinsically disordered regions
TRESI – Time-Resolved ElectroSpray Ionization
PMMA – PolyMethyl MethAcrylate
DDA – Data Dependent Acquisition
DIA – Data Independent Acquisition
PLGS – ProteinLynx Global Server
PTM – Post-Translated Modifications
RFU – Relative Fractional Uptake
IMM – Inner Mitochondrial Membrane
SEC – Size Exclusion Chromatography
SDS-PAGE – Sodium Dodecyl-Sulfate PolyAcrylamide Gel Electrophoresis
MSP – Membrane Scaffolding Protein
PDB – Protein Data Bank
EPR – Electron Paramagnetic Resonance
FTIR – Fourier Transform InfraRed
HSQC – Heteronuclear Single Quantum Coherence
ATR-IR – Attenuated Total Reflection InfraRed
FRET – Fluorescence Resonance Energy Transfer
NR – Nuclear Receptors
LBD – Ligand Binding Domain
DIE – Diindolyl-Ethane
CITCO – 6-(4-chlorophenyl)imidazo[2,1-b][1,3]thiazole-5-carbaldehyde O-(3,4-dichlorobenzyl)oxime
TCPOBOP - 1,4-Bis [2-(3,5-Dichloropyridyloxy)] benzene
PPARγ – Peroxisome Proliferator-Activated Receptor Gamma
AF-2 – Activation Function 2
DBD – DNA- Binding Domain
2-AG – 2-Archidonoylglycerol
CINPA1 – Ethyl [5-[(diethylamino)acetyl]-10,11-dihydro-5H-dibenz[b,f]azepin-3-yl]carbamate
SRC-1 – Steroid Receptor Coactivator-1
TR – Thyroid Hormone Receptor
RA – Retinoic Acid
NCoR – Nuclear Receptor Corepressor
ITC – Isothermal Titration Calorimetry
SPR – Surface Plasmon Resonance
ROS – Reactive Oxygen Species
H_2O_2 – Hydrogen Peroxide
PCSK9 – Proprotein Convertase Subtilisin/Kexin Type 9
LDLR – Low-Density Lipoporteins Receptor
FPOP – Fast Photochemical Oxidation of Protein
VLP – Virus-Like Particles
LiP – Limited Proteolysis
ETD – Electron Transfer Dissociation
UVPD – Ultraviolet PhotoDissociation

List of Publications

1. **Chow, V**.; Lento, C.; Wilson, D.J. Probing the Conformational Dynamics of Cytochrome c upon Interaction with Anion Phospholipid Nanodiscs using Hydrogen-Deuterium Exchange Mass Spectrometry. *J. Am. Soc. Mass Spectrom.* **2025**, 36 (5), 1052-1059, https://doi.org/10.1021/jasms.4c00478.
2. Wang, X.; Zhang, G.; Bian, Z.; **Chow, V.**; Grimaldi, M.; Carivenc, C.; Sirounian, S.; Li, H.; Sladekova, L.; Motta, S.; Luperi, Y.; Gong, Y.; Costello, C.; Li, L.; Jachimowicz, M.; Guo, M.; Hu, S.; Wilson, D.; Balaguer, P.; Bourguet, W.; Mani, S.; Bonati, L.; Peng, H.; March, J.; Wang, H.; Wang, S.; Krause, H. M.; Liu, J. An Abundant Ginger Compound Furanodienone Alleviates Gut Inflammation via the Xenobiotic Nuclear Receptor PXR in Mice. *Nat. Commun.* **2025**, *16* (1), 2133. https://doi.org/10.1038/s41467-025-57509-y.
3. Dvořák, Z.; Vyhlídalová, B.; Pečinková, P.; Li, H.; Anzenbacher, P.; Špičáková, A.; Anzenbacherová, E.; **Chow, V.**; Liu, J.; Krause, H.; Wilson, D.; Berés, T.; Tarkowski, P.; Chen, D.; Mani, S. In Vitro Safety Signals for Potential Clinical Development of the Anti-Inflammatory Pregnane X Receptor Agonist FKK6. Bioorganic Chem. 2024, 144, 107137. https://doi.org/10.1016/j.bioorg.2024.107137.
4. Liu, J.; Malekoltojari, A.; Asokakumar, A.; **Chow, V.**; Li, L.; Li, H.; Grimaldi, M.; Dang, N.; Campbell, J.; Barrett, H.; Sun, J.; Navarre, W.; Wilson, D.; Wang, H.; Mani, S.; Balaguer, P.; Anakk, S.; Peng, H.; Krause, H. M. Diindoles Produced from Commensal Microbiota Metabolites Function as Endogenous CAR/Nr1i3 Ligands. *Nat. Commun.* **2024**, *15* (1), 2563. https://doi.org/10.1038/s41467-024-46559-3.
5. **Chow, V**.; Wolf, E.; Lento, C.; Wilson, D. J. Developments in Rapid Hydrogen–Deuterium Exchange Methods. *Essays Biochem.* **2023**, *67* (2), 165–174. https://doi.org/10.1042/EBC20220174.

Chapter One: Introduction

1.1 Protein Target as Therapeutic Solutions in Drug Discovery

Understanding protein interactions is fundamental to elucidating how biological processes are organized and regulated at the molecular level. Virtually all cellular functions depend on precise inter- and intra-molecular interactions, which enable macromolecules to adopt specific conformations necessary for their activity. Proteins, in particular, rely on such interactions with other proteins, lipids, or small-molecule ligands to undergo conformational changes to enable them to perform their diverse roles within the cell.

A well-characterized example is cytochrome c (cyt c), which facilitates electron transfer within the mitochondrial respiratory chain and exhibits peroxidase activity upon release into the cytosol during apoptosis triggered by cellular stress.[1] This release is mediated by its interaction with cardiolipin (CL), a mitochondria-specific phospholipid that anchors cyt c to the inner mitochondrial membrane.[2–5] Understanding how this interaction provides insight into the events that occur during cellular apoptosis.[1,2]

Disruptions in these tightly regulated protein functions and expression patterns are associated with numerous diseases, rendering proteins attractive targets for therapeutic interventions. Nuclear receptors provide a clear example: as ligand-activated transcription factors, they regulate gene expression in critical pathways, such as metabolic or developmental.[6] Modulating the activity of receptors such as the Constitutive Androstane Receptor (CAR) has been shown to influence xenobiotic metabolism, glucose homeostasis and hepatic function.[7–9]

To fully understand the molecular mechanisms underlying health, disease and therapeutic responses, it is essential to resolve how biomolecular interactions influence protein structure and function. Several techniques are available to probe these interactions at high resolutions. X-ray crystallography, while time-consuming and resource-intensive, remains the gold standard for obtaining atomic-level detail of protein structures and interaction interfaces.[10] However, because this method requires crystallized proteins and provides static snapshots, it may fail to capture the conformational dynamics critical to protein function.[11] In contrast, nuclear magnetic resonance (NMR) spectroscopy can provide structural and dynamic information through chemical shift and relaxation measurements.[10,11] Nevertheless, NMR requires isotopic labelling and is limited in its application to lower resolutions for large protein complexes, typically above 40kDa.[11]

Mass spectrometry (MS), while lacking atomic resolution, offers an orthogonal approach by providing valuable structural and interaction data under more native-like conditions. Techniques such as hydrogen-deuterium exchange (HDX) and cross-linking mass spectrometry (XL) enable the investigation of conformational flexibility and interaction interfaces, even for large or heterogeneous protein assemblies. Together, these methods provide insight to advance our understanding of protein behaviour in physiological and pathological contexts, guiding the development of targeted therapies and effective biopharmaceuticals.

1.2 Mass Spectrometry

Following nearly a century of instrumentation and software innovation, mass spectrometry (MS) has emerged as a powerful analytical technique with broad applications, ranging from small molecule identification to the characterization of large protein assemblies.[12] One of the key strengths of MS lies in its ability to be coupled with chromatographic separation techniques, such as liquid chromatography (LC)[13,14], gas chromatography (GC)[15], and capillary electrophoresis (CE)[16], thereby enabling multidimensional analysis. Furthermore, modern mass spectrometers often have advanced components such as collision cells and ion mobility separation modules (discussed in 1.2.3), which provide additional structural and conformational information.[17,18] These developments have collectively established mass spectrometry as an indispensable platform in many disciplines, such as proteomics, lipidomics, and organic chemistry.

A typical mass spectrometer consists of four main components: (1) an ion source, (2) a mass analyzer, (3) an ion detector, and (4) a data acquisition system (Figure 1.1).[12,19] While the mass analyzer and detector usually operate under vacuum conditions, specific configurations also house the ion source under vacuum, depending on the specific analytical application.[12] The subsequent sections will provide a detailed discussion of each of these components.

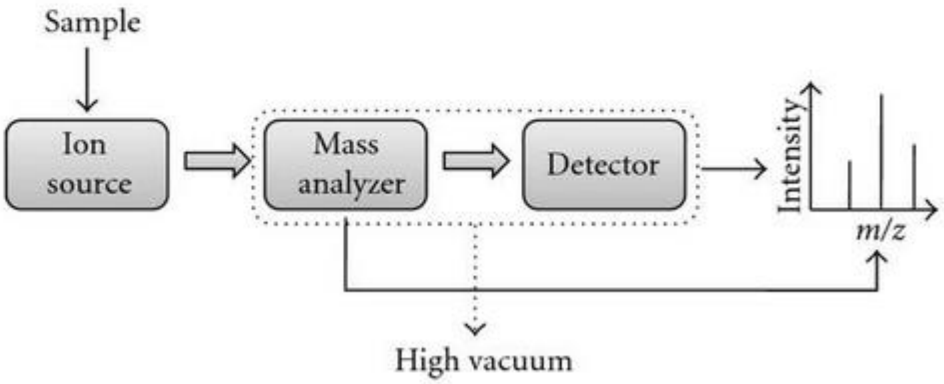

Figure 1.1| Schematic of the basic components of a mass spectrometer. Reproduced with permission from Benerjee and Mazumdar (2012).[19]

1.2.1 Ion Source: Electrospray Ionization

To enable mass spectrometric detection, analytes must first be ionized and transferred into the gas phase from either solution or solid phase and subsequently introduced into the vacuum environment of the mass analyzer.[20] Various ion sources are commercially available, each with distinct advantages and limitations. Electrospray ionization (ESI) and matrix-assisted laser desorption/ionization (MALDI) are the most widely adopted techniques for biological samples.[21,22] These soft ionization methods allow for the ionization of biomolecules without extensive fragmentation of covalent bonds.[19] Notably, ESI can often preserve non-covalent interactions, making it particularly valuable for probing protein structure and macromolecular complexes.[20,23]

In electrospray ionization, a high voltage is applied to a liquid sample introduced through a capillary at atmospheric pressure (Figure 1.2A).[19,21] In positive-ion mode, the anode is applied to the capillary tip, while the cathode serves as the counter electrode. The intense electric field at the capillary tip induces deformation of the liquid meniscus into a pointed structure known as a Taylor cone.[24] This cone emits a fine jet of charged droplets (Figure 1.2B).[19] As these primary droplets traverse toward the counter electrode, aided by a combination of source heating and nebulizing gas flow, solvent evaporation occurs. This evaporation reduces droplet size, and as the surface charge density increases, electrostatic repulsion eventually overcomes surface tension. This leads to Coulombic jet fission, whereby the primary droplet fragments into smaller progeny droplets. This cascade continues until gas-phase ions are formed, which are then directed into the mass analyzer.[21,25]

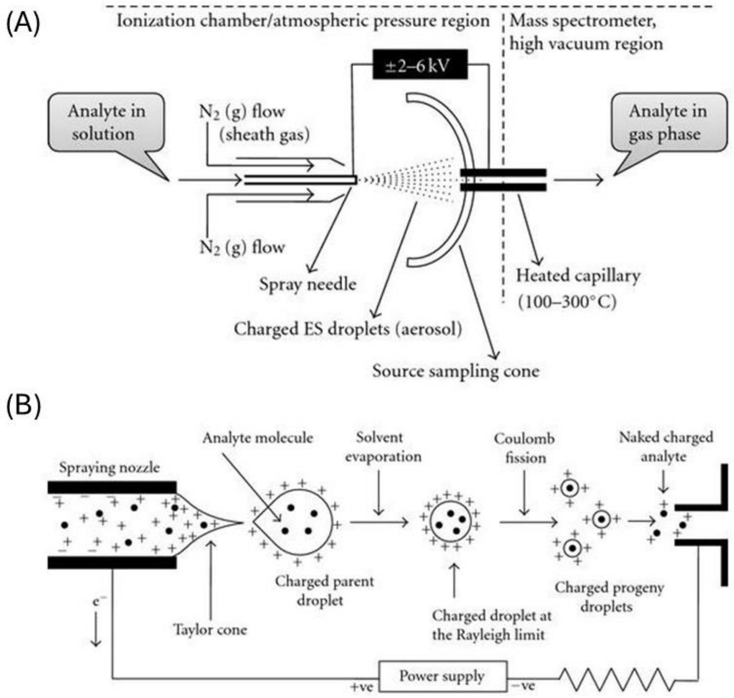

Figure 1.2| Schematic representation of the electrospray ionization process. (A) schematic representation of the ESI-ion source. Reproduced with permission from Banerjee and Mazumdar (2012).[19] (B) The "Taylor cone" emits a jet of liquid drops. Reproduced with permission from Banerjee and Mazumdar (2012).[19]

It is particularly noteworthy how the charge distribution of ions transferred from the aqueous to the gas phase during the ESI process often exceeds the theoretical charge predicted by the protein's primary sequence.[26] Several models, including the ion evaporation model (IEM)[27], the charged residue model (CRM)[28], and the chain ejection model (CEM)[29,30] (Figure 1.3), have been proposed to explain the formation of gaseous protein ions during ESI.[26,31]

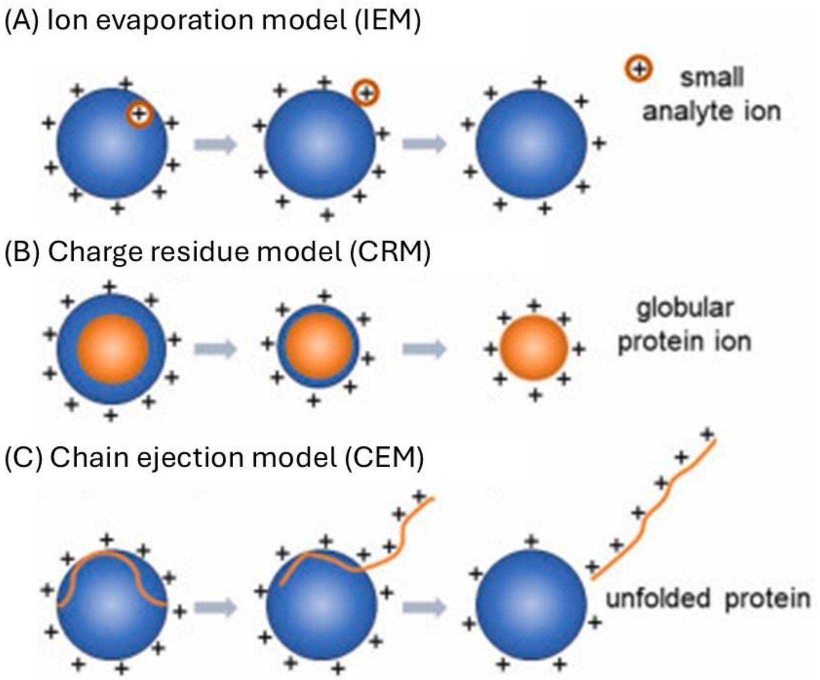

Figure 1.3| Three proposed electrospray mechanisms. (A) Ion evaporation model (IEM), (B) Charge residue model (CRM) and (C) Chain-ejection model (CEM). Reproduced with permission from Li *et al.* (2025).[31]

The IEM, typically applied to small-molecule analytes, suggests that after a charged droplet exits the Taylor cone, compact, pre-charge species desorb directly from the droplet.[26] This mechanism proposed by Iribarne and Thomson suggest three main factors influence the activation energy, such as (a) attraction between the escaping ion and the solvent by which the droplet is composed, (b) Coulomb repulsion of the escaping ion by the remaining charges on the droplet surface, and (c) ion desolvation energy.[19,32,33] In contrast, the CRM posits that the ions form upon complete evaporation of nanodroplets to dryness. The desolvation of the droplet causes its charges to land on the analyte molecule and is retained in the gas phase.[19] Originally hypothesized by Dole *et al* (1968)[34], and expanded by Schmelzeisen-Redeker *et al* (1995)[35], that the analytes like proteins follow CRM model, because of the Rayleigh limit charging, which deals with the Rayleigh stability limit for coulomb fission of the charged droplet has the same radius as the analyte protein (Equation 1.1).[19] According to this model, folded proteins produce $[M+zH]^{z+}$ ions with charge states approximating the Rayleigh limit ($z \approx zR$).[26]

$$r_{\text{droplet}} \approx r_{\text{protein}} \quad (1.1)$$

Lastly, the CEM offers an alternative pathway for proteins unfolded in solution.[29,30] In this model, proteins are expelled from the droplet due to electrostatic repulsion, particularly when hydrophobic residues are exposed to the solvent, causing the unfolded protein to migrate to the droplet surface.[26] This configuration allows the unfolded protein chain to accommodate many mobile protons (H^+), resulting in a protein with a significantly higher charge upon ejection.[26]

1.2.2 Quadrupole and Time-of-Flight Mass Analyzers

Once ions have entered the gas phase, they are guided into the mass analyzer, where the ions are separated based on their mass-to-charge (m/z) ratios and then transferred to the detector. The detector converts the electrical signal into a digital output, a chromatogram or mass spectrum. A wide range of mass analyzers is commercially available, including quadrupole (Q) and time-of-flight (TOF), as well as hybrid configurations like the quadrupole-time-of-flight (Q-TOF) analyzers, such as the Waters Synapt G2-S, which was used to collect the data for Chapter 2 of this thesis.

While quadrupoles provide excellent selectivity and robustness, they typically exhibit moderate resolving power (~20000 FWHM)[36], making them only suitable for the mass analysis of relatively simple mixtures or targeted quantitation in complex matrices. As stand-alone analyzers, their resolution can be limiting, particularly for complex samples.[12,21] To counter this drawback, tandem mass analyzers, where a combination of two or more mass analyzers are used. Some examples are the triple quadrupole (QQQ), which is placed in series, with the first(Q1) and third(Q3) quadrupole mass filters, and the second(Q2) is used as a collision cell.[21] Quadrupoles are also integral components in hybrid instruments, such as Q-TOF systems, where they function as mass filters, selecting ions within a narrow m/z range before downstream analysis by high-resolution analyzers.[37] This configuration significantly enhances the instrument's overall selectivity and sensitivity by isolating precursor ions for subsequent fragmentation.

In contrast, TOF analyzers separate ions based on the time required to traverse a field-free drift tube. All ions are accelerated to the same kinetic energy ($E=1/2mv^2$), resulting in lighter ions achieving higher velocities than their heavier counterparts.[38] This mass-dependent variation in ion velocity allows for the separation as ions traverse the drift region of the time-of-flight (TOF) analyzer. By measuring the time taken for ions to travel from the pusher to the detector, the mass-to-charge (m/z) ratio can be calculated using Equation 1.2, where U denotes the pusher voltage, l is the flight path length, and t represents the measured time-of-flight.[39]

$$\sqrt{\frac{m}{z}} = \frac{t\sqrt{2eU}}{l} \quad (1.2)$$

Unlike quadrupoles, TOF instruments simultaneously capture the entire mass spectrum through pulsed ion introductions, providing broad mass range coverage and rapid data acquisition. However, early TOF systems suffered from relatively poor mass resolution, limiting their utility for high-precision measurements. This limitation was addressed mainly with the development of reflectrons in the 1970s. Reflectrons, or ion mirrors, consist of a series of gridless mirrors that generate retarding electric fields, reversing the path of incoming ion packets. Ions with the same m/z but varying kinetic energies penetrate the reflectrons to different depths, correcting for initial energy spread and refocusing ions onto the detector.[40] This process significantly sharpens peak resolution and enhances mass accuracy, extending the observable mass range of TOF instruments. Reflectrons can further improve separation by increasing the effective path length in each instrument, enhancing the separation of closely spaced ions, including isotopic variants.[40]

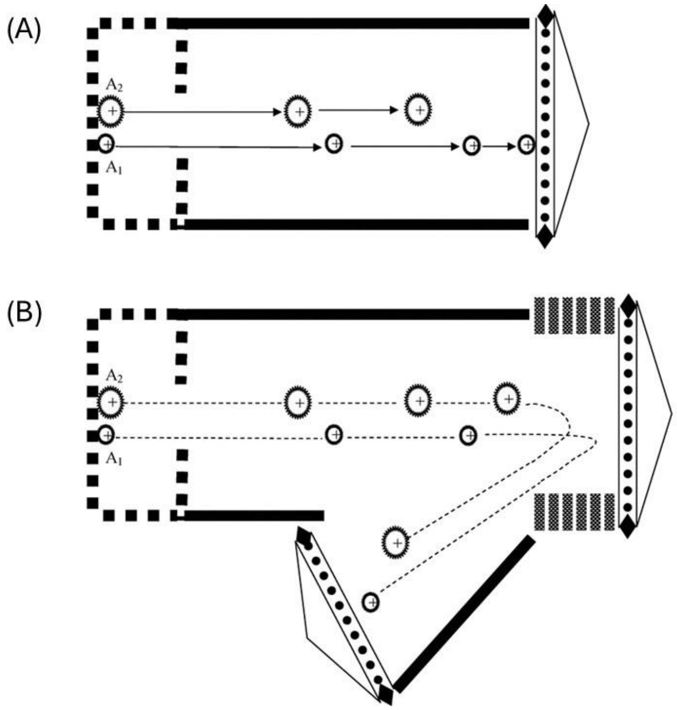

Figure 1.4| Schematic representation of Time-of-flight mass analyzer. (A) Conventional TOF, (B) a reflectron-type TOF. Reproduced with permission from El-Aneed *et al*. (2009).[21]

1.2.3 Ion Mobility Spectrometry (IMS): Principles and Instrumentation

Ion mobility spectrometry (IMS) provides an additional dimension of gas-phase separation by distinguishing ions based on their mobility through a neutral buffer gas under the influence of an electric field. In its most fundamental form, ions are pulsed into a drift tube filled with a buffer gas, such as helium or nitrogen, and are separated as they traverse the tube at different velocities.[41] Ion-gas interactions dictate these velocities, and the resulting drift times are recorded at the detector as an ion current over time. Although IMS alone does not rival the mass resolution or mass accuracy of high-performance mass analyzers, it is increasingly incorporated as a complementary technique in hybrid instruments, such as the Waters Synapt G2-Si and Select Series Cyclic-IMS, to enhance structural resolution and molecular characterization (Figure 1.5).[41–44]

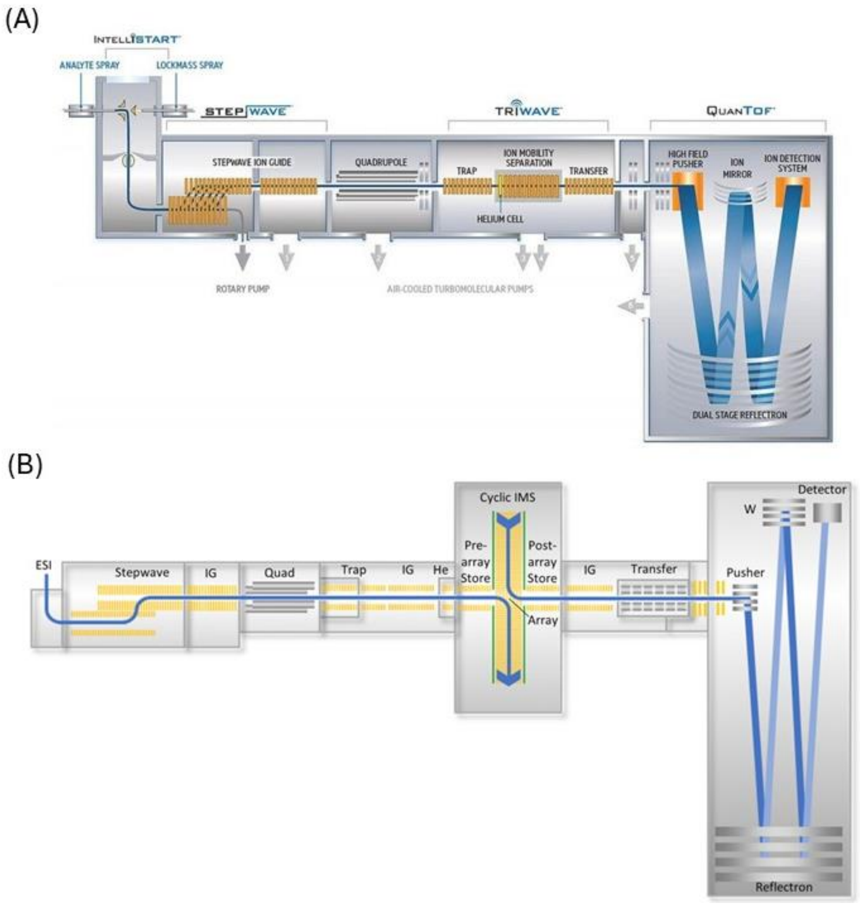

Figure 1.5| Schematic representation of the Synapt G2-Si and Cyclic-IMS configuration. (A) The hybrid mass spectrometer, Waters Synapt G2-Si, is equipped with both a quadrupole and TOF mass analyzer and has fragmentation and size separation (IMS) capabilities. Reproduced with permission from Williams *et al*. (2021).[44] (B) Q-cIMS-TOF, Waters Select Series Cyclic-IMS MS. Reproduced with permission from Giles *et al*. (2019).[42]

In IMS, an electric field propels ions through the separation chamber while colliding with a counter-flowing buffer gas. The ion mobility (K) is the proportionality between the ion's drift velocity (V_d) and the applied electric field, E, as shown in Equation 1.3.[42,43,45] The ion's velocity is linked to an observable measurement of the time (t_d) the ion takes to traverse and the length (l) of the mobility cell. However, the effective mobility is influenced by various parameters, including the ion's charge, reduced mass, temperature, buffer gas density, and the ion's collisional cross section (CCS, Ω).[43] The Mason-Schamp equation (Equation 1.4) integrates these parameters to provide a more accurate physical model of ion mobility behaviour in the gas phase.[43,45,46]

$$K = \frac{V_d}{E} = \frac{l}{t_d E} \quad (1.3)$$

$$\mathrm{K} = \frac{3}{16}\sqrt{\frac{2\pi}{\mu k_B T}} * \frac{ze}{N\Omega} \quad (1.4)$$

IMS devices are commonly classified based on the mechanism by which the electric field is applied. Drift tube IMS (DTIMS) employs a uniform electric field, allowing direct correlation between drift time and CCS (Figure 1.6A).[47] In this setup, smaller or more compact ions experience fewer collisions and thus transit the drift tube more quickly than larger or more extended ions, resulting in shorter drift times.

In contrast, Travelling Wave IMS (TWIMS) utilizes a series of pulsed low-voltage waves that push ions forward through stacked ring electrodes.[48] Smaller and more mobile ions effectively "ride" the wavefronts, while larger ions lag behind (Figure 1.6B). Since the motion of ions in TWIMS is influenced by wave height and velocity, the term arrival time is used rather than drift time. As a result, CCS values in TWIMS cannot be directly calculated and instead require calibration using known standards, typically derived from DTIMS.[43,47]

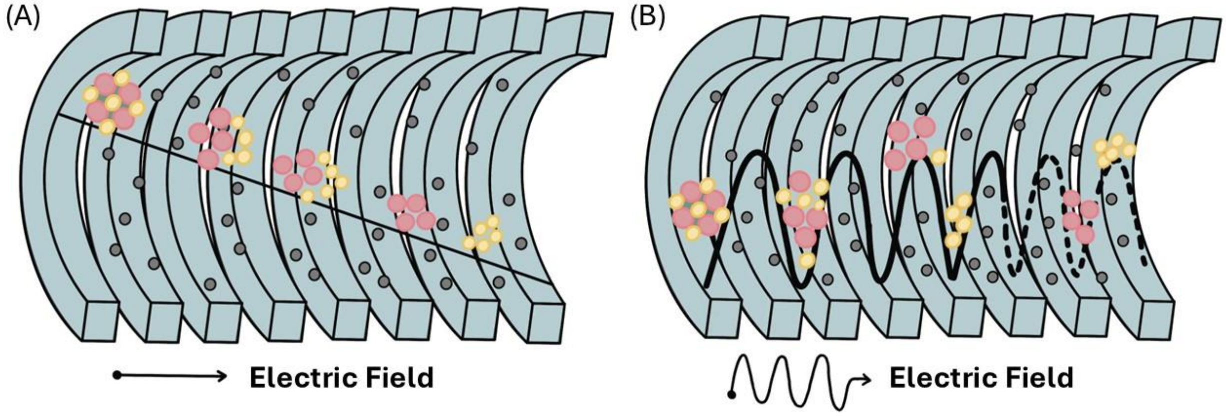

Figure 1.6| Separation of different techniques of ion mobility spectrometry (IMS). (A) Drift tube IMS (DTIMS), (B) Travelling Wave IMS (TWIMS). Reproduced with permission from Christofi and Barran. (2023).[47]

A more recent innovation, the Waters Select Series Cyclic-IMS (cIMS), features a closed-loop or "racetrack "configuration that permits ions to make multiple passes through the mobility separation region.[48] When coupled with HDX and front-end liquid chromatography (LC), cIMS offers improved sequence coverage for protein analysis compared to conventional linear IMS systems such as the Synapt G2-Si.[42,49] However, extended path lengths can increase ion losses, gas-phase heating, activation or fragmentation, and reduce sensitivity.[42,48]

Additionally, cyclic designs may introduce “wrap-around” effects, in which faster-moving ions overtake slower ones, complicating data interpretation.[42]

1.2.4 Gas-Phase Fragmentation for Structural Elucidation in Proteomics

Fragmentations of gas-phase analyte ions play a pivotal role in structural elucidation, particularly in bottom-up HDX. In this approach (detailed further in Section 1.3.2), proteins are enzymatically digested into peptides before being introduced into the mass spectrometer. The resulting peptide precursor ions are then analyzed by tandem mass spectrometry (MS/MS), where fragmentation patterns—consisting of product ions—allow researchers to deduce the peptide sequence and reconstruct the primary structure of the original protein.[50]

The gradual refinement of MS/MS techniques created the basis for peptide sequencing by MS, which has become increasingly powerful over the last two decades due to the improvement of LC techniques in combination with ESI.[50] MS/MS analysis mode involves selecting a specific precursor ion in the quadrupole mass filter, followed by collision-induced dissociation (CID) within a dedicated collision cell.[51] This process generates fragment ions that are subsequently analyzed in the second stage of mass spectrometry (MS^2). Fragmentations of peptide ions following CID occur predominantly at the peptide backbone by proton-induced fragmentation reactions.[52] In theory, peptide backbone cleavage can generate six distinct fragment ions: the N-terminal a-, b-, and c- ions and the C-terminal x-, y-, and z- ions (Figure 1.7).[22,50,53] However, under CID conditions, cleavage predominantly occurs at the amide bonds of the peptide backbone, producing primarily b and y ions.[53] These ion types dominate MS^2 spectra and serve as a key signature for peptide sequencing.[50]

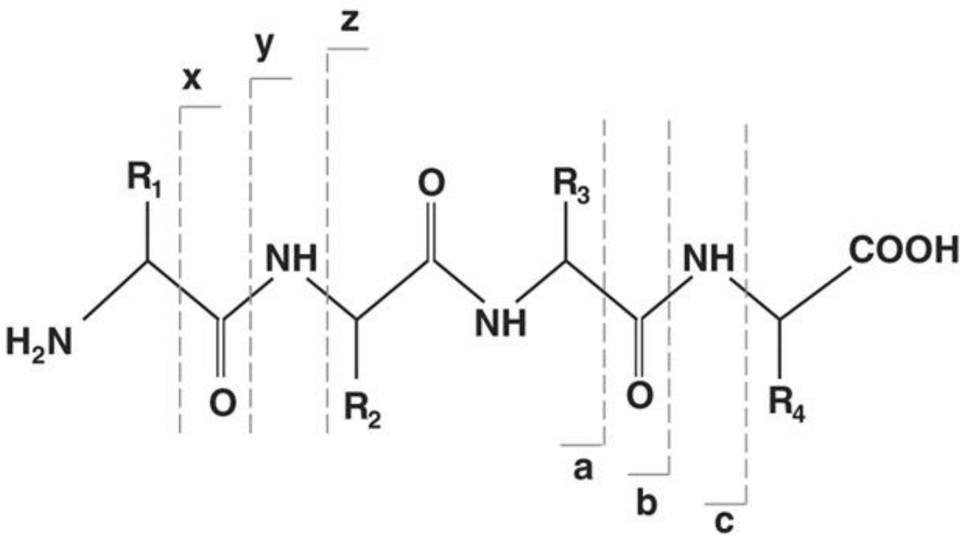

Figure 1.7| Nomenclature of sequence specific peptide fragments. CID cleavage of peptide backbone; a-, b-, and c- type ions containing the N-terminus; x-, y-, and z- ions contain the C-terminus. R_1, R_2 and R_3 represent the side chains of the amino acid residues. Reproduced with permission from Seidler *et al*. (2010).[50]

CID operates on the principle of gas-phase ion activation through collisions. When precursor ions collide with inert gas molecules (commonly Argon(Ar), Helium(He), or Nitrogen(N_2)), kinetic energy is converted into internal vibrational energy within the ion.[52] This vibrational excitation can lead to unimolecular dissociation, producing characteristic fragment ions.[50,54] The quasi-equilibrium theory (QET)[55] and the Rice-Ramsperger-Kassel-Marcus (RRKM)[56] theory provide a foundation framework for understanding unimolecular dissociation of ions in the gas phase under high vacuum conditions. These theories assume that the internal energy of an ion is statistically distributed among its available degrees of freedom- including vibration, rational, translation and electronic modes- which are treated as independent oscillators.[54] Molecular dissociation is described on a multidimensional potential energy surface, where the system evolves from reactants to products by crossing an energy barrier corresponding to a transition state (Figure 1.8).[54] This mechanistic framework is illustrated by the dissociation of an ionized molecule, AB^+, upon collision with a neutral gas molecule, M. The initial collision produces a transient, energetically excited state $[AB^+]^*$. If sufficient internal energy accumulates, the ion can evolve to a transition state $[AB^+]^\#$ and subsequently fragment into product ions A+ and B (Equation 1.5).

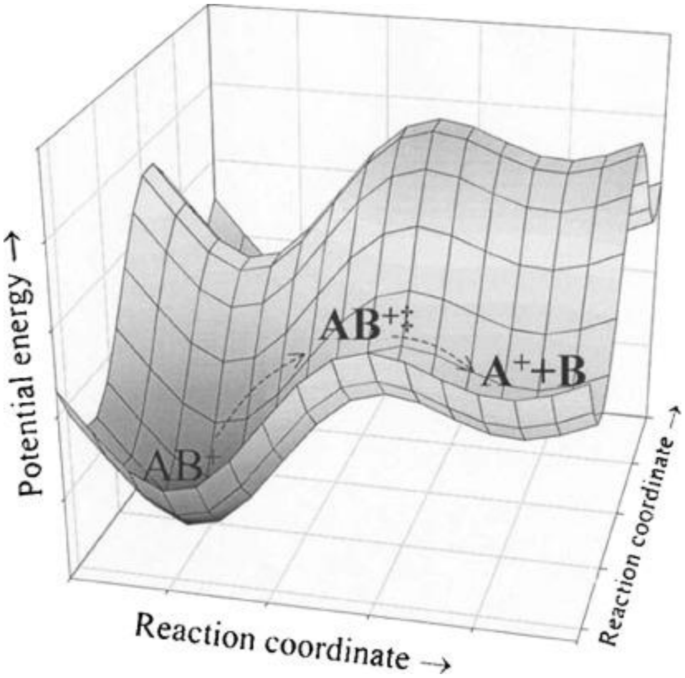

Figure 1.8| 3-dimensional potential energy surface illustration of possible dissociation pathways. Reproduced with permission from Sleno and Volmer (2004).[54]

$$AB^+ + M \underset{k_{-1}}{\overset{k_1}{\rightleftharpoons}} [AB^+]^* + M \xrightarrow{k_{critical}} [AB^+]^{\#} \overset{k_2}{\rightarrow} A^+ + B \quad (1.5)$$

In this equation, k_1 represents the rate of energy uptake through collision, $k_{critical}$ the rate of reaching the transition state, and k_2 the rate of bond dissociation.[54] According to the RRKM theory, the redistribution of energy within the ion is typically much faster than bond cleavage (i.e., $k_1 >> k_{critical} + k_2$), justifying the assumption of statistical equilibrium prior to fragmentation.[54] Importantly, larger biomolecules with greater internal degrees of freedom can store more vibrational energy, requiring more extensive activation to achieve fragmentation.[52,54] This statistical model explains the relationship between internal energy, molecular size, and fragmentation efficiency in gas-phase ion dissociation.

1.3 Analyzing Protein and Peptides Charge Envelopes using ESI-MS

Once the gas-phase ions enter the mass spectrometer, the corresponding ESI-mass spectrum represents the intact molecular species with variable charges. Proteins are ionized into multiple charged species for intact mass analysis, resulting in a pattern of peaks called the charge state envelope (Figure 1.9).[57] Each peak in the spectrum corresponds to a specific charge state z, and its measured mass-to-charge ratio (m/z, equation 1.6) is related to the analyte's neutral mass M.

.

$$\frac{m}{z} = \frac{M+z*m_p}{z} \quad (1.6)$$

where the mass of the uncharged protein, M, obtains several additional protons, n, and m_p is the mass of a single proton (~ 1.0073 Da). From the charge state envelope, one can determine the molecular mass of the analyte. First, two adjacent peaks are identified, m_1 and m_2, where the difference is the addition of a proton, and can therefore be written as:

$$m_1 = \frac{M+z*m_p}{z} \; and \; m_2 = \frac{M+(z+1)*m_p}{(z+1)} \quad (1.7)$$

The m_1 represents the peak with a larger m/z value, and the m_2 represents the peak with a smaller m/z value. Considering these peaks correspond to the same analyte, the mass, M, should be the same and therefore the two equations could be written as:

$$M = m_1 z - z*m_p \quad (1.8)$$

$$M = m_2(z+1) - (z+1)*m_p (1.9)$$

$$m_1 z - z*m_p = m_2(z+1) - (z+1)*m_p \quad (1.10)$$

Lastly, the charge of these two adjacent peaks can be determined by rearranging 1.11 for z.

$$z = \frac{m_2 - m_p}{m_1 - m_2} \quad (1.11)$$

Once the charge has been determined, the neutral mass of the analyte can be calculated by substituting the z back into 1.12 and rearranging for mass, M.

$$M = z*(m_1 - m_p) \quad (1.12)$$

Alternative deconvolution algorithms, such as maximum entropy (built into the MassLynx, Waters Corporation software)[58], or online tools, such as ESIprot[57], enable the determination of the neutral mass by taking the user's entered values of two or more m/z corresponding to peaks within the charge envelope and estimating possible integer values of charge states with the lower standard deviation.[57,59]

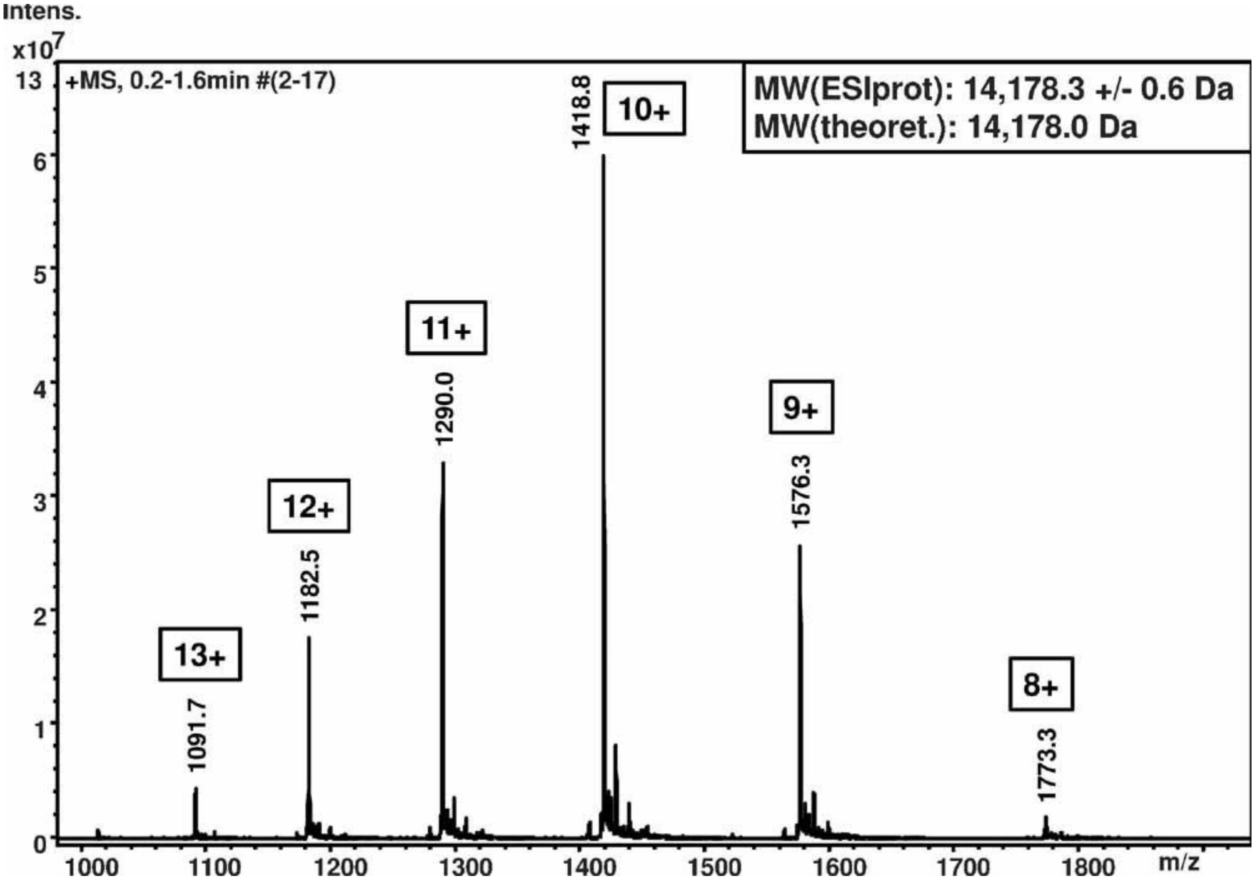

Figure 1.9| Charge state envelope for α-lactalbumin. ESI-MS spectrum with calculated charge states, with ESIProt mass determination in the insert. Reproduced with permission from Winkler *et al*. (2010).[57]

Whereas, on the other hand, important for the analysis of HDX-MS (discussed in 1.4), the resolving power of the MS instrument plays a crucial role in distinguishing minor mass differences, such as those between isotopic variants (e.g. ^{12}C vs. ^{13}C). In isotope distributions, the mass difference between two adjacent peaks is approximately 1 atomic mass unit (amu), more precisely 1.00335Da due to the mass of the neutron for ^{13}C relative to ^{12}C. The m/z spacing between these isotopic peaks is inversely proportional to the charge state of the ion, following the relationship:

$$\Delta\left(\frac{m}{z}\right) = \frac{1.00335\ Da}{z} \quad (1.13)$$

Thus, by measuring the spacing between the two adjacent isotopic peaks in high-resolution MS, the charge state, z, can be calculated:

$$z = \frac{1.00335\ Da}{\Delta(\frac{m}{z})} \quad (1.14)$$

For example, in Figure 1.10, using the peptide bradykinin 2-9 (sequence: RPPGFSPFP), the most intense (monoisotopic) peak appears at m/z 452.74, and the next isotope peak appears at m/z 453.24, showing a spacing of 0.50 Da. Using the formula:

$$z = \frac{1.00335\ Da}{\Delta(\frac{m}{z})} = \frac{1.00335}{(453.24-452.74)} \approx 2 \quad (1.15)$$

To the closed integer value, the bradykinin ion carries a +2 charge. Once the charge state is known, like intact mass, the neutral mass M of the peptide can be calculated using:

$$M = Z * \left(\frac{m}{z} - m_p\right) = 2 * (452.74 - 1.00728) \approx 903.5\ Da \quad (1.16)$$

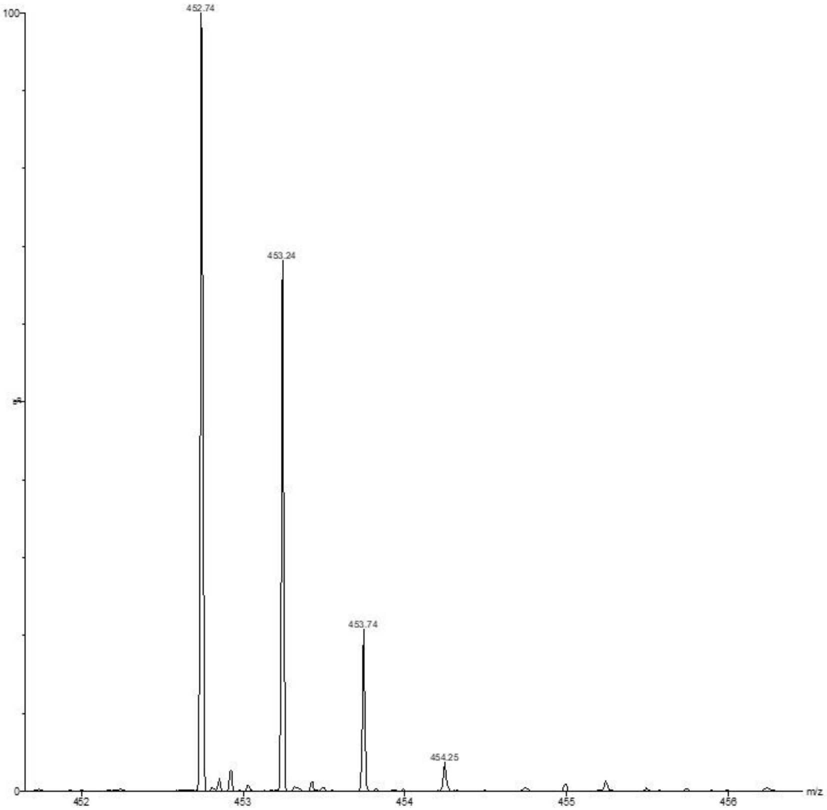

Figure 1.10|Mass spectrum of Bradykinin 2-9.

1.4 Hydrogen-Deuterium Exchange (HDX)

Hydrogen-deuterium exchange Mass spectrometry (HDX-MS) has been recognized as a powerful approach for characterizing protein conformational flexibility, complementary to conventional structural analyses, X-ray crystallography and NMR.[60–64] Unlike traditional structural methods, HDX-MS leverages the natural exchange of backbone amide hydrogens with deuterium when exposed to a deuterated solvent (e.g. D_2O).[61,65] For proteins, the labile hydrogens are continuously exchanging with the solvent, so when exposed to a deuterated solvent, the mass increase of approximately 1 atomic mass unit (amu) due to the isotopic exchange of a hydrogen to deuterium (+1 nucleus) is measured using a mass spectrometer.[65] The exchange rate is influenced by the hydrogen bonding network, secondary structure, and solvent accessibility, which provide insight into protein conformation and dynamics (discussed further in 1.4.2).[63,64] Comparing the deuterium uptake under different conditions, such as ligand-bound and unbound, allows researchers to identify structural dynamics, protein behaviours (unfolding), ligand-induced conformational shifts, and allosteric effects. Therefore, HDX-MS is a highly effective technique for studying proteins and their interactions in solution.[62,63,65]

1.4.1 Exploring the Chemistry Behind HDX: Amide Proton Exchange Mechanism

Hydrogens bound to heteroatoms, such as oxygen, nitrogen, and sulphur, are more readily available for isotopic exchange than hydrogens bound to carbon due to the electronegativity of the heteroatom.[61,65] It is the monitoring of exchange rates of the amide backbone employed in conventional HDX-MS experiments. Amide backbone hydrogens are distributed along the polypeptide backbone (except proline) and often participate in hydrogen-bonding networks of basic secondary structures (the α-helices and β-sheets).[61]

In general, the event of a proton transfer reaction depends on the diffusion-limited collision of a proton donor (AH) with a proton acceptor (B), and the success of this transfer is dependent on the collision rate and the proton affinity between the proton donor and the proton acceptor (Equation 1.17).[65] The overall forward rate constant for the proton transfer (k_{tr}) is given by Equation 1.18.[66]

$$AH + B \underset{k_{-1}}{\overset{k_1}{\rightleftharpoons}} A - H \cdots B \underset{k_{-2}}{\overset{k_2}{\rightleftharpoons}} A \cdots H - B \underset{k_{-3}}{\overset{k_3}{\rightleftharpoons}} A + HB \quad (1.17)$$

$$k_{tr} = k_1\left(\frac{10^{\triangle pK}}{10^{\triangle pK}+1}\right) = k_{int} \quad (1.18)$$

The success of proton transfer depends on the proton acceptor having a pK_a higher than the proton donor. The equation predicts that the larger the difference between the pK_a of the proton acceptor and donor, the greater the likelihood of successful proton transfer upon each collision. Overall, the success of proton transfer substantially depends on more than just the pK_a and the probability of a collision between acceptor and donor.[65,66] It is substantially dependent on whether the amide is protected or unprotected (participation in hydrogen bonding), the pH and temperature of the solvent, the primary sequence and lastly, the structure and dynamics of the protein (a.k.a. the breathing motions of the protein).

Proton transfer at unprotected amide hydrogens is sensitive to pH. The mechanism of exchange is primarily acid (H_3O^+), base (OH^-), or, to a small extent, water (H_2O), and the reaction mechanism is presented in Figure 1.11. In base catalysis (above pH 3), the amide (donor) proton is abstracted by an OH^- or, in a deuterated solvent, OD^-, by nucleophilic attack, producing the amidate anion. This amidate anion will be reprotonated by abstracting a proton from water (H_2O) or deuterated solvent (D_2O). Two mechanisms can occur in acid catalysis via N- or O-protonation. Acid catalysis via N protonation occurs in the exact mechanism as base catalysis, but only in the reverse order of protonation. The amide is initially protonated by H_3O^+ (or D_3O^+), followed by the deprotonation by H_2O or D_2O. For acid-catalysis via O-protonation, the amide carbonyl oxygen becomes protonated by H_3O^+ or D_3O^+, leading to an acidification of the NH proton. This allows the NH proton to be abstracted by water (or D_2O), producing an imidic acid, which subsequently can be protonated by H_3O^+ (D_3O^+) to form the amide. Since HDX can proceed via acid- and base-catalyzed mechanisms, the overall exchange rate constant (k_{ex}) is determined by the combined contributions of these intrinsic pathways, equation 1.19.[10,65–67]

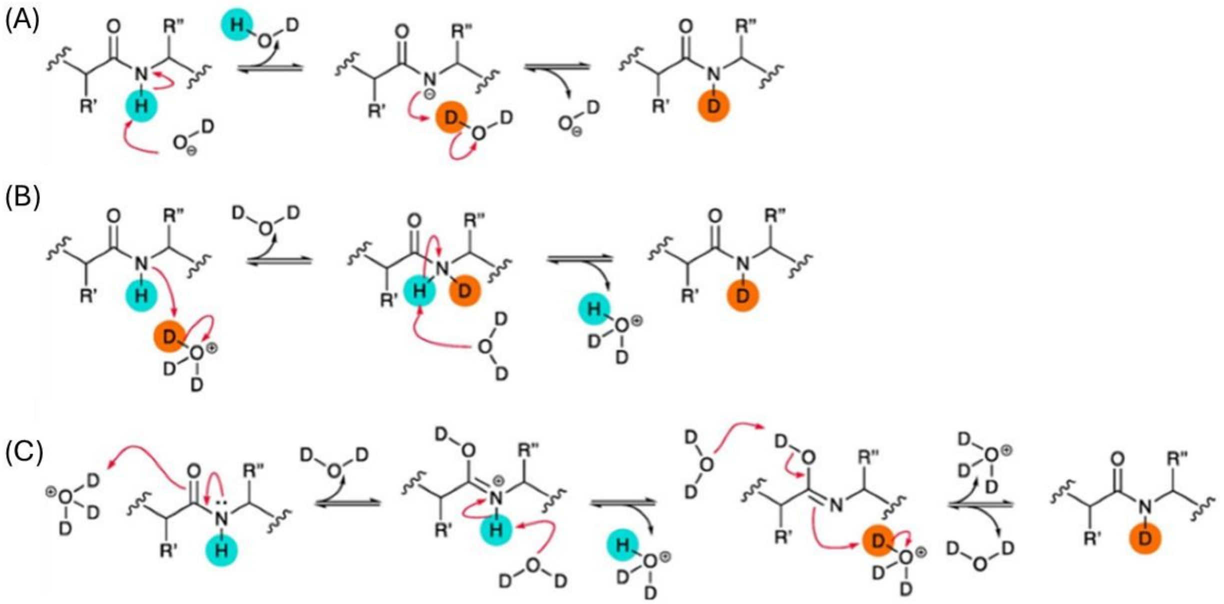

Figure 1.11| Reaction mechanism of base- and acid-catalyzed hydrogen exchange of backbone amide. (A) base catalysis, (B) Acid catalysis via protonation of the peptide group N-atom, (C) Acid catalysis via protonation of the peptide group O-atom. Reproduced with permission from Oganesyan *et al*. (2018).[67]

$$k_{ex} = k_{int,acid}[D_3O^+] + k_{int,base}[OD^-] + k_{int,water} \quad (1.19)$$

Each amino acid has an associated intrinsic exchange rate—often used interchangeably with the chemical rate constant—which defines the rate at which an amide hydrogen exchanges with solvent in the absence of any stabilizing secondary or tertiary protein structure. Various factors influence this rate, including pH, temperature, pressure, ionic strength, and the chemical nature of neighbouring residues.[65,66]

The seminal work from Englander's lab laid the groundwork for understanding hydrogen-deuterium exchange (HDX) as a tool for probing protein structure and dynamics.[68,69] In particular, Bai *et al*. (1993) used 1D NMR spectroscopy to investigate how the intrinsic rate constants for the acid-, base-, and water-catalyzed reaction affects the hydrogen exchange rate of the central amide hydrogen of poly-DL-alanine (PDLA).[70] Experimentally, they exposed the peptide to deuterated solvent and monitored the decay of the NH proton signal over time – a direct readout of hydrogen-to-deuterium exchange as the ND form does not produce a detectable proton signal in the same spectrum region. The rate constant were then determined as $k_{int,acid}$=

41.67 M^{-1} min^{-1}, $k_{int,base}$= 1.12x10^{10} M^{-1} min^{-1}, $k_{int,water}$= 3.16x10^{-2} M^{-1} min^{-1} for poly-D, L-alanine peptide at 20°C, in low salt conditions.[70]

Expanding on this approach, they systematically measured exchange rates for all 20 amino acids across a range of solution pH values. The data produced a characteristic V-shaped curve when the amino-acid-averaged log (exchange rate) was plotted against pH (Figure 1.12A).[65–67,71] This relationship revealed three key principles of proton transfer in the context of hydrogen exchange: (i) at pH values near or above physiological conditions (pH 5-8), proton transfer is predominantly base-catalyzed; (ii) the slowest exchange rate occurs at approximately pH 2.7, corresponding to the minimum point on the curve; and (iii) at pH values below ~3, proton transfer becomes predominantly acid-catalyzed, as the concentration of OD^- (the base form in deuterated solvent) is insufficient to drive the base-catalyzed pathway.[67,71]

Temperature significantly impacts hydrogen exchange rates, primarily influencing the water ionization constant, k_w. As temperature increases, the ionization of water increases, leading to higher concentrations of both H^+ (protons) and OH^- (hydroxide ions) in solution.[66] Since both acid- and base-catalyzed pathways rely on these ions to promote exchange, the elevated concentrations accelerate the exchange rate. The intrinsic exchange rate and temperature relationship follows an exponential dependence, as described by 1.20 and illustrated in Figure 1.12B.[65–67]

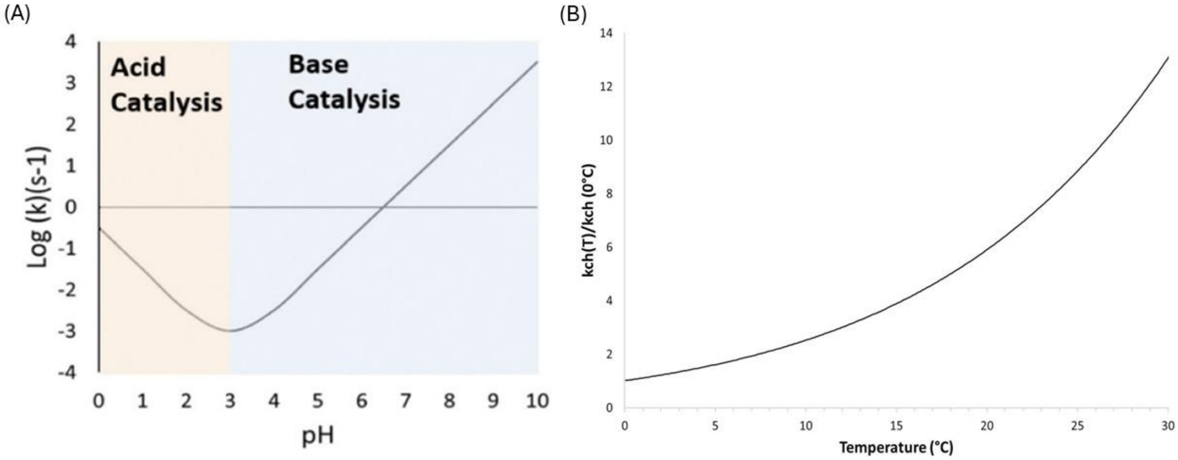

Figure 1.12| The effects of pH and temperature on the success of proton transfer. (A) The intrinsic rate of exchange (k_{ch}) of poly-DL-alanine (PDLA) depends on pH. Reproduced with permission from Brown and Wilson. (2017).[71] (B) The intrinsic rate of amide exchange as a function of temperature for base-catalyzed exchange. Reproduced with permission from Oganesyan *et al*.(2018).[67]

$$k_{ch}(T) = k_{rc}(293)exp(-\frac{E_a}{R}[\frac{1}{T} - \frac{1}{293}]) \text{ (1.20)}$$

Beyond the effects of pH and temperature, the neighbouring side chains in the peptide sequence can cause inductive and steric effects on the chemical exchange rate.[65,66] For example, if the amide hydrogen is flanked by two bulky side chain amino acids, i.e., the isobutyl group of isoleucine, it would cause a steric effect by blocking solvent accessibility, and therefore slowing down the rate of exchange compared to if two alanine side chains flanked the same amide hydrogen. For inductive impact, if the amide hydrogen is flanked with polar side chains, it increases the acidity, thereby accelerating the abstraction of amide proton by OH^- during base-catalyzed exchange.[72]

1.4.2 Amide Hydrogen Exchange in Folded Proteins

Understanding the factors that influence amide HX rates provides valuable insight into the structural characteristics of unfolded and folded polypeptides. Amides of unstructured peptides readily exchange at this determined intrinsic exchange rate because (i) the backbone amide hydrogen is accessible to the solvent, and (ii) it is free from any intra- and intermolecular interactions. Meanwhile, amide hydrogens of a natively folded protein can form a hydrogen bond with backbone carbonyl oxygen to form secondary structures and, therefore, may be protected from undergoing HX at the intrinsic rate.[73]

Since the 1950s, recognizing that proteins are dynamic rather than static structures has significantly advanced our understanding of HDX.[11,74] Pioneering work by Linderstrom-Lang, Aase Hvidt, and colleagues established a fundamental link between protein conformational dynamics and the exchange behaviour of amide hydrogens in folded proteins.[66,75] This concept remains relevant today (that H-bond fluctuations govern HDX). Although amide hydrogens in structured regions exchange 1-2 orders of magnitude more slowly than those in the unstructured areas, they can still undergo HDX.[65] According to the Linderstrom-Lang model, proteins experience transient structural fluctuations or local/global unfolding events that temporarily disrupt hydrogen bonding and are solvent accessible.[75] During these brief moments, the local protection is lost, exposing the amide's hydrogen that can readily exchange with the solvent. In this transiently unfolded state, the exchange rate of these protected hydrogens approaches their intrinsic rate as if they were in a fully unstructured conformation. The following equation, equation 1.21, illustrates how an amide hydrogen within a folded protein can exchange with deuterated solvent through transient “breathing” motions, represented by structural opening (op) and closing (cl) events.[65,66,73]

$$cl(H) \underset{k_{cl}}{\overset{k_{op}}{\rightleftharpoons}} op(H) \underset{D_2O}{\overset{k_{ch}}{\rightarrow}} op(D) \underset{k_{op}}{\overset{k_{cl}}{\rightleftharpoons}} cl(D) \ (1.21)$$

The observed HDX rate constant (k_{obs}) of an amide hydrogen in a structured region is thus governed by two factors: (i) the unfolding and folding event, and (ii) the intrinsic exchange rate, equation 1.22. For completely disordered proteins, all regions are effectively in the open state; therefore, the observed HDX exchange rate can be simplified to $k_{obs} = k_{ex}$.[10,65,66] Whereas folded protein rapidly returns to the folded state, where $k_{cl} >> k_{op}$, equation 1.23 better reflects native steady-state conditions.

$$k_{obs} = \frac{k_{op}k_{ch}}{k_{op} + k_{cl} + k_{ch}} \ (1.22)$$

$$k_{obs} = \frac{k_{op}k_{ch}}{k_{cl} + k_{ch}} \ (1.23)$$

The reduction in HX of protected amides is termed the “protection factor” (PF), equation 1.24. The protection factor provides a quantitative value that measures how much slower a particular amide hydrogen (in a folded region) exchanges with deuterium than if it were fully exposed (in an unfolded region). Therefore, the larger the protection factor, the more structure that region has.

$$PF = \frac{k_{ex}}{k_{obs}} \geq 1 \ (1.24)$$

During HDX experiments, measurements occur over timescales in which proteins undergo multiple opening and closing events. Two kinetic regimes can be observed depending on the relative rates of these conformational fluctuations and the chemical exchange steps: EX1 and EX2. In the EX1 regime, the rate of structural closing (k_{cl}) is much slower than the rate of chemical exchange (k_{ch}), such that $k_{cl} << k_{ch}$.[11,76] Once a protein region opens, all access amide hydrogens exchange before the structure recloses. As a result, the observed exchange (k_{ex}) is determined solely by the unfolding rate (k_{op}), and the exchange is independent of the chemical rate. Therefore, the exchange rate is simplified to: $k_{ex} = k_{op}$. Under native conditions, however, proteins are typically well-folded and stable. In these cases, the closing rate is much faster than the chemical exchange step ($k_{cl} >> k_{ch}$), placing the system in the EX2 regime.[76] Here, amide hydrogens only exchange during the brief period that the structure is transiently open. The observed exchange rate depends on the equilibrium constant for opening and the chemical exchange rate, Equation 1.25. This relationship allows for a quantitative analysis of protein conformational dynamics. Since the equilibrium constant k_{op} is linked to the free energy of opening (ΔG_{op}), HDX measurements provide insights into protein regions' thermodynamic stability and flexibility.[10,65,66]

$$k_{ex} = k_{op}k_{ch} = \frac{k_{op}}{k_{cl}}k_{ch} \ (1.25)$$

Figure 1.13 illustrates the distinct signatures of EX1 and EX2 kinetics observed in conventional HDX-MS experiments. In the EX1 regime, the protein unfolding (or opening) event is slower than the chemical exchange step. As a result, once the structure opens, multiple amide hydrogens exchange with deuterium simultaneously before the region recloses. This leads to a characteristic bimodal distribution in the mass spectrum. Two distinct isotopic envelopes are observed: (i) a lower-mass envelope corresponding to molecules that have not undergone exchange (i.e. remained folded), and (ii) a higher-mass envelope corresponding to molecules that have exchanged (i.e. unfolded).[10,65,67,76]

In contrast, under EX2 conditions, the refolding (closing) rate is much faster than the chemical exchange rate. Therefore, amide hydrogens exchange gradually during repeated, transient opening events. This creates a smoothly shifting isotopic envelope throughout the labelling time course. The centroid of this envelope gradually increases in mass-to-charge (m/z) as more protected amide hydrogens undergo exchange over time.[10,65,67,76]

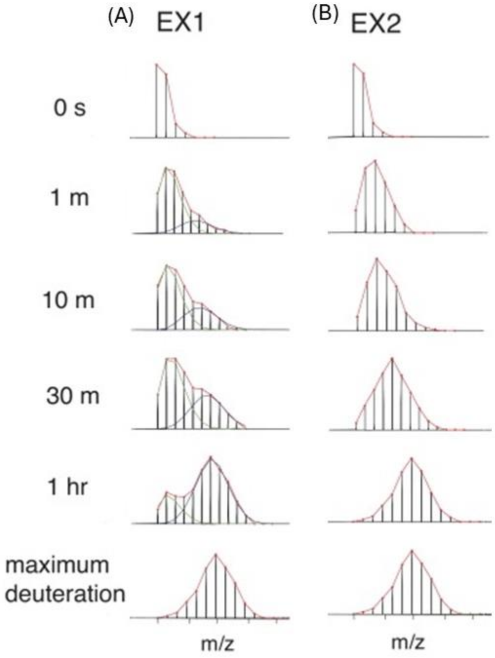

Figure 1.13| Mass spectral signatures of EX1 and EX2 kinetics in HDX-MS. (A) EX1 kinetics occurs when interconversions between folded and unfolded conformations occur slower than the timescale of the HDX measurement. This results in a bimodal distribution of m/z values, reflecting separate populations of exchanged (unfolded) and unexchanged (folded) molecules. (B) EX2 kinetic occurs when the refolding rate is much faster than the intrinsic exchange of the amide hydrogen. This produces a binomial distribution, where the centroid of the isotopic envelope steadily increases in m/z as more amide hydrogens undergo exchange. Reproduced with permission from Zheng *et al*. (2019).[10]

In some rare situations, it has been observed that the rate of structural closing is neither significantly faster nor slower than the chemical exchange rate but rather comparable to it. Xiao *et al*. (2005) reported a bimodal distribution resembling EX1 kinetics, along with a gradual shift in isotopic envelope characteristic of EX2 kinetics. They termed this intermediate behaviour “EXX kinetics”.[77]

1.4.3 Bottom-up HDX Workflow for Protein Analysis

HDX-MS can be performed at global (whole-protein) and peptide-resolved levels, providing valuable insight into protein conformational dynamics in solution. At the peptide level, HDX-MS offers enhanced spatial resolution by mapping relative exchange rates across different regions of the protein structure. Depending on the approach, top-down, middle-down, or bottom-up, HDX-MS experiments can capture structural dynamics at varying depths (Figure 1.14). In top-down HDX (Figure 1.14A), peptide fragments are generated directly in the mass spectrometer through gas-phase fragmentation. Middle-down HDX-MS (Figure 1.14B) combines both strategies: initial peptides generated by protease digestion are followed by further fragmentation inside the mass spectrometer.[61] In bottom-up HDX (Figure 1.14C), peptides are produced by acid-active protease digestion following the quench step.

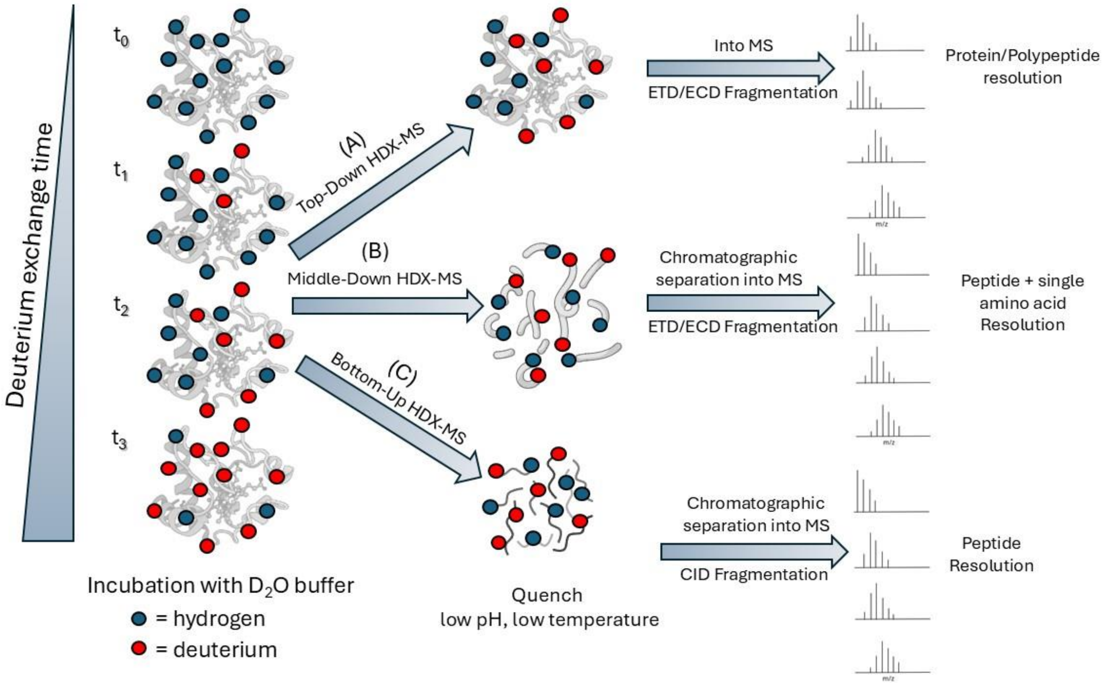

Figure 1.14| Representation of three primary methods of HDX-MS experiments. (A) top-down method, (B) middle-down method, and (C) bottom-up method.

The work presented in this thesis focuses specifically on bottom-up HDX-MS. As outlined in Section 1.3.1, the rate of amide hydrogen exchange is influenced by both uncontrollable factors (solvent accessibility, the hydrogen bonding network, and side-chain environment) and controllable parameters (pH, temperature, and deuteration time). Careful control of these parameters is essential to ensure accurate interpretation of HDX-MS data.

In a typical bottom-up HDX-MS workflow, the protein of interest is diluted into deuterated solvent and incubated for various time intervals during the labelling step.[78] This step is typically performed at or near physiological pH to preserve the protein's native structure. The exchange reaction is then quenched by lowering the pH to approximately 2.5-2.7, where the exchange rate reaches its minimum, followed by proteolytic digestion using an acid-active protease. The resulting peptides are usually desalted, separated via C18 reverse-phase liquid chromatography, and analyzed by mass spectrometry. Additionally, temperature directly influences the exchange rate, which is carefully controlled throughout the HDX-MS workflow. The protein is incubated at 25 °C during the labelling step, while all subsequent steps- including quench and digestion - are carried out at 0 °C and 15°C, respectively.[78,79]

At each step, inherent factors such as data quality, processing time, and back-exchange must be addressed, and these often require adjustment based on the specific protein analyte. The conditions below represent typical settings used in conventional bottom-up HDX-MS workflows that minimize back exchange, improve digestion, and increase protein sequence coverage and redundancy, to name a few. Optimizing these conditions allows data to provide structural information, a balancing act.

Adequate HDX-MS studies aim to generate the highest possible number of peptides, thereby maximizing both sequence coverage (the portion of the protein sequence monitored by HDX-MS) and redundancy (the number of unique peptides covering each amide position within the protein). Using denaturants, combining proteases, and optimizing liquid chromatography (LC) separation can significantly enhance peptide recovery and redundancy. Ideally, the protein should be fully denatured to facilitate efficient proteolytic digestion and to ensure optimal protease activity. However, many proteins are inherently destabilized at low pH and, as a result, may not require the addition of denaturants for effective digestion, especially within the time and temperature constraints of a typical HDX-MS workflow. When denaturants are necessary to promote unfolding and improve digestion, chaotropic agents, such as urea and guanidinium, are highly effective for HDX-MS applications.[80,81] Significantly, while high concentrations of these agents do not substantially impact back-exchange, they can inhibit protease activity. A two-step quench approach is typically employed to overcome this limitation: the deuterium-labelled protein is mixed with a high denaturant concentration to promote unfolding. It is then diluted before protease introduction to allow efficient digestion.[65] On the topic of improving digestion, if the protein contains a disulphide bond, the use of reducing agents may be effective. The reduction of disulphide bonds can be done through chemical reduction, such as using phosphine-based reducing agents. Tris 2-carboxyethyl phosphine (TCEP) is the most commonly used, as it retains moderate activity under HDX quench conditions.[82] Or through reduction, via electrochemical reducing cells (ERCs), where the protein flows through a pair of electrodes with oscillating potentials, reducing disulphide bonds.[83,84] The ERCs can be applied before or after digestion and are effective under quench conditions while maintaining low levels of back-exchange.[84]

Ideally, the protease of choice should generate many overlapping peptides, enabling analysis at the peptide-level resolution. However, the limited availability of proteases suitable for HDX-MS workflows presents a significant challenge. Porcine pepsin remains the most commonly used protease in HDX-MS experiments. In recent years, alternative acid-active enzymes have been explored, including aspartic proteases derived from *Nepenthes* carnivorous plants.[85,86] A homologue, nepenthesis II (nepII), has been shown to exhibit activity comparable to pepsin while offering enhanced resistance to denaturants.[85] This process is highlighted here, as most of the data presented in this thesis was generated using either a pepsin-only or a combined NepII-pepsin column. A defining characteristic of these proteases is their nonspecific cleavage behaviour, which produces many overlapping peptides while remaining active under HDX-MS conditions, including low pH, low temperature, and high-pressure environments. This lack of specificity is both an advantage and a limitation. While it facilitates broad sequence coverage, the lack of strict cleavage specificity complicates peptide identification and the reliable prediction of cleavage products.[65,85] Whether the protease is immobilized in-house or obtained commercially, developing immobilized proteases in a column format has proven highly advantageous over traditional in-solution digestion. One of the key benefits is the ability to achieve a significantly higher enzyme-to-substrate ratio, which enables efficient digestion within a relatively short timeframe, thereby minimizing back-exchange. The use of shortened digestion times also creates the opportunity to raise the temperature of the protease column, enhancing proteolytic activity without substantially impacting deuterium retention. For instance, in conventional HDX-MS workflows, the temperature of the digestion chamber is often increased from 0 °C to 15 °C to improve protease efficiency. Additionally, immobilizing the protease in a column format allows integration with high-pressure systems, such as liquid chromatography, further enhancing digestion efficiency and reproducibility under HDX-MS conditions.[65]

Typically, in bottom-up HDX workflows, digested peptides are first passed through a desalting column before being separated on a reverse-phase column for analysis. Although maintaining a quenched pH of 2-3 and a low temperature (0 °C) is relatively straightforward, these conditions often lead to poor chromatographic separation as peptides elute from the reverse-phase column. This challenge can be addressed through careful optimization of the elution gradient and, when available, incorporating ion mobility separation (IMS) to improve peptide separation. As previously discussed, amide hydrogens exchange with half-lives in the 30-120 minutes range, highlights the importance of keeping peptides' separation times as short as possible to minimize deuterium loss- a persistent analytical challenge. An LC gradient of less than 10 minutes for small proteins is typically sufficient for adequate peptide separation. However, peptide co-elution often becomes unavoidable for larger proteins, limiting both resolution and sequence coverage. Several research groups have proposed alternative strategies to optimize chromatographic conditions for HDX-MS peptide separation to address this.[87,88] For example, Venable *et al*. (2013) demonstrated successful LC separation at -30 °C, which enabled an extended 120-minute gradient without any measurable increase in back-exchange.[88] Historically, HDX-MS sample preparation was performed manually, which remains common in many laboratories. However, the complexity of coordinating multiple time points while maintaining strict conditions to minimize back-exchange has long posed a barrier to the entire automated HDX-MS workflow.

1.4.4 Time-Resolved HDX: Illuminating Transient Structural States

Intrinsically disordered proteins (IDPs) and regions (IDRs) play essential roles in numerous biological processes, yet their structural characterization remains challenging due to their highly dynamic and heterogeneous nature.[89,90] Focusing on HDX-MS, without stable amide hydrogen bonding in disordered regions, results in extremely fast exchange rates, often approaching the intrinsic chemical limits on sub-second timescales.[89,90] Therefore, access to shorter labelling timepoints is especially critical for capturing transient structure features. In addition, it is helpful in terms of looking at weak binding protein-ligand interactions, which may only perturb local solvent accessibility for a brief period before dissociation.

Therefore, to resolve rapid dynamics, specialized rapid-HDX workflows have been developed to allow precise control over mixing and labelling on the millisecond-to-second timescale. Recent advances in rapid-HDX instrumentation and workflow, which we reviewed in 2023 (Chow *et al*,.2023), highlighted the evolution of strategies to achieve this, including the use of microfluidic chips, narrow-diameter capillary-based mixers, and gas-phase analyte labelling techniques.[91] Historically, these methods required in-house apparatus, as no commercial systems were available. One such approach, time-resolved electrospray ionization HDX (TRESI-HDX), was pioneered by Wilson and Konermann and remains a technique in the Wilson Lab today.[92]

TRESI-HDX employs a capillary-based mixer coupled to an online proteolysis setup using a laser-engraved polymethyl methacrylate (PMMA) digestion chip (Figure 1.15A).[93] The incubation time is defined by the delay volume between the point at which the sample is introduced (through the notch) into the deuterated buffer (outer capillary) and its arrival at the quench mixer. Longer incubation achieved by increasing the distance of the inner capillary from the quench mixer. In addition, this use of syringe-based fluid delivery introduced flow instability under back-pressure, and the system's incompatibility with HPLC prompted ion mobility spectrometry for orthogonal separation. Before HDX-MS experiments, protein samples were exchanged in buffer into ammonium acetate to optimize ionization, despite its poor buffering capacity at physiological pH, which occasionally led to precipitation and clogging.

A breakthrough was achieved by Anacleto *et al*. (2023), with the integration of the TRESI-HDX platform to a conventional LC system equipped with an autosampler-mediated plug injection (Figure 1.15B).[94] Along with the improvements of replacing the PMMA digestion chip with a short, immobilized protease column, this significantly improved the robustness and reproducibility of HDX-MS experiments. This development marked a substantial step towards broader adoption of rapid-HDX methodologies, offering enhanced experimental stability, compatibility with conventional LC hardware and greater flexibility for studying a wider range of protein targets and buffer conditions.

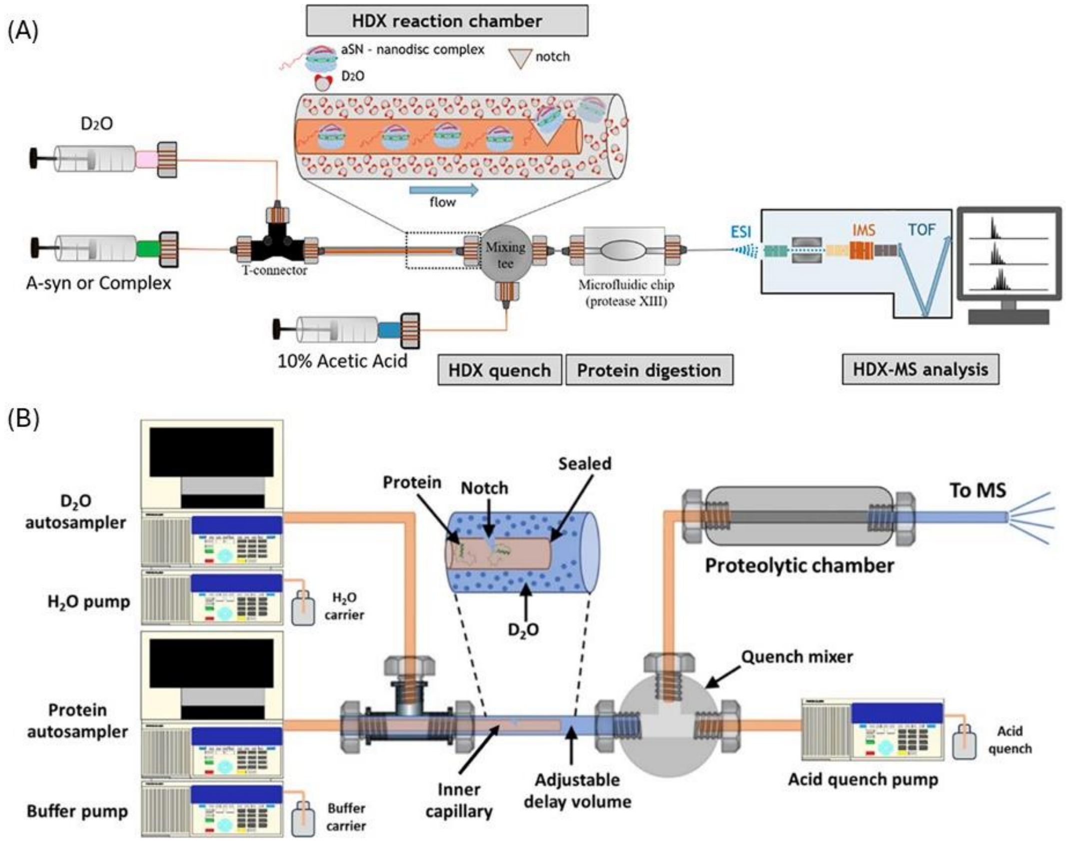

Figure 1.15| TRESI-HDX MS capillary-based mixer and experimental set-up. (A) Syringe-based fluid online bottom-up HDX using laser-engraved polymethyl methacrylate (PMMA). Reproduced with permission from Oganeyan *et al*.(2021).[93] (B) Schematic of automated TRESI-HDX. Reproduced with permission from Anacleto *et al*. (2023).[94]

1.4.5 Peptide Identification

The first step in the bottom-up HDX-MS experiments is peptide identification, achieved through data-dependent acquisition (DDA) or data-independent acquisition (DIA). Taking the peptides produced during the protease digestion from non-deuterated samples, the precursor peptides are fragmented by collision-induced dissociation (CID), which has been integrated into all modern MS platforms. This allows researchers to obtain MS/MS and HDX-MS measurements in a single platform. The abundant or most intense precursor ions are mass isolated and fragmented in data-dependent acquisition to obtain a clean MS/MS spectrum for all prevalent ions in the LC chromatogram.[95,96] In this approach, the process must be repeated several times to identify all the ions. Not to mention, it can be time-consuming considering the need to optimize the collisional energies. Often, DDA misses some low-abundant peptides during the initial survey scan and causes a threshold in the peptides that can be identified.[96,97]

While this method allows for identifying the peptides produced, it is the traditional approach. With advances in mass spectrometers used for HDX-MS, a data-independent acquisition allows for more identification, where MS/MS spectra are collected on as many observable peptides as possible. In DIA, the peptides are fragmented simultaneously, and their MS/MS spectra and precursor ions are assigned through alignment with their retention time. In addition, it can perform mobility separation, adding a separation dimension. Retention time and mobility separation improve resolving and characterizing low-abundance peptides.

Using processing software, such as ProteinLynx Global Server (PLGS) by Waters Corporation, the fragment ion spectra, along with the exact mass of the precursor ion, are used to predict peptide sequence from a digestion of a protein sequence database, while matching MS features, such as retention time and mobility.[98] Since most of the proteases selected for HDX-MS experiments are non-specific, the software considers cleavage after all residues when performing these peptide searches. Furthermore, it is crucial to identify potential post-translational modifications (PTMs), since they could alter the mass of several peptides.[99] That said, HDX-MS studies are typically performed on purified proteins, and database searches are generally restricted to the target protein, the proteases used for the sample processing, and any known contaminants. Dobb et al. published a comprehensive list of common protein contaminants originating from widely used expression and purification systems in structural proteomics to minimize the risk of false-positive identifications.[100]

1.4.6 Data Analysis for HDX-MS Experiments

Integrating peaks and calculating deuterium uptake is often analyzed by software independent from the software used to identify the observable peptide. The generated list of observed peptides is used in the next step of HDX-MS data analysis, which integrates the isotopic peak profiles from all the deuterated data. DynamX by Waters Corporation is the software commonly used to perform all data analysis represented in this thesis. The software uses retention and mobility time alignment algorithms to accurately extract clean, resolved peaks suitable for deuterium uptake analysis. It is common to lose some peptides (not analyzed) from the list due to various factors, including low signal-to-noise or spectral overlap, which occurs once species become deuterated. Another software that allows for the deuterium uptake calculation of peptides in two states is MassSpec Studio 1, created by Dr. David Schriemer's lab.[74,101]

Since mass spectrometry is an ensemble averaging technique, multiple individual protein/peptide molecules are averaged into a mass spectral envelope, which reflects the natural abundance of heavy isotopes (i.e. ^{13}C and ^{15}N). Since deuterium is a heavier isotope than hydrogen, it increases the mass envelope when proteins exchange hydrogens for deuterium. With the incorporation of deuterium in HDX experiments, the spectral envelope of deuterated samples shifts to a higher m/z, depending on the amount of deuterium exchanged with the amide backbone. However, the exchange is not uniform but resembles a binomial distribution. The area under the curve defines the magnitude of each spectral peak, and the weighted mean of the distribution can be calculated (Figure 1.16A, equation 1.26) to calculate the centroid of the mass spectral envelope.[66,74]

$$centroid = \frac{\sum m_i I_i}{\sum I_i} \quad (1.26)$$

Lastly, when multiplied by the charge, z, the difference between the nondeuterated centroid and deuterated centroid gives the average deuterium uptake value for the protein or a particular peptide (Figure 1.16B).[66,74]

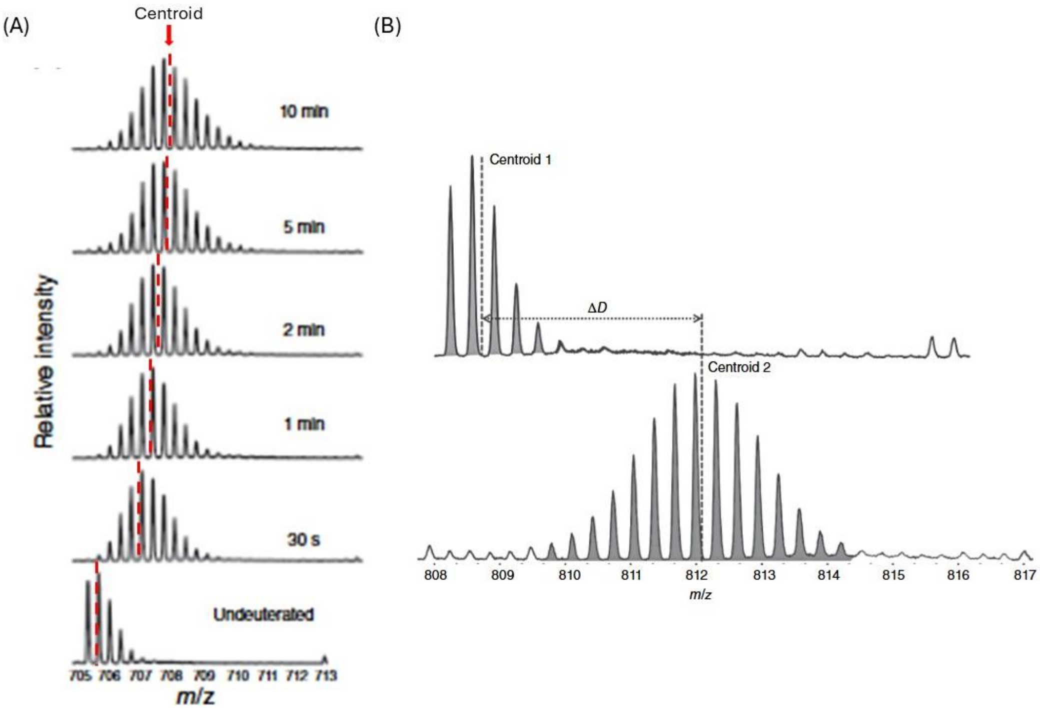

Figure 1.16| Example of a peptide spectrum undergoing HDX at various timepoints. (A) The centroid shift occurs as more deuterium is incorporated into the peptide with high exchange times. Adopted from Jensen and Rand.(2016).[66] (B) The difference between centroids of the deuterated spectral envelope (centroid 2) and the undeuterated spectral envelope (centroid 1) giving the average deuterium uptake value for a particular peptide (ΔD). Reproduced with permission from Wang *et al*. (2016).[74]

Finally, constructing kinetic plots provides information regarding the extent of the protein's structure and dynamics. Figure 1.17 outlines the predicted kinetic curves of (A) an unstructured peptide, (B) a structured peptide, and (C) a dynamic peptide.[102]

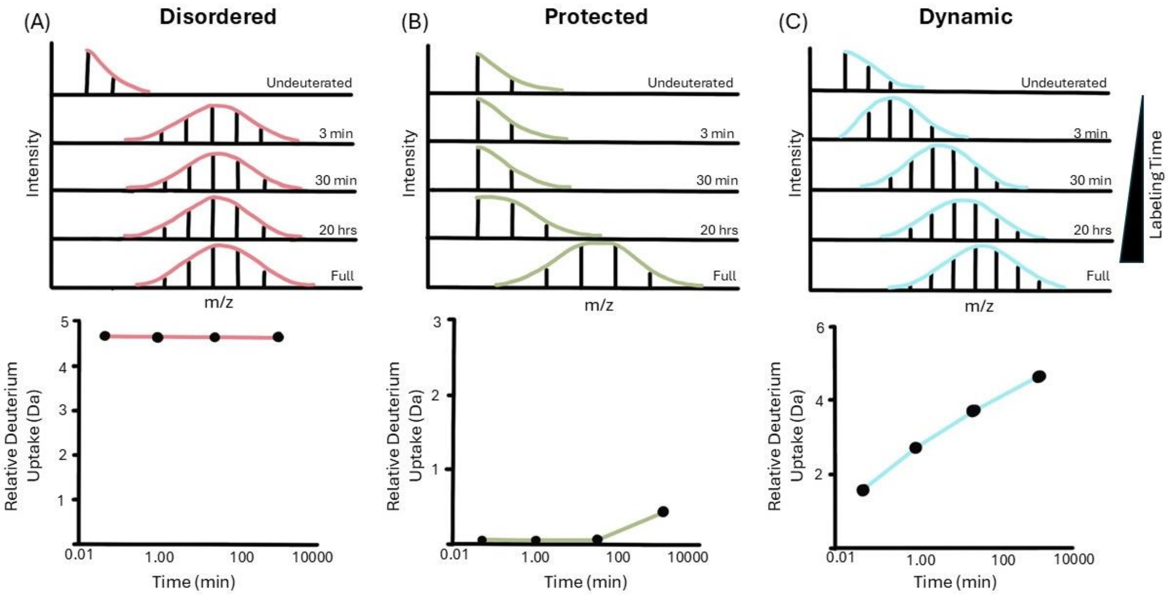

Figure 1.17| Three predicted HDX kinetic plots. (A) Peptide in a disordered region, (B) Peptide in a protected region, and (C) Peptide in a dynamic region. Reproduced with permission from Hodge *et al*. (2019).[102]

1.5 Application of HDX-MS in Drug Discovery

As mentioned previously, protein interactions are essential for understanding how molecular structures drive biological functions. These interactions, whether between proteins or with ligands, trigger conformational changes that enable processes like ion transport, signalling, and cellular regulation, making proteins drug targetable.[12] When studying these interactions, researchers are often interested in where the ligand or protein interaction occurs and how tightly this interaction is (i.e., binding affinity).[103] Almost all protein-protein interactions are usually non-covalent and reversible and exist in equilibrium among the relevant species in the solution, as depicted in Equation 1.27. As shown in equation 1.27, the shift from protein to complex depends on the on-rate constant (k_{on}), which depends on the concentration of the free protein and the free ligand.[104]

$$P + L \underset{k_{off}}{\overset{k_{on}}{\rightleftharpoons}} PL \; (1.27)$$

In HDX-MS experiments designed to study protein-ligand interactions, the on-rate constant (k_{on}) and off-rate constant (k_{off}) play a critical role in interpreting differential exchange patterns. The on rate depends on the free protein and free ligand concentration. At higher concentrations, the free ligand is more likely to encounter a free protein and bind, therefore reflecting how quickly a ligand associates with the protein.[65,104] While the off rate is concentration independent, it measures how rapidly the ligand dissociates. Together, these values define the dissociation constant, equation 1.28, which represents the binding affinity of the ligand for the protein. When the ligand binds tightly (low K_d) and the complex remains intact/ stable throughout the HDX labelling period, regions of the protein involved in binding or allosteric regulations often show changes in deuterium uptake. However, if the off rate is high (high K_d), the ligand may dissociate during the labelling step, leading to weaker or inconsistent protection patterns. Therefore, understanding the kinetic properties of the interaction is essential for designing HDX-MS experiments to map ligand binding sites accurately. Equation 1.29 determines how much protein-ligand complex (PL) has been formed depending on the total protein concentration(P_0), total ligand concentration(L_0) and the dissociation constant (K_d).[104,105] Achieving a complex stable state during the labelling steps allows accurate deuterium uptake kinetics between the protein's free (unbound) and bound states. It can localize and track the structural changes associated with the binding event.

$$K_d = \frac{[P][L]}{[PL]} = \frac{k_{off}}{k_{on}} \quad (1.28)$$

$$[\mathrm{PL}] = ([P_0] + [L_0] + K_d - \sqrt{([P_0] + [L_0] + K_d)^2 + 4([P_0][L_0])} \quad (1.29)$$

When looking at the structural dynamics of two states, protein-bound (holo state) vs. protein unbound (apo state), the kinetic curve for each state, precisely the difference in deuterium uptake between each state, provides information about the perturbations to the protein in the presence and absence of the ligand. Ligands with a high binding affinity to protein will either have a fast association time (large K_{on}) or a slow dissociation (small K_{off}); the kinetic curve between the bound and unbound state will persistently diverge (Figure 1.18B). In contrast, the opposite will occur for ligands with low binding affinities. Low-affinity ligands will cycle through association and dissociation during the labelling step of the HDX-MS experiment, and the kinetic curve will quickly converge (Figure 1.18A). This is due to the duration for which the ligand is dissociated from the protein, which exists in the apo conformation. Therefore, the labelling rate between bound and unbound will quickly represent the apo conformation. At the same time, HDX-MS is effective in characterizing the protein interface and ligand binding events, allostery, as a result of the binding mode, can be tremendously insightful (Figure 1.18C).

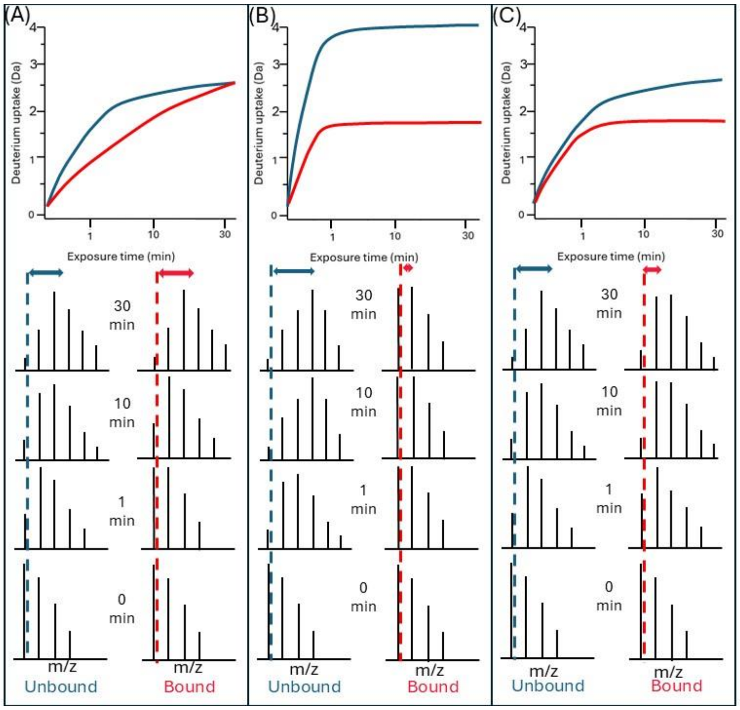

Figure 1.18| Deuterium difference kinetic curves. A)low-affinity binders, (B)high-affinity binders and (C)allostery effect

The difference in deuterium uptake can be expressed as the number of deuterons (Da) incorporated or as a percentage of relative fractional uptake (RFU, %, equation 1.30). To calculate the relative fractional uptake, the amount of deuterium incorporated (D) for a given peptide is divided by the number of exchangeable amides (N) in the peptide.[65] Given equation 1.31, the total number of exchangeable amides in the peptide (T) is subtracted by the number of prolines, if present, and by 1, for the N-terminus hydrogen, which rapidly back-exchange, multiplied by 100, for percentage. The majority of HDX-MS experiments are done with >80% deuterated solvents. However, in some rare cases, mentioned in section 1.3.3, where the amount of deuterated solvent is 50%, it is necessary to multiply the relative fractional uptake by 2 to account for the difference in dilution.

$$RFU\ (\%) = \frac{D}{N} * 100\%\ (1.30)$$

$$N = T - Pro - 1\ (1.31)$$

To quantify ligand-induced structural changes in HDX-MS experiments, we calculated the difference in deuterium uptake (ΔHDX) between bound and unbound protein states at each timepoint. This difference is defined as equation 1.32:

$$\Delta HDX_{time\ point} = \chi_{bound} - \chi_{unbound} (1.32)$$

Where χ represents the percent deuterium incorporation averaged across technical replicates.

To access variability, the standard deviation (σ) was calculated for each condition (bound and unbound) using three technical replicates, Equation 1.33;

$$\sigma_{bound\ or\ unbound} = \sqrt{\frac{(\chi_{technical\ replicate\ 1} - \overline{\chi})^2 + (\chi_{technical\ replicate\ 2} - \overline{\chi})^2 + (\chi_{technical\ replicate\ 3} - \overline{\chi})^2}{n}} \ (1.33)$$

The propagated error (P) associated with each (ΔHDX) value was then calculated as the root-sum-square of the standard deviations from the bound and unbound states, Equation 1.34;

$$P_{\Delta HDX} = \sqrt{(\sigma_{bound})^2 + (\sigma_{unbound})^2} \ (1.34)$$

To evaluate cumulative significance across multiple timepoints (60, 600, and 1800 sec), we summed the individual ΔHDX values to obtain a total uptake difference (ΔHDX_t) for each peptide, Equation 1.35;

$$\Delta HDX_t = \sum \Delta HDX_{60\ sec} + \Delta HDX_{600\ sec} + \Delta HDX_{1800\ sec} \ (1.35)$$

Along with the corresponding summed propagated error (P_t) was calculated by summing the individual propagated errors and multiplying by a factor of 3 to represent a 99.7% confidence interval, Equation 1.36;

$$P_t = 3\ x \sum P_{\Delta HDX_{60\ sec}} + P_{\Delta HDX_{600\ sec}} P_{\Delta HDX_{1800\ sec}} \ (1.36)$$

This conservation error propagation method preserves the statistical independence of each timepoint and avoids underestimating uncertainty in cumulative HDX differences.[103]

Lastly, various visualization options, such as heat maps or butterfly plots, are available. These tools are often used as an illustration summary of the deuterium uptake at different time points of the various peptides, where a gradient is used to display regions of protection or deprotection comprehensively. Furthermore, if high-resolution structures are available, such as X-ray crystal structures, the changes in HDX-MS patterns are illustrated on the 3D structure, obtained from the protein data bank (PDB) or AlphaFold[106] predictions, an open-access structural prediction software.[78]

1.6 Research Objectives

This work aimed to utilize HDX-MS to investigate protein conformational dynamics and interaction mechanisms across structurally and functionally diverse systems. In Chapter 2, we examined cytochrome c and its interactions with membrane-bound phospholipids. The aim is to elucidate how cardiolipin and analogous lipids modulate cytochrome c conformation during the early states of apoptosis. Using millisecond time-resolved HDX-MS with nanodisc-embedded lipid systems, we identified specific binding surfaces engaged by anionic phospholipids. Chapter 3 focused on two nuclear receptors, CAR and PXR, as well as the lipid hydrolase ABHD2. For CAR and PXR, we sought to define how structurally distinct ligands influence activation through differential stabilization of their ligand-binding domains. In PXR, we examined the potential for cooperative binding between FDN and steroidal ligands (E2, EE2). For ABHD2, we mapped the binding interface of two candidate inhibitors and to assess how mutation of the catalytic serine residue (S207A) altered conformational stability and ligand interactions. Lastly, in Chapter 4, we explored the relationship between structural dynamics and functional output by comparing agonist and inverse agonist activity in CAR, with particular attention to how heterodimerization with RXRα modulates these effects. These studies demonstrate the versatility of HDX-MS in capturing dynamic structural responses to diverse molecular interactions.

Chapter Two: Probing the Conformational Dynamics of Cytochrome C upon Interaction with Anion Phospholipid Nanodiscs using Hydrogen-Deuterium Exchange Mass Spectrometry

Vimanda Chow[1], Cristina Lento[1], and Derek J. Wilson[1]

[1]Department of Chemistry, York University, Toronto, ON, M3J1P3

This chapter has been published in Journal of the American Society for Mass Spectrometry 2025, 36(5), 1052-1059

V.C and D.J.W. contributed equally to writing the manuscript. **V.C.** conducted protein purification, size-exclusion chromatography, nuclear magnetic resonance, mass spectrometry and data processing. D.J.W. and C.L. provided supervision.

2.1 Summary

The interplay between the anionic phospholipid cardiolipin(CL) and cytochrome c (cyt c) holds significance in the early stages of apoptosis. Despite identification of up to four potential sites of interaction between cytochrome c and cardiolipin bearing membranes, the exact mode of interaction remains unexplained, especially given that some of the putative binding surfaces are mutually exclusive. In this study, we utilize millisecond time-resolved electrospray ionization hydrogen−deuterium exchange mass spectrometry (TRESI-HDX-MS) to investigate conformational and dynamic changes in cytochrome c in the presence of various phospholipids (1,2-dimyristoyl-*sn*-glycero-3-phosphocholine(DMPC), 1-palmitoyl-2-oleoyl-*sn*-glycero-3-phospho-1’-rac-glycerol (POPG), and CL) incorporated into nanodiscs. We observe that, among the proposed binding sites, the adjacent “L”- and “A”-sites exhibited a decrease in deuterium exchange, while the “N” site remained unperturbed, suggesting a specific orientation of cytochrome c with respect to cell membranes upon binding. We also demonstrate that negatively charged phospholipids with physical differences(i.e., POPG and CL) exhibit essentially the same interaction with cytochrome c, supporting the utility of POPG nanodiscs as a model for cytochrome c−membrane interactions.

2.2 Introduction

Proteins can undergo various changes in their structural conformation, depending on pathological and physiological processes within the cell. Therefore, it is essential to understand the shifts in structure and conformational dynamics proteins undergo to perform their biological functions. Cytochrome c (cyt c) is a common “model” protein that plays crucial roles in the mitochondrial respiratory chain and the early steps of cell apoptosis.[107–110] Under normal cell conditions, cyt c has been well characterized as a shuttle that transfers electrons from cyt c reductase (complex III) to cyt c oxidase (complex IV). Once the cell experiences stress, it may undergo the early stages of apoptosis, where cyt c acts as a peroxidase, resulting in the oxidation of cardiolipin, altering the fluidity of the inner mitochondrial membrane. The disruption in the normal packing of lipids within the membrane, results in the release of cyt c into the cytosol where apoptosomes are formed leading to cell death.[1,108,109,111,112] Over the past decade, many researchers have studied the involvement of cytochrome c in the early stages of apoptosis, where it undergoes a conformational change that converts it from electron carrier to active peroxidase.[113,114] This process is relevant for disease interventions, particularly in the wide range of pathologies involving cells that become insensitive to apoptotic signaling.[1,113]

In healthy cells, cyt c is a 12 kDa heme protein located in the inner mitochondrial membrane, where 15% is bound to an anionic phospholipid headgroup, cardiolipin (CL). The other 85% is free or loosely bound to the membrane via electrostatic interactions.[3,113,115] Upon cell stress, cyt c forms a complex with CL through four particular interaction sites: A-site, L-site, N-site, and C-site (Figure 2.1).[1,107,113,115] Upon complexation, cyt c unfolds into a non-native conformation that acts primarily as a peroxidase.[1,113,116,117] Although the physiology of cyt c has been understood for more than half a century, the mechanisms of cyt c/CL complex formation have remained underexplored and, where information is acquired, contentious.

There exists a degree of agreement in that the interaction is initially charge-driven, with positively charged amino acid residues of cyt c interacting electrostatically with the negatively charged phospholipid headgroups of the membrane.[108,112–114,118,119] Among the potential binding sites, it has been suggested that the A-site initiates complex formation through interactions involving Lys72, Lys63, Lys86, and Lys87 as key residues, followed by additional contacts within the C-site (Figure 2.1A).[113,119] The A-site interactions are thought to be primarily electrostatic, while the C-site is involved in hydrogen bonds and potentially hydrophobic interactions (through insertion of a lipid tail into the hydrophobic cavity of cytochrome c).[5,118,120] Another positively charged patch of residues, the L-site, has been proposed to be involved in complex formation, specifically Lys22, Lys25, His26, Lys27, and His33 (Figure 2.1A).[113,121] In addition, the fourth binding site, N-site, was recently discovered via NMR to participate in the binding of liposomes to mediate membrane fusion (Figure 2.1A).[1,109,113]

There is a long-running debate as to whether all four of these binding sites are directly involved in the interaction with CL, particularly the C and L sites. Among those who have studied structural changes that occur when cyt c interacts with CL liposomes, C-site and L-site binding are observed under highly acidic conditions (pH 2.6) and slightly below pH 7, respectively.[121,122] Since C-site binding is thought to be relevant only at low pH, and we do not observe unexpected evidence for it in this (physiological pH) study, we have omitted it from the discussion. However, from a biological perspective, as the local cell environment changes pH during the electron transport chain, different structural conformations of cyt c are present, making all other binding sites at least potentially relevant.[1,107,115]

There is also substantial debate around cyt c undergoing significant structural changes following complexation with CL membranes. Some have proposed that cyt c undergoes a two-step unfolding event where the His26-Pro44 hydrogen bond breaks, leading to tertiary unfolding at the N- to C-termini and peroxidase activity-associated M80-heme coordination (Figure 2.1B).[114] Multiple studies have shown that forming the cyt c/CL complex leads to a broad unfolding of the tertiary structure necessary for peroxidase activity.[4,114,123]

Among the few proposed specific structural models for phospholipid binding, the lipid anchoring model, which holds that one or two acyl chains of CL protrude out of the membrane and is/are inserted into a hydrophobic cavity of the protein (driving the "misfolding" of cyt c into its peroxidase configuration), is likely the most widely promoted. In particular, it has been argued that this occurrence may be necessary for CL-oxidation, which is a hallmark of apoptosis.[4,107,116,124] Nonetheless, it can be argued that this model would involve an exceptionally high free energy barrier for "flipping" of the acyl chain(s).[120]

Currently, all published studies looking at the structural changes of cyt c utilize CL-liposomes or unilamellar vesicles. Although these often provide a suitable bilayer membrane mimic, for peripheral membrane proteins in particular, the interaction with the curved bilayer and surrounding solution can affect the interaction between protein and phospholipid headgroups.[1,125] Therefore, it is essential to consider if the membrane mimic used is representative or if it ignores the interaction between the bilayer and the relationship with the membrane.[126] Specific to the formation of the cyt c- CL complex, Elmer-Dixon *et al*. (2020) along with other studies showed that the curvature of liposomes might provide structural information that may not be physiologically relevant as the surface of the inner mitochondrial membrane (IMM) is concave, while the majority of the aforementioned studies measure binding to the convex outer surface of the CL liposome.[112,127] Mohammadyani *et al*. (2018) used coarse-grained molecular dynamics modeling to validate that CL presence in the eukaryotic mitochondrial and bacterial membranes induces a negative curvature.[109] In this study, we use nanodiscs, which provide a more organized, controlled, and "flat" membrane mimic. We aim to characterize the structure and dynamics of cyt c in its "unbound" configuration (absent of phospholipids nanodiscs) compared to the "bound" configuration using millisecond hydrogen−deuterium exchange mass spectrometry (HDX-MS). HDX-MS measures which regions of the protein become more or less protected from solvent exchange upon complexation, resulting either from intermolecular interactions or rearrangement of the intramolecular hydrogen bonding network.[91] Using short HDX labeling time points (milliseconds to seconds) allows for the detection of changes in the structure of weak (or fast cycling)binding interactions or subtle shifts in conformation.[91]

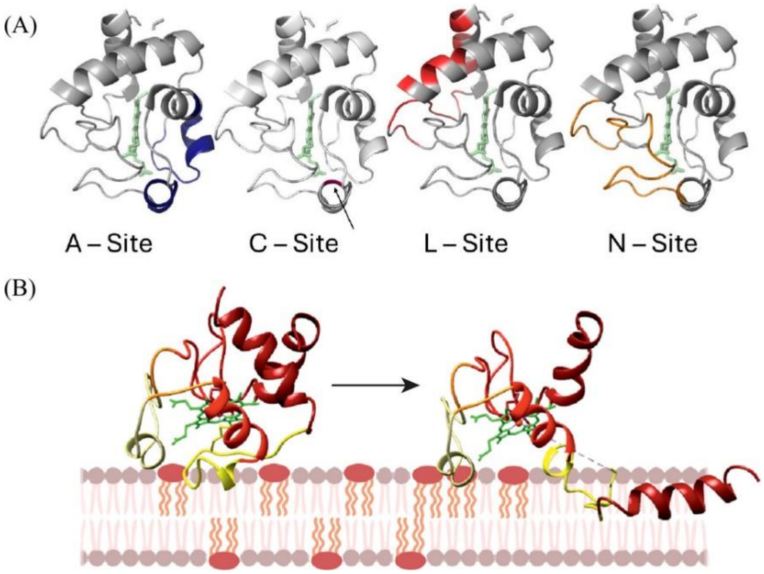

Figure 2.1| Schematic of proposed binding interaction between cytochrome c (cyt c) and mitochondrial membrane. (A) Structural models (PDB 1HRC) showing proposed sites of interaction between cytochrome c and phospholipid membranes, corresponding to the A-site (T49-K55, N70-I81), the C-site (N52), the L-site (V3-K27, Y97-A101), and the N-site (E21-Y48, K53). (B) A proposed model for cytochrome c phospholipid interactions with structural changes, adopted from Diaz-Quintana *et al*. (2020).[1]

2.3 Results and Discussion

2.3.1 Verification of Nanodiscs using Size-Exclusion Chromatography and NMR

Nanodiscs were assembled using phospholipids with different headgroups, which were stabilized and structurally defined by the membrane scaffolding protein that encircles the lipid bilayer to maintain a discoidal, soluble nanoparticle. The purification and verification of nanodiscs was conducted using size-exclusion chromatography (SEC), SDS-PAGE, and 1D ^{31}P NMR. Figure 2.2A−D illustrates the UV280 trace of DMPC, POPG,CL, and DMPC:POPG, respectively, along with the SDS-PAGE bands corresponding to the membrane scaffolding protein (MSP) in specific fractions. Due to the heterogeneity of nanodisc assembly, SEC allowed for the initial evaluation of the preparation, where the chromatograms are normalized to the maximum peak intensity and the relative yield of nanodiscs compared to empty liposomes or lipid-free MSP. SDS-PAGE analysis of the SEC fractions reveals a protein band corresponding to MSP1D1(∼24 kDa) with high purity (Figure A1). In DMPC and POPG samples, the ratio between MSP and lipids resulted mainly in aggregation/liposomal formation in addition to nanodiscs, as confirmed by SEC.[128] Although aggregation/liposomes were found in the sample preparation, only fractions containing the highest concentration of MSP1D1 (with a retention time of~14 min) were used in further analysis.

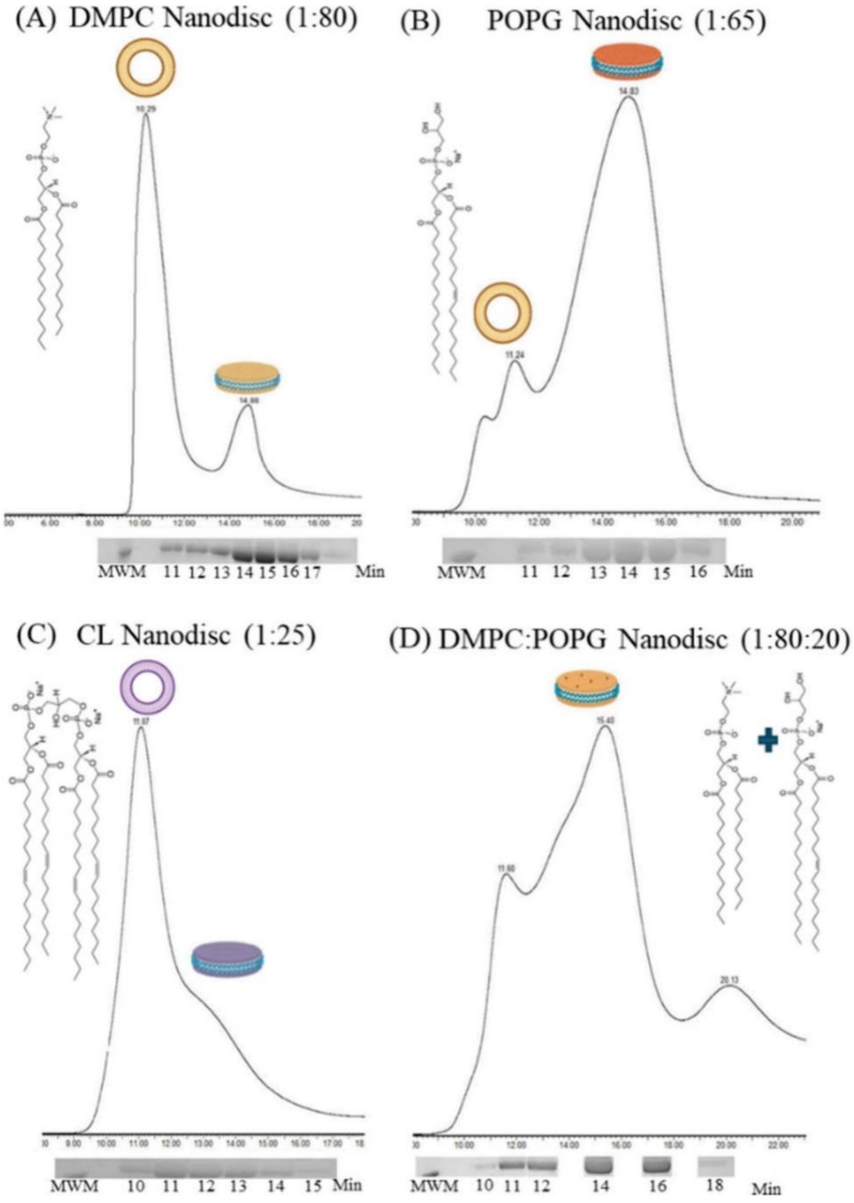

Figure 2.2| Size-exclusion chromatography with corresponding SDS-PAGE protein bands of prepared nanodiscs. (A) 1,2-Ditetradecanoyl-sn-glycerol-3-phosphocholine DMPC 14:0 nanodiscs, (B)1-exadecanoyl-2-(9Z-octadecenoyl)-sn-glycero-3-phospho-(1′-rac-glycerol) (sodium salt)16:0/18:1 POPG nanodiscs, (C) cardiolipin CL 18:0 nanodiscs, and (D) mixture of 80%DMPC and 20% POPG nanodiscs. The chemical formulas of DMPC, POPG, and CL are displayed in each panel A−C. Samples were run on a Superdex 200 prep grade column (300 mm × 7.8 mm),monitoring absorbance at 280 nm. SDS-PAGE gels are displayed under the respective chromatograms corresponding to fractions collected. The molecular weight marker (MWM) band corresponds to the 25 kDa standard (Thermofisher, cat no. 26620).

Interestingly, peaks of CL nanodiscs shift toward a shorter retention time compared to POPG nanodiscs, from which the CL phospholipid is derived.[1,129] Since the size of the nanodiscs is governed by the packing protein used in both cases (MSP1D1), this shift in retention may be a consequence of interactions between the agarose-dextran matrix of the column beads rather than a size difference.[130] Differences in retention times have been observed with different ratios of differently charged phospholipids[131], but in this case these differences likely reflect different charge densities for “cylindrical” single tailed phospholipids (POPG), and “conical” double tailed phospholipids like CL, something that will come into play for nanodisc/cyt c interactions.[127,132,133] It is also a possibility that CL is forming noncanonical nanodisc-like structures, for example with alternate MSP wrapping[134], that have a larger average size than the canonical form. Selected fractions from DMPC (14 min), POPG (14 min),and CL (11 min) nanodiscs were verified by using 1D ^{31}PNMR (Figure A2 B,D,F,G). The presence of formed nanodiscs was characterized by a sharp peak around 0 ppm in each NMR spectrum. The NMR peaks produced from nanodiscs were compared to the NMR peaks produced from liposomes(Figure A2 A,C,E). These results correlated well with those of others who have previously confirmed the presence of nanodiscs using ^{31}P NMR.[135–137]

2.3.2 The Cyt c Nanodisc Binding Interface

TRESI-HDX-MS was used to obtain conformational insight into the interactions between cyclic cation and various phospholipid headgroups in nanodiscs. As previously described, this method allows for insight into conformational dynamics with labeling times in the millisecond to second time regime, with the ability to detect both direct interactions and subtle changes in conformational dynamics due to complex formation.[91,94] TRESI-HDX is particularly useful in difference HDX measurements when the “bound” condition involves rapid cycling between “on” and “off” states, which is common for weak binding interactions (but, less appreciated, also quite possible for relatively “tight” binders if k_{on} and k_{off} are both high). This situation results in an early (ms to s time scale) “time of maximum difference” between kinetic profiles arising from the bound and unbound conditions. While the kinetics and thermodynamics of the interactions between cyt c and nanodiscs have not been characterized, the low amplitude of our HDX difference data suggest a relatively weak interaction, and the early times of maximum difference support a fast-cycling one.

Sequence coverage of 87.6%, and 3.00 redundancy was achieved using an in-house NHS-pepsin column (Figure A3). These experiments included three time-points (0.5, 2, and 5 s) of four different protein states: cyt c alone, cyt c with 10 nm DMPC nanodiscs, cyt c with 10 nm POPG nanodiscs, and cyt c with 10 nm CL nanodiscs. Figure 2.3A−D bar plots illustrate the summed difference in deuterium uptake between bound cyt c and free cyt c, integrated over 3 time points (each of which was measured in quadruplicate, Figures A4−A7). These differences are mapped onto the 1HRC PDB structure for POPG and CL nanodiscs in Figure 2.3E,F. The observed HDX differences are small, suggesting a relatively weak and dynamic interaction, but they are reproducible, consistently independently measured in redundant peptides, and statistically significant (to 2σ, n = 4−12). It is essential to note that these differences were observed for nanodiscs containing 100% anionic phospholipid (POPG and CL), but not for nanodiscs containing DMPC. This is expected, since DMPC is neutral, and it was used here as a negative control to determine if phospholipid or MSP affected the deuterium uptake of cyt c in the absence of significant specific interactions. Furthermore, in support of our findings, Imai *et al*. (2016) observed similar results when conducting para-magnetic-quench EPR experiments on horse heart cyt c, supporting the idea that other negatively charged lipids (specifically in their case DOPG) can elicit CL-like structural changes in cyt c.[138]

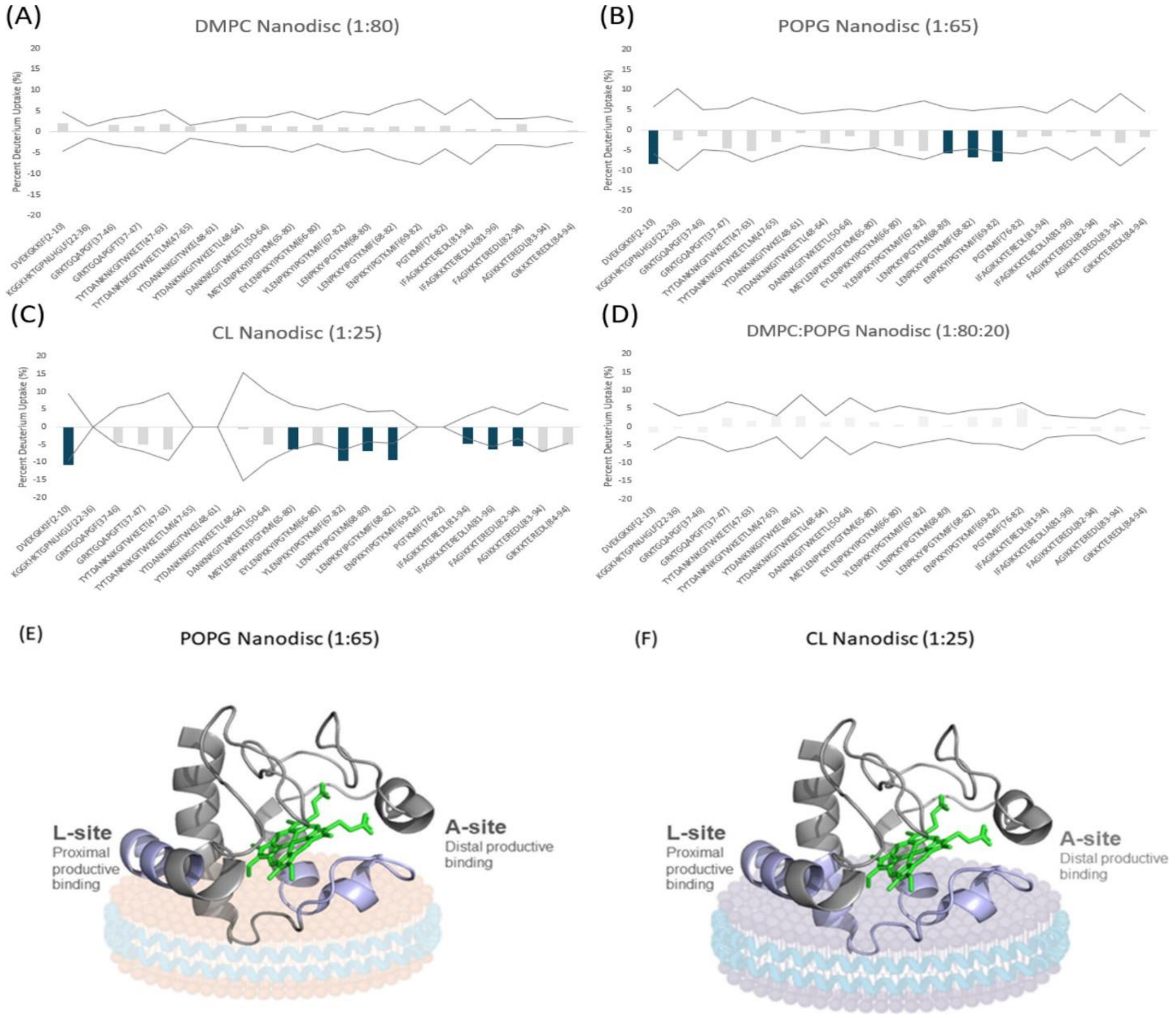

Figure 2.3|Summed difference plot of % deuterium uptake of the complex with nanodisc and cyt c. (A) HDX difference plot of cyt c in the presence of DMPC nanodisc , (B) HDX difference plot of cyt c in the presence of POPG nanodiscs, (C) HDX difference plot of cyt c in the presence of CL nanodiscs, and (D) HDX difference plot of cyt c in the presence of 80:20 DMPC: POPG nanodiscs. (E and F) Structural visualization of the interaction between the A- and L-site of cyt c (PDB: 1HRC) and the nanodisc surface. Statistically significant decreases in deuterium uptake upon complexation are depicted by the colored bars, with a significance determined by a threshold for each peptide (2σ, n = 4−12). The gray-colored bars displays nonstatistically significant changes between the bound and unbound states. To be considered statistically significant, the ΔHDX must exceed the gray line, which is two times the summed propagated error.

Upon complexation, significant deuterium uptake differences are observed in two regions of cyt c, corresponding to a.a. D2-F10 and M65-F82. These regions are exactly in agreement with the putative L and A binding sites, as proposed from various studies using NMR, FTIR, and MALDI-TOF.[1,109,111,121] In addition, Mohommadyani *et al*. (2018) provided evidence of simultaneous engagement of two binding sites, which overlapped mainly with the A- and L-sites using molecular docking, which was evaluated using solution NMR.[109] These two hydrophobic patches on the protein's surface may serve as a membrane anchor, as both domains are near lysine residues, providing additional electrostatic interactions with the phospholipid head groups (Figure 2.3E,F).[109,111] Importantly, in the presence of CL, HDX an additional decrease in uptake was observed in peptides F82-L94. Recently, Li *et al*. (2019) observed, using solid-state NMR, that upon complexation with LUVs containing CL, I81 and F82 induce spectral changes.[139] Furthermore, dynamic changes in the residues N70−I85 loop have been reported as a selectivity for CL.[139]

2.3.3 Conformational Restructuring of Cyt c upon Complexation

Apart from the sites of initial interaction, there has been extensive debate about the nature (or occurrence) of substantial structural changes in cyt c upon complexation. Multiple groups have observed significant differences in cyt c structure in the presence of phospholipids and attributed them to tertiary structural changes of the protein upon binding.[1,107,110,112,121] It remains to be seen if the observed tertiary structural changes are due to a large [cyt c]/[CL] ratio[120] or perhaps crowding of cyt c on the membrane surface, as this ensemble is challenging to probe.[1] The current published literature has shown that two distinct types of CL-bound cyt c conformations can be observed: a largely unfolded one and another with native-like compactness.[140–142] However, others have provided evidence that cyt c upon CL-binding remains unaltered. Wand and collaborators provided evidence using reverse lipid micelles by NMR to show that upon binding to CL phospholipid, cyt c remains unaltered.[142] This latter model is in line with our HDX data, which provide no evidence of significant unfolding of cyt c upon complexation.

Other research groups have also provided evidence of this using different methods like HSQC (NMR), and the structural conformation of cyt c in the presence and absence of vesicles overlapped quite well.[2] Solid-state NMR showed that in the presence of DOPC/CL unilamellar vesicles, the cyt c/CL complex promoted peroxidase activity without substantially affecting the ^{31}P or the ^{13}C frequencies of the lipid glycerol signals.[2] This further supports our data that cyt c in the presence of CL phospholipids remains largely structurally unaltered. It was not until recently that various research groups, such as Ripanti *et al*. (2021), provided evidence against the lipid anchorage model.[120] Their study using Attenuated Total Reflection InfraRed spectroscopy (ATR-IR) and Fluorescence Resonance Energy Transfer (FRET) experiments concluded that there was no evidence of the insertion of a lipid acyl chain in the cyt c hydrophobic core. Instead, the insertion occurred only when the ratio of [Cyt c]/[CL lipids] exceeded 0.15. CD measurements also supported this finding where evidence of tertiary structural changes was observed on the protein when the ratio of [Cyt c]/[CL lipids] was more significant than 0.2.[120,140] Therefore, it remains unclear whether the structural differences observed are related to the experimental conditions or methods used. It is also hard to determine if liposomes are biologically relevant in understanding the structural dynamics of cyt c in the presence of CL because various groups have determined tertiary unfolding while others using similar methods showed no differences.[141] Furthermore, some have attempted to use molecular modeling to manually dock one or two acyl chains into the heme moiety. Still, results demand a substantial conformational change to provide a channel where the acyl chain may be lodged.[119,143] Ultimately, our HDX data do not support a substantial degree of lipid anchorage even for 100% CL nanodiscs.

2.3.4 Mixed Lipid Nanodiscs

It can be argued that the conformational changes observed in 100% CL nanodiscs are not representative of the mitochondrial membrane and can drive nonphysiological conformational changes of cyt c. In mitochondria, CL phospholipids typically represent between 5 and 20% of the total lipid content of the inner membrane; therefore, producing nanodiscs that contained 80% DMPC and 20% CL would be ideal. However, after various attempts, we were not successful in making multicomplex nanodiscs with DMPC and CL.[1] This could be due to the differences in sample preparation using the two different lipids. We were able to generate nanodiscs using an 80:20 DMPC:POPG ratio; however, we were unable to detect binding to these nanodiscs (Figure 2.3D), which may result from strongly favored incorporation of DMPC during reconstitution or simply binding below our threshold of detection. Nonetheless, our data suggest that the general features of cyt c membrane interactions-interactions at the A- and L- sites, without a substantial subsequent conformational change-are retained for different negatively charged phospholipids, so that even pure POPG nanodiscs can serve as a reasonable in vitro model for cyt c membrane interactions.

2.4 Conclusion

Cyt c exhibits great functional complexity despite being a small protein with a relatively simple global fold. Here, we have provided evidence regarding the interaction of cyt c with flat-structured nanodisc membrane mimics. In HDX, the membrane-bound protein reveals aspects of the initial membrane interaction through the proposed A-site and L-site under physiological pH conditions. Further characterization of the dynamics of cyt c in the presence of CL compositions, such as tetra-stearyl-cardiolipin[124] and tetra-myristoyl-cardiolipin[4], embedded nanodiscs is required, as the affinity of cyt c to these lipids differ and correlates to its peroxidase activities. In addition to the presence of H_2O_2, such studies provide a better understanding of the mechanism required to release cyt c during the early stages of apoptosis. It may support further development of therapeutic approaches.

2.5 Materials and Methods

2.5.1 Protein Purification

Membrane Scaffolding Protein (MSP1D1) was expressed and purified from E. coli BL21-CodonPlus (DE3) cells containing the pET28a-MSP1D1 vector (Addgene). The protein purification process is described in detail by Oganesyan *et al*. (2018).[144] In short, the sonicated supernatant post lysis was purified using Ni2+ affinity gravity chromatography with three washes of increasing concentration of imidazole followed by an elution buffer using 0.4 M imidazole. The protein was concentrated to 4 mg/mL and stored in 20 mM Tris/HCl, 100 mM NaCl, and1 mM EDTA buffer pH 7.0 with 25% glycerol at −80 °C for future use. This particular length of MSP1D1 produces nanodiscs with a diameter size of 10 nm, which is acceptable for cyt c with a diameter of 3.4 nm.[111]

2.5.2 Analysis of Nanodiscs using Nuclear Magnetic Resonance and Size-Exclusion Chromatography

Nanodiscs were made according to establishedprotocols.[145–147] For this study, four types of lipid constituents for nanodiscs were used: 100% 14:0 DMPC (1,2-dimyristoyl-sn-glycero-3-phosphocholine, Avanti Polar Lipids cat no.850345P) as the negative control, 100% 16:0−18:1 POPG(1-palmitoyl-2-oleoyl-sn-glycero-3-phospho-(1′-rac-glycerol)(sodium salt), Avanti Polar Lipids cat no. 840457P) as the positive control, 100% 18:1 CL (1′3′-bis[1,2-dioleoyl-sn-glycero-3-phospho]-glycerol (sodium salt), Avanti Polar Lipids cat no. 710335P), and 80:20

DMPC:POPG. All nanodiscs were formed using MSP1D1 as the membrane scaffolding protein. First, DMPC and POPG lipids were suspended in HPLC-grade water to a final concentration of 200 mM, diluted further in 100 mM sodium chlorate, and sonicated in a heat bath until the lipid solution appeared clear. The lipid-to-MSP ratio was calculated where the ratios for DMPC, POPG, CL, and DMPC:POPG are 1:80, 1:60, 1:25, and 1:80:20,respectively. Nanodiscs containing DMPC lipids were first incubated at its transition temperature at room temperature(transition temperature is 25 °C) for 20 min and then at 4 °C for 1 h, and POPG lipids (transition temperature is 4 °C) were incubated at 4 °C for 1 h before incubation with biobeads SM Absorbents (Biorad, cat no. 152-8920). DMPC was incubated with biobeads for 2 h at 4 °C, while POPG required 4 h at 4°C. For the formation of CL nanodiscs, the following protocol provided the best results: 5 mg of CL lipids was resuspended in20 mM HEPES buffer, pH 7.2, and sonicated until transparent before adding 2 mg of MSP1D1 to a final volume of 1.5 mL. The transition temperature of CL is ∼50 °C; therefore, the sample was then incubated in a 48−50 °C water bath until the solution appeared clear with no visible lipid particles. Size exclusion chromatography (SEC), SDS-PAGE, and nuclear magnetic resonance (NMR) were used for nanodisc purification and validation. Nanodiscs were purified from free lipids or MSP using SEC on Waters H-class using an in-house packed column packed with Superdex 200 prep-grade beads(300 × 7.8 mm) in 20 mM HEPES pH 7.2 (Cytiva, cat no. 17-1043-01). Protein standards (Biorad, cat no.1511901) were used to evaluate the separation of the in-house column (Figure A8) at a flow rate of 1 mL/min. Nanodisc were purified at a flow rate of 0.5 mL/min. Fraction volumes of 0.5 mL were collected, and 12.5% SDS-PAGE gels were used to confirm that fractions contained MSP. Fractions that contained MSP were collected and concentrated to 150−300 μM with 20% D_2O final concentrations for NMR verification. Nanodisc verifications were acquired on a Bruker DRX600NMR spectrometer operated with XWINNMR software, version 3.5. The samples were prepared in a 3 mm NMR tube and acquired with a 5 mm broadband observe probe at 22°C. The 1H decoupled ^{31}P NMR spectra were acquired using a 30-degree 4.8-s pulse, 131,072 data points, and a relaxation delay of 0.1 s. The data was processed using a 2 Hz line broadening function. The instrument was calibrated using phosphoric acid and spectrum processed using TopSpin v4.1.3.

2.5.3 Deuterium Uptake Analysis of Cyt C/DMPC Nanodiscs, Cyt C/POPG Nanodiscs, Cyt C/Cardiolipin Nanodiscs compared to free Cyt C

The complexes were assembled at a 1:1 molar ratio before TRESI-HDX-MS experiments, where the final concentration of cyt c was 5 μM in 20 mM HEPES at pH 7.2. The experimental setup design followed an established protocol with minor modifications.[148,149] The protein complex passes through the notched region of the inner capillary, mixing with D_2O in the outer capillary with a final concentration of 50% D_2O, for various time points. Before protease digestion, the labelled sample was quenched using 0.5% formic acid in water. The resulting peptides were desalted, trapped, and separated on an ACQUITY UPLC BEH C18 VanGuard Pre-column(Waters, MA). Eluted peptides were ionized by electrospray and detected using a Synapt G2S mass spectrometer (Waters,MA). The mass spectrometer was equipped with an IMS to provide additional peptide separation. An LC gradient from 5% to 35% 0.1% FA in acetonitrile was used to elute peptides for analysis, followed by a 15 min hold at 85% acetonitrile to elute trapped lipids between each injection. The generated peptides were identified using ProteinLynx Global Server (PLGS), Table A1. All time points were acquired in quadruplicate technical replicates.

Chapter Three: HDX-MS as a Tool for Elucidating Structure-Activity Relationships in Ligand-Protein Complexes

Jiabao Liu[1], Ainaz Malekoltojari[1,2], Anjana Asokakumar[3], **Vimanda Chow[4]**, Linhao Li[5], Hao Li[6], Marina Grimaldi[7], Nathanlown Dang[3], Jhenielle Campbell[2], Holly Barrett[8], Jianxian Sun[8,9], William Navarre[2], Derek Wilson[4], Hongbing Wang[5], Sridhar Mani[6], Patrick Balaguer[7], Sayeepriyadarshini Anakk[3], Hui Peng[8,9], Henry M Krause[1,2]

[1]Donnelly Centre for Cellular and Biomolecular Research, University of Toronto, Toronto, ON, M5S 3E1, Canada
[2] Department of Molecular Genetics, University of Toronto, Toronto, ON, M5S 3E1, Canada
[3] Department of Molecular and Integrative Physiology, University of Illinois Urbana-Champaign, Urbana, IL, 61801, USA
[4]Department of Chemistry, York University, Toronto, ON, M3J1P3, Canada
[5] Department of Pharmaceutical Sciences, University of Maryland School of Pharmacy, 20 Penn Street, Baltimore, MD, 21201, USA
[6] Department of Molecular Pharmacology; Department of Genetics; Department of Medicine; Albert Einstein College of Medicine, Bronx, NY, 10461, USA
[7] Institut de Rescherche en Cancérologie de Montpellier (IRCM), Université Montpellier, Institut régional du Cancer de Montpellier (ICM), Montpellier, Inserm, U1194, France
[8] Department of Chemistry, University of Toronto, Toronto, ON, M5S 3H6, Canada
[9] School of the Environment, University of Toronto, Toronto, ON, M5S 3H6, Canada

A portion of this chapter has been published in Nature Communications 2024, 15, 2563, 10.1038/s41467-024-46559-3, Copyright © 2024 Liu et al.
Open access under Creative Commons CC BY

V.C conducted all HDX-MS and data processing. D.J.W. provided supervision. J.L and A.M provided purified Constitutive Androstane receptor (CAR) and Ligands.

Xiaojuan Wang[1], Guohui Zhang[2], Zhiwei Bian[1], **Vimanda Chow**[3], Marina Grimaldi[4], Coralie Carivenc[5], Savannah Sirounian[5], Hao Li[6], Lucia Sladekova[6,7], Stefano Mott[8], Yulia Luperi[8], Yufeng Gong[9], Cait Costello[10], Linhao Li[11], Matthew Jachimowicz[12,13], Miao Guo[2], Shian Hu[1], Derek Wilson[3], Patrick Balaguer[4], William Bourguet[5], Sridhar Mani[6], Laura Bonati[8], Hui Peng[9,14], John March[10], Hongbing Wang[11], Shengpeng Wang[2], Henry M Krause[12,13], Jiabao Liu[12]
[1]School of Pharmacy, Lanzhou University, Lanzhou, Gansu, People's Republic of China
[2]State Key Laboratory of Quality Research in Chinese Medicine, Institute of Chinese Medical Sciences, University of Macau, Macau, People's Republic of China
[3]Department of Chemistry, York University, Toronto, ON, Canada
[4]Institut de Rescherche en Cancérologie de Montpellier (IRCM), Université Montpellier, Institut régional du Cancer de Montpellier (ICM), Montpellier, Inserm, U1194, France
[5]Centre de Biologie Structurale, INSERM, CNRS, Université de Montpellier, Montpellier, France

[6]Department of Molecular Pharmacology; Department of Genetics; Department of Medicine, Albert Einstein College of Medicine, Bronx, NY, USA
[7]Department of Cell Biology and Genetics, Faculty of Science, Palacký University, Olomouc, Czech Republic
[8]Department of Earth and Environmental Sciences, University of Milano-Bicacca, Milan, Italy
[9]Department of Chemistry, University of Toronto, Toronto, ON, Canada
[10]Department of Pharmaceutical Sciences, University of Maryland School of Pharmacy, Baltimore, MD, USA
[11]Donnelly Centre for Cellular and Biomolecular Research, University of Toronto, Toronto, ON, Canada
[12]Department of Molecular Genetics, University of Toronto, Toronto, ON, Canada
[13]School of the Environment, University of Toronto, Toronto, ON, Canada

A portion of this chapter has been published in Nature Communications 2025, 16, 1280, 10.1038/s41467-025-56624-0, Copyright © 2025 Liu et al.
Open access under Creative Commons CC BY

V.C conducted all HDX-MS and data processing. D.J.W. provided supervision. J.L and A.M provided purified Pregnane X receptor (PXR) and Ligands.

3.1 Summary

Hydrogen-deuterium exchange mass spectrometry (HDX-MS) has emerged as a powerful tool for probing protein conformational dynamics and ligand interactions under near-physiological conditions. Here, we apply HDX-MS to investigate the structural mechanisms underlying ligand-mediated modulation of three pharmacologically relevant proteins: the nuclear receptors constitutive androstane receptor (CAR) and pregnane X receptor (PXR), and the lipid hydrolase (ABHD2). In CAR, HDX-MS revealed that ligand-induced stabilization of helix 11(H11), rather than helix 12 (H12), more closely correlates with transcriptional activation. Full agonist 6-(4-cholorophenyl)imidazo[2,1-b]thiazole-5-carbaldehyde-O-(3,4-dichlorobenxyl)oxime), CITCO, and partial agonist diindolyl-ethane,DIE, elicited distinct structural rearrangements, suggesting different modes of receptor activation despite shared binding regions. In PXR, we demonstrate that furanodienone (FDN) cooperatively binds with estrogenic steroids (E2 and EE2) to stabilize helices H3 and H12, producing synergistic activation that mimics full agonist behaviour. Finally, in the absence of crystallographic data, HDX-MS enabled mapping of the ligand-binding interface in ABHD2 and revealed that inhibitory compounds 191R and 192 stabilize regions proximal to the predicted catalytic triad. Comparative analysis of a catalytically inactive S207A mutant further confirmed mutation-

induced structural stabilization and altered ligand responsiveness. Collectively, these findings highlight HDX-MS as a robust and versatile platform for elucidating protein-ligand interactions, guiding the rational development of selective small-molecule modulators for therapeutically important targets.

3.2 Introduction

Since its development, hydrogen-deuterium exchange mass spectrometry (HDX-MS) has rapidly become an indispensable tool in the drug discovery pipeline for probing protein structure and dynamics.[62] HDX-MS has been widely applied to study protein folding, oligomerization, and interactions with lipids, nucleic acids, and small molecules- several of which are discussed throughout this thesis.[62,78,150] A persistent bottleneck in drug development is the identification of potent, selective lead compounds with favourable physicochemical properties.[151] Following hit identification, structural studies- often relying on X-ray crystallography- are typically used to elucidate the mechanism of action.[151] However, many protein targets are difficult to crystallize. Nuclear magnetic resonance (NMR) spectroscopy provides an alternative approach to resolving residue-specific structural changes upon ligand binding.[152] Nevertheless, NMR is limited by protein size constraints, high sample requirements, and often necessitates isotopic labelling to enhance spectral resolution.[62,152]

HDX-MS overcomes many of these limitations. It is compatible with near-native conditions, requires lower sample quantities, and does not depend on isotopic labelling. Recent advances in automation and analytical software have further enhanced its accessibility and throughput, making it particularly attractive for applications in protein biopharmaceutical research.[65] This chapter showcases the application of HDX-MS as a medium–to–high–throughput orthogonal biophysical method to investigate structure-dynamics-function relationships of small-molecule ligand binding to target proteins in solution.

The first two case studies focus on the nuclear receptors (NRs) constitutive androstane receptor (CAR) and Pregnane X receptor (PXR), both of which play key roles in xenobiotic clearance. Like other NRs, CAR and PXR possess large, flexible ligand-binding domains (LBDs) that accommodate diverse ligands, including drugs, environmental toxicants, herbal metabolites, and industrial chemicals (Figure 3.1).[153] These receptors are predominantly expressed in intestinal tissues and the liver, where they regulate genes involved in drug metabolism and clearance, such as CYP2B6, CYP3A4, and UGT.[154] Modulating the activity of

CAR and PXR alters the expression of drug-metabolizing enzymes and transporters, with protective roles against bile acid toxicity and intestinal inflammation.[153,155] However, sustained activation has been linked to hepatocarcinogenesis.[155] Despite their pharmacological importance, there remains a lack of potent and selective CAR and PXR modulators that have progressed to clinical evaluation.[110]

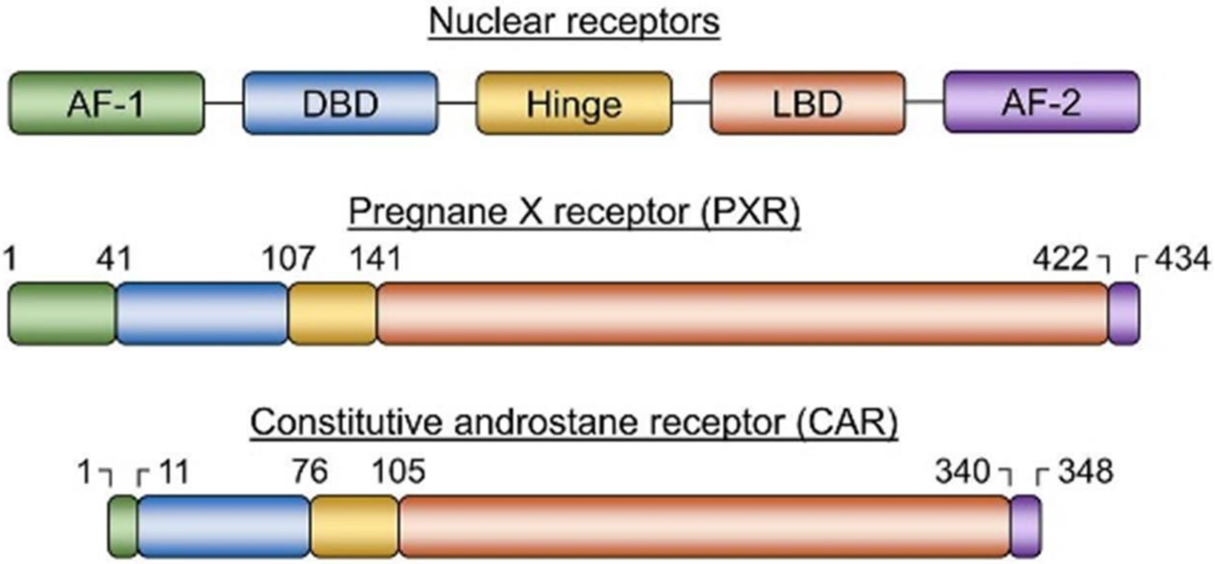

Figure 3.1| General schematic of nuclear receptor domains for Pregnane X receptor (PXR) and Constitutive androstane receptor (CAR). Schematic representation of the modular domain organization of the Pregnane X receptor (PXR) and constitutive androstane receptor (CAR), highlighting the DNA-binding domain (DBD), hinge region, and ligand-binding domain (LBD). Reproduced with permission from Poudel *et al*. (2023).[156]

Recently, diindolyl-ethane (DIE) emerged as a promising CAR activator. In CAR-driven luciferase reporter assays, DIE demonstrated comparable activation to CITCO (6-(4-chlorophenyl)imidazo[2,1-b][1,3]thiazole-5-carbaldehyde O-(3,4-dichlorobenzyl)oxime), a well-characterized CAR agonist.[7] While both ligands enhanced CAR transactivation, CITCO exhibited a greater maximal effect and is thus considered a full agonist, whereas DIE is characterized as a partial agonist.[7] Importantly, DIE treatment did not elicit the adverse effects commonly associated with CITCO in primary hepatocytes and mouse liver models.[7] These findings underscore the need to understand the structural basis for CAR modulation by DIE versus CITCO, which has implications for the design of safer CAR-targeting therapeutics. HDX-

MS was employed to characterize ligand-induced structural dynamics within the CAR-LBD and to investigate whether a graded structural response correlates with each compound's activity profile.

In addition to synthetic molecules, bioactive constituents from dietary and herbal sources have long been investigated for their therapeutic potential. Ginger, widely used in traditional medicine for treating intestinal inflammation, contains furanodienone (FDN), which has recently been identified as a PXR activator.[157] While the crystal structure of the PXR-FDN complex was successfully resolved, HDX-MS provided complementary insight by validating the dynamic binding interface in solution. Previous studies have shown that steroid compounds such as estradiol (E2) and 17α-ethinylestradiol (EE2) can synergistically affect nuclear receptors.[158,159] Co-treatment of PXR with FDN and E2 in luciferase reporter assay produced activity levels comparable to SR12813, a benchmark PXR agonist (data collected by collaborators, data not shown). To better understand the impact of dual ligand binding on PXR conformation, HDX-MS was used to map structural perturbations in the LBD in the presence of SR12813, FDN, FDN/E2, and FDN/EE2.

Furthermore, developing selective small-molecule modulators for nuclear receptors (NRs) remains a critical challenge, partly due to the intrinsic structural flexibility of their ligand-binding domains (LBDs). This conformational plasticity often results in overlapping ligand affinities across receptor subtypes, complicating the design of receptor-specific compounds. For example, CITCO, initially identified as a selective agonist for CAR, was later shown to bind PXR.[8,156] Despite this cross-reactivity, CITCO elicits divergent biological responses, potently activating CAR while exhibiting minimal or antagonistic effects on PXR activity.

Given that CAR and PXR play essential roles in xenobiotic and drug metabolism and broader physiological processes such as glucose homeostasis, lipid regulation, obesity, and liver function, the need for highly selective ligands is paramount. The dual roles of these receptors in pharmacological and metabolic regulation mean that both their activation and inhibition can yield either therapeutic benefits or unintended detrimental effects, depending on the receptor. Thus, we employed HDX-MS to evaluate the interactions between CAR and FDN at the same molar concentrations, to directly compare ligand-induced structural responses and assess the potential for differential receptor activation.

The final example highlights the use of HDX-MS to characterize ligand binding to α/β hydrolase domain-containing protein 2 (ABHD2), a poorly characterized serine hydrolase localized to the extracellular membrane of sperm flagella. ABHD2 has been proposed as a non-genomic progesterone receptor that activates the sperm-specific ion channel CatSper, which is essential for sperm motility and hyperactivation.[160] Two small-molecule inverse agonists, **191R** and **192**, were investigated for their ability to inhibit ABHD2 activity. The development of such inhibitors could provide a non-hormonal alternative to conventional contraceptives, potentially mitigating the side effects associated with hormone-based approaches. HDX-MS was used to identify the ligand-binding interfaces of 191R and 192, offering mechanistic insight into their inhibitory actions.

Together, these case studies illustrate HDX-MS's versatility in elucidating dynamic structural changes associated with ligand binding, facilitating a deeper understanding of structure-activity relationships across diverse therapeutic targets.

3.3 Results and Discussion

3.3.1 Conformational Differences within the hCAR(CITCO) and hCAR(DIE) Monomer

To investigate the binding interactions between DIE and human constitutive androstane receptor (hCAR), HDX-MS experiments were performed at three time points: 1,10, and 30 minutes in a deuterated buffer. These experiments achieved an average sequence coverage of 94.1%, with a peptide redundancy of 5.49 (Figure B1). Both CITCO, a known full agonist, and DIE, a partial agonist, induced statistically significant perturbations in the ligand-binding domain (LBD) of the hCAR monomer (Figure B2). Notably, three regions – F129-H140 in helix 2(H2), L151-H165 in helix 3 (H3), and Y224-G233 in helix 6 (H6) – exhibited altered deuterium uptake upon ligand binding (Figure 3.2).

Structural interpretations were aided by the co-crystal structure of hCAR bound to CITCO and molecular docking simulations.[161] These indicated that residues M168-V169 in H3 and F243 in the loop between H6 and H7 are involved in ligand interactions, consistent with the regions exhibiting HDX differences.[162] These findings align with previous studies mapping ligand-binding interfaces within the CAR LBD.[155] Despite structural similarities, CITCO and DIE elicited distinct patterns of protection across helices 10/11(H10/H11), the hinge region (Hx), and helix 12 (H12), suggesting that these elements contributed to the differential transactivation capacity of each ligand. While both ligands induced similar protection in H2, H3, and H6 – indicative of comparable core binding interactions – CITCO uniquely stabilized H10/H11, Hx, and H12 to a greater extent than DIE. Specifically, CITCO induced a robust reduction in deuterium exchange in H11, Hx (-10 to -15%), and H12, whereas DIE exhibited moderate protection in H11 and Hx (-7%) and, notably, caused significant deprotection in H12 (+10%). These results imply that DIE activates CAR through a mechanism that does not require H12 stabilization. Due to the lack of structural data for the hinge and DNA-binding domains, which were unavailable in this study because of expression and purification limitations, potential long-range allosteric effects contributing to ligand-specific receptor modulation could not be fully assessed.

The structural role of H10/H11 in CAR transactivation is further supported by available mouse CAR (mCAR) crystal structures in active and inactive states (PDB: 1XLS and 1XNX, respectively).[163,164] In the active conformation, H11 appears as an extension of H10, forming a continuous helix, whereas in the inactive state, H10 splits into two discrete helices, with H11 comprising the C-terminal segment.[163,164] Wright *et al*. (2012) performed HDX-MS and mutagenesis studies on mCAR to probe conformational differences between agonist (TCPOBOP) and inverse agonist (androstenol) bound states. Their findings demonstrated that stabilization of H10/H11 is correlated with transcriptional activity and coactivator recruitment. For example, the full agonist TCPOBOP binding to mCAR induced substantial protection in H10 (-32%), compared to the partial agonist meclizine (-10%).[155] Our observations in hCAR with CITCO and DIE are consistent with these findings, further implicating H10/H11 dynamics as a key determinant of CAR activation.

Moreover, mutagenesis of H11 residues revealed that restricting the flexibility of this helix enhances CAR activation, reinforcing its central role in receptor modulation. The Griffin group has reported similar trends in studies of Peroxisome Proliferator-Activated Receptor Gamma (PPARγ), where partial and intermediate agonists failed to stabilize H12, indicating that alternative mechanisms of activation may bypass canonical AF-2 (activation function-2) helix stabilization.[165] Although DIE-induced H12 destabilization did not confer an apparent functional advantage in our studies, the observed H11 stabilization may serve as a proxy for transcriptional efficacy.

Our results highlight distinct ligand-induced conformational responses within the CAR LBD, particularly in helices H10-H12, that underpin graded receptor activation levels. These findings provide mechanistic insight into the modulation of CAR by structurally related agonists and establish a foundation for the rational design of compounds with tunable transcriptional activity. Furthermore, this study contributes to a growing body of evidence suggesting that H11 may serve as an allosteric conduit for inter-subunit communication, as previously shown in estrogen receptor dimers and other NRs. The differential engagement of H12 and H11 observed here highlights the potential of targeting these helices to finely tune NR function.

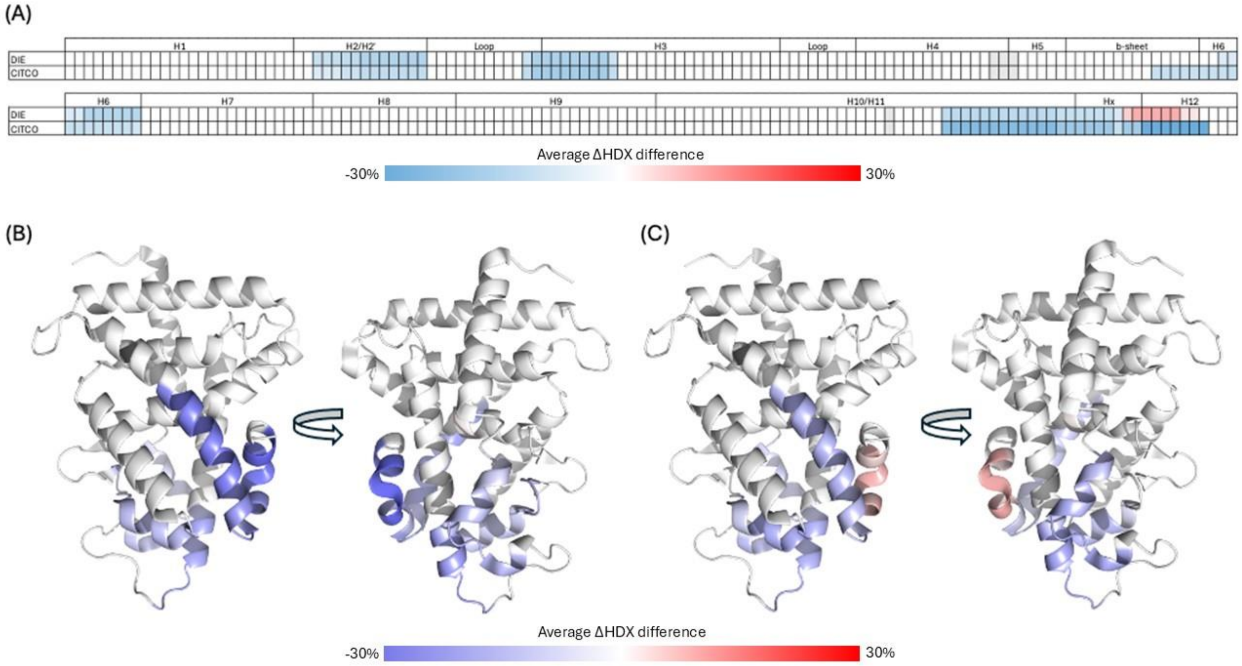

Figure 3.2| Differential hydrogen-deuterium exchange analysis of hCAR revealing binding interactions for CITCO and DIE. (A)Heatmap of average differences in percent deuterium uptake. Structural illustrations mapping the differential HDX data for hCAR upon binding (B) CITCO and (C) DIE onto the crystal structure (PBD code 1XVP). Structures are coloured according to the average relative fractional uptake differences in the percentage of deuterium incorporation (%D). Structured coloured in blue denotes decreased deuterium incorporation in the bound state, whereas red denotes increases in deuterium incorporation in the bound state.

3.3.2 Synergistic Binding of FDN and Steroid in the Adjacent LBD of PXR

HDX-MS was employed alongside the solved crystal structure of the PXR-FDN complex to characterize the binding interactions of furanodienone (FDN) with the pregnane X receptor

(PXR). While the crystallographic data revealed key contacts within the ligand-binding domain (LBD), molecular docking studies indicated the presence of additional unoccupied space within the LBD that could potentially accommodate a second ligand.[157] This observation is consistent with previous work by Delfosse *et al*. (2021), who demonstrated cooperative binding of endosulfan and estradiol (E2) to PXR, resulting in synergistic activation.[158] Inspired by this model, we used HDX-MS to explore whether FDN could support simultaneous co-binding with E2 or 17α-ethinylestradiol (EE2), thus offering structural insight into potential synergistic mechanisms relevant for drug or nutraceutical combination therapies.

HDX-MS analysis achieved an average sequence coverage of 75.6% with a peptide redundancy of 2.83 for the SR12813, FDN, FDN/E2, and FDN/EE2 complexes (Figure B3). In parallel, PXR-E2 and PXR-EE2 complexes were analyzed separately, yielding comparable coverage (78.5%) and redundancy (2.76) (Figure B4). Notably, no statistically significant deuterium exchange differences were detected for the E2- or EE2-bound complexes alone, suggesting minimal impact on PXR structural dynamics when each steroid is administered independently. This observation is further supported by the limited volumetric occupancy of E2 and EE2 within the spacious PXR ligand-binding cavity – estimated to be > 1,300Å^3 – compared to their smaller molecular volumes (~260-280 Å^3), which likely prevents sufficient stabilization for transcriptional activation.[156] Consistent with this, luciferase-based cell assays revealed no significant activation of PXR by E2 or EE2 alone.[157] Although solubility limitations during HDX labelling resulted in an estimated ligand-bound fraction of ~75%, previous studies have demonstrated that partial occupancy—particularly by weak binders—can still yield statistically significant HDX-MS signals. For example, Wolf *et al*. (2024) demonstrated that ligand-bound fractions as low as 15-20% are still sufficient to generate statistically significant, HDX-detectable binding events.[103]

Upon comparing PXR bound to FDN alone and in combination with E2 or EE2, marked structural compaction was observed in the LBD, particularly in helices H3 (M246-F257), H6/H7(L319-K325), H9/H10 (L400-L411), and H12(L412-L428). H12, the canonical activation function-2 (AF-2) helix, is critical for co-activator recruitment (Figure 3.3, Figure B5). In the presence of FDN alone, H12 exhibited a 15% reduction in deuterium uptake, indicating partial stabilization. However, adding E2 or EE2 led to further reductions, to 18.9% and 19.4%, respectively, indicating enhanced stabilization of the AF-2 surface. These values closely approximated the protection observed with the full agonist SR12813, suggesting that combining FDN with either steroid shifts the receptor conformation towards a more transcriptionally competent state.

Although not previously characterized in detail for PXR, the AF-2 region in other nuclear receptors, such as PPARγ, has been conceptualized as a “H3-H12 clamp”, where the simultaneous stabilization of these two helices correlates with full agonist activity.[166] Intriguingly, HDX-MS profiles for FDN, FDN/E2 and FDN/EE2 all demonstrated stronger protection in H3 compared to SR12813 (Figure B6). Specifically, deuterium protection increased from 25.9% for FDN alone to 29.8% and 30.2% for FDN/E2 and FDN/EE2, respectively. These results strongly support the hypothesis that E2 and EE2 enhance FDN-induced PXR activation by cooperatively stabilizing critical structural elements of the LBD.

These structural findings were further corroborated by molecular docking analyses, luciferase reporter assays, and gene expression data (not discussed in detail here). Notably, co-treatment with FDN and EE2 significantly increased the transcription of canonical PXR target genes, including *Mdr1* and *Cyp3a4*. Moreover, the combination reduced the EC_{50} to the nanomolar range and elevated E_max to levels comparable to SR12813 (Figure B7).[157] These data highlight a cooperative mechanism by which FDN and steroidal co-ligands synergistically stabilize PXR in a conformation associated with maximal transcriptional output.

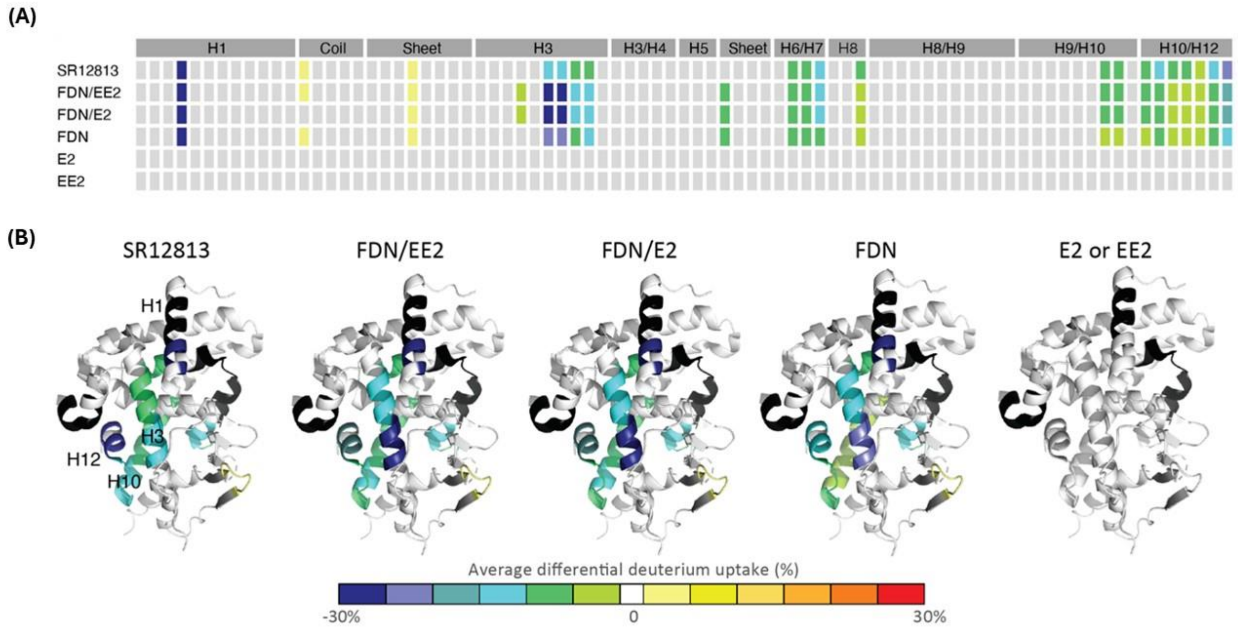

Figure 3.3| Differential hydrogen-deuterium exchange analysis of PXR revealing synergistic binding interactions for FDN + steroids, E2 and EE2. (A)Fractional uptake difference heatmaps showing variations of deuterium uptake between ligand-bound PXR-SRC1. (B)Crystal structure overlaying differential HDX indicates alterations in the structural conformation of PXR-SRC1 due to SR12813, FDN, FDN/E2 or FDN/EE2 (PDB ID: 3HVL) binding. Structures are colour-coded according to the colour bar at the bottom of the figures, where colours represent average differences in deuterium uptake (%D). Regions highlighted in black are areas not covered in the HDX analysis.

Lastly, we employed HDX-MS to evaluate the structural impact of FDN on CAR at equimolar concentrations, enabling a direct comparison of ligand-induced responses between receptors. HDX-MS analysis achieved an average sequence coverage of 81.5% with a peptide redundancy of 3.03 of CAR-LBD (Figure B8). HDX-MS revealed that FDN does not elicit any measurable conformational changes within the CAR ligand-binding domain (LBD), providing compelling evidence that FDN is a selective PXR ligand (Figure B9). The ability to discriminate between closely related nuclear receptors is critical, particularly in the context of drug metabolism, where off-target activation can lead to adverse pharmacokinetic or toxicological effects. Identifying a PXR-selective modulator such as FDN presents a valuable advancement toward developing more targeted therapeutics, enabling precise modulation of PXR-regulated pathways without unintended CAR activation. This selectivity is especially advantageous for fine-tuning drug-drug interaction profiles and improving therapeutic safety in liver-related disorders.

3.3.3 Inhibition Molecule Blocking Steroid Binding Pocket, Preventing Hyper-Fertilization

This study presents a case in which co-crystallization of the α/β hydrolase domain-containing protein 2 (ABHD2) with its ligands was unsuccessful, despite extensive efforts. As a result, HDX-MS was employed to characterize the ligand-binding interface for two structurally related candidate inhibitors:**191R** and **192**. Differential HDX-MS analysis was performed at 1, 10, and 30 minutes for apo-ABHD2 and ABHD2 in complex with 10μM of either **191R** or **192**. These experiments yielded an average sequence coverage of 88.5% and an average peptide redundancy of 4.01 (Figure B10).

Given the physiological relevance of progesterone in ABHD2 activation, we first evaluated the structural dynamics of ABHD2 in the presence of this endogenous steroid. Progesterone has been shown to bind ABHD2 and activate its catalytic triad, thereby promoting the hydrolysis of 2-AG and triggering calcium influx essential for fertilization.[167] HDX-MS was performed at protein: ligand molar ratios of 1:20 and 1:40 to assess structural consequences, exceeding the reported sub-micromolar binding affinity.[167–169] As shown in Figure 3.4, progesterone induced modest protection ($\Delta D \leq 5\%$) in residues V231-L240, M301-N306, and Y320-C326 (Figure B11). In the absence of high-resolution structural data for the ABHD2-progesterone complex, these HDX-MS results serve as a valuable reference point for comparing synthetic inhibitors' binding profiles and structural effects. Notably, no significant allosteric perturbations were detected in the catalytic triad upon progesterone binding, suggesting that the progesterone activates ABHD2 through alternative mechanism.

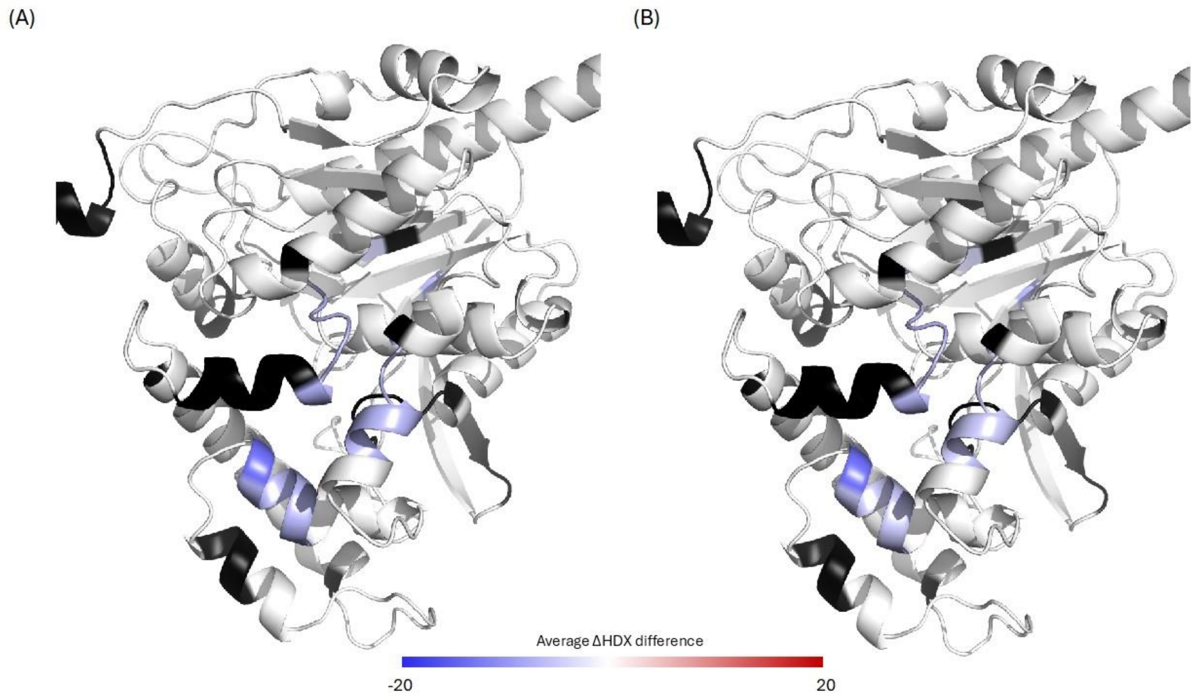

Figure 3.4| Differential HDX-MS analysis of WT ABHD2 in the presence of progesterone at varying ligand concentrations. HDX-MS profile of WT ABHD2 in the presence of progesterone, mapped onto the Alpha-fold predicted structure (AF-P08910-F1-model_v4), at (A) a 1:20 and (B) a 1:40 protein: ligand molar ratio. Colours represent the average relative fractional uptake difference in deuterium incorporation (%ΔD) compared to the apo state, averaged across all time points. Regions lacking HDX-MS coverage are shown in black.

Next, we assessed the binding profiles of the two inhibitor candidates, **191R** and **192**, and their effects on the conformational dynamics of WT ABHD2. Both compounds induced distinct and statistically significant protection from deuterium exchange in four major regions of the ABHD2 sequence: residues A158-M176, V231-M264, Y295-C326, and V340-L352 (Figure B11). The most pronounced changes were observed within the V231-M264 and Y295-C326 segments. Additionally, **191R** specifically also stabilized M128-T145. These results suggest that both compounds engage a binding interface within the ABHD2 protein, reducing local conformational dynamics (Figure 3.5). Due to the absence of an experimentally resolved crystal structure of ABHD2, AlphaFold-predicted structural models were used to visualize HDX differences. Notably, the protected regions correspond closely to the predicted progesterone interaction site, proving that both 191R and 192 function as competitive inhibitors.

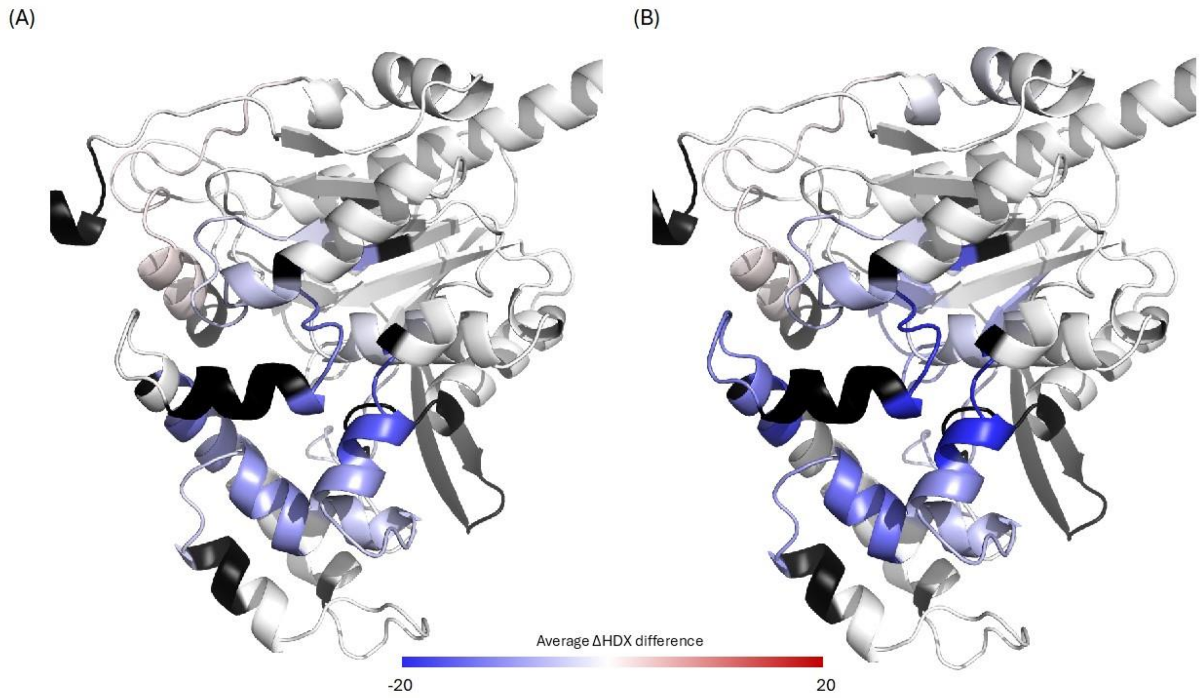

Figure 3.5| Ligand-induced structural dynamics of WT ABHD2 in the presence of inhibitory compounds 191R and 192. Differential HDX analysis of wild-type ABHD2 bound to (A) compound 192 and (B) compound 191R reveals localized structural stabilization [near the predicted active site] (AlphaFold model: AF-P08910-F1-model_v4). Colour gradients indicate the average relative fractional uptake difference (%ΔD) in deuterium incorporation, with regions lacking sequence coverage shown in black.

ABHD2 is a lipid hydrolase implicated in sperm capacitation and steroid signalling. Its enzymatic function depends on a serine-histidine-aspartate catalytic triad (S207-H376-D354), which facilitates the hydrolysis of endogenous lipid substrates, such as the endocannabinoid 2 2-arachidonoylglycerol (2-AG).[160] Disruption of any residues within this triad is expected to impair enzymatic activity. A mutation at the serine residue (S207A) was generated and analyzed to test this, with a sequence coverage of 88.8% and peptide redundancy of 3.51 (Figure B12). Thermal shift assays (data collected by collaborators, data not shown) revealed an increase in thermostability of the S207A mutant relative to the wild-type (WT) protein, indicating enhanced conformational rigidity. HDX-MS analysis comparing WT and S207A ABHD2 confirmed a global reduction in conformational dynamics in the mutant (Figure B13). Differential uptake analysis revealed increased protection in residues Q235-L240, F255-M264, M301-N306, Y320-C326, A342-L352, and W407-T417 in S207A relative to WT. In contrast, regions T63-L82 and N161-P167 – proximal to the interactive site- showed significantly increased deuterium uptake, potentially reflecting altered flexibility due to the loss of catalytic serine function (Figure 3.6). These data and thermal stability results indicate that the S207A mutation leads to a more stabilized and structurally distinct ABHD2 conformation, which might be necessary for inhibiting hydrolase activity.

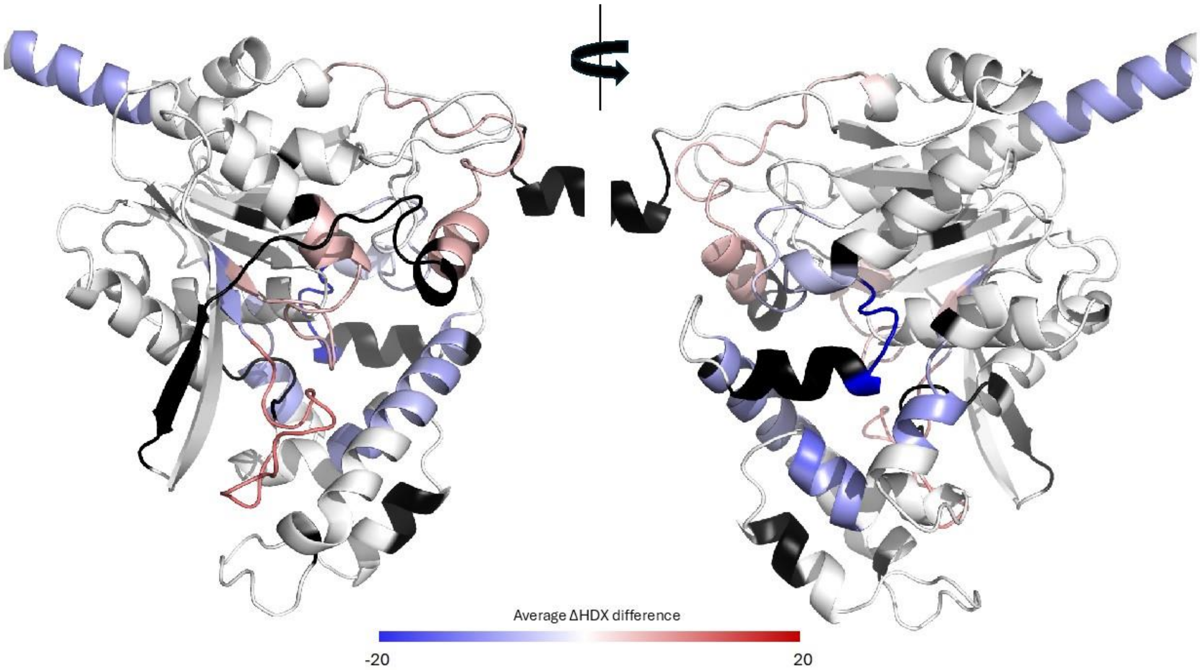

Figure 3.6| Comparative HDX-MS analysis of WT and S207A mutant ABHD2 reveals mutation-induced conformational stabilization. Differential deuterium uptake between the ABHD2 S207A mutant and WT ABHD2 is mapped onto the Alpha-fold predicted structure (AF-P08910-F1-model_v4). Blue and red represent the average difference in relative deuterium incorporation (S207A-WT) across three time points. Blue regions indicate increased protection (decreased exchange) in the mutant, while red regions denote increased flexibility (increased exchange). Regions without HDX-MS coverage are shown in black.

To explore whether these structural changes affect ligand binding, HDX-MS was repeated for S207A in the presence of **191R** and **192**. While the magnitude of protection was reduced in the mutant, particularly across residues C230-M264 and M308-C326, the overall binding profiles were similar to those observed with WT ABHD2 (Figure 3.6). This outcome is consistent with the increased rigidity of the mutant protein and the expectation that stabilization in the interactive site would limit further “hydrolase” activity.

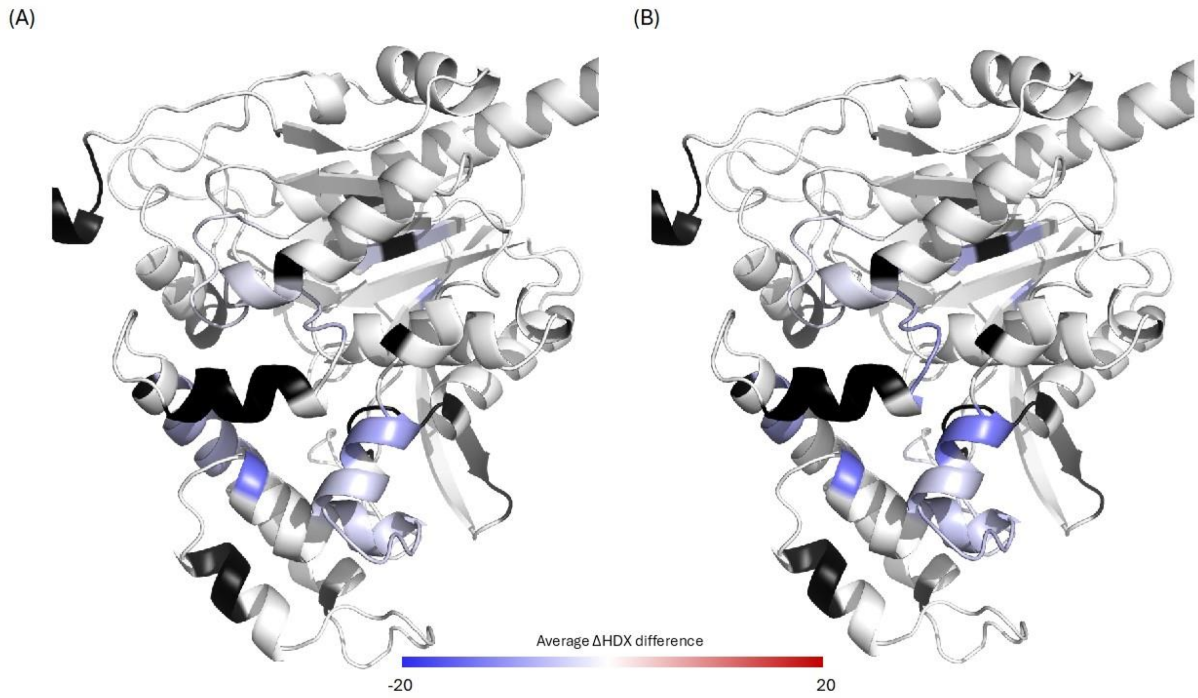

Figure 3.6| Ligand-induced structural dynamics of ABHD2 S207A mutant in the presence of inhibitors 192 and 191R. Differential HDX-MS analysis of the ABHD2 S207A mutant bound to (A) compound 192 and (B) compound 191R, mapped onto the Alpha-fold predicted structure (AF-P08910-F1-model_v4). Colour gradients indicate the average relative fractional uptake difference in deuterium incorporation (%ΔD) compared to the unbound S207A control, averaged across three time points. Regions lacking HDX-MS coverage are shown in black.

Together, these findings suggest that **191R** and **192** engage key regions of the ABHD2, overlapping with the putative substrate-binding site and inhibiting activity via stabilization of local structure. The use of HDX-MS, in lieu of crystallographic data, has provided critical insight into the binding mechanism of these ligands and offers a structural basis for the development of non-hormonal contraceptive agents targeting ABHD2.

3.4 Conclusion

HDX-MS has become an increasingly valuable bioanalytical tool within the biopharmaceutical community for probing protein structure, conformational dynamics, and ligand-induced modulation under near-physiological conditions. In this study, we demonstrate the utility of HDX-MS through three mechanistically distinct examples, each highlighting the technique’s ability to provide high-resolution insights into ligand-protein interactions that would otherwise remain inaccessible due to the absence or limitation of crystallographic data.

For CAR, HDX-MS revealed that ligand-induced stabilization of H11- rather than H12- may play a more critical role in driving transcriptional activation. The differential effects of CITCO and DIE on H11 and H12 suggest that CAR activation can proceed through distinct structural mechanisms. However, the precise influence of these helices on allosteric communication with the heterodimer partner RXRα and coactivator recruitment remains to be elucidated.

In the PXR system, HDX-MS revealed a cooperative interaction between FDN and estrogenic steroids, E2 and EE2, that promotes enhanced stabilization of key regulatory helices, particularly H3 and H12. While E2 and EE2 alone had negligible effects on PXR conformational dynamics and transcriptional activation, their presence in combination with FDN led to additional protection from deuterium exchange in both helices. This synergistic structural stabilization correlated with increased transcriptional output, approaching the levels observed with the full agonist, SR12813. HDX-MS analyses confirmed that FDN does not induce conformational changes in the CAR LBD, supporting its functional selectivity for PXR over CAR. These findings provide mechanistic insight into dual-ligand activation of PXR and suggest that combinatorial ligand strategies can selectively potentiate receptor activity. Such an approach holds promise for the design of tailored PXR-targeted therapies that achieve enhanced efficacy while minimizing off-target effects.

Lastly, in the case of ABDH2, HDX-MS enabled interface mapping for small-molecule inhibitors 191R and 192, even without a crystal structure. The technique also revealed limited conformational changes upon progesterone binding, suggesting that its role in ABHD2-mediated sperm activation may not involve strong or sustained direct interaction. Furthermore, mutagenesis and comparative HDX analysis of the non-catalytic S207A mutant provided additional insight into the structural stability and ligand responsiveness of the enzyme’s active site.

Together, these findings indicate the versatility of HDX-MS as a medium-to-high-throughput method for interrogating dynamic protein-ligand interactions. The ability to resolve subtle conformational shifts and infer functional consequences without needing crystallographic resolution makes HDX-MS a powerful orthogonal tool for fundamental research and applied drug discovery. As demonstrated across nuclear receptors and lipid hydrolase, HDX-MS continues to advance our understanding of how structurally similar ligands can differentially modulate protein activity, offering valuable guidance for the rational design of selective modulators and therapeutics.

3.5 Materials and Methods

3.5.1 HDX-MS for hCAR: Ligands

Human CAR protein was prepared at 10 µM in 100 mM ammonium acetate, pH 7.25, and diluted into either equilibration buffer (10 mM phosphate buffer, pH 7.5) or deuterated reaction buffer (10 mM phosphate buffer, 150 mM NaCl, pH 7.5 in D_2O). After 1, 10 or 30 min labelling at 25 °C, samples were mixed with equal volumes of quench buffer (100 mM phosphate buffer, pH 2.5) at 0 °C. For protein-ligand complex samples, hCAR was mixed 1:10 with CITCO or DIE compound at a final concentration of 100 µM with 2% DMSO. HDX-MS was performed using a commercial Waters HDX system (M-class ACQUITY UPLC and Waters Cyclic IMS Mass Spectrometer). Leucine enkephalin was used for mass correction, and all time points were carried out in triplicate. Samples were digested using an Enzymate BEH Pepsin column (2.1 × 30 mm, Waters) at 15 °C. Peptides were desalted on an ACQUITY UPLC BEH C18 VanGuard Pre-column (2.1 × 5 mm, Waters) and separated using an ACQUITY UPLC BEH C18 column (100 × 1 mm, Waters). ProteinLynx Global server (PLGS) and DynamX software were used for peptide identification and deuterium uptake analysis. PyMOL 2.5 was used for structural visualization.

3.5.2 HDX-MS for hPXR: Ligands/Steroids

PXR-SRC1 (20 mM Hepes, 150 mM NaCl, pH 8.2) was incubated with SR12813, FDN, FDN/E2, and FDN/EE2 at a 1:10 molar ratio (protein: ligand) with a final concentration of 6% DMSO. PXR-SRC1 was also incubated with a 1:10 molar ratio with EE2 and a 1:40 molar ratio with E2. CAR-SRC1 was incubated with FDN at the same molar ratios, with a final DNSO concentration of 2%. A 3 µL protein sample was diluted into 57 µL equilibration buffer (10 mM phosphate buffer, pH 7.5) or deuterated reaction buffer (10 mM phosphate buffer, 150 mM NaCl, pH 7.5 in D_2O). After 1, 10, and 30 min labelling at 25 °C, samples were mixed with equal volumes of quench buffer (100 mM phosphate buffer, pH 2.5) at 0 °C. Subsequently, the quenched sample was injected into the HDX platform, where the protein underwent digestion by passing through an enzymatic Nepenthesin-2/Pepsin column (2.1 × 20 mm, Affipro, AP-PC-006) at 15 °C. The resulting peptides were captured and desalted using a (size) ACQUITY UPLC

BEH C18 VanGuard Pre-column (2.1 × 5 mm, Waters, 186003975), followed by separation on an ACQUITY UPLC BEH C18 column (2.1 × 50 mm, Waters, 186002350) with a linear gradient of 5–35% acetonitrile over 12 min at 4 °C. Mass spectrometer data were acquired using a Cyclic IMS Mass spectrometer (Waters, MA). HDX analyses were conducted in triplicate with a single preparation of each protein-ligand complex. Deuterium incorporation was converted to a percentage and averaged over all time points. A 3σ statistical significance of the differential HDX was calculated. Peptide identification and deuterium uptake were analyzed using ProteinLynx Global server (PLGS) and DynamX. PyMOL 2.5 software was utilized for protein visualization.

3.5.3 HDX-MS for ABHD2: Ligands/Steroids

Bottom-down HDX was conducted to understand conformational changes that ABHD2 undergoes in the presence of 192, 191-R, and 128. ABHD2- ligand complexes were formed by incubating a 1:10 protein: ligand ratio in 50mM TRIS, 500mM NaCl, pH 8 (10% glycerol and 2mM TCEP) with a final concentration of 10μM and 2% DMSO. For progesterone, samples were prepared at a 1:20 and 1:40 protein: ligand ratio with a final concentration of 10uM in 4% DMSO. During the labelling process, samples were diluted into either equilibration buffer (10mM phosphate buffer, pH 7.5) or deuterated buffer (10mM phosphate buffer, 150mM NaCl, pH 7.5 in D2O) for 1,10 and 30 minutes at 25°C. Reaction was quenched using equal volumes of quench buffer (100mM phosphate buffer, 7.5M Guanidine HCl, 0.5M TCEP, pH 2.5) for 3 minutes at 0°C, then further diluted with 100mM phosphate buffer, pH 2.5, before LC-MS. A commercial Waters HDX system, consisting of an M-class ACQUITY UPLC and a Waters Cyclic IMS Mass Spectrometer, performed HDX-MS. All samples were digested using an in-line Enzymate BEH Pepsin column (2.1x30mm, Waters). Peptides were desalted using an ACQUITY UPLC BEH C18 VanGuard Pre-column (2.1x5mm, Waters) before LC separation using an ACQUITY UPLC BEH C18 column (100x1mm, Waters). For mass correction, Leucine enkephalin was used. All time points were collected randomly and in triplicate. Lastly, peptides were identified using the ProteinLynx Global server (PLGS), and DynamX software was used for the HDX analysis. PyMOL 2.5 software was used to display structural differences between ABDH2 and in the presence of ligands.

Chapter 4: Allosteric regulation of the CAR-RXRα heterodimer by graded ligand modulations

Vimanda Chow[1], Jiabao Liu[2], Cristina Lento[1], Henry M Krause[2,3] and Derek J. Wilson[1]

[1]Department of Chemistry, York University, Toronto, ON, M3J1P3
[2]Donnelly Centre for Cellular and Biomolecular Research, University of Toronto, Toronto, ON, M5S 3E1, Canada
[3]Department of Molecular Genetics, University of Toronto, Toronto, ON, M5S 3E1, Canada

V.C. mass spectrometry and data processing. J.L. provided protein and compounds, J.L performed ITC experiments. D.J.W. and C.L. provided supervision.

A manuscript for this chapter is being prepared.

4.1 Summary

The Constitutive Androstane receptor (CAR) operates as an obligate heterodimer with the Retinoid X receptor (RXR), with both receptors modulated by diverse endogenous and exogenous ligands. Here, we demonstrate that ligand binding modulates the structural dynamics of the CAR ligand-binding domain (LBD), particularly within helix 10/11. Transcriptional agonists stabilize this region, while inverse agonists induce its destabilization. Notably, ligand engagement within the CAR LBD also influences the conformation of helix 10 in RXRα, located at the heterodimer interface. Dual agonist binding to both CAR and RXRα further alters the stability of the CAR LBD, suggesting cooperative allosteric communications across the dimer interface. Unexpectedly, inverse agonist binding in the presence of RXRα agonism led to H10/H11 stabilization in CAR, mimicking an agonist-like conformation. Together, these findings reveal a mechanism for ligand-dependent modulation of nuclear receptor crosstalk and suggest a molecular basis for the selective activity of nuclear receptor modulators.

4.2 Introduction

The constitutive androstane receptor (CAR, NR1I3) and Pregnane X receptor (PXR, NR1I2) function as key xenobiotic sensors and transcriptional regulators of genes involved in detoxification and metabolic homeostasis.[170,171] As a nuclear receptor, CAR orchestrates the expression of a broad range of enzymes critical to drug metabolism and xenobiotic clearance, including cytochrome P450 enzymes such as CYP3A and CYP2C.[171] Dysregulation of CAR activity has been implicated in the pathogenesis of several human diseases, including metabolic disorders[172], hepatotoxicity[173], and certain cancers[174], outlining its critical role in maintaining physiological and metabolic balance.[7]

A variety of synthetic molecules have been investigated as modulators of hCAR, including the agonist CITCO and diindolyl-ethane (DIE), inverse agonists PK11195 and Ethyl [5-[(diethylamino)acetyl]-10,11-dihydro-5H-dibenz[b,f]azepin-3-yl]carbamate (CINPA1), and antagonists such as clotrimazole, mecline, and S07662, among others.[7,9,162,175,176] Depending on their mechanism of action, these compounds function by stabilizing CAR in either its transcriptionally active or inactive conformation.[177–179] In hCAR, helix 11(H11) is uniquely connected to helix 12(H12) by a short, single-turn helical segment (termed Hx)(Figure 4.1A).[180] This architectural feature is proposed to underlie hCAR's unusual ability to exhibit basal transcriptional activity in the absence of ligand, a property that distinguishes it from most other nuclear receptors.[162] In the broader context of nuclear receptor structure, ligand-induced transcriptional regulation is typically mediated through conformational changes in H12, which forms part of the canonical charge clamp pocket involving H3 and H4. This pocket serves as a critical docking interface for co-activator recruitment, such as steroid receptor coactivator-1 (SRC-1)(Figure 4.1B).[181] Computational modelling, hydrogen-deuterium exchange (HDX) experiments, and mutational analyses have demonstrated that the CAR LBD's active conformation supports co-activator binding at the AF-2 surface, thereby enhancing transcription above basal levels.[155] Conversely, disruption of the charge clamp pocket impairs transcriptional activity.[181] The transcriptionally repressed (inactive) state is characterized by a pronounced kink between H10 and H11, disordering of Hx and displacement of H12 from the co-activator binding site, favouring interactions with co-repressors instead.[162]

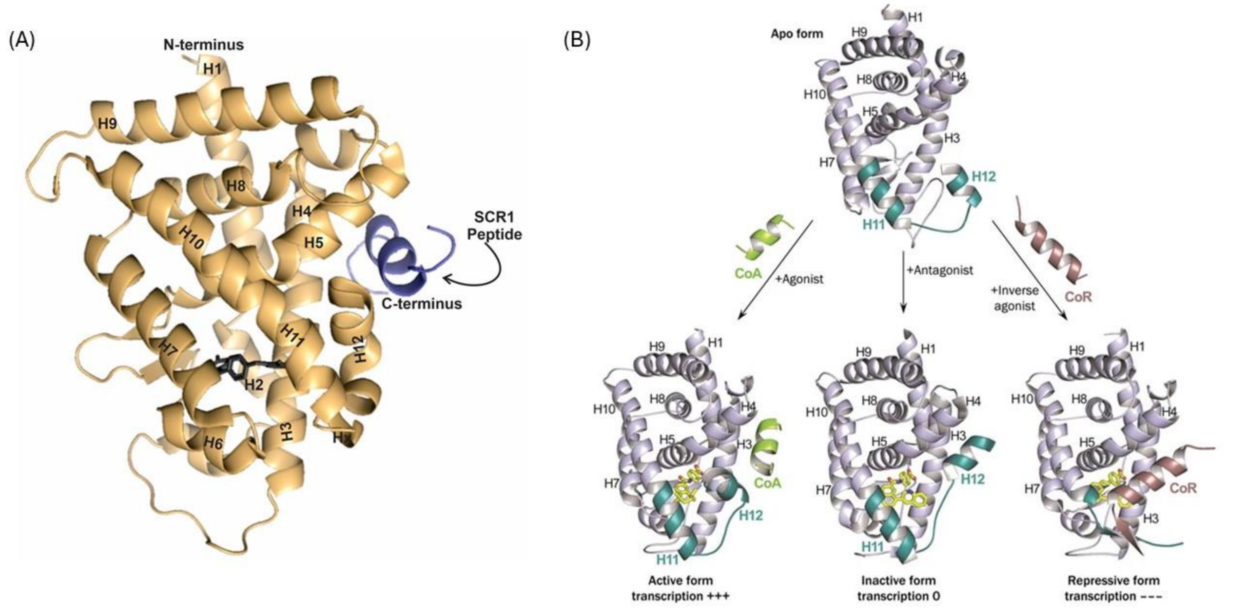

Figure 4.1| Schematic of CAR ligand-binding domain (LBD). (A) Crystal structure of the CAR LBD highlighting each helix (PDB 1XVP). (B) Structural depiction of the canonical charge clamp pocket, where helix H12 is positioned in close proximity to helices H3 and H4 – an arrangement essential for coactivator binding. Reproduced with permission from Delfosse *et al*. (2014)[182]

Despite extensive efforts to characterize nuclear receptor modulators, the graded activity of the ligands and their ability to fine-tune receptor conformational dynamics remain poorly understood. In particular, it is unclear how ligand binding to one member of the NR heterodimer influences co-regulator recruitment and functional outcomes in its dimeric partner. Many NRs, including CAR, function as obligate heterodimers with RXRα, adopting permissive or non-permissive signalling modes.[152,181,183,184] In permissive heterodimers (e.g. PPARy: RXRα), ligands targeting either partner can activate the complex, often producing additive or synergistic effects.[152] Conversely, in non-permissive heterodimers (e.g. Thyroid Hormone Receptor (TR): RXRα), activation typically depends on the presence of the partner ligand, with RXRα ligands alone eliciting little to no transcriptional response.[152,183]

Using hydrogen-deuterium exchange mass spectrometry (HDX-MS), we investigated the conformational and allosteric consequences of ligand binding across a series of CAR modulators spanning the pharmacological spectrum from full agonists to inverse agonists. Subtle structural differences among ligands induced significant shifts in transcription activity, highlighting a graded spectrum of activation. These dynamic changes illuminate the importance of long-range allosteric communication within the CAR: RXRα heterodimer. Notably, RXRα ligands alone (e.g. 9-cis-retinoic acid(RA) and LG100268) did not alter CAR conformation, supporting the classification of RXRα as a non-permissive partner in this context. Furthermore, specific ligand combinations- such as an RXRα agonist with a CAR partial agonist or inverse agonist- produced no significant statistical effects, suggesting the potential for fine-tuned modulation of transcriptional output occurs within other regions of the protein, not within the LBD, such as the hinge or DBD. Therefore, studying the full-length CAR and RXRα offers a promising direction for future research and drug design.

4.3 Results and Discussion

4.3.1 Graded Response of CAR Modulators

In this study, we focused on a panel of six CAR modulators, including two established agonists (CITCO and DIE), two inverse agonists (CINPA1 and PK11195), and two high-affinity antagonists, (D)-ENL and (L)-ENL (Figure 4.2A). No systematic comparison has linked CAR ligand-specific structural rearrangements with corresponding transcriptional activity. To address this, we classified each modulator according to its transactivation potential using a dual-luciferase reporter assay in HepG2 cells, employing a GAL4/UAS system with the hCAR LBD fused to the GAL4 DNA-binding domain (work done by our collaborators, data not shown). We performed hydrogen-deuterium exchange mass spectrometry (HDX-MS) on hCAR in complex with each ligand at three time points (1, 10 and 30 minutes) to probe the structural dynamics underlying graded transcriptional response. Ligands were incubated at a 10-fold molar excess (37.5μM) relative to the protein (3.75μM) to ensure <80% binding saturation. We employed a CAR construct fused to the SRC-1 activator LXXLL motif for enhanced physiological relevance via a flexible linker.

HDX-MS revealed ligand-specific protection patterns across the CAR LBD (Figure 4.2B). All tested modulators conferred protection to regions encompassing helix 2 (residues 131Q-142F) and helix 3 (residues 151L-160H), with varying degrees of protection in helices 10/11 (residues 319L-337S). Notably, agonists CITCO and DIE induced moderate stabilization in H11 (ΔHDX ~-5 to -15%), a region also protected by antagonists (D)-ENL and (L)-ENL, suggesting that antagonists may stabilize a heterodimer-compatible conformation. These observations parallel findings in mCAR, where HDX and mutational studies linked stabilization of H10/H11 to enhance transactivation and coactivator binding.[155] In contrast, inverse agonists CINPA1 and PK11195 resulted in mild deprotection of H11 (ΔHDX ~3 to 5%), suggesting a shift toward a transcriptionally repressive conformation.

In nuclear receptors, the inactive state is often characterized by repositioning H12, exposing the AF-2 surface to favour co-repressor binding.[164] Corepressor motifs, such as that of NCoR, are typically longer than coactivator motifs (e.g. SRC-1).[181] The structural rearrangement of the LBD may be required for optimal binding. These data are supported by structural studies of mCAR, where inactive states show H10 dissociation and formation of a shortened H11.[164] These results suggest that CAR modulators differentially stabilize conformational ensembles corresponding to transcriptionally active and repressive states.

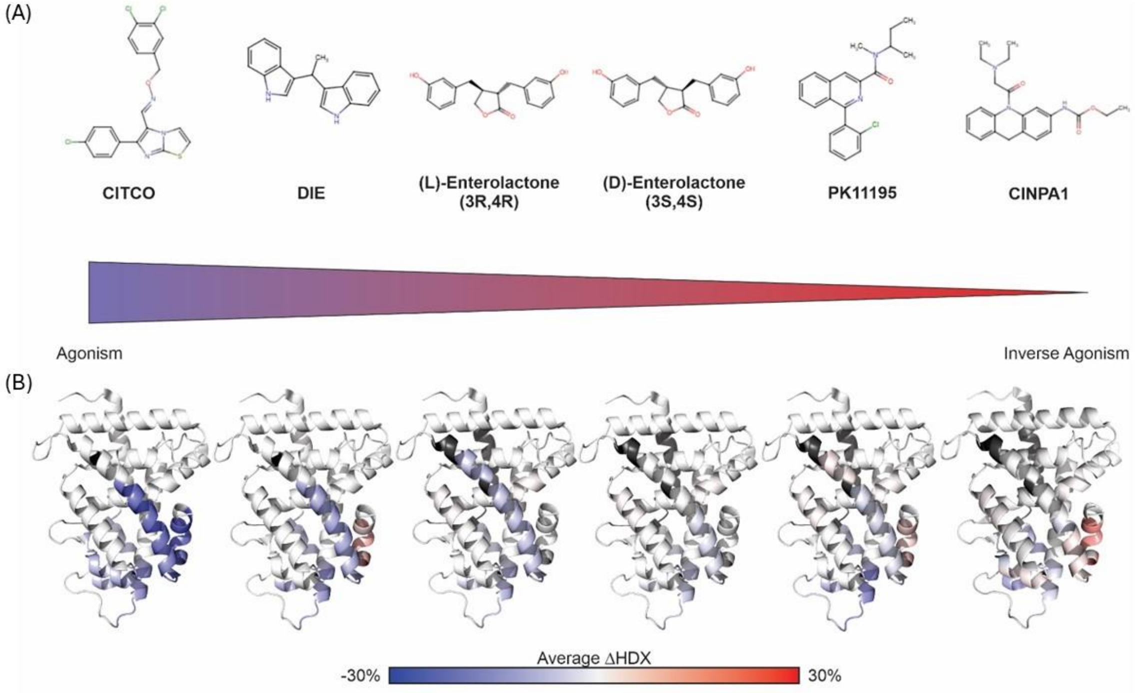

Figure 4.2| Ligand-dependent conformational stabilization of the CAR ligand-binding domain (LBD). (A) Chemical structure of six CAR modulators arranged from agonist (left) to inverse agonist (right). (B) Differential hydrogen-deuterium exchange (HDX) data mapped on the CAR LBD available crystal structure (PDB: 1XVP, chain D) highlight ligand-induced conformational changes. Blue regions indicate protection (reduced deuterium uptake), red indicates increased exchange (deprotection), white denotes no change, and grey marks regions lacking sequence coverage. Data reflect cumulative deuterium uptake across all time points, comparing ligand-bound versus unbound CAR. Values represent mean ±3 s.d. from three technical replicates (n=3). The colour scale for HDX differences is consistent throughout the study.

Previous studies on other nuclear receptors have established a strong correlation between the stability of H12 and transcriptional activity.[155,165,185] However, additional function assays are needed to establish robust structure-activity relationships for compounds that modulate NR function via H12-independent mechanisms (e.g. DIE).[7,165] In the case of CAR, our HDX-MS results reveal that ligand-induced stabilization of H11 and the Hx region provides a more reliable structural correlation of CAR activation. H11, in particular, emerges as a defining feature of the active conformation of CAR and may also play a role in allosteric communications with its heterodimer partner, RXRα.[155,186] These findings align with the growing appreciation that H11 contributes to co-regulator recruitment and functional specificity in nuclear receptor signalling.[186] Moreover, a finely tuned mechanism that indirectly modulates H12 conformation has been proposed to explain how nuclear receptors elicit graded transcriptional responses, ranging from partial to full agonism, without directly stabilizing the AF-2 surface. Yet, it remains unclear how partial agonists that fail to stabilize AF-2 can still support high gene expression levels. To resolve this paradox, further investigation is required into how the CAR-RXRα heterodimer functions in the context of diverse ligand combinations and how crosstalk between the two subunits contributes to overall transcriptional output.

4.3.2 The RXRα-CAR Heterodimer Interface

To confirm the formation and stability of the CAR-RXRα heterodimer under HDX-MS conditions, we first compared the deuterium uptake profiles of the heterodimer to those of the individual CAR and RXRα LBDs. Differential HDX analysis revealed statistically significant protection within H10 of RXRα (residues 419L-434E) upon complex formation with CAR, indicating a conformational stabilization in the dimer interface region (Figure 4.3B). CAR LBD exhibited significant protection in the H8-H9 loop (residues 226A-280E) and H10/11 (318E-328Y) when complexed with RXRα, compared to its monomeric form. These results suggest specific regions within both receptors undergo structural rearrangements upon heterodimer formation, consistent with known interaction surfaces (Figure 4.3A).

Given that RXRα is known to form homodimers without a nuclear receptor partner, we further validated the stoichiometry and assembly of the heterodimeric complex using native mass spectrometry. We analyzed three species: (1) CAR-SRC1 monomer (theoretical mass: 32.900kDa), (2) RXRα-SRC1 monomer (theoretical mass: 28.915 kDa) and homodimer (theoretical mass: 57.830kDa), and (3) RXRα-SRC1 monomer, CAR-SRC1 monomer, CAR-SCR1-RXRα-SRC1 heterodimer (theoretical mass: 61.815kDa) (Figure 4.4). The detection of the RXRα-SRC1 homodimer supports the limited HDX changes observed in H7-9 upon heterodimerization, as these regions may already be structurally constrained in the homodimer state. Notably, the largest HDX differences observed in both CAR and RXRα map to the predicted dimerization interface, in agreement with previously reported crystal structures, thus confirming the specific and high-affinity nature of the CAR-RXRα interaction.

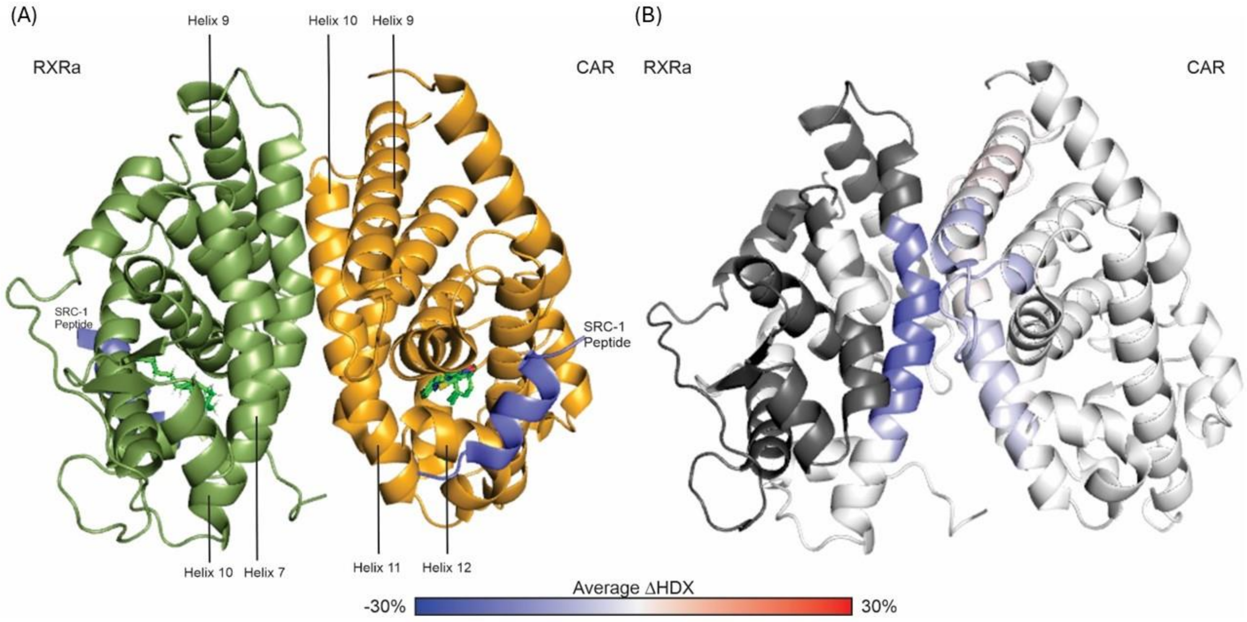

Figure 4.3| Conformational dynamics at the CAR-RXRα heterodimer interface revealed by HDX-MS. (A) Structural model of the CAR-RXRα heterodimer (PDB: 1XVP) with labelled helices previously implicated in the dimerization interface. Reproduced with permission from Choi *et al*. (2023).[186] (B) Ligand-free CAR induced conformational changes in RXRα LBD, and ligand-free RXRα induced conformational changes in CAR LBD. The average differential HDX of each LBD in the presence versus absence of the heterodimer partner is mapped onto the available crystal structure. HDX differences are visualized using the same colour scale defined in Figure 4.2.

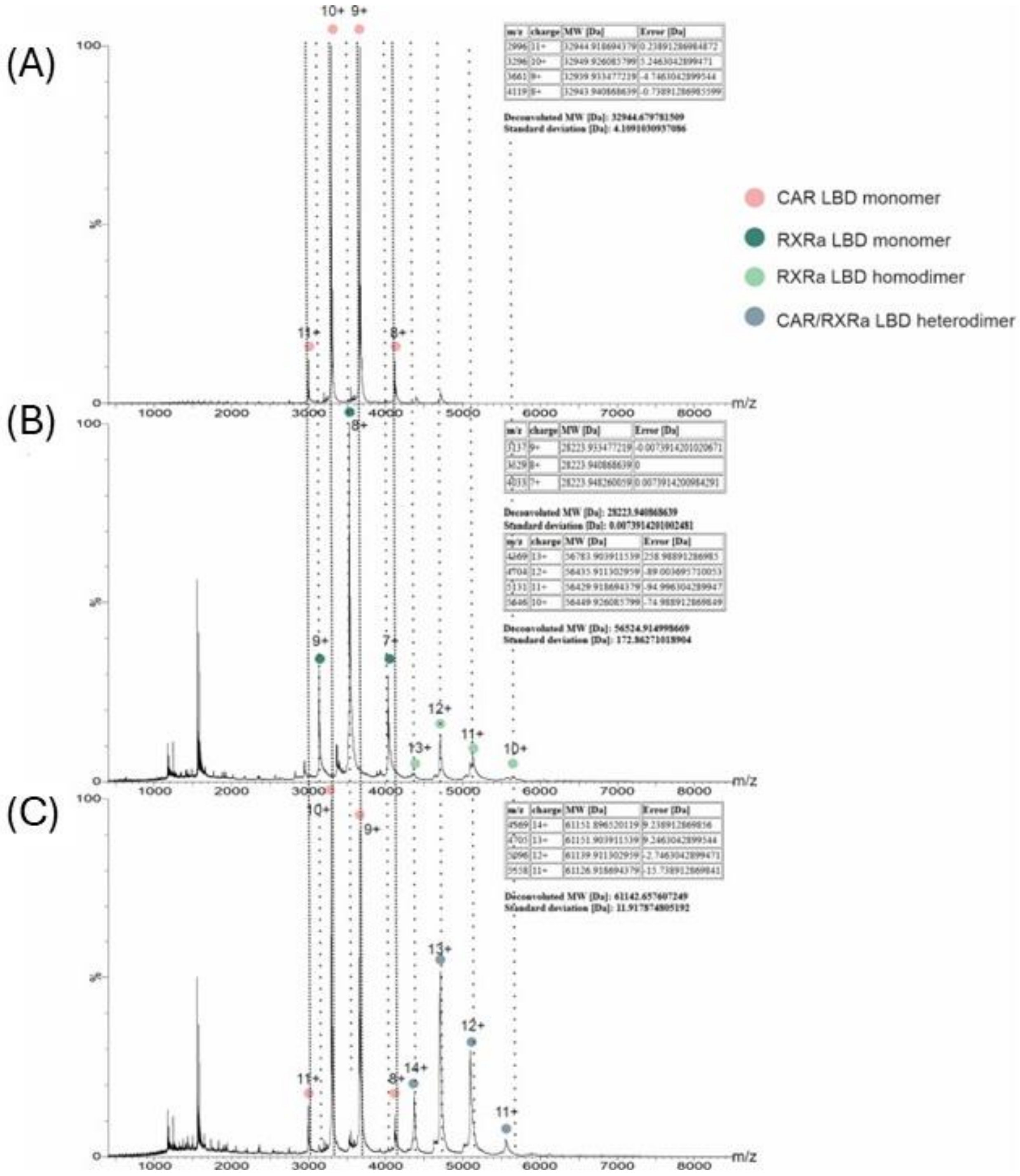

m/z	charge	MW [Da]	Error [Da]
2996	11+	32944.918694379	0.23891286984872
3296	10+	32949.926085799	5.2463042899471
3661	9+	32939.933477219	-4.7463042899544
4119	8+	32943.940868639	-0.73891286985599

Deconvoluted MW [Da]: 32944.679781509
Standard deviation [Da]: 4.1091030937086

m/z	charge	MW [Da]	Error [Da]
3137	9+	28223.933477219	-0.0073914201020671
3529	8+	28223.940868639	0
4033	7+	28223.948260059	0.0073914200984291

Deconvoluted MW [Da]: 28223.940868639
Standard deviation [Da]: 0.0073914201002481

m/z	charge	MW [Da]	Error [Da]
4369	13+	56783.903911539	258.98891286985
4704	12+	56435.911302959	-89.003695710053
5131	11+	56429.918694379	-94.996304289947
5646	10+	56449.926085799	-74.988912869849

Deconvoluted MW [Da]: 56524.914998669
Standard deviation [Da]: 172.86271018904

m/z	charge	MW [Da]	Error [Da]
4369	14+	61151.896520119	9.238912869856
4705	13+	61151.903911539	9.2463042899544
5096	12+	61139.911302959	-2.7463042899471
5558	11+	61126.918694379	-15.738912869841

Deconvoluted MW [Da]: 61142.657607249
Standard deviation [Da]: 11.917874805192

Figure 4.4| Native mass spectrometry analysis of CAR-RXRα heterodimer formation. (A) Native mass spectrum of CAR alone, with inset showing the predicted molecular mass of monomeric CAR. (B) Native mass spectrum of RXRα alone, with inset highlighting its predicted dimer state and monomeric mass. (C) Native mass spectrum of CAR and RXRα mixed at a 1:1 molar ratio, showing formation of heterodimeric species. The inset displays predicted molecular masses of observed species. Molecular weights were determined using ESIProt software (https://mass-tools.ipbs.fr/mass-tools/prot/).[57]

4.3.3 Ligand Signalling in CAR-RXRα Heterodimer

Having confirmed that the CAR-RXRα heterodimer is stable under HDX-MS conditions, we next investigated the mechanisms driving allosteric communication between the receptor partners. To determine whether the observed HDX changes in RXRα were allosterically driven, we analyzed the deuterium uptake of RXRα alone in the presence and absence of CAR-targeted modulators (Table C1). HDX-MS profiles of RXRα incubated with these modulators revealed no significant changes in structural dynamics, indicating that, at concentrations sufficient to alter CAR conformation, the modulators do not directly impact RXRα. This conclusion was further supported by isothermal titration calorimetry (ITC) performed by our collaborators, which showed no detectable change in heat released between the reference cell (containing CAR +modulator) and sample cell (titrant: RXRα and titrand: CAR +modulator)(Figure C1).

We then assessed RXRα structural changes within the CAR-RXRα heterodimer upon modulator binding. HDX-MS revealed that RXRα dynamics were modulator-dependent, with notable reduction in deuterium exchange observed in H10 (residues 418L-442I) in the presence of CITCO, DIE, (L)-ENL and (D)-ENL (Δ HDX ~ -4 to -7%)(Figure 4.5). In contrast, PK11195 and CINPA1 elicited no changes in RXRα. The stabilization of H10 mirrors the conformational effects induced by RXRα agonists, such as 9-cis-RA and LG100268, alone (Figure 4.6), suggesting that ligands binding to CAR can allosterically prime RXRα toward an active-like state, thereby enhancing CAR-mediated transcription. Interestingly, this allosteric effect did not extend to the AF-2 domain of RXRα, which is consistent with previous findings that activation of RXRα does not strictly require AF-2 stabilization.[152,184]

Regardless of the ligands used, HDX-MS revealed consistent patterns of structural protection at the heterodimer interface, reinforcing the notion that heterodimer formation is energetically and structurally favourable. These findings imply that heterodimerization may be essential for engaging DNA response elements and modulating transcription.[186] Moreover, in light of studies demonstrating that the DNA binding domain itself can trigger conformational changes in nuclear receptors LBDs, it is plausible that additional layers of regulation, beyond ligand binding, contribute to the graded transcriptional responses observed, particularly in the presence of partial agonists.

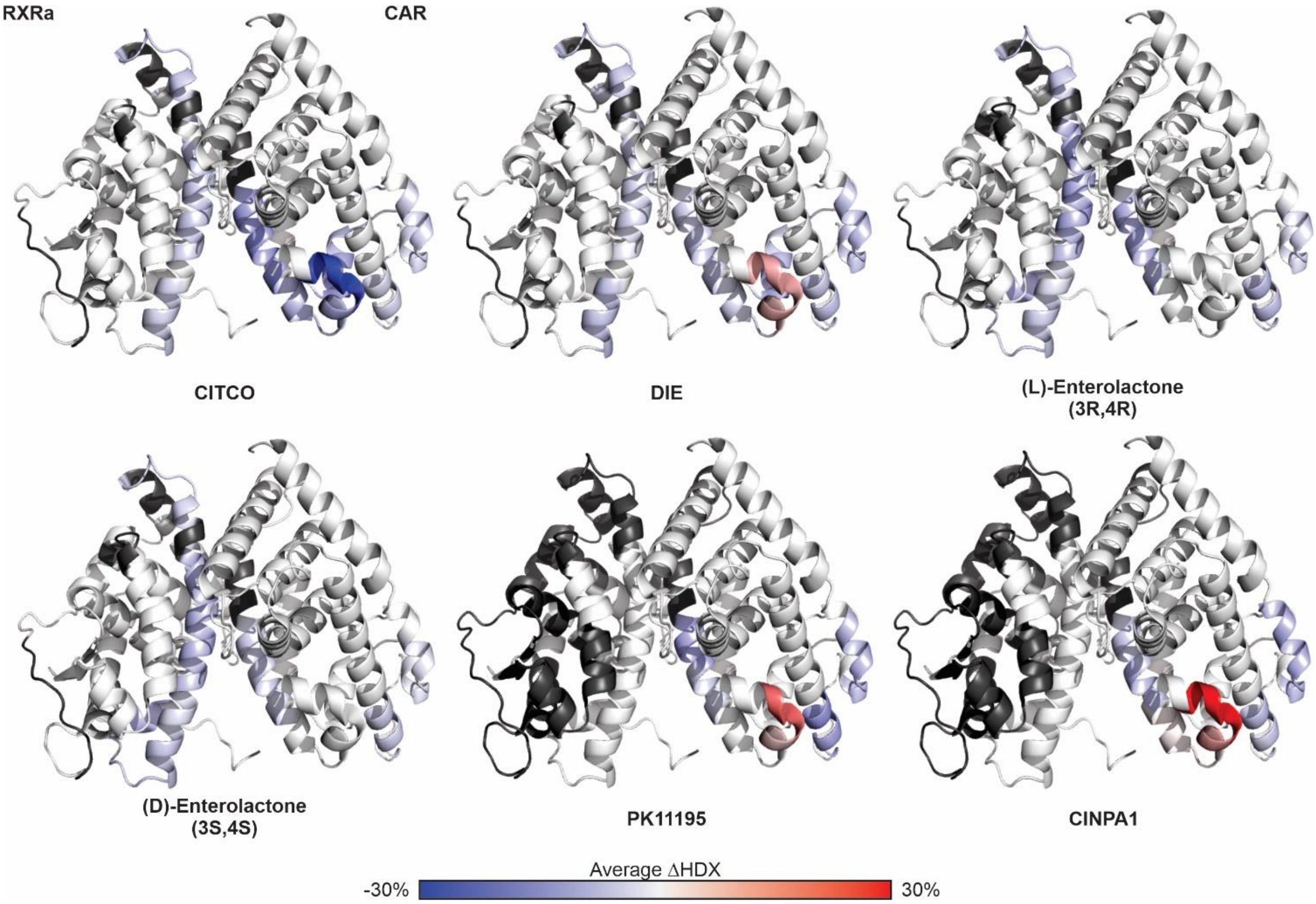

Figure 4.5| Modulator-dependent allosteric communication with RXRα in the CAR-RXRα heterodimer. Average differential HDX of RXRα LBD in the CAR-RXRα complex, in the absence versus presence of various CAR modulators, mapped onto the RXRα chain (PDB: 1XVP, chain C). Regions showing modulator-induced protection or deprotection are visualized using the previously defined colour scale (see Figure 4.2). White indicates no change; grey indicates regions without sequence coverage.

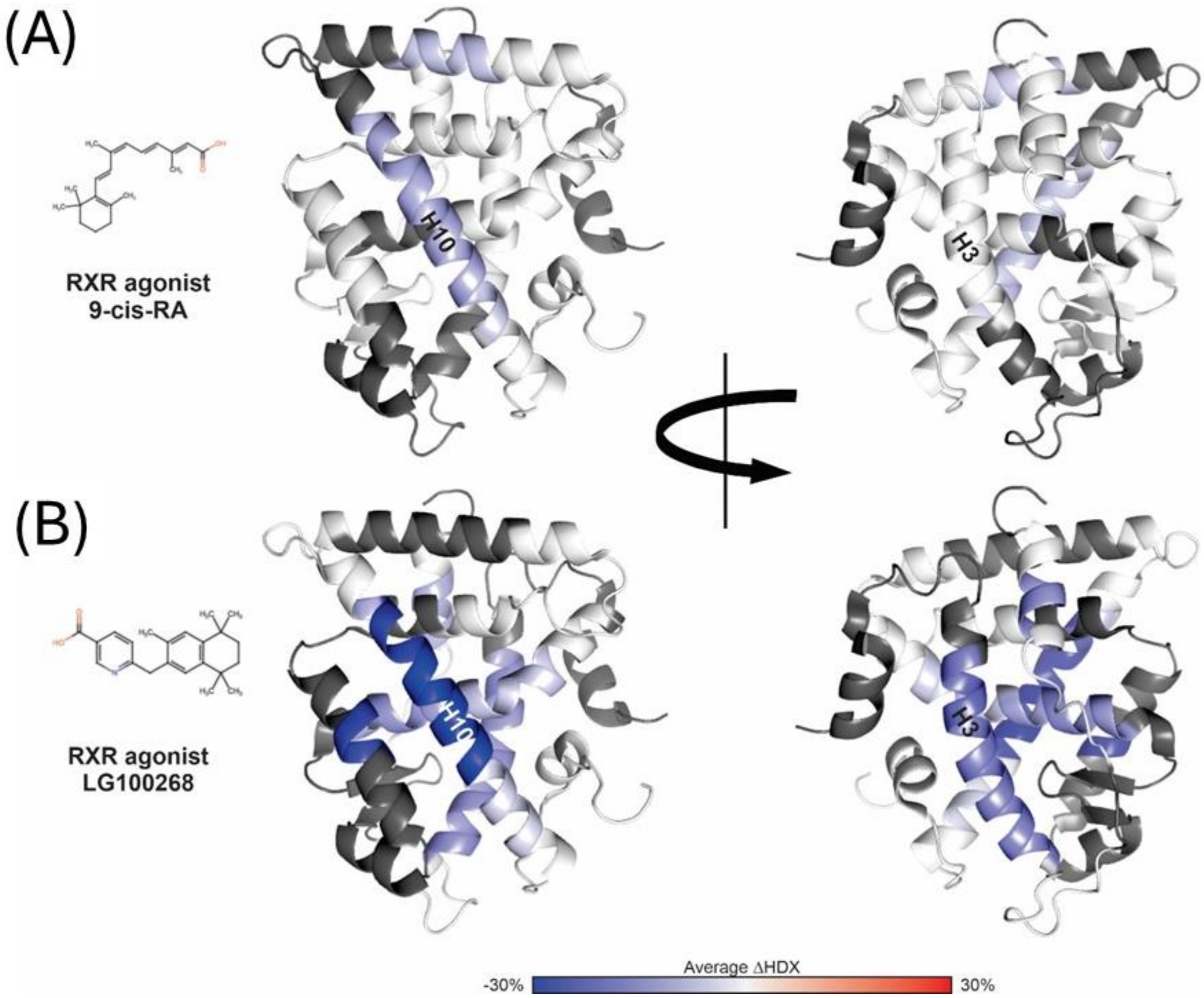

Figure 4.6| Ligand-induced structural dynamics within RXRα LBD upon 9-cis-retinoic acid and LG100268 binding. (A) Average differential HDX of RXRα LBD in the absence versus presence of its endogenous ligand, 9-cis-retinoic acid (9-cis-RA), mapped onto the RXRα chain. (B) Average differential HDX of RXRα LBD in the absence versus presence of its exogenous ligand, LG100268, mapped onto the RXRα chain. Modulation of structural dynamics is visualized using the previously define HDX colour scale.

To further substantiate heterodimer formation in the presence of CAR modulators, our collaborators conducted ITC, which confirmed that these compounds promote stable CAR-RXRα complex formation (Figure C2).[187] In parallel, we attempted to employ native mass spectrometry (native MS) – a well-established method for determining the stoichiometry and assembly of protein complexes- to detect the modulator-bound state of CAR alone or in complex with RXRα.[185,188] Despite multiple experimental conditions, we could not resolve the bound state of either CAR alone (Figure C3) or CAR-RXRα heterodimer (data not shown) in the presence of modulators. This outcome may reflect these interactions' transient or conformationally dynamic nature, which can challenge the capture of intact complexes under native MS conditions.

4.3.4 Conformational Dynamics Control RXRα Permissiveness

Nuclear receptors (NRs) are known to signal through two primary heterodimeric mechanisms, permissive and non-permissive pathways.[152] In permissive heterodimers, both receptors can be independently activated by their respective ligands, often resulting in additive or synergistic transcriptional outcomes. In contrast, non-permissive heterodimers exhibit ligand dependency on only one partner, where activation requires ligand binding exclusively to the non-RXRα partner. Such a heterodimer remains unresponsive to RXRα ligands unless ligands of the partner receptor are present, thereby limiting its functional contribution.[152,184]

To investigate whether RXRα functions as a permissive or non-permissive partner to CAR, we conducted HDX-MS analyses on CAR in the presence and absence of two RXRα agonists: 9-cis-RA and LG100268. If RXRα were permissive, we hypothesize that these ligands would be expected to stabilize the CAR active conformation, particularly helices H11 and Hx, mimicking the conformational dynamics induced by CAR agonists such as DIE, (L)-ENL, and (D)-ENL. However, HDX analysis revealed no significant alterations in CAR deuterium uptake upon RXRα ligand treatment (Figure 4.7), indicating that RXRα ligands alone do not induce conformational changes within CAR. These findings are consistent with a non-permissive mode of CAR-RXRα heterodimerization. Further functional assays, such as luciferase reporter analysis, will be required to confirm that RXRα ligands do not enhance CAR-mediated transcriptional activity.

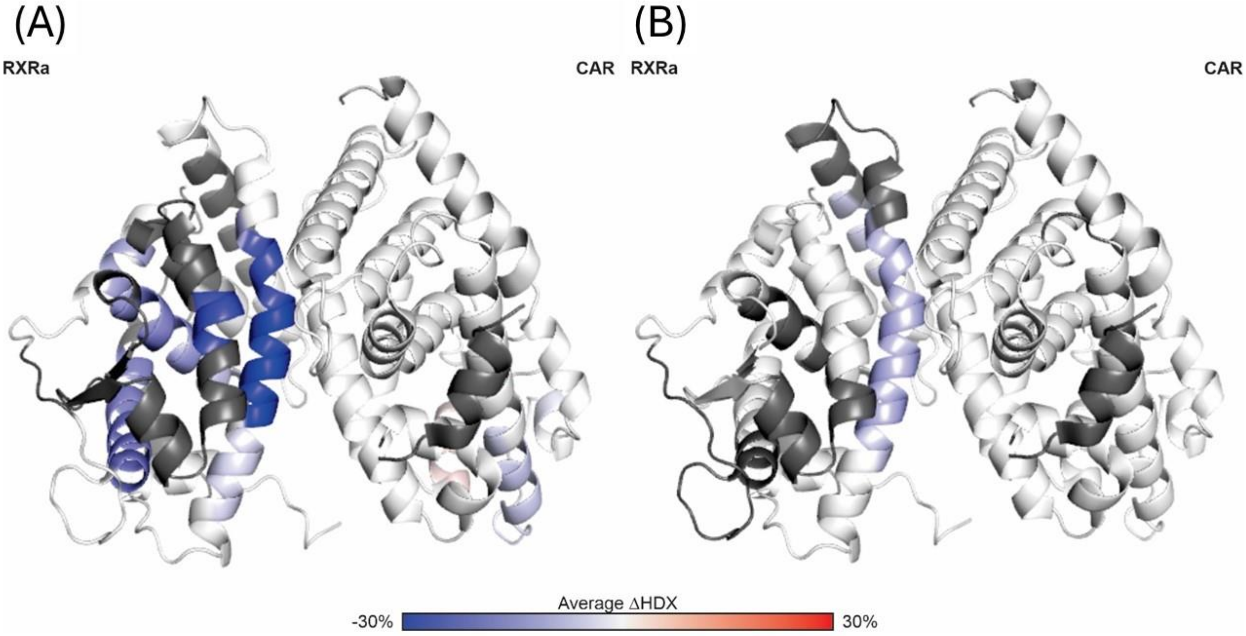

Figure 4.7| Modulator-dependent allosteric communication with CAR in the CAR-RXRα heterodimer. Average differential HDX of CAR LBD in the CAR-RXRα complex, in the absence versus presence of (A) endogenous ligand, 9-cis-RA and (B) exogenous ligand, LG100268, mapped onto the RXRα chain (PDB: 1XVP, chain C). The HDX colour scale described in Figure 4.2, is used to visualize regions of protection and deprotection.

Tzameli *et al* (2000) previously demonstrated that RXRα ligands can influence CAR-RXRα function in a ligand-dependent manner.[189] Notably, surface plasmon resonance (SPR) assays revealed that coactivator recruitment to CAR-RXRα is reduced in the presence of the inverse agonist androstanol. Still, this repression is alleviated upon co-treatment with 9-cis-RA, suggesting an indirect modulatory role for RXRα.[189] Furthermore, RXRα agonist did not interfere with the effects of CAR agonist TCPOBOP, but rather maintained their activity when combined, indicating that RXRα may modulate CAR activity in a specific ligand context.[189]

To further investigate the interplay between CAR and RXRα ligands, we conducted differential HDX-MS profiling of CAR-RXRα complexes treated with a combination of CAR and RXRα modulators. In the presence of LG100268 (an RXRα agonist) and DIE (a partial CAR agonist), CAR exhibited stabilization patterns comparable to those observed with DIE alone (Figure 4.8A). Conversely, co-treatment with LG100268 and the CAR inverse agonist CINPA1 produced a profile resembling that of CINPA1 alone, with only attenuated protection observed in specific regions such as helices H11 and H12 (Figure 4.8B). These findings suggest that co-binding of RXRα and CAR ligands does not induce additional structural rearrangements within the CAR-RXRα complex beyond those elicited by the CAR ligand alone. Potential allosteric effects in distal regions, such as the hinge or DBD, cannot be excluded. These observations highlight the need for complementary functional studies to determine whether combinatorial ligand treatments modulate CAR-dependent transcriptional activity.

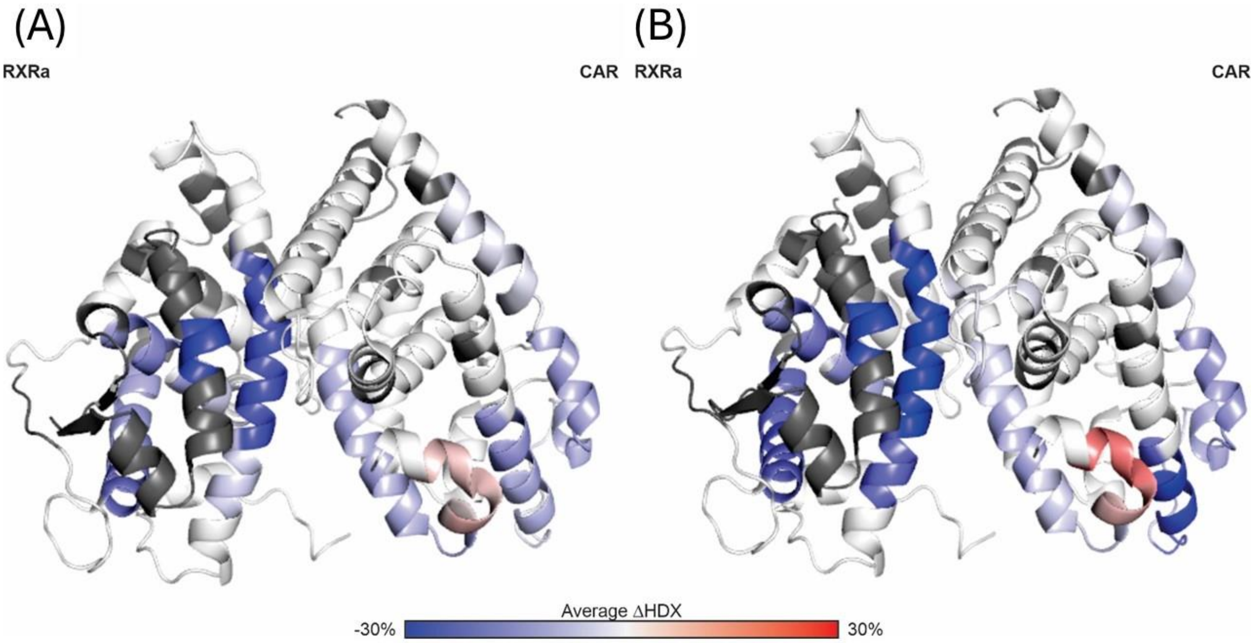

Figure 4.8| Dual-ligand binding structural dynamics within CAR-RXRα heterodimer LBD. (A)CAR-RXRα heterodimer binding of both LG100268 and DIE, (B) CAR-RXRα heterodimer binding of both LG100268 and CINPA1. Differential HDX patterns reflect modulator-induced conformational dynamics within the heterodimer and are visualized using the HDX colour scale defined in Figure 4.2 (PDB: 1XVP).

Next, we examined the CAR-RXRα heterodimer's conformational dynamics in response to the endogenous RXRα ligand 9-cis-RA co-incubated with DIE or CINPA1. Notably, these dual-ligand conditions did not result in statistically significant structural alterations compared to the profiles of CAR and RXRα alone (Figure 4.9). In line with findings using the synthetic RXRα ligand, LG100268, these results indicate that RXRα ligands- whether endogenous or exogenous- do not modulate the structural dynamics of CAR within the heterodimer. As with previous observations, further validation using transcriptional assays is necessary to determine the functional consequences of these structural findings.

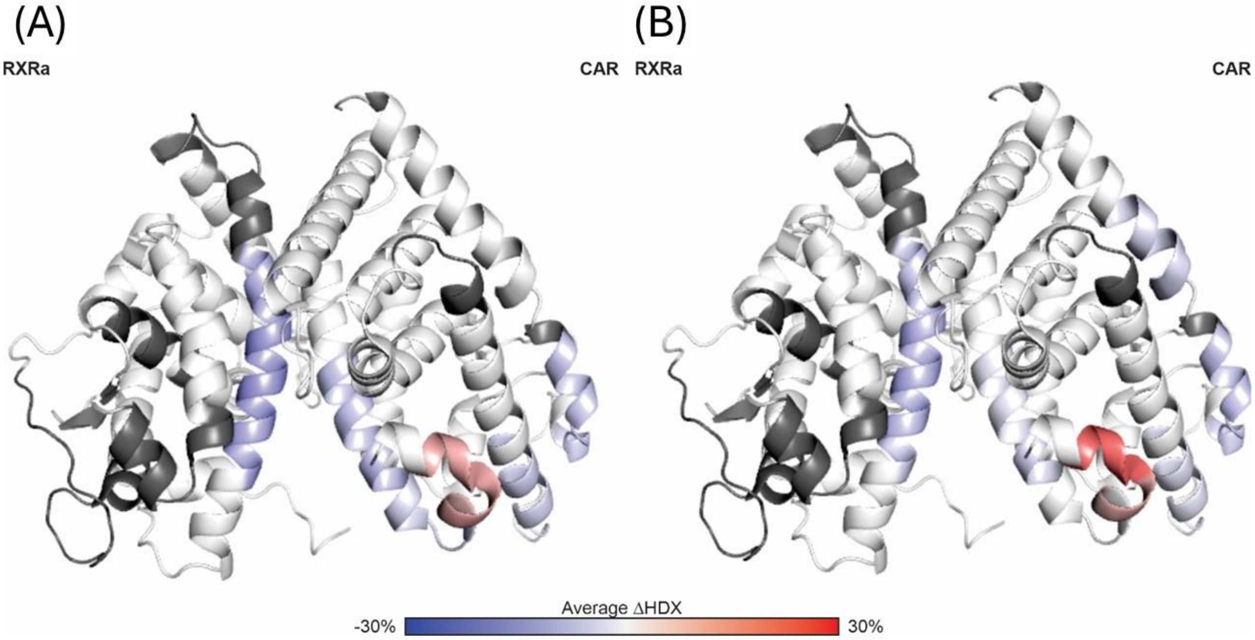

Figure 4.9| Dual-ligand binding structural dynamics within CAR-RXRα heterodimer LBD. (A)CAR-RXRα heterodimer binding of both 9-cis-RA and DIE, (B) CAR-RXRα heterodimer binding of both 9-cis-RA and CINPA1. Differential HDX patterns reflect modulator-induced conformational dynamics within the heterodimer and are visualized using the HDX colour scale defined in Figure 4.2 (PDB: 1XVP).

4.4 Conclusion

In this study, we comprehensively characterized the structural and functional dynamics of the human CAR in response to a spectrum of pharmacological modulators, ranging from full agonists to inverse agonists. Using hydrogen-deuterium exchange mass spectrometry (HDX-MS), we demonstrated that each ligand elicits distinct conformational signatures, particularly within the H11 and Hx regions—key structural elements associated with the CAR activation state. Our findings further support that H11 stabilization is a hallmark of the active conformation and may also play a pivotal role in mediating heterodimer interactions with RXRα.

We further established that RXRα acts as a non-permissive heterodimer partner for CAR, as RXRα ligands alone failed to induce structural changes in CAR. However, allosteric effects were observed when CAR ligands were present, revealing that CAR activation can render conformational transitions within RXRα, particularly in H10. These changes occurred independently of RXRα's AF-2 stabilization, suggesting an alternative co-regulator recruitment and transcriptional activation pathway. Combinatorial ligand treatments unveiled no capacity for additive or intermediate structural outcomes.

Looking ahead, structural studies of isolated ligand-binding domains have largely informed our functional knowledge of nuclear receptors, leaving the interplay between domains in full-length receptors poorly understood.[184,186] Emerging evidence suggests that ligand binding to the LBD can allosterically influence the DBD, potentially altering its DNA-binding affinity and specificity.[186] Therefore, future investigations must expand beyond the LBD to include the hinge and DBD regions, likely critical conduits for allosteric signalling. Zhang and colleagues proposed that DNA-dependent alterations in the LBD directly modulate the coactivator binding activity of the heterodimer complex.[184] Defining the full extent of interdomain communications will be essential to fully elucidate how nuclear receptors integrate chemical signals into precise transcriptional responses.

4.5 Materials and Methods

Hydrogen-deuterium exchange mass spectrometry (HDX-MS). Differential hydrogen-deuterium exchange (HDX) experiments were performed as previously described[78]. Briefly, exchange reactions were carried out at 25 °C in either equilibration buffer (10 mm phosphate buffer, pH 7.5) or deuterated solvent (10 mm phosphate buffer, 150 mm NaCl, pD 7.5). Reactions were quenched by adding a quench buffer (100 mm phosphate buffer, pH 2.5) at 1 °C. Proteins were passed through an online NepIIPepsin column (2.1 mm x 20mm, Affipro) at a 200 µL/min flow rate. The resulting peptides were captured on a C18 trap column (2.1mm x 5mm C18 column, Waters Corporation) and separated using a linear gradient of 5% to 85% acetonitrile, over 12 minutes. Protein digestion was carried out at 15 °c, while peptide separation was maintained at 2 °c. Electrospray ionization introduced eluted peptides into the Waters Cyclic ion mobility mass spectrometer. Each on-exchange time point (1, 10 and 30 minutes) was analyzed in triplicate for all states. Peptides were identified by submitting MS/MS raw data to the ProteinLynx Global Server (PLGs) and analyzed using Waters DynamX and Microsoft Excel software. Structural visualization was performed using PyMOL version 2.5. Sequence coverage for CAR and RXRα can be found in Figure C4 and C5, respectively. The deuterium uptake plots for all the HDX-MS experiments are provided in the Supplementary Figure C6

Native mass spectrometry. Human CAR LBD and RXRα LBD were buffer-exchanged into 250 mm ammonium acetate (pH ~8.0)using an Amicon Ultra centrifugal filter (Merck Millipore). Heterodimer formation was achieved by mixing equimolar amounts of CAR LBD and RXRα LBD to achieve dimer concentrations of 10μM. Ligand was added to the required samples to a final concentration of 100μM. Native mass spectra were acquired on a Synapt G2 instrument (Waters Corporation).

Chapter Five: Conclusions and Future Work

5.1 Conclusion

Hydrogen-deuterium exchange mass spectrometry is a complementary and orthogonal strategy in the structural biology toolkit. It can validate structural models, map binding interfaces, and guide the rational design of therapeutics targeting conformationally regulated proteins.

Chapter 1 provided foundational context by outlining the architecture of modern mass spectrometers. It emphasizes how hybrid instruments integrate multiple mass analyzers and how soft ionization techniques, such as electrospray ionization (ESI), facilitate the transfer of ions from solution to the gas phase. This chapter also introduces HDX-MS, focusing on bottom-up workflows that monitor backbone amide hydrogens exchange rates to probe protein folding, flexibility, and solvent accessibility.

Chapter 2 explored the interaction of cytochrome c with nanodisc membrane mimics, particularly through A-site and L-site interactions under physiological pH conditions. Variations in binding to anion phospholipid-containing nanodiscs, such as those embedded with cardiolipin species, may modulate cytochrome c's peroxidase activity and apoptosis function, highlighting potential therapeutic applications.

Chapter 3 illustrated the extent of HDX-MS in characterizing protein-ligand interactions and conformational changes in the absence of crystallographic data. Using three distinct systems-CAR, PXR, and ABHD2- HDX-MS revealed unique ligand-dependent structural modulations. For CAR, stabilization of helix 11 was identified as a critical feature of activation. In PXR, the combinatorial binding of FDN with estrogenic steroids, E2 and EE2, leads to synergistic stabilization of regulatory helices, enhancing transcriptional output. In the case of ABHD2, HDX-MS enabled inhibitor mapping and indicated minimal conformational response to progesterone. Collectively, these studies underscore the utility of HDX-MS in guiding selective ligand design.

Chapter 4 presented a detailed HDX-MS analysis of CAR in response to diverse ligands, uncovering distinct conformational profiles, particularly in helices H11 and Hx. H11 stabilization was again highlighted as an activation marker and potential mediator of interaction with RXRα. While RXRα ligands alone failed to induce conformational changes in CAR, CAR ligands triggered conformational transitions in RXRα, particularly in helix H10, suggesting an allosteric mechanism. These results emphasize the importance of extending structural studies beyond isolated ligand-binding domains to full-length nuclear receptors, while interdomain communications likely play a pivotal role in modulating transcriptional responses.

5.2 Future Work

In chapter 2, we employed TRESI-HDX-MS to reveal that cyt c interacts with anionic phospholipid head groups primarily via the A-site and L-site under physiological conditions. Beyond its canonical function in the mitochondrial electron transport chain (ETC), cyt c has also been implicated in apoptosis through its activity as a cardiolipin peroxidase. To further elucidate the mechanistic role of cyt c in programmed cell death, a compelling avenue of future investigation would be exploring how reactive oxygen species (ROS), such as hydrogen peroxide (H_2O_2), influences cyt c unfolding and expose the heme-associated ROS-binding site. This structural transition could facilitate the peroxidation of cardiolipin, converting it from a non-oxidized to oxidized state. Oxidized cardiolipin disrupts inner mitochondrial membrane (IMM) integrity and promotes the release of cyt c into the cytosol, a critical step in the apoptotic cascade.[150] Understanding these oxidative structural transitions in cyt c could provide deeper insight into the lipid- mediated regulation of cell death.

In chapter 3 and 4, we focused on nuclear receptors (NRs), particularly CAR and its heterodimeric partner RXRα. Our HDX-MS results demonstrated that ligand-specific conformational changes in the CAR LBD propagate across the dimer interface, eliciting allosteric effects on RXRα. Interestingly, RXRα's influence within heterodimers can be categorized as either permissive or non-permissive, depending on whether RXRα ligand alone can activate the dimer partner. For CAR, RXRα ligand alone does not structurally stabilize the heterodimer; however, simultaneous engagement of ligands for both CAR and RXRα produces synergistic structural and functional outcomes, structurally. Despite advances in characterizing NR LBDs, structural information on full-length receptors- including the DNA-binding domain (DBD) and hinge region – remains scarce. Investigating how ligand binding induces long-range allosteric effects on these poorly understood domains could clarify how transcriptional selectivity is achieved at specific response elements.

A particularly promising direction for future work involves directly monitoring the recruitment of co-regulatory proteins - such as co-activator and co-repressor peptides- in the presence of distinct ligands. This would provide functional insight into how ligand-induced conformational changes at the LBD translate into altered transcriptional outcomes. Expanding HDX-MS and complementary structural techniques to include full-length receptors and coregulator interactions will be essential for building a holistic model of nuclear receptor function and advancing the rational design of selective modulators.

5.3 Limitations and Future Prospects in HDX-MS

Like many analytical techniques, HDX-MS has its limitations. While the method excels in probing conformational dynamics and transient protein interactions, certain biological systems pose unique challenges that remain unmet with current workflows. Two such examples – proprotein convertase subtilisin/kexin type 9 (PCSK9) and fimbrial proteins – highlight these constraints and the important need for continued methodological innovation.

PCSK9 plays a central role in cholesterol homeostasis by mediating the degradation of low-density lipoproteins receptors (LDLRs) in the liver.[190] Gain-of-function mutations in PCSK9 are associated with autosomal dominant hypercholesterolemia. In collaboration with researchers at the University of Ottawa Heart Institute, we applied HDX-MS to investigate how an intrinsically disordered region (IDR) of PCSK9 modulates its conformational state and LDLR-binding activity. HDX-MS, which uniquely allows for the analysis of disordered and flexible protein regions not captured by crystallographic methods, successfully revealed that the IDR functions as a regulatory lid- dampening interaction with LDLR and thus reducing PCSK9 activity. However, a large portion of PCSK9 could not be evaluated due to the presence of 12 disulfide bonds within a highly structured domain. These bonds are not readily reduced under conventional HDX quench conditions, limiting sequence coverage and precluding full structural interpretation. Future integration of electrochemical reduction modules into HDX-MS workflows may offer a path forward by enabling real-time disulfide bond cleavage prior to proteolysis, thereby improving access to currently inaccessible structural features.

A second case study involved attempts to map antibody epitopes on fimbrial proteins, which are either organized into rigid polymeric assemblies or exist as highly flexible monomers – both of which pose considerable challenges for classical structural approaches. Although HDX-MS or limited proteolysis (LiP) is a powerful solution-phase strategy for interrogating protein-antibody interfaces, the proteolytic resistance and low solvent accessibility of native fimbrial subunits hinder peptide generation and spatial resolution.[191] These limitations severely restrict the utility of HDX-MS in this context, especially for vaccine-related epitope mapping. An alternative approach, such as fast photochemical oxidation of proteins (FPOP), may overcome these constraints.[192] Unlike HDX, FPOP irreversibly labels solvent-accessible side chains via hydroxyl radicals generated by laser-induced photolysis.[193] This allows subsequent sample manipulations (e.g. heating, denaturation, proteolysis with non-acid proteases) that would otherwise erase reversible HDX labels.[192,193] FPOP's compatibility with structurally rigid targets, including fimbrial proteins, presents an attractive and complementary strategy for epitope mapping and immunogen design.[192]

Together, these case studies illustrate both the strengths and current limitations of HDX-MS. They also highlight how the integration of emerging technologies - such as electrochemical cell modules or orthogonal covalent labelling strategies like FPOP - could expand the reach of HDX-MS into new and previously inaccessible domains of structural biology.

5.4 Advances in HDX-MS: Expanding Scope and System Complexity

Over the past decade, HDX-MS has undergone a major transformation, propelled by instrumental advancements and increasingly sophisticated sample-handling workflows. Once limited by manual labelling and low-throughput analysis, HDX-MS has evolved into a robust, middle-to-high-throughput technique with high spatial resolution, in large part due to the introduction of robotic autosamplers such as those developed by LEAP Technologies. A key driver of this evolution has been the integration of advanced front-end analytical separation, enabling HDX-MS to interrogate protein conformational dynamics and interactions within complex biological matrices - including lipid environments, detergent micelles, and virus-like particles (VLPs). Previously, the presence of lipids and detergents posed substantial obstacles for HDX-MS workflows, including ion suppression, signal interference with peptide ions. However, the development of the LEAP X-Press filtration module, integrated with the PAL autosampler platform, has made it possible to incorporate zirconium oxide-based lipid removal directly into the quench and injection sequence. This advancement permits lipid removal without introducing additional delay or back-exchange, ensuring compatibility with the temporal constraints of HDX-MS analysis.

Moreover, modular fluidic architectures now allow for pre-proteolysis separation techniques, such as size exclusion chromatography (SEC), even under low-pH quench conditions. This addition facilitates the removal of unbound ligands and lipids while preserving downstream digestion and analysis. Notably, Hammerschmid *et al.* (2018) introduced a three-valve system integrating an online zirconium oxide column for lipid removal with valve-controlled regeneration capability, improving column longevity and minimizing contamination.[194] In contrast, attempts to adapt this method to a conventional two-valve setup proved less effective, as undisclosed impurities from the zirconium oxide resin interfered with protease performance due to continuous exposure. These findings underscore the importance of system architecture and reagent purity in tailoring HDX-MS workflows for lipid-rich or membrane-associated protein systems.

Instrument sensitivity and resolution have also benefited from the adoption of ion mobility spectroscopy (IMS)- coupled MS platforms, which introduce a powerful additional separation dimension. Recent iterations, such as the Select Series cIMS-MS, offer significantly improved spectral clarity and sensitivity compared to earlier models. These systems are particularly valuable for HDX-MS applications involving proteomes or metabolomes characterized by high complexity and low mass-range resolution. In parallel, high-flowrate LC systems have demonstrated equivalent or superior performance in peptide separation, providing further gains in experimental throughput and minimizing back-exchange.[195]

Beyond hardware, the field is also progressing toward site-resolved structural dynamics. While most HDX-MS data are currently interpreted at the peptide level, the use of nonergodic fragmentation techniques (e.g. electron transfer dissociation (ETD) or ultraviolet photodissociation (UVPD)) now enables deuterium incorporation to be localized to individual amino acids. These capabilities promise transformative insights into protein folding, allosteric signaling, and epitope mapping.[196,197]

Collectively, these developments are redefining the scope of HDX-MS. As workflows become faster, more robust, and less reliant on sample purity, HDX-MS is increasingly being applied to large-scale and previously intractable systems. Looking forward, the field is poised to expand into cell-derived and potentially whole-cell analysis, enabling structural proteomics to bridge the gap between in vitro and in vivo environments. These advancements firmly establish HDX-MS not only as an orthogonal tool for structural biology but as a central platform for the next generation of dynamic, system-level biomolecular research.

References

(1) Díaz-Quintana, A.; Pérez-Mejías, G.; Guerra-Castellano, A.; De La Rosa, M. A.; Díaz-Moreno, I. Wheel and Deal in the Mitochondrial Inner Membranes: The Tale of Cytochrome *c* and Cardiolipin. *Oxid. Med. Cell. Longev.* **2020**, *2020*, 1–20. https://doi.org/10.1155/2020/6813405.

(2) Mandal, A.; Hoop, C. L.; DeLucia, M.; Kodali, R.; Kagan, V. E.; Ahn, J.; van der Wel, P. C. A. Structural Changes and Proapoptotic Peroxidase Activity of Cardiolipin-Bound Mitochondrial Cytochrome c. *Biophys. J.* **2015**, *109* (9), 1873–1884. https://doi.org/10.1016/j.bpj.2015.09.016.

(3) Garrido, C.; Galluzzi, L.; Brunet, M.; Puig, P. E.; Didelot, C.; Kroemer, G. Mechanisms of Cytochrome c Release from Mitochondria. *Cell Death Differ.* **2006**, *13* (9), 1423–1433. https://doi.org/10.1038/sj.cdd.4401950.

(4) Belikova, N. A.; Vladimirov, Y. A.; Osipov, A. N.; Kapralov, A. A.; Tyurin, V. A.; Potapovich, M. V.; Basova, L. V.; Peterson, J.; Kurnikov, I. V.; Kagan, V. E. Peroxidase Activity and Structural Transitions of Cytochrome c Bound to Cardiolipin-Containing Membranes. *Biochemistry* **2006**, *45* (15), 4998–5009. https://doi.org/10.1021/bi0525573.

(5) Tuominen, E. K. J.; Wallace, C. J. A.; Kinnunen, P. K. J. Phospholipid-Cytochrome c Interaction. *J. Biol. Chem.* **2002**, *277* (11), 8822–8826. https://doi.org/10.1074/jbc.M200056200.

(6) Weikum, E. R.; Liu, X.; Ortlund, E. A. The Nuclear Receptor Superfamily: A Structural Perspective. *Protein Sci. Publ. Protein Soc.* **2018**, *27* (11), 1876–1892. https://doi.org/10.1002/pro.3496.

(7) Liu, J.; Malekoltojari, A.; Asokakumar, A.; Chow, V.; Li, L.; Li, H.; Grimaldi, M.; Dang, N.; Campbell, J.; Barrett, H.; Sun, J.; Navarre, W.; Wilson, D.; Wang, H.; Mani, S.; Balaguer, P.; Anakk, S.; Peng, H.; Krause, H. M. Diindoles Produced from Commensal Microbiota Metabolites Function as Endogenous CAR/Nr1i3 Ligands. *Nat. Commun.* **2024**, *15* (1), 2563. https://doi.org/10.1038/s41467-024-46559-3.

(8) Lin, W.; Bwayi, M.; Wu, J.; Li, Y.; Chai, S. C.; Huber, A. D.; Chen, T. CITCO Directly Binds to and Activates Human Pregnane X Receptor. *Mol. Pharmacol.* **2020**, *97* (3), 180–190. https://doi.org/10.1124/mol.119.118513.

(9) Cherian, M. T.; Chai, S. C.; Wright, W. C.; Singh, A.; Casal, M. A.; Zheng, J.; Wu, J.; Lee, R. E.; Griffin, P. R.; Chen, T. CINPA1 Binds Directly to Constitutive Androstane Receptor and Inhibits Its Activity. *Biochem. Pharmacol.* **2018**, *152*, 211–223. https://doi.org/10.1016/j.bcp.2018.03.029.

(10) Zheng, J.; Strutzenberg, T.; Pascal, B. D.; Griffin, P. R. Protein Dynamics and Conformational Changes Explored by Hydrogen/Deuterium Exchange Mass Spectrometry. *Curr. Opin. Struct. Biol.* **2019**, *58*, 305–313. https://doi.org/10.1016/j.sbi.2019.06.007.

(11) Konermann, L.; Pan, J.; Liu, Y.-H. Hydrogen Exchange Mass Spectrometry for Studying Protein Structure and Dynamics. *Chem Soc Rev* **2011**, *40* (3), 1224–1234. https://doi.org/10.1039/C0CS00113A.

(12) Domon, B.; Aebersold, R. Mass Spectrometry and Protein Analysis. *Science* **2006**, *312* (5771), 212–217. https://doi.org/10.1126/science.1124619.

(13) Mejía-Carmona, K.; Soares Da Silva Burato, J.; Borsatto, J. V. B.; De Toffoli, A. L.; Lanças, F. M. Miniaturization of Liquid Chromatography Coupled to Mass Spectrometry. *TrAC Trends Anal. Chem.* **2020**, *122*, 115735. https://doi.org/10.1016/j.trac.2019.115735.

(14) López-Fernández, O.; Domínguez, R.; Pateiro, M.; Munekata, P. E. S.; Rocchetti, G.; Lorenzo, J. M. Determination of Polyphenols Using Liquid Chromatography–Tandem Mass Spectrometry Technique (LC–MS/MS): A Review. *Antioxidants* **2020**, *9* (6), 479. https://doi.org/10.3390/antiox9060479.

(15) Gruber, B.; David, F.; Sandra, P. Capillary Gas Chromatography-Mass Spectrometry: Current Trends and Perspectives. *TrAC Trends Anal. Chem.* **2020**, *124*, 115475. https://doi.org/10.1016/j.trac.2019.04.007.

(16) Lapizco-Encinas, B. H.; Zhang, Y. V.; Gqamana, P. P.; Lavicka, J.; Foret, F. Capillary Electrophoresis as a Sample Separation Step to Mass Spectrometry Analysis: A Primer. *TrAC Trends Anal. Chem.* **2023**, *164*, 117093. https://doi.org/10.1016/j.trac.2023.117093.

(17) Borsdorf, H.; and Eiceman, G. A. Ion Mobility Spectrometry: Principles and Applications. *Appl. Spectrosc. Rev.* **2006**, *41* (4), 323–375. https://doi.org/10.1080/05704920600663469.

(18) Paglia, G.; Smith, A. J.; Astarita, G. Ion Mobility Mass Spectrometry in the Omics Era: Challenges and Opportunities for Metabolomics and Lipidomics. *Mass Spectrom. Rev.* **2022**, *41* (5), 722–765. https://doi.org/10.1002/mas.21686.

(19) Banerjee, S.; Mazumdar, S. Electrospray Ionization Mass Spectrometry: A Technique to Access the Information beyond the Molecular Weight of the Analyte. *Int. J. Anal. Chem.* **2012**, *2012* (1), 282574. https://doi.org/10.1155/2012/282574.

(20) Drachman, N.; Lepoitevin, M.; Szapary, H.; Wiener, B.; Maulbetsch, W.; Stein, D. Nanopore Ion Sources Deliver Individual Ions of Amino Acids and Peptides Directly into High Vacuum. *Nat. Commun.* **2024**, *15* (1), 7709. https://doi.org/10.1038/s41467-024-51455-x.

(21) El-Aneed, A.; Cohen ,Aljandro; and Banoub, J. Mass Spectrometry, Review of the Basics: Electrospray, MALDI, and Commonly Used Mass Analyzers. *Appl. Spectrosc. Rev.* **2009**, *44* (3), 210–230. https://doi.org/10.1080/05704920902717872.

(22) Jonsson, A. P. Mass Spectrometry for Protein and Peptide Characterisation. *Cell. Mol. Life Sci. CMLS* **2001**, *58* (7), 868–884. https://doi.org/10.1007/PL00000907.

(23) Arevalo Jr, R.; Ni, Z.; Danell, R. M. Mass Spectrometry and Planetary Exploration: A Brief Review and Future Projection. *J. Mass Spectrom.* **2020**, *55* (1), e4454. https://doi.org/10.1002/jms.4454.

(24) Prabhu, G. R. D.; Williams, E. R.; Wilm, M.; Urban, P. L. Mass Spectrometry Using Electrospray Ionization. *Nat. Rev. Methods Primer* **2023**, *3* (1), 23. https://doi.org/10.1038/s43586-023-00203-4.

(25) Loo, J. A. Studying Noncovalent Protein Complexes by Electrospray Ionization Mass Spectrometry. *Mass Spectrom. Rev.* **1997**, *16* (1), 1–23. https://doi.org/10.1002/(SICI)1098-2787(1997)16:1<1::AID-MAS1>3.0.CO;2-L.

(26) Pimlott, D. J. D.; Konermann, L. Using Covalent Modifications to Distinguish Protein Electrospray Mechanisms: Charged Residue Model (CRM) vs. Chain Ejection Model (CEM). *Int. J. Mass Spectrom.* **2021**, *469*, 116678. https://doi.org/10.1016/j.ijms.2021.116678.

(27) Aliyari, E.; Konermann, L. Formation of Gaseous Proteins via the Ion Evaporation Model (IEM) in Electrospray Mass Spectrometry. *Anal. Chem.* **2020**, *92* (15), 10807–10814. https://doi.org/10.1021/acs.analchem.0c02290.

(28) Pimlott, D. J. D.; Konermann, L. Using Covalent Modifications to Distinguish Protein Electrospray Mechanisms: Charged Residue Model (CRM) vs. Chain Ejection Model (CEM). *Int. J. Mass Spectrom.* **2021**, *469*, 116678. https://doi.org/10.1016/j.ijms.2021.116678.

(29) Metwally, H.; Duez, Q.; Konermann, L. Chain Ejection Model for Electrospray Ionization of Unfolded Proteins: Evidence from Atomistic Simulations and Ion Mobility Spectrometry. *Anal. Chem.* **2018**, *90* (16), 10069–10077. https://doi.org/10.1021/acs.analchem.8b02926.

(30) Donor, M. T.; Ewing, S. A.; Zenaidee, M. A.; Donald, W. A.; Prell, J. S. Extended Protein Ions Are Formed by the Chain Ejection Model in Chemical Supercharging Electrospray Ionization. *Anal. Chem.* **2017**, *89* (9), 5107–5114. https://doi.org/10.1021/acs.analchem.7b00673.

(31) Li, Y.; Li, W.; Zheng, Y.; Wang, T.; Pu, R.; Zhang, Z. Desalting Strategies for Native Mass Spectrometry. *Talanta* **2025**, *281*, 126824. https://doi.org/10.1016/j.talanta.2024.126824.

(32) Fenn, J. B. Ion Formation from Charged Droplets: Roles of Geometry, Energy, and Time. *J. Am. Soc. Mass Spectrom.* **1993**, *4* (7), 524–535. https://doi.org/10.1016/1044-0305(93)85014-O.

(33) Gamero-Castano, M.; Mora, J. F. Kinetics of Small Ion Evaporation from the Charge and Mass Distribution of Multiply Charged Clusters in Electrosprays. *J. Mass Spectrom. JMS* **2000**, *35* (7), 790–803. https://doi.org/10.1002/1096-9888(200007)35:7<790::AID-JMS21>3.0.CO;2-7.

(34) Dole, M.; Mack, L. L.; Hines, R. L.; Mobley, R. C.; Ferguson, L. D.; Alice, M. B. Molecular Beams of Macroions. *J. Chem. Phys.* **1968**, *49* (5), 2240–2249. https://doi.org/10.1063/1.1670391.

(35) Schnier, P. D.; Gross, D. S.; Williams, E. R. On the Maximum Charge State and Proton Transfer Reactivity of Peptide and Protein Ions Formed by Electrospray Ionization. *J. Am. Soc. Mass Spectrom.* **1995**, *6* (11), 1086–1097. https://doi.org/10.1016/1044-0305(95)00532-3.

(36) Hager, J. W. Recent Trends in Mass Spectrometer Development. *Anal. Bioanal. Chem.* **2004**, *378* (4), 845–850. https://doi.org/10.1007/s00216-003-2287-1.

(37) Chernushevich, I. V.; Loboda, A. V.; Thomson, B. A. An Introduction to Quadrupole–Time-of-Flight Mass Spectrometry. *J. Mass Spectrom.* **2001**, *36* (8), 849–865. https://doi.org/10.1002/jms.207.

(38) Li, C.; Chu, S.; Tan, S.; Yin, X.; Jiang, Y.; Dai, X.; Gong, X.; Fang, X.; Tian, D. Towards Higher Sensitivity of Mass Spectrometry: A Perspective From the Mass Analyzers. *Front. Chem.* **2021**, *9*. https://doi.org/10.3389/fchem.2021.813359.

(39) Boesl, U. Time-of-Flight Mass Spectrometry: Introduction to the Basics. *Mass Spectrom. Rev.* **2017**, *36* (1), 86–109. https://doi.org/10.1002/mas.21520.

(40) Scherer, S.; Altwegg, K.; Balsiger, H.; Fischer, J.; Jäckel, A.; Korth, A.; Mildner, M.; Piazza, D.; Reme, H.; Wurz, P. A Novel Principle for an Ion Mirror Design in Time-of-Flight Mass Spectrometry. *Int. J. Mass Spectrom.* **2006**, *251* (1), 73–81. https://doi.org/10.1016/j.ijms.2006.01.025.

(41) Borsdorf, H.; and Eiceman, G. A. Ion Mobility Spectrometry: Principles and Applications. *Appl. Spectrosc. Rev.* **2006**, *41* (4), 323–375. https://doi.org/10.1080/05704920600663469.

(42) Giles, K.; Ujma, J.; Wildgoose, J.; Pringle, S.; Richardson, K.; Langridge, D.; Green, M. A Cyclic Ion Mobility-Mass Spectrometry System. *Anal. Chem.* **2019**, *91* (13), 8564–8573. https://doi.org/10.1021/acs.analchem.9b01838.

(43) Borsdorf, H.; Mayer ,Thomas; Zarejousheghani ,Mashaalah; and Eiceman, G. A. Recent Developments in Ion Mobility Spectrometry. *Appl. Spectrosc. Rev.* **2011**, *46* (6), 472–521. https://doi.org/10.1080/05704928.2011.582658.

(44) Williams, J. P.; Morrison, L. J.; Brown, J. M.; Beckman, J. S.; Voinov, V. G.; Lermyte, F. Top-Down Characterization of Denatured Proteins and Native Protein Complexes Using Electron Capture Dissociation Implemented within a Modified Ion Mobility-Mass Spectrometer. *Anal. Chem.* **2020**, *92* (5), 3674–3681. https://doi.org/10.1021/acs.analchem.9b04763.

(45) Gabelica, V.; Rosu, F.; Witt, M.; Baykut, G.; De Pauw, E. Fast Gas-Phase Hydrogen/Deuterium Exchange Observed for a DNA G-Quadruplex. *Rapid Commun. Mass Spectrom.* **2005**, *19* (2), 201–208. https://doi.org/10.1002/rcm.1772.

(46) Borsdorf, H.; and Eiceman, G. A. Ion Mobility Spectrometry: Principles and Applications. *Appl. Spectrosc. Rev.* **2006**, *41* (4), 323–375. https://doi.org/10.1080/05704920600663469.

(47) Christofi, E.; Barran, P. Ion Mobility Mass Spectrometry (IM-MS) for Structural Biology: Insights Gained by Measuring Mass, Charge, and Collision Cross Section. *Chem. Rev.* **2023**, *123* (6), 2902–2949. https://doi.org/10.1021/acs.chemrev.2c00600.

(48) Harrison, J. A.; Pruška, A.; Bittner, P.; Muck, A.; Cooper-Shepherd, D. A.; Zenobi, R. Advancing Cyclic Ion Mobility Mass Spectrometry Methods for Studying Biomolecules: Toward the Conformational Dynamics of Mega Dalton Protein Aggregates. *Anal. Chem.* **2022**, *94* (36), 12435–12443. https://doi.org/10.1021/acs.analchem.2c02406.

(49) Gabelica, V.; Marklund, E. Fundamentals of Ion Mobility Spectrometry. *Curr. Opin. Chem. Biol.* **2018**, *42*, 51–59. https://doi.org/10.1016/j.cbpa.2017.10.022.

(50) Seidler, J.; Zinn, N.; Boehm, M. E.; Lehmann, W. D. De Novo Sequencing of Peptides by MS/MS. *PROTEOMICS* **2010**, *10* (4), 634–649. https://doi.org/10.1002/pmic.200900459.

(51) Mitchell Wells, J.; McLuckey, S. A. Collision-Induced Dissociation (CID) of Peptides and Proteins. In *Methods in Enzymology*; Biological Mass Spectrometry; Academic Press, 2005; Vol. 402, pp 148–185. https://doi.org/10.1016/S0076-6879(05)02005-7.

(52) Macias, L. A.; Santos, I. C.; Brodbelt, J. S. Ion Activation Methods for Peptides and Proteins. *Anal. Chem.* **2020**, *92* (1), 227–251. https://doi.org/10.1021/acs.analchem.9b04859.

(53) Paizs, B.; Suhai, S. Fragmentation Pathways of Protonated Peptides. *Mass Spectrom. Rev.* **2005**, *24* (4), 508–548. https://doi.org/10.1002/mas.20024.

(54) Sleno, L.; Volmer, D. A. Ion Activation Methods for Tandem Mass Spectrometry. *J. Mass Spectrom.* **2004**, *39* (10), 1091–1112. https://doi.org/10.1002/jms.703.

(55) Kuznetsov, N. M. Kinetics for the Dissociation of Molecules in a Molecular Gas. *Theor. Exp. Chem.* **1973**, *7* (1), 17–26. https://doi.org/10.1007/BF00527588.

(56) Baercor, T.; Mayerfn, P. M. Statistical Rice-Ramsperger-Kassel-Marcus Quasiequilibrium Theory Calculations in Mass Spectrometry. *J. Am. Soc. Mass Spectrom.* **1997**, *8* (2), 103–115. https://doi.org/10.1016/S1044-0305(96)00212-7.

(57) Winkler, R. ESIprot: A Universal Tool for Charge State Determination and Molecular Weight Calculation of Proteins from Electrospray Ionization Mass Spectrometry Data. *Rapid Commun. Mass Spectrom.* **2010**, *24* (3), 285–294. https://doi.org/10.1002/rcm.4384.

(58) Ferrige, A. G.; Seddon, M. J.; Green, B. N.; Jarvis, S. A.; Skilling, J.; Staunton, J. Disentangling Electrospray Spectra with Maximum Entropy. *Rapid Commun. Mass Spectrom.* **1992**, *6* (11), 707–711. https://doi.org/10.1002/rcm.1290061115.

(59) Liepold, L.; Oltrogge, L. M.; Suci, P. A.; Young, M. J.; Douglas, T. Correct Charge State Assignment of Native Electrospray Spectra of Protein Complexes. *J. Am. Soc. Mass Spectrom.* **2009**, *20* (3), 435–442. https://doi.org/10.1016/j.jasms.2008.10.024.

(60) Deng, B.; Lento, C.; Wilson, D. J. Hydrogen Deuterium Exchange Mass Spectrometry in Biopharmaceutical Discovery and Development – A Review. *Anal. Chim. Acta* **2016**, *940*, 8–20. https://doi.org/10.1016/j.aca.2016.08.006.

(61) Vinciauskaite, V.; Masson, G. R. Fundamentals of HDX-MS. *Essays Biochem.* **2023**, *67* (2), 301–314. https://doi.org/10.1042/EBC20220111.

(62) Masson, G. R.; Jenkins ,Meredith L.; and Burke, J. E. An Overview of Hydrogen Deuterium Exchange Mass Spectrometry (HDX-MS) in Drug Discovery. *Expert Opin. Drug Discov.* **2017**, *12* (10), 981–994. https://doi.org/10.1080/17460441.2017.1363734.

(63) Narang, D.; Lento, C.; J. Wilson, D. HDX-MS: An Analytical Tool to Capture Protein Motion in Action. *Biomedicines* **2020**, *8* (7), 224. https://doi.org/10.3390/biomedicines8070224.

(64) Trabjerg, E.; Nazari, Z. E.; Rand, K. D. Conformational Analysis of Complex Protein States by Hydrogen/Deuterium Exchange Mass Spectrometry (HDX-MS): Challenges and Emerging Solutions. *TrAC Trends Anal. Chem.* **2018**, *106*, 125–138. https://doi.org/10.1016/j.trac.2018.06.008.

(65) James, E. I.; Murphree, T. A.; Vorauer, C.; Engen, J. R.; Guttman, M. Advances in Hydrogen/Deuterium Exchange Mass Spectrometry and the Pursuit of Challenging Biological Systems. *Chem. Rev.* **2022**, *122* (8), 7562–7623. https://doi.org/10.1021/acs.chemrev.1c00279.

(66) Jensen, P. F.; Rand, K. D. Hydrogen Exchange: A Sensitive Analytical Window into Protein Conformation and Dynamics. In *Hydrogen Exchange Mass Spectrometry of Proteins*; John Wiley & Sons, Ltd, 2016; pp 1–17. https://doi.org/10.1002/9781118703748.ch1.

(67) Oganesyan, I.; Lento, C.; Wilson, D. J. Contemporary Hydrogen Deuterium Exchange Mass Spectrometry. *Methods* **2018**, *144*, 27–42. https://doi.org/10.1016/j.ymeth.2018.04.023.

(68) Englander, S. W. Hydrogen Exchange and Mass Spectrometry: A Historical Perspective. *J. Am. Soc. Mass Spectrom.* **2006**, *17* (11), 1481–1489. https://doi.org/10.1016/j.jasms.2006.06.006.

(69) Englander, S. W.; Sosnick, T. R.; Englander, J. J.; Mayne, L. Mechanisms and Uses of Hydrogen Exchange. *Curr. Opin. Struct. Biol.* **1996**, *6* (1), 18–23. https://doi.org/10.1016/S0959-440X(96)80090-X.

(70) Bai, Y.; Milne, J. S.; Mayne, L.; Englander, S. W. Primary Structure Effects on Peptide Group Hydrogen Exchange. *Proteins* **1993**, *17* (1), 75–86. https://doi.org/10.1002/prot.340170110.

(71) A. Brown, K.; J. Wilson, D. Bottom-up Hydrogen Deuterium Exchange Mass Spectrometry: Data Analysis and Interpretation. *Analyst* **2017**, *142* (16), 2874–2886. https://doi.org/10.1039/C7AN00662D.

(72) Molday, R. S.; Englander, S. W.; Kallen, R. G. Primary Structure Effects on Peptide Group Hydrogen Exchange. *Biochemistry* **1972**, *11* (2), 150–158. https://doi.org/10.1021/bi00752a003.

(73) Claesen, J.; Politis, A. POPPeT: A New Method to Predict the Protection Factor of Backbone Amide Hydrogens. *J. Am. Soc. Mass Spectrom.* **2019**, *30* (1), 67–76. https://doi.org/10.1007/s13361-018-2068-x.

(74) Wang, L. C.; Krishnamurthy, S.; Anand, G. S. Hydrogen Exchange Mass Spectrometry Experimental Design. In *Hydrogen Exchange Mass Spectrometry of Proteins*; John Wiley & Sons, Ltd, 2016; pp 19–35. https://doi.org/10.1002/9781118703748.ch2.

(75) Englander, S. W.; Mayne, L.; Bai, Y.; Sosnick, T. R. Hydrogen Exchange: The Modern Legacy of Linderstrøm-Lang. *Protein Sci. Publ. Protein Soc.* **1997**, *6* (5), 1101–1109. https://doi.org/10.1002/pro.5560060517.

(76) Konermann, L.; Tong, X.; Pan, Y. Protein Structure and Dynamics Studied by Mass Spectrometry: H/D Exchange, Hydroxyl Radical Labeling, and Related Approaches. *J. Mass Spectrom.* **2008**, *43* (8), 1021–1036. https://doi.org/10.1002/jms.1435.

(77) Xiao, H.; Hoerner, J. K.; Eyles, S. J.; Dobo, A.; Voigtman, E.; Mel'čuk, A. I.; Kaltashov, I. A. Mapping Protein Energy Landscapes with Amide Hydrogen Exchange and Mass Spectrometry: I. A Generalized Model for a Two-State Protein and Comparison with Experiment. *Protein Sci. Publ. Protein Soc.* **2005**, *14* (2), 543–557. https://doi.org/10.1110/ps.041001705.

(78) Masson, G. R.; Burke, J. E.; Ahn, N. G.; Anand, G. S.; Borchers, C.; Brier, S.; Bou-Assaf, G. M.; Engen, J. R.; Englander, S. W.; Faber, J.; Garlish, R.; Griffin, P. R.; Gross, M. L.; Guttman, M.; Hamuro, Y.; Heck, A. J. R.; Houde, D.; Iacob, R. E.; Jørgensen, T. J. D.; Kaltashov, I. A.; Klinman, J. P.; Konermann, L.; Man, P.; Mayne, L.; Pascal, B. D.; Reichmann, D.; Skehel, M.; Snijder, J.; Strutzenberg, T. S.; Underbakke, E. S.; Wagner, C.; Wales, T. E.; Walters, B. T.; Weis, D. D.; Wilson, D. J.; Wintrode, P. L.; Zhang, Z.; Zheng, J.; Schriemer, D. C.; Rand, K. D. Recommendations for Performing, Interpreting and Reporting Hydrogen Deuterium Exchange Mass Spectrometry (HDX-MS) Experiments. *Nat. Methods* **2019**, *16* (7), 595–602. https://doi.org/10.1038/s41592-019-0459-y.

(79) Zhang, Z.; Smith, D. L. Determination of Amide Hydrogen Exchange by Mass Spectrometry: A New Tool for Protein Structure Elucidation. *Protein Sci.* **1993**, *2* (4), 522–531. https://doi.org/10.1002/pro.5560020404.

(80) Hamuro, Y.; Coales, S. J. Optimization of Feasibility Stage for Hydrogen/Deuterium Exchange Mass Spectrometry. *J. Am. Soc. Mass Spectrom.* **2018**, *29* (3), 623–629. https://doi.org/10.1007/s13361-017-1860-3.

(81) Möller, I. R.; Slivacka, M.; Hausner, J.; Nielsen, A. K.; Pospíšilová, E.; Merkle, P. S.; Lišková, R.; Polák, M.; Loland, C. J.; Kádek, A.; Man, P.; Rand, K. D. Improving the Sequence Coverage of Integral Membrane Proteins during Hydrogen/Deuterium Exchange Mass

Spectrometry Experiments. *Anal. Chem.* **2019**, *91* (17), 10970–10978. https://doi.org/10.1021/acs.analchem.9b00973.

(82) Burns, J. A.; Butler, J. C.; Moran, J.; Whitesides, G. M. Selective Reduction of Disulfides by Tris(2-Carboxyethyl)Phosphine. *J. Org. Chem.* **1991**, *56* (8), 2648–2650. https://doi.org/10.1021/jo00008a014.

(83) Comamala, G.; Krogh, C. C.; Nielsen, V. S.; Kutter, J. P.; Voglmeir, J.; Rand, K. D. Hydrogen/Deuterium Exchange Mass Spectrometry with Integrated Electrochemical Reduction and Microchip-Enabled Deglycosylation for Epitope Mapping of Heavily Glycosylated and Disulfide-Bonded Proteins. *Anal. Chem.* **2021**, *93* (49), 16330–16340. https://doi.org/10.1021/acs.analchem.1c01728.

(84) Comamala, G.; Wagner, C.; de la Torre, P. S.; Jakobsen, R. U.; Hilger, M.; Brouwer, H.-J.; Rand, K. D. Hydrogen/Deuterium Exchange Mass Spectrometry with Improved Electrochemical Reduction Enables Comprehensive Epitope Mapping of a Therapeutic Antibody to the Cysteine-Knot Containing Vascular Endothelial Growth Factor. *Anal. Chim. Acta* **2020**, *1115*, 41–51. https://doi.org/10.1016/j.aca.2020.04.014.

(85) Zheng, J.; Strutzenberg, T. S.; Reich, A.; Dharmarajan, V.; Pascal, B. D.; Crynen, G. C.; Novick, S. J.; Garcia-Ordonez, R. D.; Griffin, P. R. Comparative Analysis of Cleavage Specificities of Immobilized Porcine Pepsin and Nepenthesin II under Hydrogen/Deuterium Exchange Conditions. *Anal. Chem.* **2020**, *92* (16), 11018–11028. https://doi.org/10.1021/acs.analchem.9b05694.

(86) Bekalu, Z. E.; Dionisio, G.; Brinch-Pedersen, H. Molecular Properties and New Potentials of Plant Nepenthesins. *Plants* **2020**, *9* (5), 570. https://doi.org/10.3390/plants9050570.

(87) Anderson, K. W.; Hudgens, J. W. Chromatography at −30 °C for Reduced Back-Exchange, Reduced Carryover, and Improved Dynamic Range for Hydrogen–Deuterium Exchange Mass Spectrometry. *J. Am. Soc. Mass Spectrom.* **2022**, *33* (7), 1282–1292. https://doi.org/10.1021/jasms.2c00096.

(88) Venable, J. D.; Okach, L.; Agarwalla, S.; Brock, A. Sub-Zero Temperature Chromatography for Reduced Back-Exchange and Improved Dynamic Range in Amide Hydrogen Deuterium Exchange Mass Spectrometry. *Anal. Chem.* **2012**, *84* (21), 9601–9608. https://doi.org/10.1021/ac302488h.

(89) Parson, M. A. H.; Jenkins, M. L.; Burke, J. E. Investigating How Intrinsically Disordered Regions Contribute to Protein Function Using HDX-MS. *Biochem. Soc. Trans.* **2022**, *50* (6), 1607–1617. https://doi.org/10.1042/BST20220206.

(90) Seetaloo, N.; Zacharopoulou, M.; Stephens, A. D.; Kaminski Schierle, G. S.; Phillips, J. J. Millisecond Hydrogen/Deuterium-Exchange Mass Spectrometry Approach to Correlate Local Structure and Aggregation in α-Synuclein. *Anal. Chem.* **2022**, *94* (48), 16711–16719. https://doi.org/10.1021/acs.analchem.2c03183.

(91) Chow, V.; Wolf, E.; Lento, C.; Wilson, D. J. Developments in Rapid Hydrogen–Deuterium Exchange Methods. *Essays Biochem.* **2023**, *67* (2), 165–174. https://doi.org/10.1042/EBC20220174.

(92) Wilson, D. J.; Konermann, L. A Capillary Mixer with Adjustable Reaction Chamber Volume for Millisecond Time-Resolved Studies by Electrospray Mass Spectrometry. *Anal. Chem.* **2003**, *75* (23), 6408–6414. https://doi.org/10.1021/ac0346757.

(93) Oganesyan, I.; Lento, C.; Tandon, A.; Wilson, D. J. Conformational Dynamics of α-Synuclein during the Interaction with Phospholipid Nanodiscs by Millisecond Hydrogen–Deuterium Exchange Mass Spectrometry. *J. Am. Soc. Mass Spectrom.* **2021**, *32* (5), 1169–1179. https://doi.org/10.1021/jasms.0c00463.

(94) Anacleto, J.; Lento, C.; Sarpe, V.; Maqsood, A.; Mehrazma, B.; Schriemer, D.; Wilson, D. J. Apparatus for Automated Continuous Hydrogen Deuterium Exchange Mass Spectrometry Measurements from Milliseconds to Hours. *Anal. Chem.* **2023**, *95* (9), 4421–4428. https://doi.org/10.1021/acs.analchem.2c05003.

(95) Pino, L. K.; Just, S. C.; MacCoss, M. J.; Searle, B. C. Acquiring and Analyzing Data Independent Acquisition Proteomics Experiments without Spectrum Libraries. *Mol. Cell. Proteomics MCP* **2020**, *19* (7), 1088–1103. https://doi.org/10.1074/mcp.P119.001913.

(96) Lou, R.; Shui, W. Acquisition and Analysis of DIA-Based Proteomic Data: A Comprehensive Survey in 2023. *Mol. Cell. Proteomics* **2024**, *23* (2), 100712. https://doi.org/10.1016/j.mcpro.2024.100712.

(97) Burns, K. M.; Rey, M.; Baker, C. A. H.; Schriemer, D. C. Platform Dependencies in Bottom-up Hydrogen/Deuterium Exchange Mass Spectrometry. *Mol. Cell. Proteomics MCP* **2013**, *12* (2), 539–548. https://doi.org/10.1074/mcp.M112.023770.

(98) Prieto, G.; Aloria, K.; Osinalde, N.; Fullaondo, A.; Arizmendi, J. M.; Matthiesen, R. PAnalyzer: A Software Tool for Protein Inference in Shotgun Proteomics. *BMC Bioinformatics* **2012**, *13*, 288. https://doi.org/10.1186/1471-2105-13-288.

(99) Liu, H.; Wang, D.; Zhang, Q.; Zhao, Y.; Mamonova, T.; Wang, L.; Zhang, C.; Li, S.; Friedman, P. A.; Xiao, K. Parallel Post-Translational Modification Scanning Enhancing Hydrogen–Deuterium Exchange-Mass Spectrometry Coverage of Key Structural Regions. *Anal. Chem.* **2019**, *91* (11), 6976–6980. https://doi.org/10.1021/acs.analchem.9b01410.

(100) Dobbs, J. M.; Jenkins, M. L.; Burke, J. E. Escherichia Coli and Sf9 Contaminant Databases to Increase Efficiency of Tandem Mass Spectrometry Peptide Identification in Structural Mass Spectrometry Experiments. *J. Am. Soc. Mass Spectrom.* **2020**, *31* (10), 2202–2209. https://doi.org/10.1021/jasms.0c00283.

(101) Sarpe, V.; Schriemer, D. C. Data Processing in Bottom-Up Hydrogen Exchange Mass Spectrometry. In *Hydrogen Exchange Mass Spectrometry of Proteins*; John Wiley & Sons, Ltd, 2016; pp 37–53. https://doi.org/10.1002/9781118703748.ch3.

(102) Hodge, E. A.; Benhaim, M. A.; Lee, K. K. Bridging Protein Structure, Dynamics, and Function Using Hydrogen/Deuterium-exchange Mass Spectrometry. *Protein Sci. Publ. Protein Soc.* **2020**, *29* (4), 843–855. https://doi.org/10.1002/pro.3790.

(103) Wolf, E.; Herasymenko, O.; Kutera, M.; Lento, C.; Arrowsmith, C.; Ackloo, S.; Wilson, D. Quantitative Hydrogen–Deuterium Exchange Mass Spectrometry for Simultaneous Structural Characterization and Affinity Indexing of Single Target Drug Candidate Libraries. *Anal. Chem.* **2024**, *96* (32), 13015–13024. https://doi.org/10.1021/acs.analchem.4c01001.

(104) Teclemichael, E.; Le, A. T. H.; Krylova, S. M.; Wang, T. Y.; Krylov, S. N. Bulk Affinity Assays in Aptamer Selection: Challenges, Theory, and Workflow. *Anal. Chem.* **2022**, *94* (44), 15183–15188. https://doi.org/10.1021/acs.analchem.2c03173.

(105) Mandell, J. G.; Falick, A. M.; Komives, E. A. Identification of Protein–Protein Interfaces by Decreased Amide Proton Solvent Accessibility. *Proc. Natl. Acad. Sci.* **1998**, *95* (25), 14705–14710. https://doi.org/10.1073/pnas.95.25.14705.

(106) Varadi, M.; Anyango, S.; Deshpande, M.; Nair, S.; Natassia, C.; Yordanova, G.; Yuan, D.; Stroe, O.; Wood, G.; Laydon, A.; Žídek, A.; Green, T.; Tunyasuvunakool, K.; Petersen, S.; Jumper, J.; Clancy, E.; Green, R.; Vora, A.; Lutfi, M.; Figurnov, M.; Cowie, A.; Hobbs, N.; Kohli, P.; Kleywegt, G.; Birney, E.; Hassabis, D.; Velankar, S. AlphaFold Protein Structure Database: Massively Expanding the Structural Coverage of Protein-Sequence Space with High-Accuracy Models. *Nucleic Acids Res.* **2022**, *50* (D1), D439–D444. https://doi.org/10.1093/nar/gkab1061.

(107) Schweitzer-Stenner, R. Relating the Multi-Functionality of Cytochrome c to Membrane Binding and Structural Conversion. *Biophys. Rev.* **2018**, *10* (4), 1151–1185. https://doi.org/10.1007/s12551-018-0409-4.

(108) Kagan, V. E.; Bayir, H. A.; Belikova, N. A.; Kapralov, O.; Tyurina, Y. Y.; Tyurin, V. A.; Jiang, J.; Stoyanovsky, D. A.; Wipf, P.; Kochanek, P. M.; Greenberger, J. S.; Pitt, B.; Shvedova, A. A.; Borisenko, G. Cytochrome c/Cardiolipin Relations in Mitochondria: A Kiss of Death. *Free Radic. Biol. Med.* **2009**, *46* (11), 1439–1453. https://doi.org/10.1016/j.freeradbiomed.2009.03.004.

(109) Mohammadyani, D.; Yanamala, N.; Samhan-Arias, A. K.; Kapralov, A. A.; Stepanov, G.; Nuar, N.; Planas-Iglesias, J.; Sanghera, N.; Kagan, V. E.; Klein-Seetharaman, J. Structural Characterization of Cardiolipin-Driven Activation of Cytochrome c into a Peroxidase and Membrane Perturbation. *Biochim. Biophys. Acta BBA - Biomembr.* **2018**, *1860* (5), 1057–1068. https://doi.org/10.1016/j.bbamem.2018.01.009.

(110) Heimburg, T.; Marsh, D. Investigation of Secondary and Tertiary Structural Changes of Cytochrome c in Complexes with Anionic Lipids Using Amide Hydrogen Exchange Measurements: An FTIR Study. *Biophys. J.* **1993**, *65* (6), 2408–2417. https://doi.org/10.1016/S0006-3495(93)81299-2.

(111) Oellerich, S.; Lecomte, S.; Paternostre, M.; Heimburg, T.; Hildebrandt, P. Peripheral and Integral Binding of Cytochrome c to Phospholipids Vesicles. *J. Phys. Chem. B* **2004**, *108* (12), 3871–3878. https://doi.org/10.1021/jp036799t.

(112) Elmer-Dixon, M. M.; Xie, Z.; Alverson, J. B.; Priestley, N. D.; Bowler, B. E. Curvature-Dependent Binding of Cytochrome *c* to Cardiolipin. *J. Am. Chem. Soc.* **2020**, *142* (46), 19532–19539. https://doi.org/10.1021/jacs.0c07301.

(113) Fiorucci, L.; Erba, F.; Santucci, R.; Sinibaldi, F. Cytochrome c Interaction with Cardiolipin Plays a Key Role in Cell Apoptosis: Implications for Human Diseases. *Symmetry* **2022**, *14* (4), 767. https://doi.org/10.3390/sym14040767.

(114) Muenzner, J.; Toffey, J. R.; Hong, Y.; Pletneva, E. V. Becoming a Peroxidase: Cardiolipin-Induced Unfolding of Cytochrome c. *J. Phys. Chem. B* **2013**, *117* (42), 12878–12886. https://doi.org/10.1021/jp402104r.

(115) Santucci, R.; Sinibaldi, F.; Cozza, P.; Polticelli, F.; Fiorucci, L. Cytochrome c: An Extreme Multifunctional Protein with a Key Role in Cell Fate. *Int. J. Biol. Macromol.* **2019**, *136*, 1237–1246. https://doi.org/10.1016/j.ijbiomac.2019.06.180.

(116) Pandiscia, L. A.; Schweitzer-Stenner, R. Coexistence of Native-like and Non-Native Partially Unfolded Ferricytochrome c on the Surface of Cardiolipin-Containing Liposomes. *J. Phys. Chem. B* **2015**, *119* (4), 1334–1349. https://doi.org/10.1021/jp5104752.

(117) Barayeu, U.; Lange, M.; Méndez, L.; Arnhold, J.; Shadyro, O. I.; Fedorova, M.; Flemmig, J. Cytochrome c Autocatalyzed Carbonylation in the Presence of Hydrogen Peroxide and Cardiolipins. *J. Biol. Chem.* **2019**, *294* (6), 1816–1830. https://doi.org/10.1074/jbc.RA118.004110.

(118) Rytömaa, M.; Kinnunen, P. K. Evidence for Two Distinct Acidic Phospholipid-Binding Sites in Cytochrome c. *J. Biol. Chem.* **1994**, *269* (3), 1770–1774. https://doi.org/10.1016/S0021-9258(17)42094-1.

(119) Sinibaldi, F.; Howes, B. D.; Droghetti, E.; Polticelli, F.; Piro, M. C.; Di Pierro, D.; Fiorucci, L.; Coletta, M.; Smulevich, G.; Santucci, R. Role of Lysines in Cytochrome c–Cardiolipin Interaction. *Biochemistry* **2013**, *52* (26), 4578–4588. https://doi.org/10.1021/bi400324c.

(120) Ripanti, F.; Di Venere, A.; Cestelli Guidi, M.; Romani, M.; Filabozzi, A.; Carbonaro, M.; Piro, M. C.; Sinibaldi, F.; Nucara, A.; Mei, G. The Puzzling Problem of Cardiolipin Membrane-Cytochrome c Interactions: A Combined Infrared and Fluorescence Study. *Int. J. Mol. Sci.* **2021**, *22* (3), 1334. https://doi.org/10.3390/ijms22031334.

(121) Kawai, C.; Prado, F. M.; Nunes, G. L. C.; Di Mascio, P.; Carmona-Ribeiro, A. M.; Nantes, I. L. pH-Dependent Interaction of Cytochrome c with Mitochondrial Mimetic Membranes. *J. Biol. Chem.* **2005**, *280* (41), 34709–34717. https://doi.org/10.1074/jbc.M412532200.

(122) Milorey, B.; Schweitzer-Stenner, R.; Kurbaj, R.; Malyshka, D. pH-Induced Switch between Different Modes of Cytochrome *c* Binding to Cardiolipin-Containing Liposomes. *ACS Omega* **2019**, *4* (1), 1386–1400. https://doi.org/10.1021/acsomega.8b02574.

(123) Reis, R. I.; Moraes, I. Probing Membrane Protein Assembly into Nanodiscs by In Situ Dynamic Light Scattering: A2A Receptor as a Case Study. *Biology* **2020**, *9* (11), 400. https://doi.org/10.3390/biology9110400.

(124) Abe, M.; Niibayashi, R.; Koubori, S.; Moriyama, I.; Miyoshi, H. Molecular Mechanisms for the Induction of Peroxidase Activity of the Cytochrome c–Cardiolipin Complex. *Biochemistry* **2011**, *50* (39), 8383–8391. https://doi.org/10.1021/bi2010202.

(125) Kyaw, A.; Roepke, K.; Arthur, T.; Howard, K. P. Conformation of Influenza AM2 Membrane Protein in Nanodiscs and Liposomes. *Biochim. Biophys. Acta BBA - Biomembr.* **2023**, *1865* (5), 184152. https://doi.org/10.1016/j.bbamem.2023.184152.

(126) Sanders, H. M.; Kostelic, M. M.; Zak, C. K.; Marty, M. T. Lipids and EGCG Affect α-Synuclein Association and Disruption of Nanodiscs. *Biochemistry* **2022**, *61* (11), 1014–1021. https://doi.org/10.1021/acs.biochem.2c00160.

(127) Gasanoff, E. S.; Yaguzhinsky, L. S.; Garab, G. Cardiolipin, Non-Bilayer Structures and Mitochondrial Bioenergetics: Relevance to Cardiovascular Disease. *Cells* **2021**, *10* (7), 1721. https://doi.org/10.3390/cells10071721.

(128) Mabrouk, M. T.; Zidan, A. A.; Aly, N.; Mohammed, M. T.; Ghantous, F.; Seaman, M. S.; Lovell, J. F.; Nasr, M. L. Circularized Nanodiscs for Multivalent Mosaic Display of SARS-CoV-2 Spike Protein Antigens. *Vaccines* **2023**, *11* (11), 1655. https://doi.org/10.3390/vaccines11111655.

(129) Schlame, M. Thematic Review Series: Glycerolipids. Cardiolipin Synthesis for the Assembly of Bacterial and Mitochondrial Membranes. *J. Lipid Res.* **2008**, *49* (8), 1607–1620. https://doi.org/10.1194/jlr.R700018-JLR200.

(130) Lundqvist, J. *Size Exclusion Chromatography*. Cytiva. https://www.cytivalifesciences.com/en/us/solutions/protein-research/knowledge-center/protein-purification-methods/size-exclusion-chromatography (accessed 2024-04-07).

(131) Wadsäter, M.; Maric, S.; Simonsen, J.; Mortensen, K.; Cárdenas, M. The Effect of Using Binary Mixtures of Zwitterionic and Charged Lipids on Nanodisc Formation and Stability. *Soft Matter* **2013**, *9*, 2329–2337. https://doi.org/10.1039/C2SM27000E.

(132) Ikon, N.; Su, B.; Hsu, F.-F.; Forteand, T. M.; Ryan, R. O. Exogenous Cardiolipin Localizes to Mitochondria and Prevents TAZ Knockdown-Induced Apoptosis in Myeloid Progenitor Cells. *Biochem. Biophys. Res. Commun.* **2015**, *464* (2), 580–585. https://doi.org/10.1016/j.bbrc.2015.07.012.

(133) Dickey, A.; Faller, R. Examining the Contributions of Lipid Shape and Headgroup Charge on Bilayer Behavior. *Biophys. J.* **2008**, *95* (6), 2636–2646. https://doi.org/10.1529/biophysj.107.128074.

(134) Dalal, V.; Arcario, M. J.; Petroff, J. T.; Tan, B. K.; Dietzen, N. M.; Rau, M. J.; Fitzpatrick, J. A. J.; Brannigan, G.; Cheng, W. W. L. Lipid Nanodisc Scaffold and Size Alter the Structure of a Pentameric Ligand-Gated Ion Channel. *Nat. Commun.* **2024**, *15* (1), 25. https://doi.org/10.1038/s41467-023-44366-w.

(135) Krishnarjuna, B.; Ravula, T.; Ramamoorthy, A. Detergent-Free Isolation of CYP450-Reductase's FMN-Binding Domain in *E. Coli* Lipid-Nanodiscs Using a Charge-Free Polymer. *Chem. Commun.* **2022**, *58* (31), 4913–4916. https://doi.org/10.1039/D1CC07193A.

(136) Ravula, T.; Ramadugu, S. K.; Di Mauro, G.; Ramamoorthy, A. Bioinspired, Size-Tunable Self-Assembly of Polymer-Lipid Bilayer Nanodiscs. *Angew. Chem. Int. Ed Engl.* **2017**, *56* (38), 11466–11470. https://doi.org/10.1002/anie.201705569.

(137) Ravula, T.; Sahoo, B. R.; Dai, X.; Ramamoorthy, A. Natural-Abundance ^{17}O NMR Spectroscopy of Magnetically Aligned Lipid Nanodiscs. *Chem. Commun.* **2020**, *56* (69), 9998–10001. https://doi.org/10.1039/D0CC04011H.

(138) Imai, M.; Saio, T.; Kumeta, H.; Uchida, T.; Inagaki, F.; Ishimori, K. Investigation of the Redox-Dependent Modulation of Structure and Dynamics in Human Cytochrome c. *Biochem. Biophys. Res. Commun.* **2016**, *469* (4), 978–984. https://doi.org/10.1016/j.bbrc.2015.12.079.

(139) Li, M.; Mandal, A.; Tyurin, V. A.; DeLucia, M.; Ahn, J.; Kagan, V. E.; van der Wel, P. C. A. Surface-Binding to Cardiolipin Nanodomains Triggers Cytochrome *c* Pro-Apoptotic Peroxidase Activity via Localized Dynamics. *Structure* **2019**, *27* (5), 806-815.e4. https://doi.org/10.1016/j.str.2019.02.007.

(140) Hong, Y.; Muenzner, J.; Grimm, S. K.; Pletneva, E. V. Origin of the Conformational Heterogeneity of Cardiolipin-Bound Cytochrome c. *J. Am. Chem. Soc.* **2012**, *134* (45), 18713–18723. https://doi.org/10.1021/ja307426k.

(141) Serpas, L.; Milorey, B.; Pandiscia, L. A.; Addison, A. W.; Schweitzer-Stenner, R. Autoxidation of Reduced Horse Heart Cytochrome c Catalyzed by Cardiolipin-Containing

Membranes. *J. Phys. Chem. B* **2016**, *120* (48), 12219–12231. https://doi.org/10.1021/acs.jpcb.6b05620.

(142) O'Brien, E. S.; Nucci, N. V.; Fuglestad, B.; Tommos, C.; Wand, A. J. Defining the Apoptotic Trigger. *J. Biol. Chem.* **2015**, *290* (52), 30879–30887. https://doi.org/10.1074/jbc.M115.689406.

(143) Dickerson, R. E.; Takano, T.; Eisenberg, D.; Kallai, O. B.; Samson, L.; Cooper, A.; Margoliash, E. Ferricytochrome c. *J. Biol. Chem.* **1971**, *246* (5), 1511–1535. https://doi.org/10.1016/S0021-9258(19)77002-1.

(144) Oganesyan, I.; Lento, C.; Wilson, D. J. Contemporary Hydrogen Deuterium Exchange Mass Spectrometry. *Methods* **2018**, *144*, 27–42. https://doi.org/10.1016/j.ymeth.2018.04.023.

(145) Sligar, S. G.; Denisov, I. G. Nanodiscs: A Toolkit for Membrane Protein Science. *Protein Sci. Publ. Protein Soc.* **2021**, *30* (2), 297–315. https://doi.org/10.1002/pro.3994.

(146) Bayburt, T. H.; Grinkova, Y. V.; Sligar, S. G. Self-Assembly of Discoidal Phospholipid Bilayer Nanoparticles with Membrane Scaffold Proteins. *Nano Lett.* **2002**, *2* (8), 853–856. https://doi.org/10.1021/nl025623k.

(147) Fox, C. A.; Romenskaia, I.; Dagda, R. K.; Ryan, R. O. Cardiolipin Nanodisks Confer Protection against Doxorubicin-Induced Mitochondrial Dysfunction. *Biochim. Biophys. Acta BBA - Biomembr.* **2022**, *1864* (10), 183984. https://doi.org/10.1016/j.bbamem.2022.183984.

(148) Oganesyan, I.; Lento, C.; Tandon, A.; Wilson, D. J. Conformational Dynamics of α-Synuclein during the Interaction with Phospholipid Nanodiscs by Millisecond Hydrogen–Deuterium Exchange Mass Spectrometry. *J. Am. Soc. Mass Spectrom.* **2021**, *32* (5), 1169–1179. https://doi.org/10.1021/jasms.0c00463.

(149) Wolf, E.; Lento, C.; Pu, J.; Dickinson, B. C.; Wilson, D. J. Innate Conformational Dynamics Drive Binding Specificity in Anti-Apoptotic Proteins Mcl-1 and Bcl-2. *Biochemistry* **2023**, *62* (11), 1619–1630. https://doi.org/10.1021/acs.biochem.2c00709.

(150) Marciano, D. P.; Dharmarajan, V.; Griffin, P. R. HDX-MS Guided Drug Discovery: Small Molecules and Biopharmaceuticals. *Curr. Opin. Struct. Biol.* **2014**, *0*, 105–111. https://doi.org/10.1016/j.sbi.2014.08.007.

(151) Goswami, D.; Marciano, D. P.; Pascal, B. D.; Chalmers, M. J.; Griffin, P. R. Application of Differential Hydrogen Exchange Mass Spectrometry in Small Molecule Drug Discovery. In *Hydrogen Exchange Mass Spectrometry of Proteins*; John Wiley & Sons, Ltd, 2016; pp 209–223. https://doi.org/10.1002/9781118703748.ch12.

(152) Kojetin, D. J.; Matta-Camacho, E.; Hughes, T. S.; Srinivasan, S.; Nwachukwu, J. C.; Cavett, V.; Nowak, J.; Chalmers, M. J.; Marciano, D. P.; Kamenecka, T. M.; Shulman, A. I.; Rance, M.; Griffin, P. R.; Bruning, J. B.; Nettles, K. W. Structural Mechanism for Signal Transduction in RXR Nuclear Receptor Heterodimers. *Nat. Commun.* **2015**, *6* (1), 8013. https://doi.org/10.1038/ncomms9013.

(153) Brožová, Z. R.; Dušek, J.; Palša, N.; Maixnerová, J.; Kamaraj, R.; Smutná, L.; Matouš, P.; Braeuning, A.; Pávek, P.; Kuneš, J.; Gathergood, N.; Špulák, M.; Pour, M.; Carazo, A. 2-Substituted Quinazolines: Partial Agonistic and Antagonistic Ligands of the Constitutive Androstane Receptor (CAR). *Eur. J. Med. Chem.* **2023**, *259*, 115631. https://doi.org/10.1016/j.ejmech.2023.115631.

(154) Swales, K.; Negishi, M. CAR, Driving into the Future. *Mol. Endocrinol.* **2004**, *18* (7), 1589–1598. https://doi.org/10.1210/me.2003-0397.

(155) Wright, E.; Busby, S. A.; Wisecarver, S.; Vincent, J.; Griffin, P. R.; Fernandez, E. J. Helix 11 Dynamics Is Critical for Constitutive Androstane Receptor Activity. *Structure* **2011**, *19* (1), 37–44. https://doi.org/10.1016/j.str.2010.11.008.

(156) Poudel, S.; Huber, A. D.; Chen, T. Regulation of Nuclear Receptors PXR and CAR by Small Molecules and Signal Crosstalk: Roles in Drug Metabolism and Beyond. *Drug Metab. Dispos.* **2023**, *51* (2), 228–236. https://doi.org/10.1124/dmd.122.000858.

(157) Wang, X.; Zhang, G.; Bian, Z.; Chow, V.; Grimaldi, M.; Carivenc, C.; Sirounian, S.; Li, H.; Sladekova, L.; Motta, S.; Luperi, Y.; Gong, Y.; Costello, C.; Li, L.; Jachimowicz, M.; Guo, M.; Hu, S.; Wilson, D.; Balaguer, P.; Bourguet, W.; Mani, S.; Bonati, L.; Peng, H.; March, J.; Wang, H.; Wang, S.; Krause, H. M.; Liu, J. Author Correction: An Abundant Ginger Compound Furanodienone Alleviates Gut Inflammation via the Xenobiotic Nuclear Receptor PXR in Mice. *Nat. Commun.* **2025**, *16* (1), 2133. https://doi.org/10.1038/s41467-025-57509-y.

(158) Delfosse, V.; Huet, T.; Harrus, D.; Granell, M.; Bourguet, M.; Gardia-Parège, C.; Chiavarina, B.; Grimaldi, M.; Le Mével, S.; Blanc, P.; Huang, D.; Gruszczyk, J.; Demeneix, B.; Cianférani, S.; Fini, J.-B.; Balaguer, P.; Bourguet, W. Mechanistic Insights into the Synergistic Activation of the RXR–PXR Heterodimer by Endocrine Disruptor Mixtures. *Proc. Natl. Acad. Sci.* **2021**, *118* (1), e2020551118. https://doi.org/10.1073/pnas.2020551118.

(159) Toporova, L.; Balaguer, P. Nuclear Receptors Are the Major Targets of Endocrine Disrupting Chemicals. *Mol. Cell. Endocrinol.* **2020**, *502*, 110665. https://doi.org/10.1016/j.mce.2019.110665.

(160) Baggelaar, M. P.; den Dulk, H.; Florea, B. I.; Fazio, D.; Bernabò, N.; Raspa, M.; Janssen, A. P. A.; Scavizzi, F.; Barboni, B.; Overkleeft, H. S.; Maccarrone, M.; van der Stelt, M. ABHD2 Inhibitor Identified by Activity-Based Protein Profiling Reduces Acrosome Reaction. *ACS Chem. Biol.* **2019**, *14* (10), 2295–2304. https://doi.org/10.1021/acschembio.9b00640.

(161) Xu, R. X.; Lambert, M. H.; Wisely, B. B.; Warren, E. N.; Weinert, E. E.; Waitt, G. M.; Williams, J. D.; Collins, J. L.; Moore, L. B.; Willson, T. M.; Moore, J. T. A Structural Basis for Constitutive Activity in the Human CAR/RXRα Heterodimer. *Mol. Cell* **2004**, *16* (6), 919–928. https://doi.org/10.1016/j.molcel.2004.11.042.

(162) Pham, B.; Arons, A. B.; Vincent, J. G.; Fernandez, E. J.; Shen, T. Regulatory Mechanics of Constitutive Androstane Receptors: Basal and Ligand-Directed Actions. *J. Chem. Inf. Model.* **2019**, *59* (12), 5174–5182. https://doi.org/10.1021/acs.jcim.9b00695.

(163) Suino, K.; Peng, L.; Reynolds, R.; Li, Y.; Cha, J.-Y.; Repa, J. J.; Kliewer, S. A.; Xu, H. E. The Nuclear Xenobiotic Receptor CAR: Structural Determinants of Constitutive Activation and Heterodimerization. *Mol. Cell* **2004**, *16* (6), 893–905. https://doi.org/10.1016/j.molcel.2004.11.036.

(164) Shan, L.; Vincent, J.; Brunzelle, J.; Dussault, I.; Lin, M.; Ianculescu, I.; Sherman, M.; Forman, B.; Fernandez, E. Structure of the Murine Constitutive Androstane Receptor Complexed to AndrostenolA Molecular Basis for Inverse Agonism. *Mol. Cell* **2004**, *16* (6), 907–917. https://doi.org/10.1016/S1097-2765(04)00728-2.

(165) Bruning, J. B.; Chalmers, M. J.; Prasad, S.; Busby, S. A.; Kamenecka, T. M.; He, Y.; Nettles, K. W.; Griffin, P. R. Partial Agonists Activate PPARγ Using a Helix 12 Independent Mechanism. *Structure* **2007**, *15* (10), 1258–1271. https://doi.org/10.1016/j.str.2007.07.014.

(166) Hughes, T. S.; Giri, P. K.; de Vera, I. M. S.; Marciano, D. P.; Kuruvilla, D. S.; Shin, Y.; Blayo, A.-L.; Kamenecka, T. M.; Burris, T. P.; Griffin, P. R.; Kojetin, D. J. An Alternate Binding Site for PPARγ Ligands. *Nat. Commun.* **2014**, *5*, 3571. https://doi.org/10.1038/ncomms4571.

(167) Mannowetz, N.; Miller, M. R.; Lishko, P. V. Regulation of the Sperm Calcium Channel CatSper by Endogenous Steroids and Plant Triterpenoids. *Proc. Natl. Acad. Sci. U. S. A.* **2017**, *114* (22), 5743–5748. https://doi.org/10.1073/pnas.1700367114.

(168) Ren, D.; Navarro, B.; Perez, G.; Jackson, A. C.; Hsu, S.; Shi, Q.; Tilly, J. L.; Clapham, D. E. A Sperm Ion Channel Required for Sperm Motility and Male Fertility. *Nature* **2001**, *413* (6856), 603–609. https://doi.org/10.1038/35098027.

(169) Rehfeld, A. Revisiting the Action of Steroids and Triterpenoids on the Human Sperm Ca2+ Channel CatSper. *Mol. Hum. Reprod.* **2020**, *26* (11), 816–824. https://doi.org/10.1093/molehr/gaaa062.

(170) Kanno, Y.; Inouye, Y. A Consecutive Three Alanine Residue Insertion Mutant of Human CAR: A Novel CAR Ligand Screening System in HepG2 Cells. *J. Toxicol. Sci.* **2010**, *35* (4), 515–525. https://doi.org/10.2131/jts.35.515.

(171) Küblbeck, J.; Niskanen, J.; Honkakoski, P. Metabolism-Disrupting Chemicals and the Constitutive Androstane Receptor CAR. *Cells* **2020**, *9* (10), 2306. https://doi.org/10.3390/cells9102306.

(172) Yan, J.; Chen, B.; Lu, J.; Xie, W. Deciphering the Roles of the Constitutive Androstane Receptor in Energy Metabolism. *Acta Pharmacol. Sin.* **2015**, *36* (1), 62–70. https://doi.org/10.1038/aps.2014.102.

(173) Hudson, G. M.; Flannigan, K. L.; Erickson, S. L.; Vicentini, F. A.; Zamponi, A.; Hirota, C. L.; Alston, L.; Altier, C.; Ghosh, S.; Rioux, K. P.; Mani, S.; Chang, T. K.; Hirota, S. A. Constitutive Androstane Receptor Regulates the Intestinal Mucosal Response to Injury. *Br. J. Pharmacol.* **2017**, *174* (12), 1857–1871. https://doi.org/10.1111/bph.13787.

(174) Huang, W.; Zhang, J.; Washington, M.; Liu, J.; Parant, J. M.; Lozano, G.; Moore, D. D. Xenobiotic Stress Induces Hepatomegaly and Liver Tumors via the Nuclear Receptor Constitutive Androstane Receptor. *Mol. Endocrinol.* **2005**, *19* (6), 1646–1653. https://doi.org/10.1210/me.2004-0520.

(175) Chai, S. C.; Lin, W.; Li, Y.; Chen, T. Drug Discovery Technologies to Identify and Characterize Modulators of the Pregnane X Receptor and the Constitutive Androstane Receptor. *Drug Discov. Today* **2019**, *24* (3), 906–915. https://doi.org/10.1016/j.drudis.2019.01.021.

(176) Mejdrová, I.; Dušek, J.; Škach, K.; Stefela, A.; Skoda, J.; Chalupský, K.; Dohnalová, K.; Pavkova, I.; Kronenberger, T.; Rashidian, A.; Smutná, L.; Duchoslav, V.; Smutny, T.; Pávek, P.; Nencka, R. Discovery of Novel Human Constitutive Androstane Receptor Agonists with the Imidazo[1,2-a]Pyridine Structure. *J. Med. Chem.* **2023**, *66* (4), 2422–2456. https://doi.org/10.1021/acs.jmedchem.2c01140.

(177) Honkakoski, P. Searching for Constitutive Androstane Receptor Modulators. *Drug Metab. Dispos.* **2022**, *50* (7), 1002–1009. https://doi.org/10.1124/dmd.121.000482.

(178) Garcia-Maldonado, E.; Huber, A. D.; Chai, S. C.; Nithianantham, S.; Li, Y.; Wu, J.; Poudel, S.; Miller, D. J.; Seetharaman, J.; Chen, T. Chemical Manipulation of an Activation/Inhibition

Switch in the Nuclear Receptor PXR. *Nat. Commun.* **2024**, *15* (1), 4054. https://doi.org/10.1038/s41467-024-48472-1.

(179) Shang, J.; Mosure, S. A.; Zheng, J.; Brust, R.; Bass, J.; Nichols, A.; Solt, L. A.; Griffin, P. R.; Kojetin, D. J. A Molecular Switch Regulating Transcriptional Repression and Activation of PPARγ. *Nat. Commun.* **2020**, *11* (1), 956. https://doi.org/10.1038/s41467-020-14750-x.

(180) Molnár, F.; Küblbeck, J.; Jyrkkärinne, J.; Prantner, V.; Honkakoski, P. An Update on the Constitutive Androstane Receptor (CAR). *dmdi* **2013**, *28* (2), 79–93. https://doi.org/10.1515/dmdi-2013-0009.

(181) Burris, T. P.; Solt, L. A.; Wang, Y.; Crumbley, C.; Banerjee, S.; Griffett, K.; Lundasen, T.; Hughes, T.; Kojetin, D. J. Nuclear Receptors and Their Selective Pharmacologic Modulators. *Pharmacol. Rev.* **2013**, *65* (2), 710–778. https://doi.org/10.1124/pr.112.006833.

(182) Delfosse, V.; Maire, A. le; Balaguer, P.; Bourguet, W. A Structural Perspective on Nuclear Receptors as Targets of Environmental Compounds. *Acta Pharmacol. Sin.* **2015**, *36* (1), 88–101. https://doi.org/10.1038/aps.2014.133.

(183) Yu, X.; Shang, J.; Kojetin, D. J. Molecular Basis of Ligand-Dependent Nurr1-RXRα Activation. *eLife 12*, e85039. https://doi.org/10.7554/eLife.85039.

(184) Zhang, J.; Chalmers, M. J.; Stayrook, K. R.; Burris, L. L.; Wang, Y.; Busby, S. A.; Pascal, B. D.; Garcia-Ordonez, R. D.; Bruning, J. B.; Istrate, M. A.; Kojetin, D. J.; Dodge, J. A.; Burris, T. P.; Griffin, P. R. DNA Binding Alters Coactivator Interaction Surfaces of the Intact VDR–RXR Complex. *Nat. Struct. Mol. Biol.* **2011**, *18* (5), 556–563. https://doi.org/10.1038/nsmb.2046.

(185) Frkic, R. L.; Marshall, A. C.; Blayo, A.-L.; Pukala, T. L.; Kamenecka, T. M.; Griffin, P. R.; Bruning, J. B. PPARγ in Complex with an Antagonist and Inverse Agonist: A Tumble and Trap Mechanism of the Activation Helix. *iScience* **2018**, *5*, 69–79. https://doi.org/10.1016/j.isci.2018.06.012.

(186) Choi, W. J.; Haratipour, Z.; Blind, R. D. Full-Length Nuclear Receptor Allosteric Regulation. *J. Lipid Res.* **2023**, *64* (8). https://doi.org/10.1016/j.jlr.2023.100406.

(187) le Maire, A.; Germain, P.; Bourguet, W. Chapter Eight - Protein-Protein Interactions in the Regulation of RAR–RXR Heterodimers Transcriptional Activity. In *Methods in Enzymology*; Pohl, E., Ed.; Retinoid Signaling Pathways; Academic Press, 2020; Vol. 637, pp 175–207. https://doi.org/10.1016/bs.mie.2020.02.007.

(188) Gavriilidou, A. F. M.; Sokratous, K.; Yen, H.-Y.; De Colibus, L. High-Throughput Native Mass Spectrometry Screening in Drug Discovery. *Front. Mol. Biosci.* **2022**, *9*, 837901. https://doi.org/10.3389/fmolb.2022.837901.

(189) Tzameli, I.; Pissios, P.; Schuetz, E. G.; Moore, D. D. The Xenobiotic Compound 1,4-Bis[2-(3,5-Dichloropyridyloxy)]Benzene Is an Agonist Ligand for the Nuclear Receptor CAR. *Mol. Cell. Biol.* **2000**, *20* (9), 2951–2958.

(190) Lambert, G.; Charlton, F.; Rye, K.-A.; Piper, D. E. Molecular Basis of PCSK9 Function. *Atherosclerosis* **2009**, *203* (1), 1–7. https://doi.org/10.1016/j.atherosclerosis.2008.06.010.

(191) Kavanaugh, D. W.; Sivignon, A.; Rossez, Y.; Chouit, Z.; Chambon, C.; Béal, L.; Bonnet, M.; Hébraud, M.; Guérardel, Y.; Nguyen, H. T. T.; Barnich, N. Biochemical Characterization of the Escherichia Coli Surfaceome: A Focus on Type I Fimbriae and Flagella. *Front. Microbiol.* **2025**, *16*. https://doi.org/10.3389/fmicb.2025.1507286.

(192) Johnson, D. T.; Di Stefano, L. H.; Jones, L. M. Fast Photochemical Oxidation of Proteins (FPOP): A Powerful Mass Spectrometry–Based Structural Proteomics Tool. *J. Biol. Chem.* **2019**, *294* (32), 11969–11979. https://doi.org/10.1074/jbc.REV119.006218.

(193) Li, K. S.; Shi, L.; Gross, M. L. Mass Spectrometry-Based Fast Photochemical Oxidation of Proteins (FPOP) for Higher Order Structure Characterization. *Acc. Chem. Res.* **2018**, *51* (3), 736–744. https://doi.org/10.1021/acs.accounts.7b00593.

(194) Hammerschmid, D.; Calvaresi, V.; Bailey, C.; Russell Lewis, B.; Politis, A.; Morris, M.; Denbigh, L.; Anderson, M.; Reading, E. Chromatographic Phospholipid Trapping for Automated H/D Exchange Mass Spectrometry of Membrane Protein–Lipid Assemblies. *Anal. Chem.* **2023**, *95* (5), 3002–3011. https://doi.org/10.1021/acs.analchem.2c04876.

(195) Peterle, D.; DePice, D.; Wales, T. E.; Engen, J. R. Increase the Flow Rate and Improve Hydrogen Deuterium Exchange Mass Spectrometry. *J. Chromatogr. A* **2023**, *1689*, 463742. https://doi.org/10.1016/j.chroma.2022.463742.

(196) Wollenberg, D. T. W.; Pengelley, S.; Mouritsen, J. C.; Suckau, D.; Jørgensen, C. I.; Jørgensen, T. J. D. Avoiding H/D Scrambling with Minimal Ion Transmission Loss for HDX-MS/MS-ETD Analysis on a High-Resolution Q-TOF Mass Spectrometer. *Anal. Chem.* **2020**, *92* (11), 7453–7461. https://doi.org/10.1021/acs.analchem.9b05208.

(197) Brodbelt, J. S.; Morrison, L. J.; Santos, I. Ultraviolet Photodissociation Mass Spectrometry for Analysis of Biological Molecules. *Chem. Rev.* **2020**, *120* (7), 3328–3380. https://doi.org/10.1021/acs.chemrev.9b00440.

(198) Lau, A. M. C.; Ahdash, Z.; Martens, C.; Politis, A. Deuteros: Software for Rapid Analysis and Visualization of Data from Differential Hydrogen Deuterium Exchange-Mass Spectrometry. *Bioinformatics* **2019**, *35* (17), 3171–3173. https://doi.org/10.1093/bioinformatics/btz022.

Appendices

Appendix A| Supplementary for Chapter 2

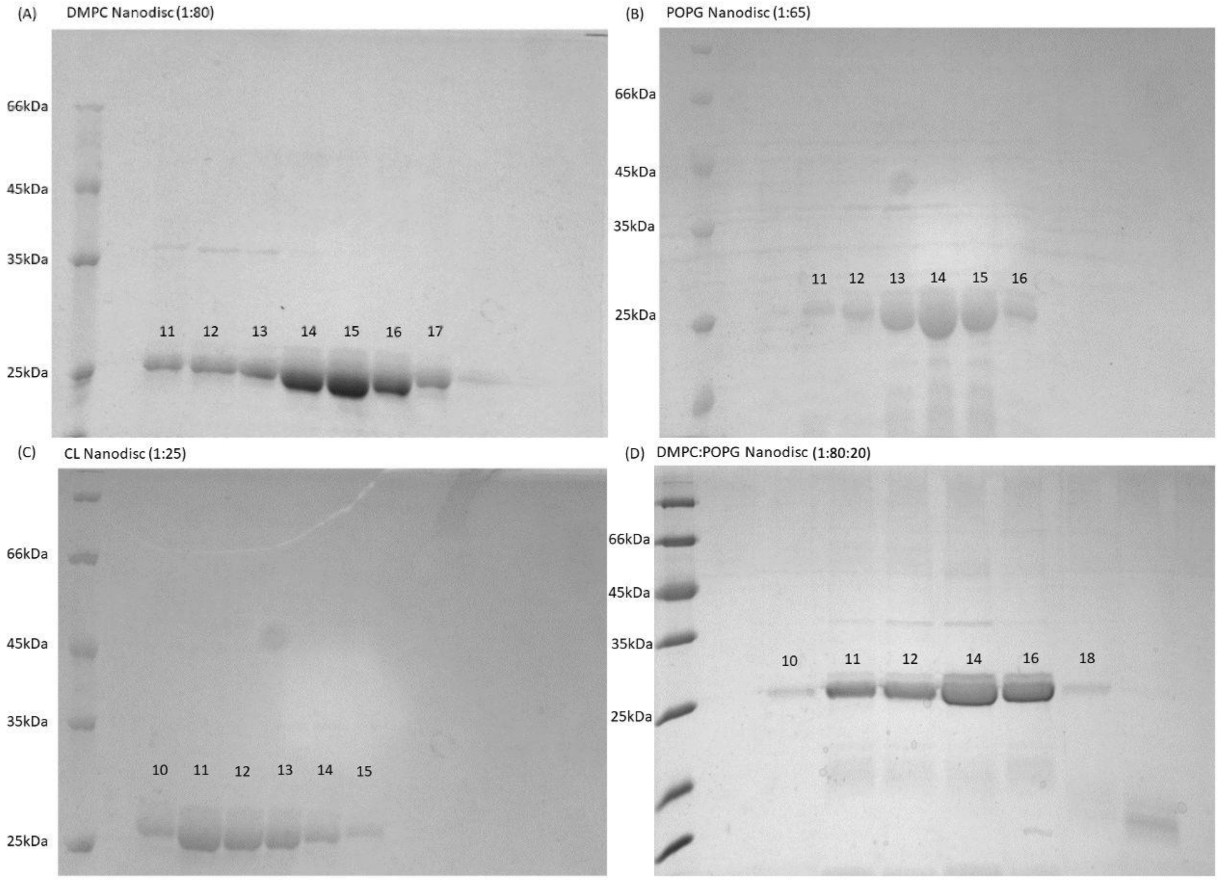

Figure A1. Representative SDS-PAGE for the fractions collected via SEC during the purification process. (A) DMPC nanodisc (1:80), (B) POPG nanodisc (1:65), (C) Cardiolipin (CL) nanodisc (1:25), (D)DMPC:POPG nanodisc (1:70:10).

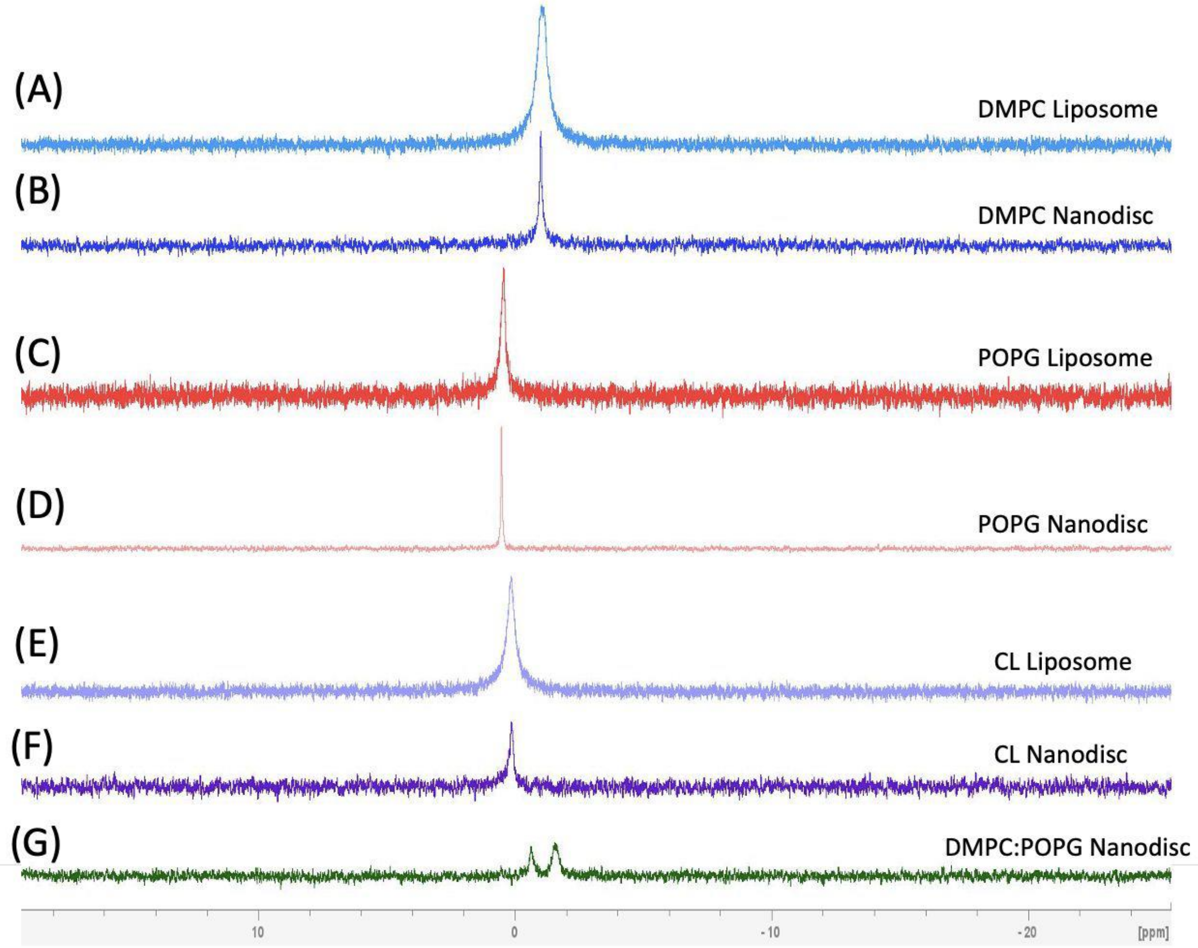

Figure A2. The 1D ^{31}P Nuclear magnetic resonance spectrum (NMR) for (A) DMPC liposome, (B) DMPC nanodisc (1:80), (C) POPG liposome, (D) POPG nanodisc (1:65), (E) CL liposome, (F) CL nanodisc (1:25), and (G) DMPC:POPG nanodiscs.

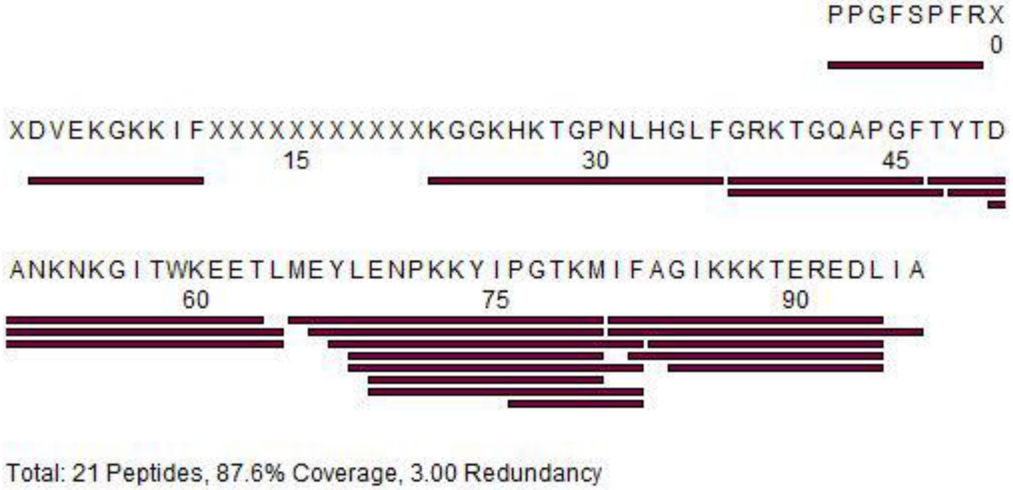

Figure A3. Peptide coverage map of horse Cytochrome C. A total of 21 peptides were generated using an in-house NHS-pepsin column, resulting in a sequence coverage of 87.6% and peptide redundancy of 3.00.

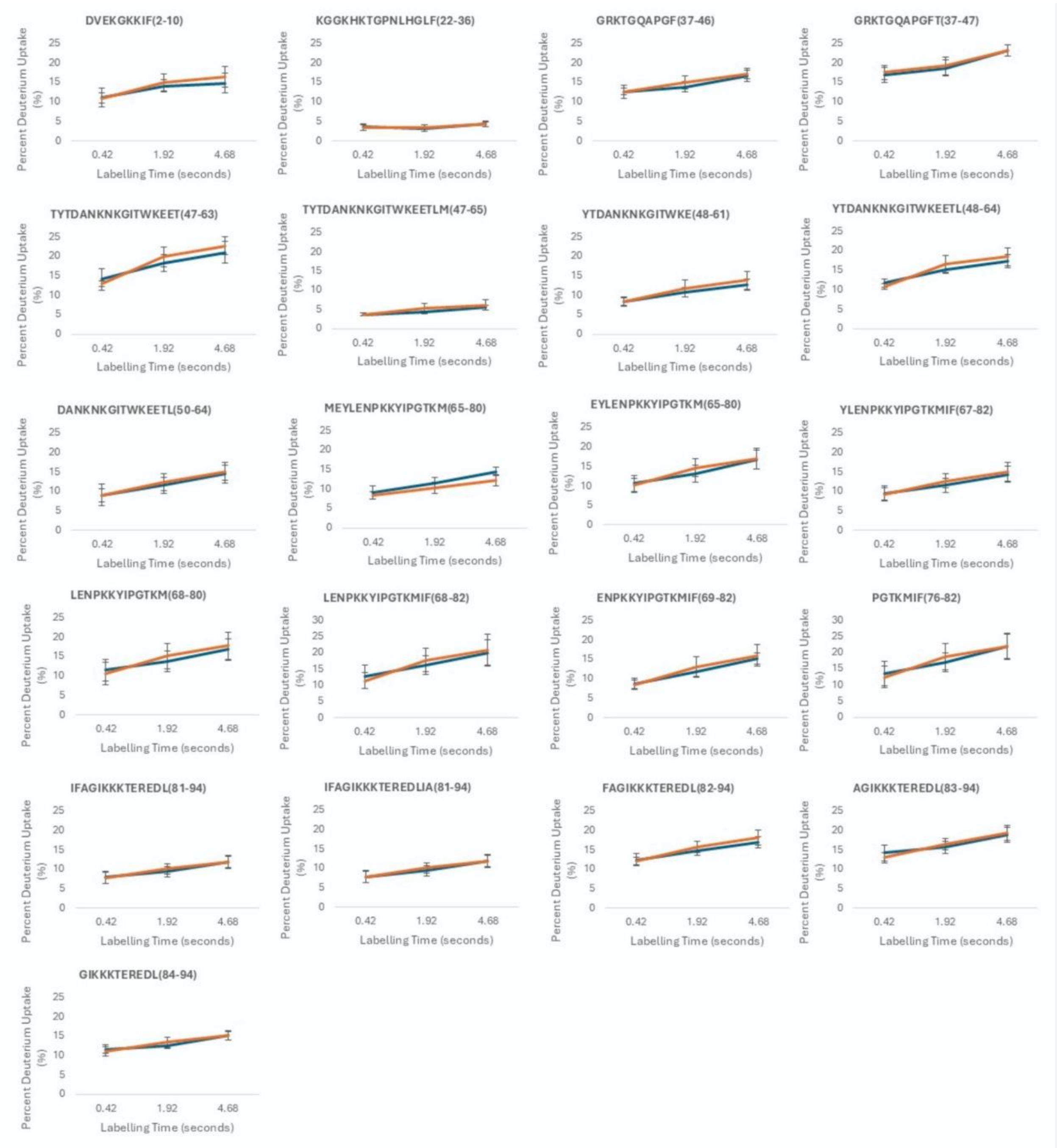

Figure A4. Unbound cytochrome c (blue) vs. cytochrome c/DMPC nanodisc (orange) deuterium uptake kinetic plots.

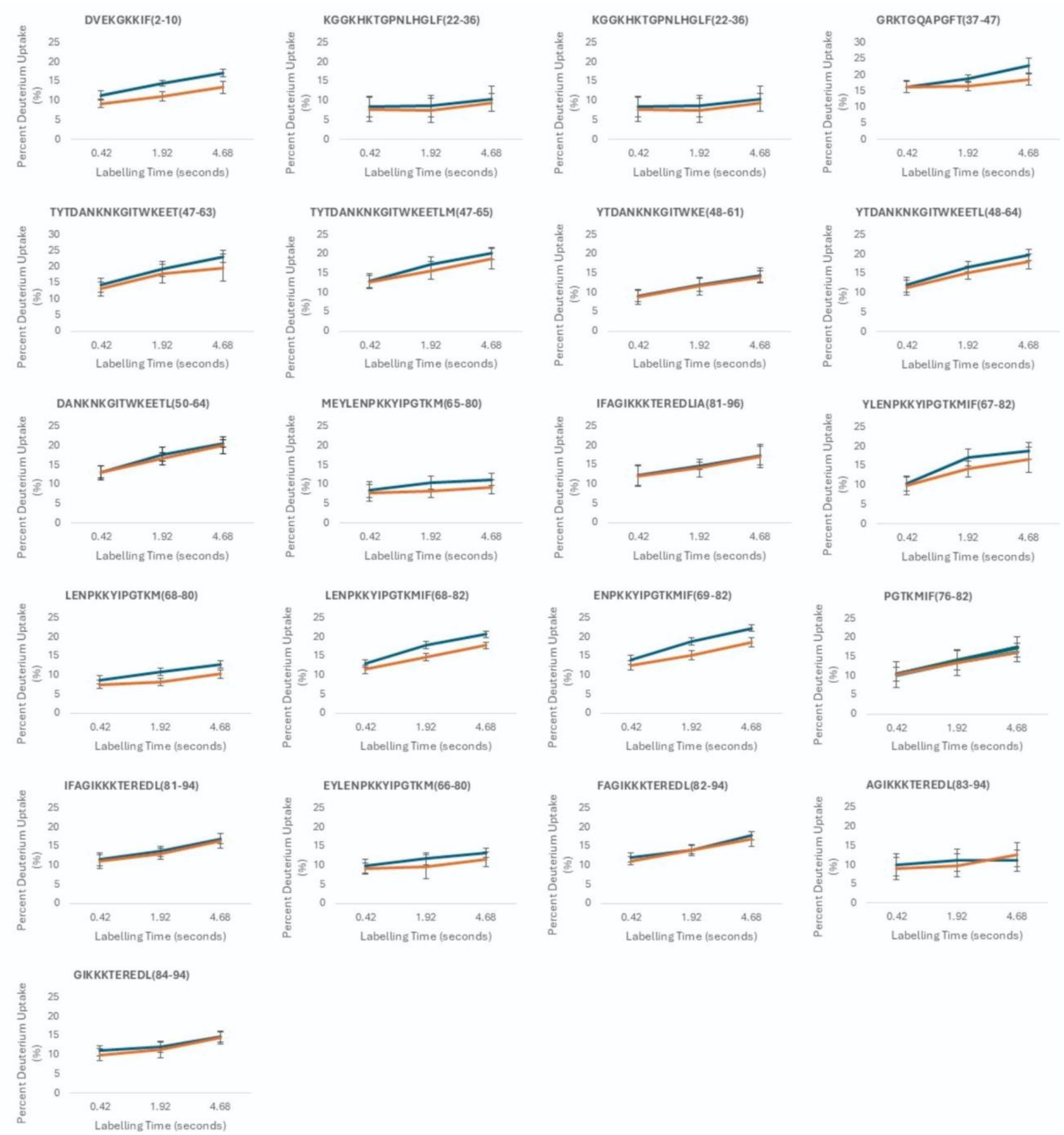

Figure A5. Unbound cytochrome c (blue) vs. cytochrome c/POPG nanodisc (orange) deuterium uptake plots.

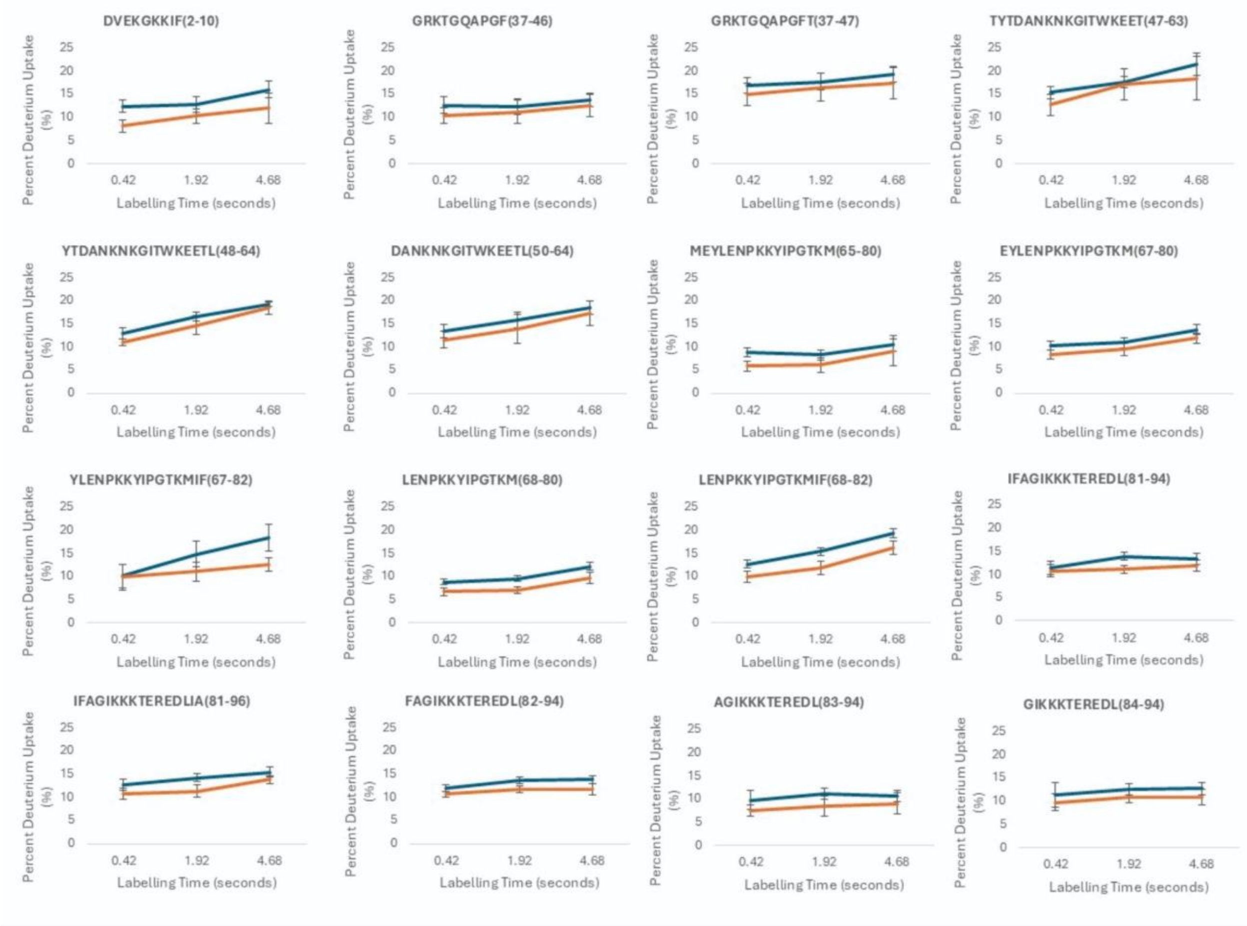

Figure A6. Unbound cytochrome c (blue) vs. cytochrome c/cardiolipin nanodisc (orange) deuterium uptake kinetic plots.

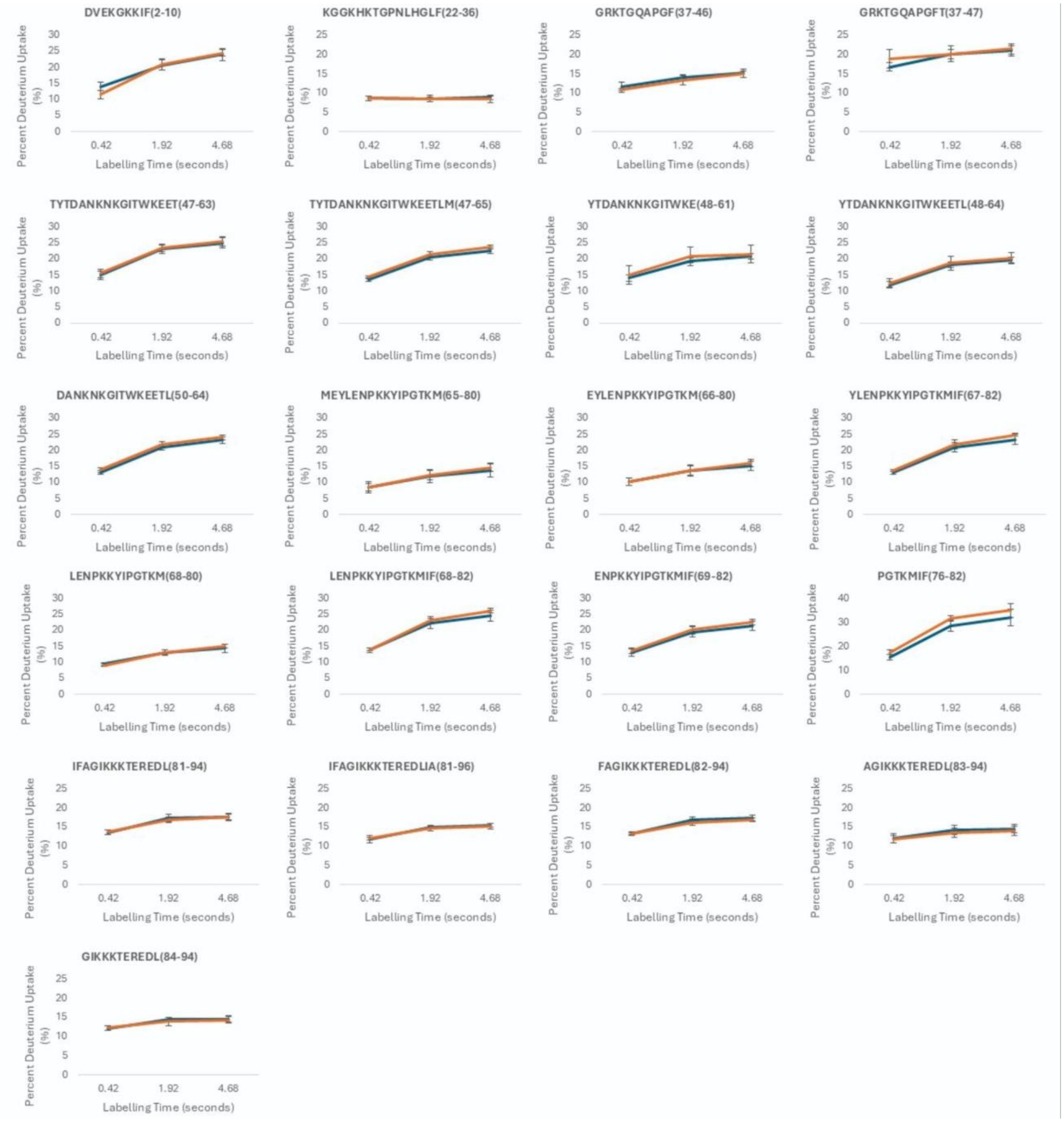

Figure A7. Unbound cytochrome c (blue) vs. cytochrome c/DMPC:POPG nanodisc (orange) deuterium uptake kinetic plots.

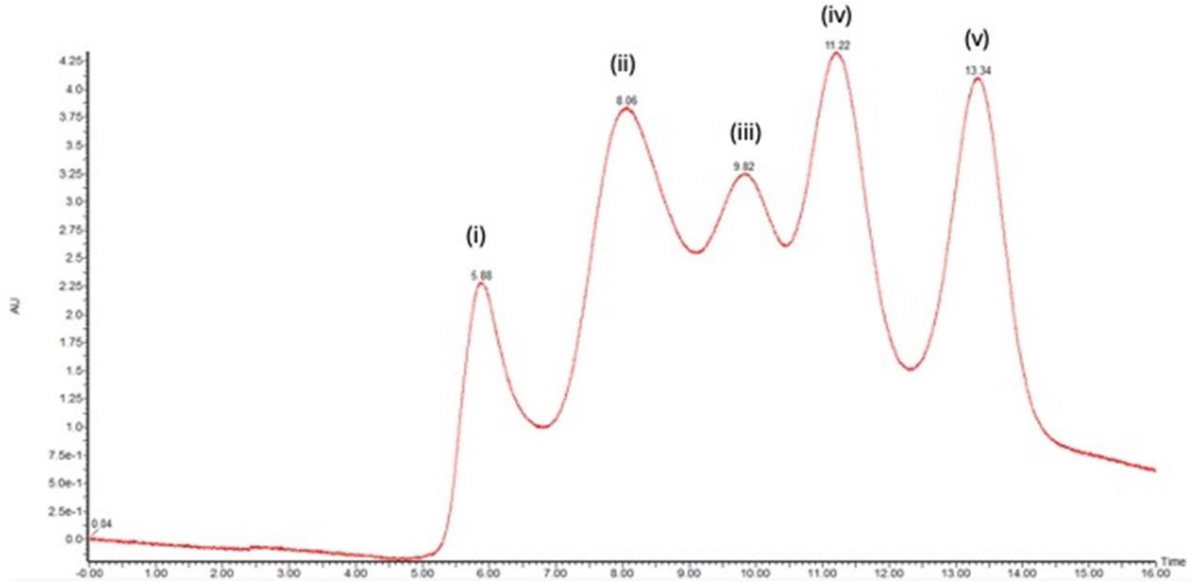

Figure A8. Size-exclusion chromatography for protein standards, (i) thyroglobin, (ii) gamma globulin, (iii) ovalbumin, (iv) myoglobin, and (v) vitamin B12. Detection at 280 nm, using in-house packed column with Superdex 200 prep-grade beads (300 x 7.8mm) in 20mM HEPES, pH 7.2 at 1 mL/min.

Table A1 table of identified peptides

m/z	z	m	Drift Time	Sequence	Start	Stop
531.8075	2	1063.615	34.78	DVEKGKKIF	2	10
397.7215	4	1590.886	22.94	KGGKHKTGPNLHGLF	22	36
559.7955	2	1119.591	37.13	GRKTGQAPGF	37	46
509.2715	2	1018.543	33.96	GRKTGQAPGFT	37	47
499.74425	4	1998.977	33.35	TYTDANKNKGITWKEET	47	63
502.75325	4	2011.013	31.01	TYTDANKNKGITWKEETLM	47	65
555.946333	3	1667.839	30.83	YTDANKNKGITWKE	48	61
582.300667	3	1746.902	35.69	YTDANKNKGITWKEETL	48	64
582.300667	3	1746.902	35.63	DANKNKGITWKEETL	50	64
485.49525	4	1941.981	30.97	MEYLENPKKYIPGTKM	65	80
603.647	3	1810.941	32.95	EYLENPKKYIPGTKM	66	80
485.51275	4	1942.051	32.93	YLENPKKYIPGTKMIF	67	82
592.995667	3	1778.987	34.94	LENPKKYIPGTKM	68	80
506.278333	3	1518.835	27.41	LENPKKYIPGTKMIF	68	82
555.301	3	1665.903	34.68	ENPKKYIPGTKMIF	69	82
468.583667	3	1405.751	25.05	ENPKKYIPGTKM	69	80
396.714	2	793.428	24.77	PGTKMIF	76	82
610.688	3	1832.064	36.47	IFAGIKKKTEREDL	81	94
411.98575	4	1647.943	23.05	IFAGIKKKTEREDLIA	81	96
511.619667	3	1534.859	28.82	FAGIKKKTEREDL	82	94
462.596667	3	1387.79	26.02	AGIKKKTEREDL	83	94
438.917667	3	1316.753	24.12	GIKKKTEREDL	84	94

Appendix B| Supplementary for Chapter 3

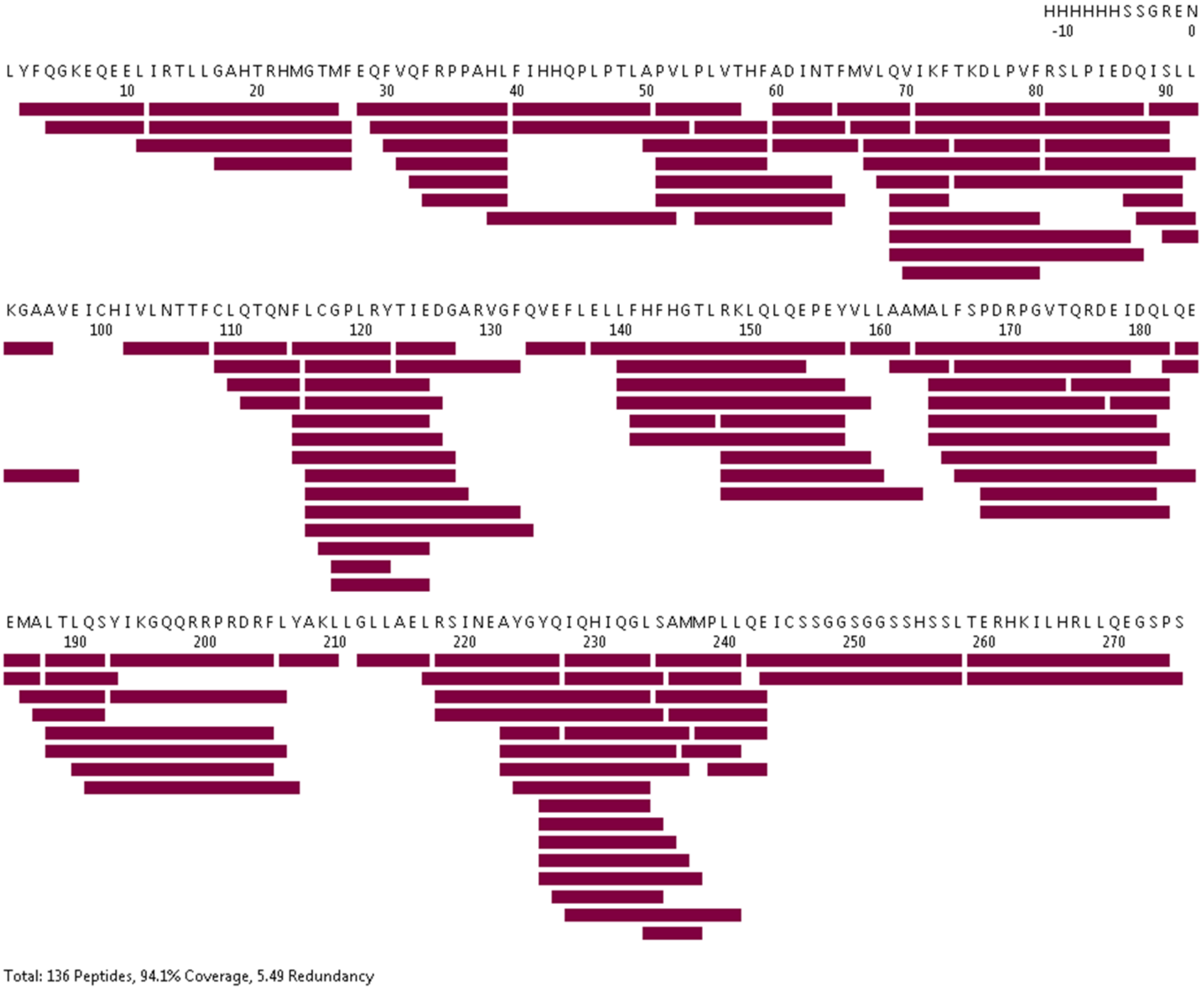

Figure B1. Sequence Coverage for CAR

Figure B2. Summed difference in deuterium uptake of CITCO and DIE binding to CAR. To be considered statistically significant, the ΔHDX must exceed the dotted gray-line, which is 3 times the summed propagated error (3σ).

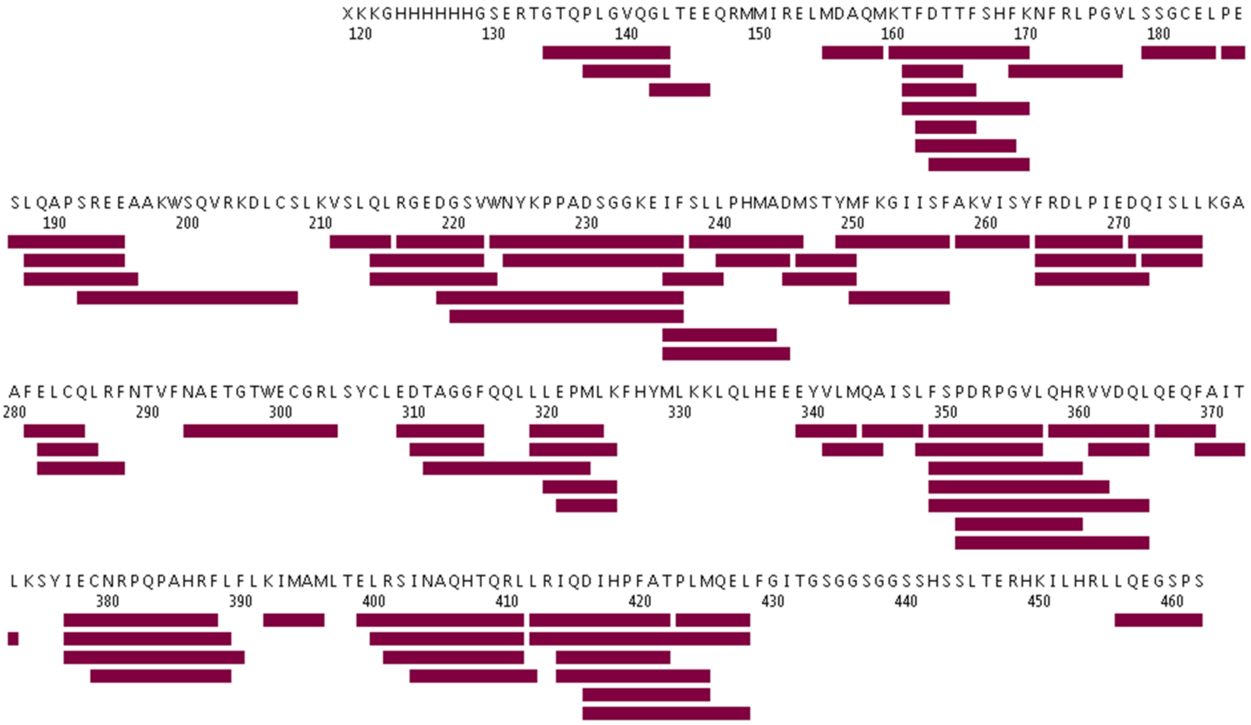

Total: 82 Peptides, 75.6% Coverage, 2.83 Redundancy

Figure B3. Sequence Coverage for PXR (for HDX experiments involving SR12813, FDN+EE2, FDN+E2, and FDN)

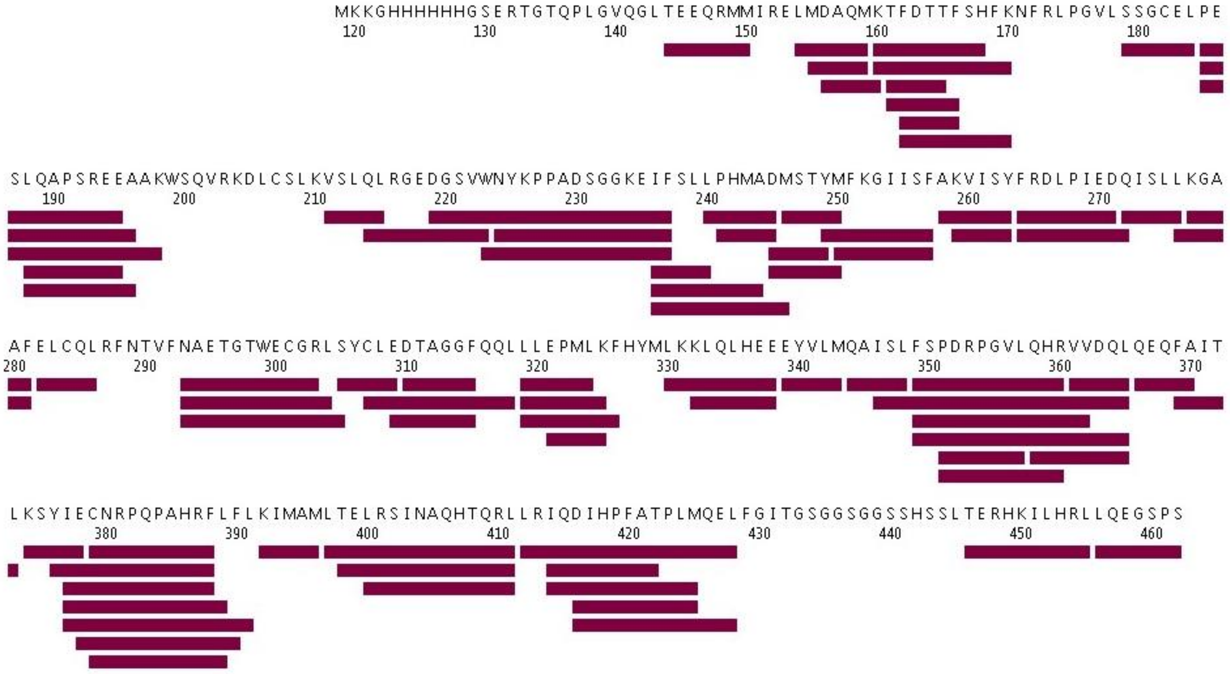

Total: 83 Peptides, 78.5% Coverage, 2.76 Redundancy

Figure B4. Sequence Coverage for PXR (for HDX experiments involving EE2 and E2 alone).

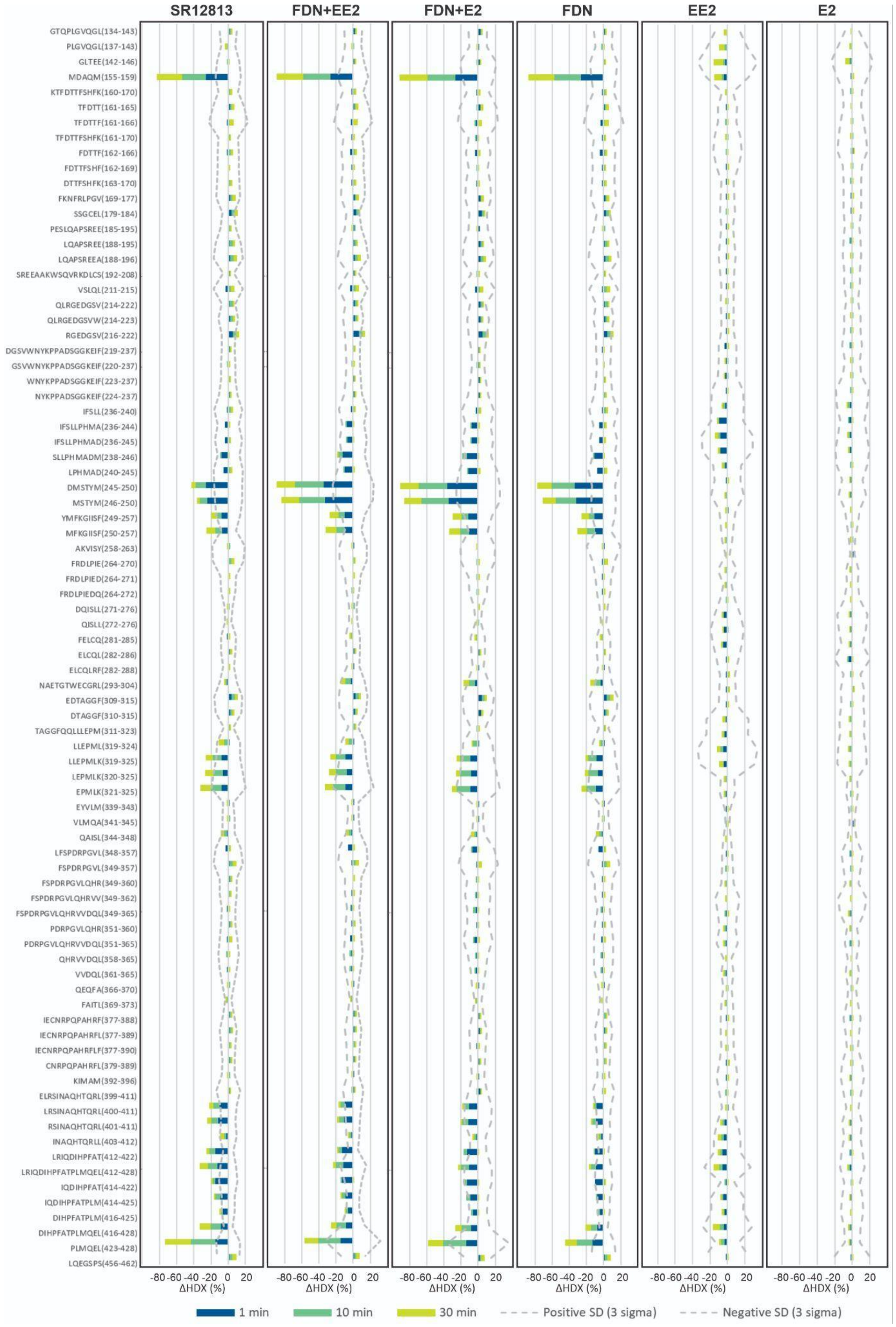

Figure B5. Summed difference in deuterium uptake of SR12813, FDN+E2, FDN+EE2, FDN, EE2, and E2 binding to PXR. To be considered statistically significant, the ΔHDX must exceed the dotted gray-line, which is 3 times the summed propagated error (3σ).

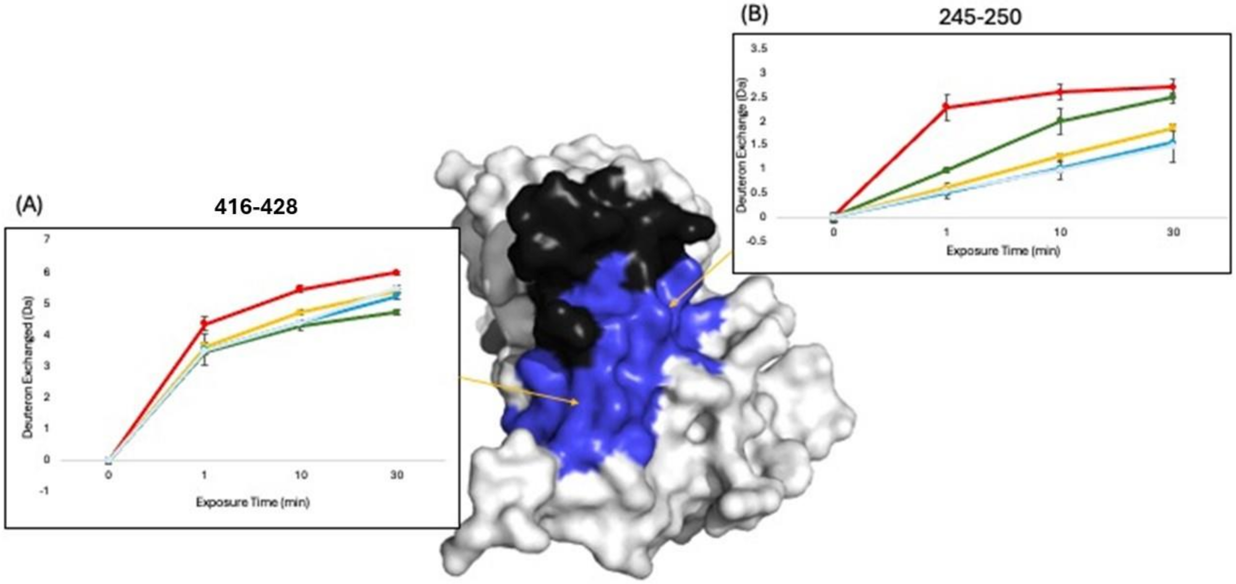

Figure B6. (A) Helix 12 (416-428) and (B)Helix 3 (245-250) regions showing differences in deuterium uptake upon binding SR12813 (green), FDN+EE2(cyan), FDN+E2(light blue) and FDN (yellow) to PXR (red). Error bars are 3σ standard deviation from triplicate measurements.

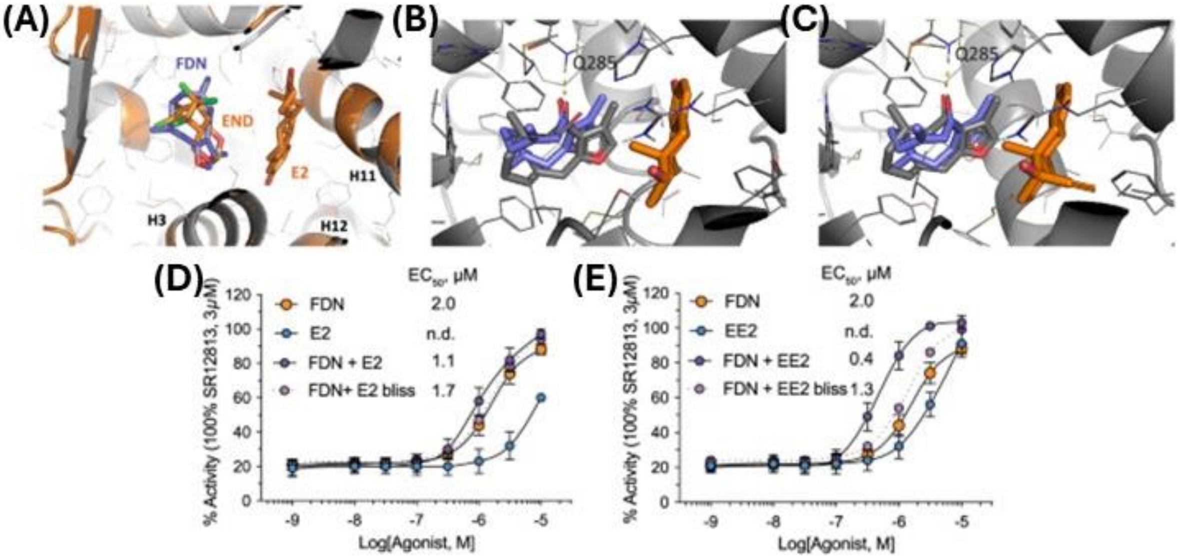

Figure B7. (A) FDN-bound PXR superpositions onto PXR bound to E2 and END (orange, PDB 7AXK). (B) Molecular docking of FDN pose in the presence of E2, where the docking pose (in gray) matches crystallographic structure for PXR: FDN (in violet, RMSD Å), and correctly reproduces the H-bond with residue Q285. (C) Molecular docking of FDN pose in the presence of EE2. The docking pose (in gray) matches the crystallographic structure (in violet, RMSD = 1.52Å), and correctly reproduces the H-bond with residue Q285. (D,E) HG5LN GAL4-PXR-LBD cells exposed to different concentrations of FDN, E2 or EE2, and in combination FDN+E2 or FDN+EE2 (n=4). Replicated with permission from Wang *et al*.(2025) [157]

Total: 79 Peptides, 81.5% Coverage, 3.03 Redundancy

Figure B8. Sequence Coverage for FDN binding to CAR experiments.

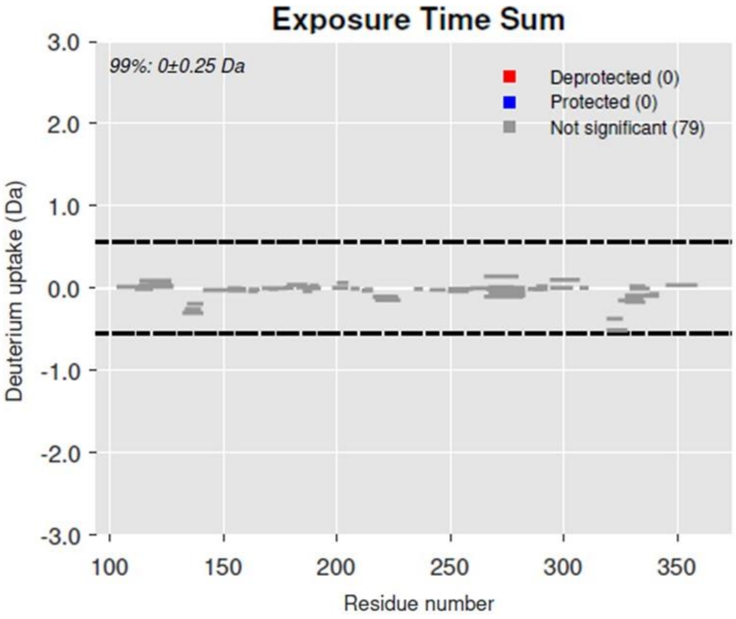

Figure B9. Summed deuterium uptake differences presented in Woods plot for structural dynamics induced by FDN on CAR. Wood plots display peptide length, and sequence coverage. Regions highlighted in red, blue or grey represent deprotected, protected and non-statistically significant peptides, respectively. A confidence limit of 99% was applied to each data set to identify peptides that are significant. Presented plots have been created in Deuteros.[198]

Total: 136 Peptides, 88.5% Coverage, 4.01 Redundancy

Figure B10. Sequence coverage for Wild-type ABHD2

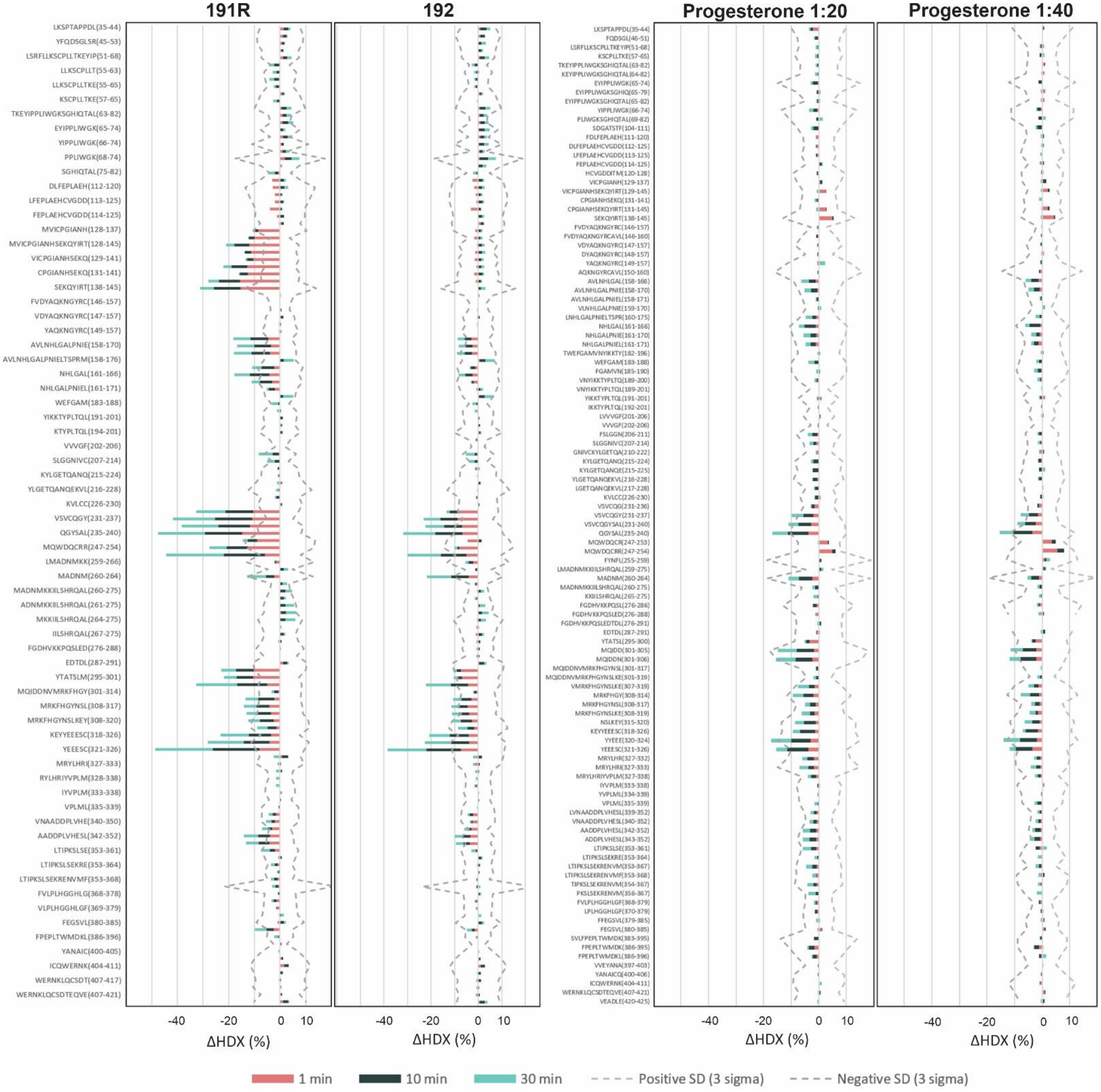

Figure B11. Summed difference in deuterium uptake of **191R**, **192**, Progesterone at 1:20 and 1:40 molar ratio binding to Wild-type ABHD2. To be considered statistically significant, the ΔHDX must exceed the dotted gray-line, which is 3 times the summed propagated error (3σ).

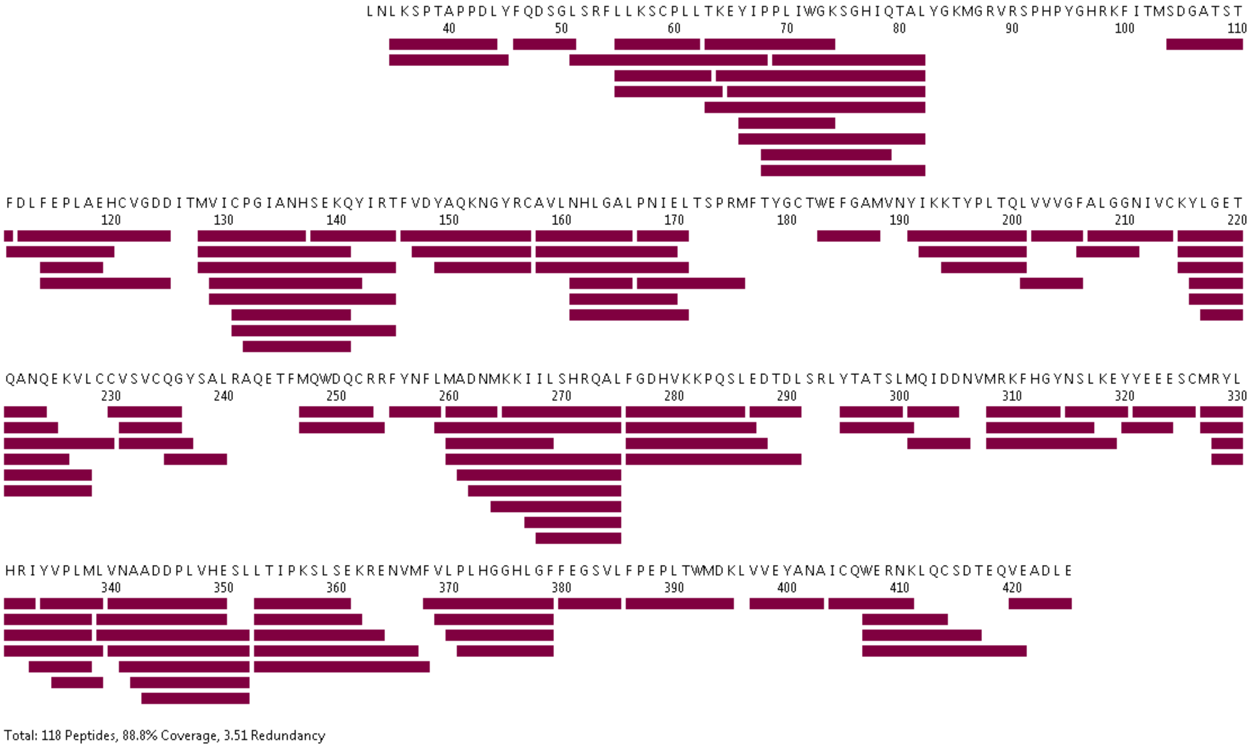

Figure B12. Sequence coverage for S207A mutant of ABHD2

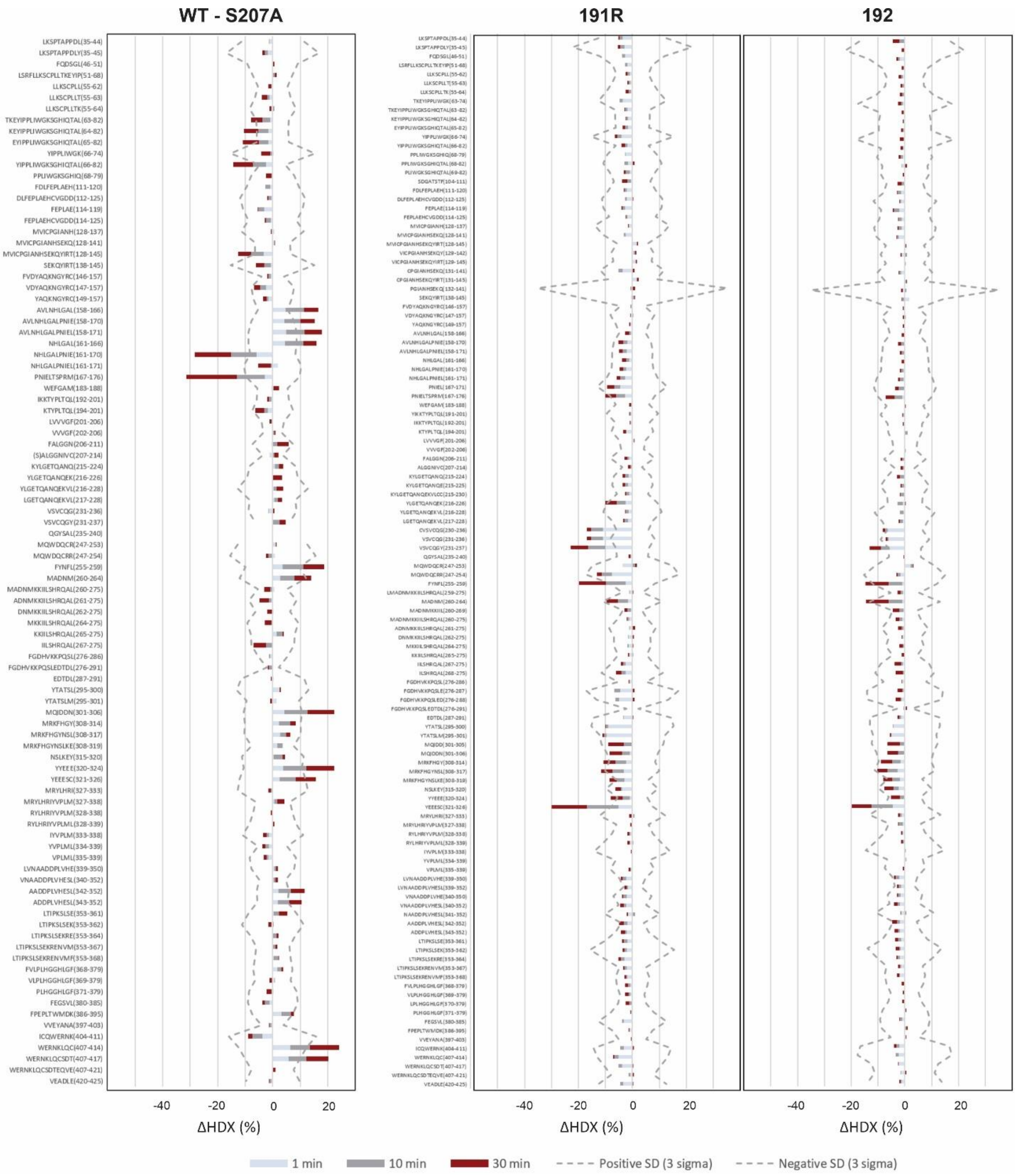

Figure B13. (A)Summed difference in deuterium uptake of **191R**, and **192** binding to S207A Mutant ABHD2. To be considered statistically significant, the ΔHDX must exceed the dotted gray-line, which is 3 times the summed propagated error (3σ). (B) Summed difference in deuterium uptake between Wild-type ABHD2 and S207A mutant.

Appendix C| Supplementary for Chapter 4

Table C1| HDX values for RXRα LBD (± CAR modulators)

RXR Sequence	CITCO ± 3s.d		DIE ± 3s.d	
SSGRENLYFQG(213-223)	0.74 ±	2.22	0.89 ±	2.65
GRENLYFQGSSANE(215-228)	0.40 ±	2.07	-0.29 ±	5.24
RILEAELA(234-241)	-0.56 ±	2.76	-1.27 ±	4.43
ADKQL(272-276)	-1.12 ±	5.57	-1.95 ±	13.71
QLFTL(275-279)	-0.88 ±	3.98	-0.68 ±	5.51
FTLVE(277-281)	1.44 ±	2.80	0.22 ±	4.87
VEWAKRIPHFSE(280-291)	0.09 ±	4.07	-0.30 ±	2.81
PLDDQV(293-298)	1.08 ±	3.19	0.85 ±	2.16
DDQVILLRAGW(295-305)	0.09 ±	4.98	0.47 ±	4.39
DDQVILLRAGWNEL(295-308)	-0.10 ±	1.00	-0.68 ±	2.24
DQVIL(296-300)	0.90 ±	2.06	0.41 ±	1.28
QVILL(297-301)	0.26 ±	0.65	-0.02 ±	0.38
RAGWNELL(302-309)	1.64 ±	3.71	-0.02 ±	6.24
RAGWNELLI(302-310)	1.00 ±	2.91	-0.10 ±	4.01
AGWNELLIASFSH(303-315)	0.79 ±	2.29	-0.16 ±	3.98
LIASFSHRS(309-317)	0.57 ±	4.49	0.12 ±	6.50
IASFSHRS(310-317)	1.17 ±	5.50	0.88 ±	13.94
ASFSHRS(311-317)	1.01 ±	4.21	0.43 ±	7.02
KDGILLATGLHVHRNSAH(321-338)	2.30 ±	2.82	1.57 ±	2.66
AHSAGVGAIFDR(337-348)	0.93 ±	2.67	0.06 ±	3.22
DMQMD(359-363)	-0.08 ±	6.32	0.26 ±	11.88
DKTELGCLRAIV(363-374)	1.18 ±	4.12	0.95 ±	8.08
GCLRAIVLFNPD(368-379)	0.59 ±	4.85	0.36 ±	9.41
RAIVLFNPDSKGLSNPAE(371-388)	0.33 ±	1.08	-0.18 ±	2.08
IVLFNPDSKGLSNPAE(373-388)	0.12 ±	1.18	-0.42 ±	2.08
IVLFNPDSKGLSNPAEVE(373-390)	0.29 ±	0.97	-0.04 ±	1.92
LFNPDSKGLSNPAE(375-388)	0.31 ±	4.41	-0.19 ±	3.30
FNPDSKGLSNPAE(376-388)	0.14 ±	1.57	-0.49 ±	3.92
FNPDSKGLSNPAEVE(376-390)	0.59 ±	3.68	0.57 ±	4.25
LREKVY(392-397)	0.16 ±	2.50	0.01 ±	2.21
YPEQPGR(408-414)	-0.34 ±	6.80	-1.58 ±	16.90
YPEQPGRF(408-415)	-0.51 ±	3.54	-0.72 ±	1.68
YPEQPGRFAK(408-417)	0.37 ±	2.69	-0.04 ±	9.61
LLRLPAL(419-425)	-1.09 ±	2.61	-1.05 ±	2.47
LLRLPALRS(419-427)	-1.30 ±	2.84	-1.11 ±	2.29
LRLPALRS(420-427)	-1.80 ±	3.48	-1.70 ±	2.78
PALRSIGLKC(423-432)	-4.93 ±	9.42	-3.37 ±	20.68
ALRSIGLK(424-431)	-0.36 ±	9.98	0.35 ±	24.18
ALRSIGLKC(424-432)	-7.23 ±	9.40	-5.17 ±	53.39
RSIGLKCL(426-433)	-0.62 ±	5.53	0.11 ±	7.06
CLEHLFF(432-438)	0.07 ±	2.74	-0.62 ±	4.65
LEHLF(433-437)	-0.53 ±	3.29	-1.30 ±	6.38
LEHLFF(433-438)	-0.27 ±	4.57	-1.33 ±	7.57
EHLFF(434-438)	0.01 ±	3.32	-0.64 ±	6.34
FFFKLIGDTPI(437-447)	-0.66 ±	3.40	-1.20 ±	7.44
FKLIGDTPID(439-448)	-0.33 ±	2.54	-0.45 ±	6.01
FKLIGDTPIDT(439-449)	-0.29 ±	2.61	-0.28 ±	5.88
FKLIGDTPIDTF(439-450)	-0.33 ±	2.46	-0.27 ±	5.20
FKLIGDTPIDTFL(439-451)	-1.29 ±	2.51	-0.57 ±	4.32
IGDTPID(442-448)	-0.18 ±	2.37	-0.41 ±	5.20
IGDTPIDTF(442-450)	-0.96 ±	1.63	-0.60 ±	6.53
IGDTPIDTFL(442-451)	-0.67 ±	2.28	-0.74 ±	3.94
FLMEM(450-454)	-0.72 ±	2.85	-0.14 ±	5.25
LMEML(451-455)	-0.53 ±	5.37	-0.69 ±	5.17
EMLEAPHQM(453-461)	0.02 ±	2.34	-1.34 ±	5.81

RXR Sequence	(L)-ENL ± 3s.d		(D)-ENL ± 3s.d		PK11195 ± 3s.d		CINPA1 ± 3s.d	
SSGRENLYFQG(213-223)	-1.08 ±	4.11	-0.33 ±	3.74	-0.64 ±	2.72	-0.64 ±	-2.37
GRENLYFQGSSANE(215-228)	-0.31 ±	2.69	-0.52 ±	3.24	-0.02 ±	1.99	-0.67 ±	-2.05
RILEAELA(234-241)	-0.60 ±	1.85	-0.65 ±	1.55	-0.29 ±	1.77	-0.59 ±	-1.64
ADKQL(272-276)	-0.89 ±	8.32	-0.87 ±	5.99	-0.29 ±	6.72	-0.53 ±	-5.39
QLFTL(275-279)	-1.18 ±	3.14	-0.17 ±	3.57	-0.61 ±	3.22	-0.69 ±	-2.20
FTLVE(277-281)	0.10 ±	2.39	0.78 ±	4.25	0.88 ±	4.01	-0.67 ±	-2.13
VEWAKRIPHFSE(280-291)	-0.85 ±	3.03	-0.58 ±	2.83	-0.04 ±	2.62	-0.43 ±	-2.54
PLDDQV(293-298)	0.19 ±	2.51	0.37 ±	2.82	0.62 ±	2.28	0.26 ±	-2.17
DDQVILLRAGW(295-305)	0.16 ±	5.33	-2.59 ±	3.62	-0.35 ±	4.03	-0.33 ±	-2.83
DDQVILLRAGWNEL(295-308)	-0.50 ±	1.12	-0.20 ±	1.20	0.11 ±	1.30	-0.08 ±	-0.88
DQVIL(296-300)	0.01 ±	1.77	-0.10 ±	2.22	0.29 ±	1.34	0.24 ±	-1.20
QVILL(297-301)	0.08 ±	1.08	0.17 ±	0.96	0.09 ±	0.73	-0.10 ±	-0.62
RAGWNEL(302-308)	-0.20 ±	4.88	1.10 ±	6.03	2.80 ±	4.13	-1.08 ±	-5.10
RAGWNELL(302-309)	0.22 ±	3.73	0.74 ±	4.12	1.39 ±	2.38	-0.50 ±	-3.78
RAGWNELLI(302-310)	0.09 ±	2.87	0.55 ±	3.45	0.97 ±	1.78	-0.62 ±	-2.60
AGWNELLIASFSH(303-315)	-0.26 ±	2.44	-0.75 ±	1.80	-0.62 ±	1.99	-0.69 ±	-1.84
LIASFSHRS(309-317)	-0.24 ±	4.69	0.33 ±	4.62	-0.15 ±	3.02	-0.88 ±	-3.93
IASFSHRS(310-317)	0.06 ±	4.87	0.04 ±	5.79	-0.03 ±	3.25	-0.63 ±	-4.45
ASFSHRS(311-317)	-0.35 ±	3.83	-0.18 ±	3.32	-0.63 ±	2.43	-0.55 ±	-3.85
KDGILLATGLHVHRNSAH(321-338)	0.15 ±	3.22	-0.55 ±	3.68	-0.68 ±	1.93	-0.67 ±	-2.04
AHSAGVGAIFDR(337-348)	-0.08 ±	2.07	-0.72 ±	2.38	-0.52 ±	2.29	-0.55 ±	-1.78
DMQMD(359-363)	-0.28 ±	4.81	0.12 ±	5.68	0.64 ±	3.92	0.05 ±	-4.87
DKTELGCLRAIV(363-374)	0.66 ±	13.44	0.42 ±	12.74	-0.57 ±	2.61	-1.19 ±	-3.09
GCLRAIVLFNPD(368-379)	-0.12 ±	4.56	-0.04 ±	4.53	-0.49 ±	3.43	-1.11 ±	-3.96
RAIVLFNPDSKGLSNPAE(371-388)	-0.26 ±	1.06	0.03 ±	1.48	0.02 ±	1.13	-0.25 ±	-1.19
IVLFNPDSKGLSNPAE(373-388)	-0.19 ±	1.16	-0.09 ±	1.36	0.21 ±	1.14	-0.25 ±	-1.10
IVLFNPDSKGLSNPAEVE(373-390)	-0.02 ±	1.22	0.00 ±	1.61	0.23 ±	1.04	-0.36 ±	-1.14
LFNPDSKGLSNPAE(375-388)	-0.28 ±	3.08	-0.68 ±	5.59	0.03 ±	3.19	-0.38 ±	-3.26
FNPDSKGLSNPAE(376-388)	-0.30 ±	1.59	-0.27 ±	1.94	0.41 ±	1.49	-0.29 ±	-1.49
FNPDSKGLSNPAEVE(376-390)	-0.38 ±	5.21	-0.59 ±	4.43	0.35 ±	3.64	-0.39 ±	-3.62
LREKVY(392-397)	-0.21 ±	2.32	-0.13 ±	2.26	0.25 ±	2.60	0.10 ±	-2.09
YPEQPGR(408-414)	0.62 ±	4.20	-0.11 ±	5.43	0.29 ±	2.99	0.20 ±	-3.15
YPEQPGRF(408-415)	-0.94 ±	2.14	-0.24 ±	2.24	-0.62 ±	2.45	-0.48 ±	-2.06
YPEQPGRFAK(408-417)	-0.27 ±	5.63	1.11 ±	5.67	0.60 ±	2.46	-0.13 ±	-2.47
LLRLPAL(419-425)	-0.28 ±	2.28	-0.41 ±	2.61	-0.58 ±	2.20	0.27 ±	-2.15
LLRLPALRS(419-427)	-0.15 ±	1.97	-0.35 ±	2.08	-0.49 ±	2.31	0.23 ±	-1.42
LRLPALRS(420-427)	-0.32 ±	3.54	-0.47 ±	2.50	-0.90 ±	2.40	0.14 ±	-2.73
LRLPALRSIGLK(420-431)	-0.54 ±	3.18	0.23 ±	3.10	0.24 ±	1.86	0.29 ±	-1.78
PALRSIGL(423-430)	0.19 ±	4.92	0.62 ±	3.66	0.99 ±	3.28	0.52 ±	-3.44
PALRSIGLK(423-431)	-0.22 ±	3.45	0.48 ±	3.23	0.44 ±	2.13	0.54 ±	-2.01
PALRSIGLKC(423-432)	1.90 ±	8.12	1.48 ±	6.76	-2.39 ±	5.64	-2.11 ±	-7.94
ALRSIGLK(424-431)	0.72 ±	10.61	-0.41 ±	7.51	-1.59 ±	5.20	-0.32 ±	-6.99
RSIGLKCL(426-433)	-10.19 ±	5.13	-11.04 ±	3.59	-1.25 ±	3.68	-1.32 ±	-5.12
CLEHLFF(432-438)	-13.44 ±	3.97	-13.18 ±	3.49	-0.66 ±	4.05	-0.33 ±	-4.37
LEHLF(433-437)	-6.36 ±	5.66	-6.85 ±	3.71	-0.50 ±	2.68	-0.18 ±	-1.99
LEHLFF(433-438)	3.71 ±	3.15	3.81 ±	2.75	-0.98 ±	3.50	-0.67 ±	-2.51
EHLFF(434-438)	2.91 ±	3.92	2.49 ±	3.69	-0.51 ±	3.96	-0.62 ±	-4.45
FFFKLIGDTPI(437-447)	22.91 ±	3.10	22.11 ±	3.23	-0.60 ±	2.78	-1.03 ±	-2.33
FKLIGDTPID(439-448)	-11.29 ±	2.51	-11.32 ±	2.03	-0.85 ±	2.44	-0.77 ±	-2.07
FKLIGDTPIDT(439-449)	3.14 ±	2.22	3.28 ±	2.00	-0.22 ±	1.65	-0.71 ±	-2.14
FKLIGDTPIDTF(439-450)	-1.52 ±	2.18	-1.41 ±	1.67	-0.12 ±	1.57	-0.88 ±	-1.72
FKLIGDTPIDTFL(439-451)	-2.59 ±	2.45	-1.85 ±	1.82	-0.11 ±	1.65	-0.44 ±	-1.57
IGDTPID(442-448)	-0.48 ±	2.63	-0.62 ±	1.79	-0.36 ±	1.70	-1.37 ±	-1.98
IGDTPIDTF(442-450)	0.28 ±	3.99	0.10 ±	1.64	0.00 ±	1.75	-0.84 ±	-1.96
IGDTPIDTFL(442-451)	-0.51 ±	2.62	-0.14 ±	1.96	-0.22 ±	1.47	-0.90 ±	-2.52
FLMEM(450-454)	-0.04 ±	4.12	0.23 ±	3.84	0.01 ±	2.65	-0.10 ±	-2.19
LMEML(451-455)	0.67 ±	6.54	0.78 ±	5.91	-0.07 ±	3.94	0.60 ±	-5.77
EMLEAPHQM(453-461)	-0.55 ±	2.09	-0.26 ±	1.39	-0.08 ±	1.73	-1.09 ±	-1.42

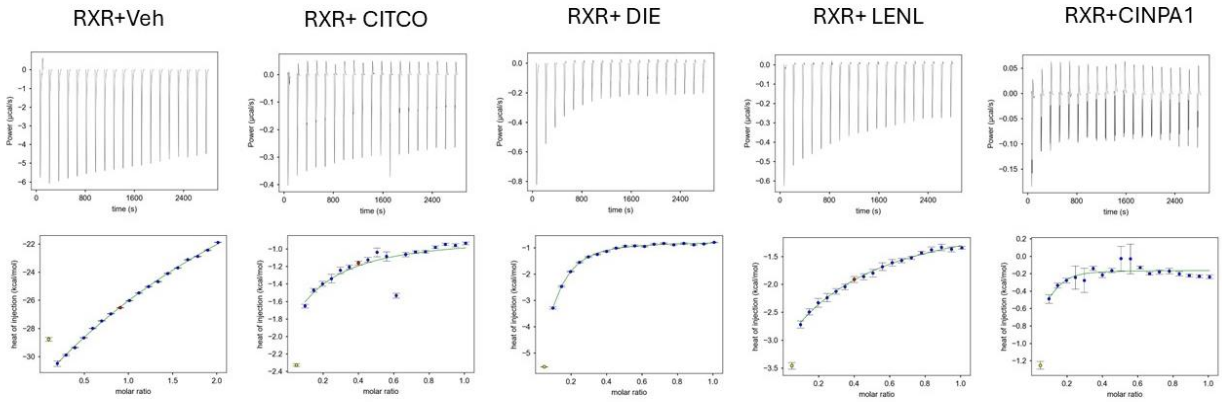

Figure C1. RXR ITC experiments for CAR ligands.

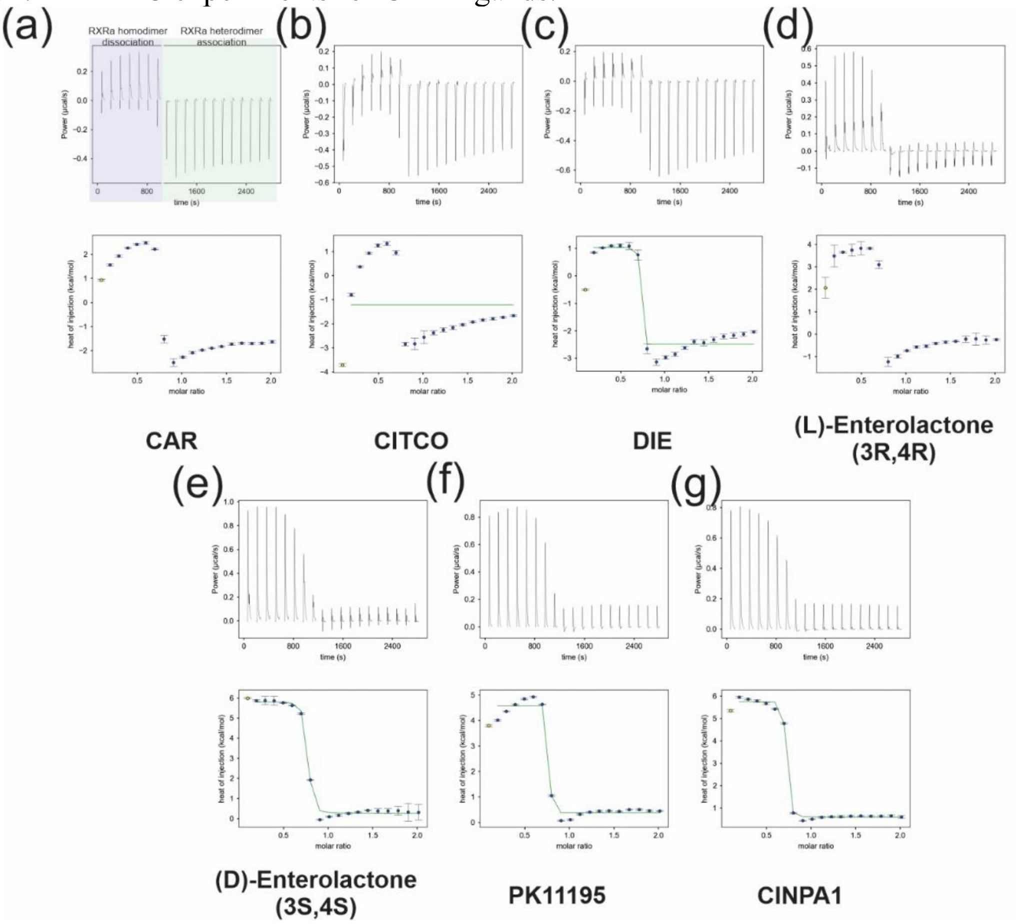

Figure C2. Thermogram and kinetic isotherm of the affinity of RXRα. ITC thermograms were obtained by titration of RXRα into CAR LBD (± CAR modulators). Isothermal calorimetric enthalpy change (top panel) and resulting binding isotherm (bottom panel) are shown. Two events occur: a first dissociation of the homodimer RXRα-RXRα LBDs and the formation of the heterodimer RXRα-CAR LBD[187]. (A) RXRα:CAR, (B) RXRα:CAR-CITCO, (C) RXRα:CAR-DIE, (D) RXRα:CAR-LENL, (E) RXRα:CAR-DENL, (F) RXRα:CAR-PK11195, (G) RXRα:CAR-CINPA1.

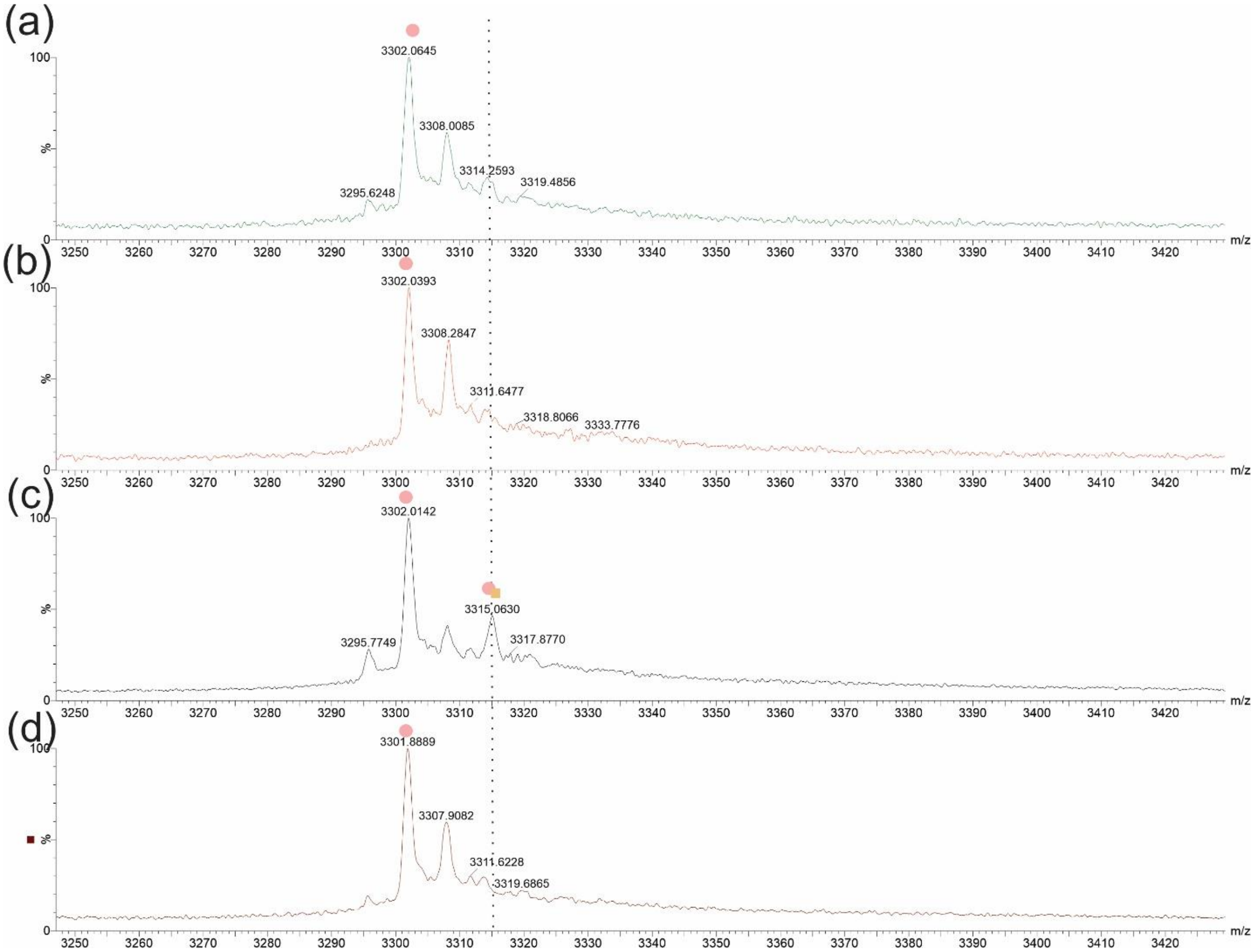

Figure C3. Native Mass spectrometry shows the effect of Ligand binding to CAR LBD. (a) CINPA1-bound CAR LBD, (b) (L)-ENL-bound CAR LBS, (c) DIE-bound CAR LBD, and (d) DMSO-treated CAR-LBD (control).

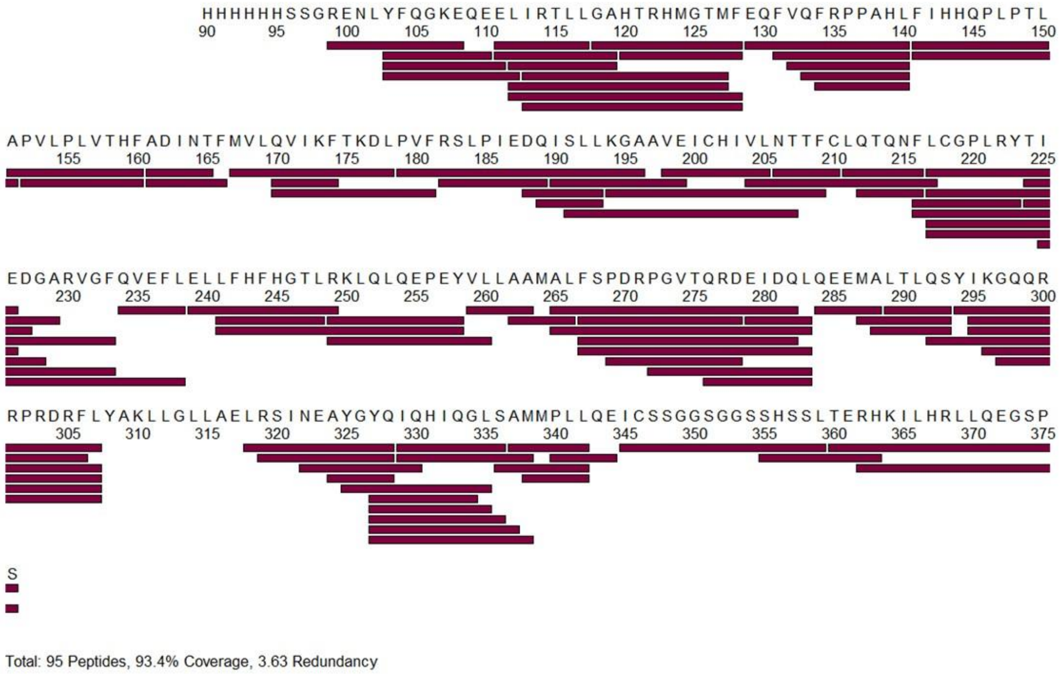

Figure C4. Sequence Coverage for CAR

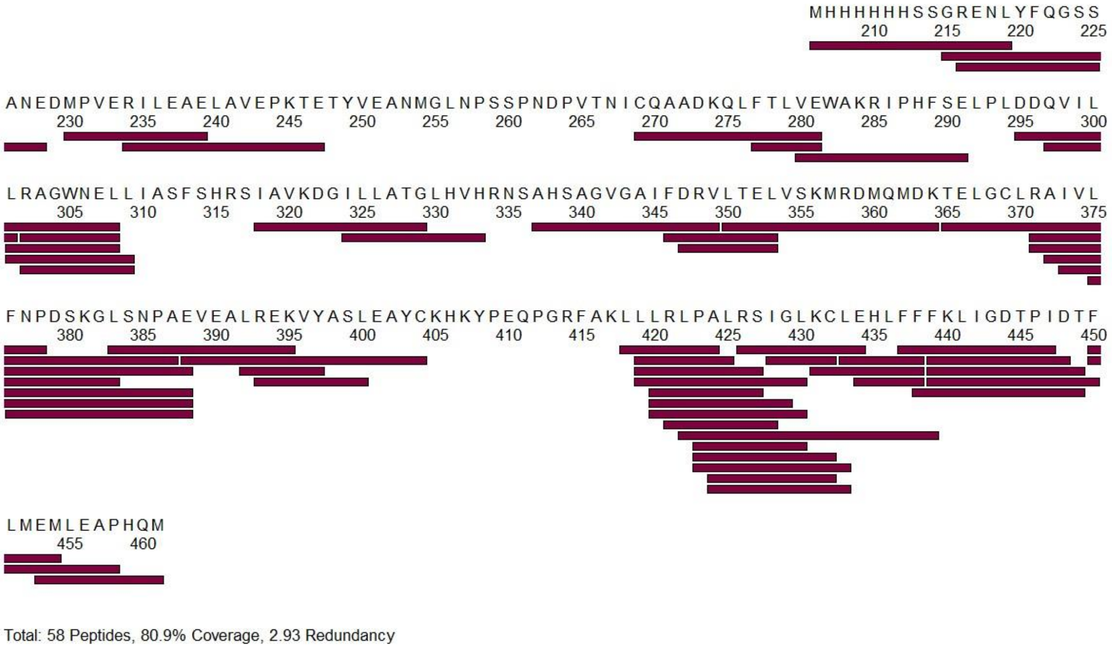

Figure C5. Sequence Coverage for RXRa

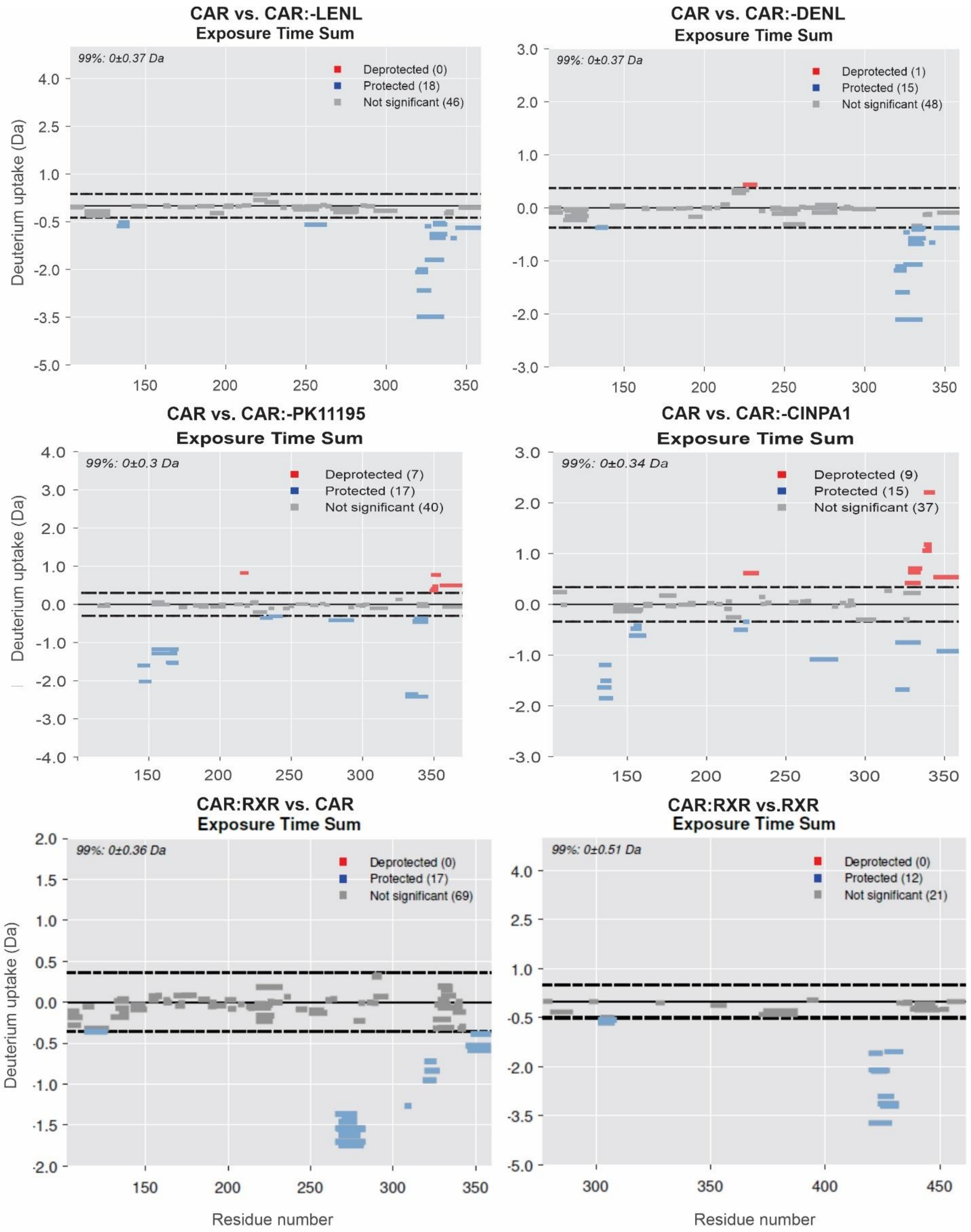
CAR vs. CAR:-LENL
Exposure Time Sum
99%: 0±0.37 Da
Deprotected (0)
Protected (18)
Not significant (46)
Deuterium uptake (Da)
4.0
2.5
1.0
-0.5
-2.0
-3.5
-5.0
150
200
250
300
350
CAR vs. CAR:-DENL
Exposure Time Sum
99%: 0±0.37 Da
Deprotected (1)
Protected (15)
Not significant (48)
3.0
2.0
1.0
0.0
-1.0
-2.0
-3.0
150
200
250
300
350
CAR vs. CAR:-PK11195
Exposure Time Sum
99%: 0±0.3 Da
Deprotected (7)
Protected (17)
Not significant (40)
Deuterium uptake (Da)
4.0
3.0
2.0
1.0
0.0
-1.0
-2.0
-3.0
-4.0
150
200
250
300
350
CAR vs. CAR:-CINPA1
Exposure Time Sum
99%: 0±0.34 Da
Deprotected (9)
Protected (15)
Not significant (37)
3.0
2.0
1.0
0.0
-1.0
-2.0
-3.0
150
200
250
300
350
CAR:RXR vs. CAR
Exposure Time Sum
99%: 0±0.36 Da
Deprotected (0)
Protected (17)
Not significant (69)
Deuterium uptake (Da)
2.0
1.5
1.0
0.5
0.0
-0.5
-1.0
-1.5
-2.0
150
200
250
300
350
Residue number
CAR:RXR vs.RXR
Exposure Time Sum
99%: 0±0.51 Da
Deprotected (0)
Protected (12)
Not significant (21)
4.0
2.5
1.0
-0.5
-2.0
-3.5
-5.0
300
350
400
450
Residue number

RXRa vs. RXRa-CITCO

Exposure Time Sum

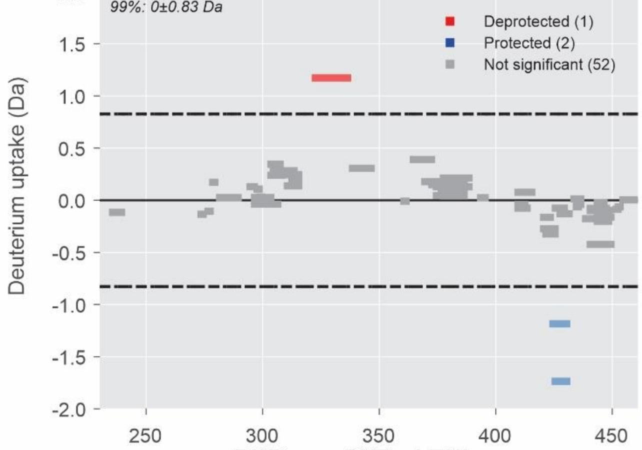

RXRa vs. RXRa-DIE

Exposure Time Sum

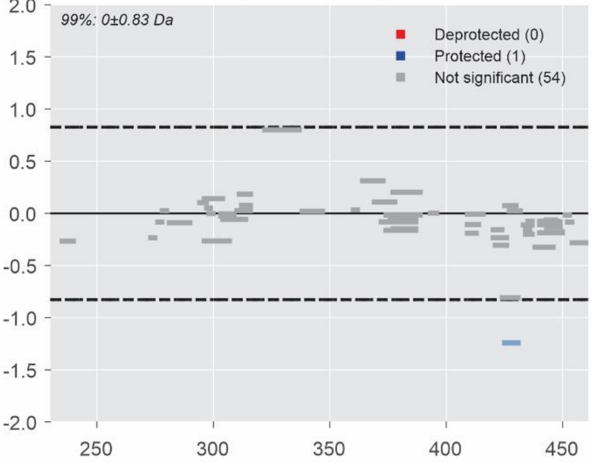

RXRa vs. RXRa-LENL

Exposure Time Sum

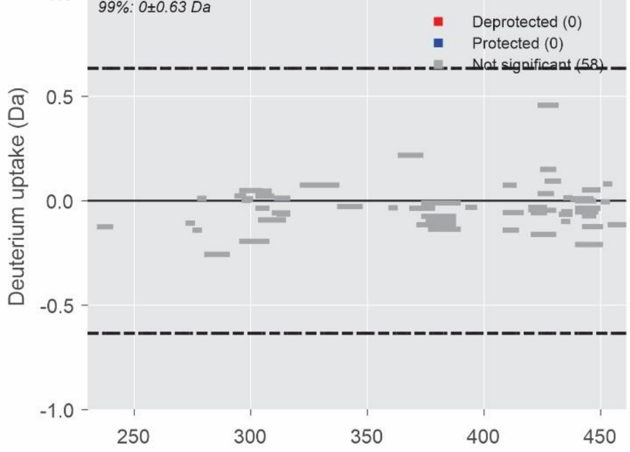

RXRa vs. RXRa-DENL

Exposure Time Sum

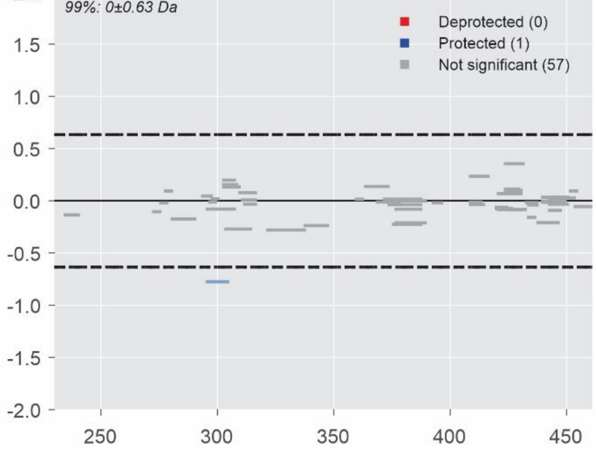

RXRa vs. RXRa-PK11195

Exposure Time Sum

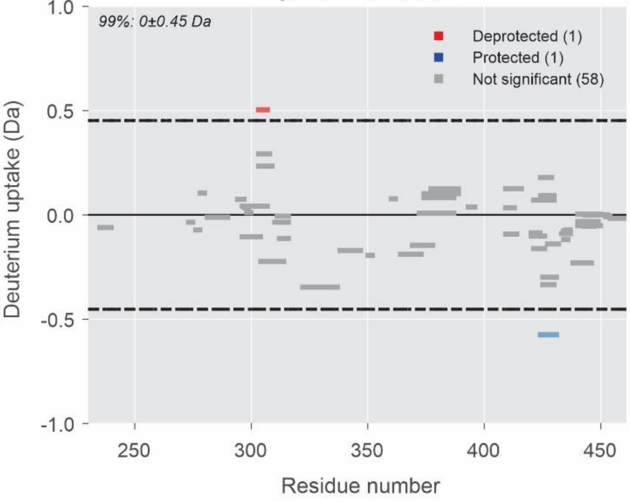

RXRa vs. RXRa-CINPA1

Exposure Time Sum

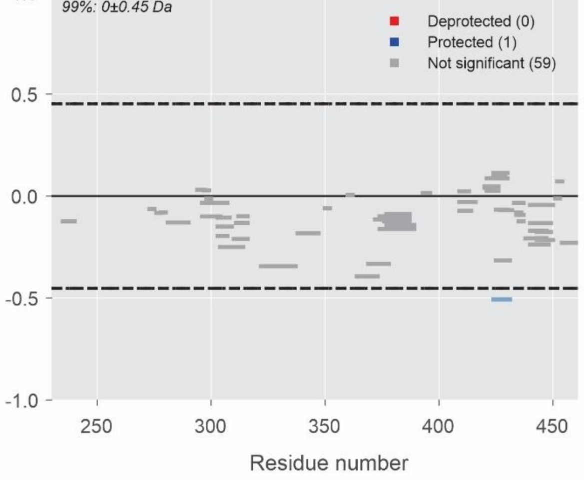

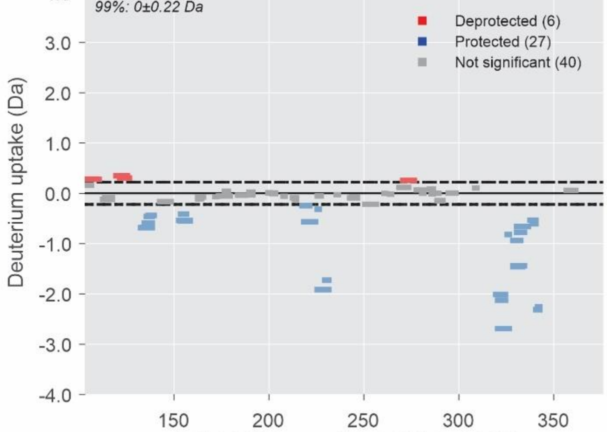

CAR:RXRa vs. CAR:RXRa-CITCO

Exposure Time Sum

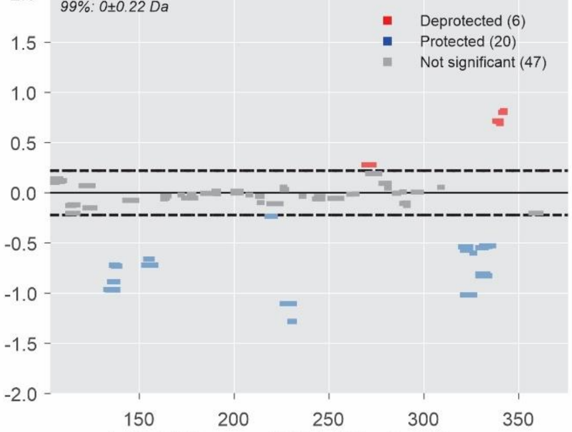

CAR:RXRa vs. CAR:RXRa-DIE

Exposure Time Sum

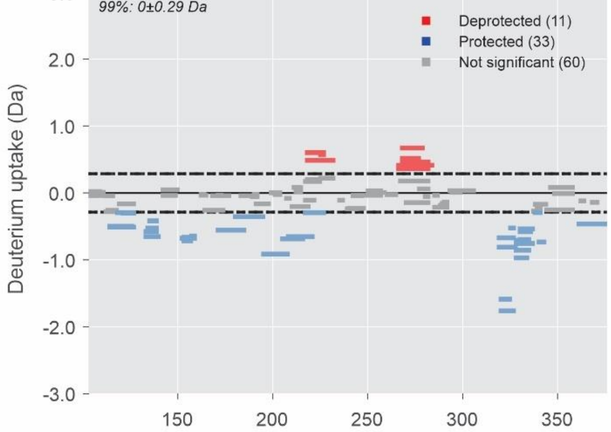

CAR:RXRa vs. CAR:RXRa-LENL

Exposure Time Sum

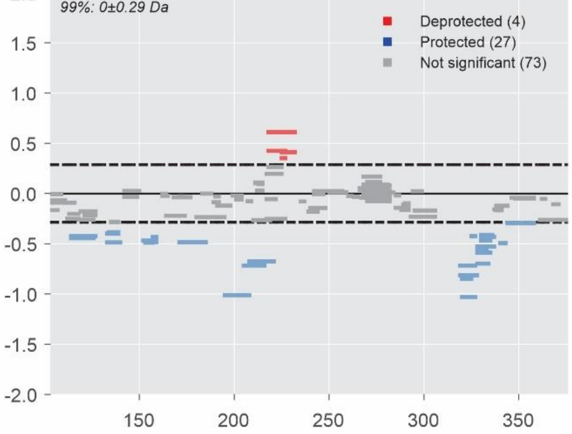

CAR:RXRa vs. CAR:RXRa-DENL

Exposure Time Sum

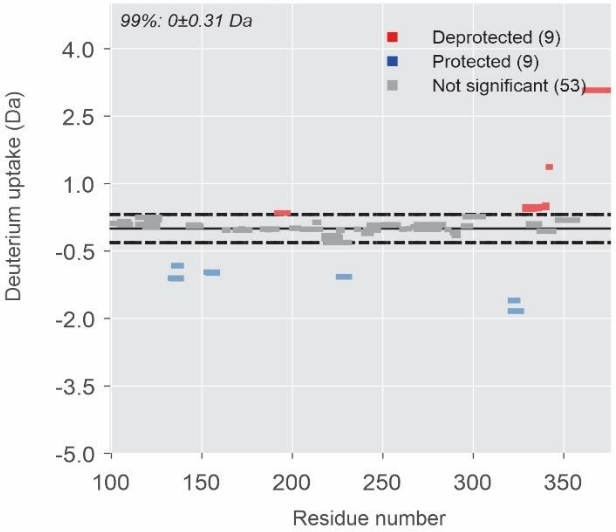

CAR:RXRa vs. CAR:RXRa-PK11195

Exposure Time Sum

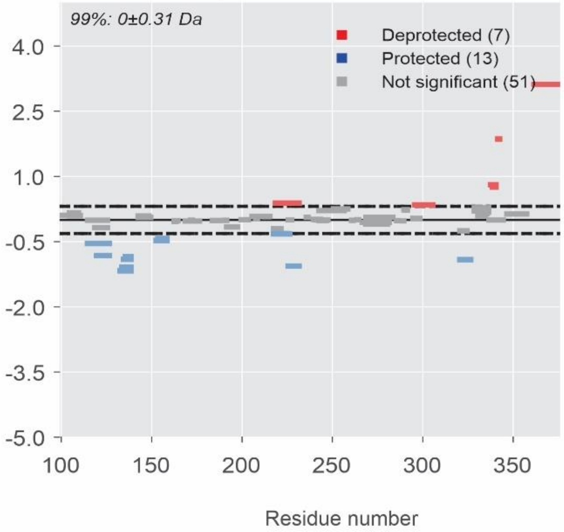

CAR:RXRa vs.CAR:RXRa-CINPA1

Exposure Time Sum

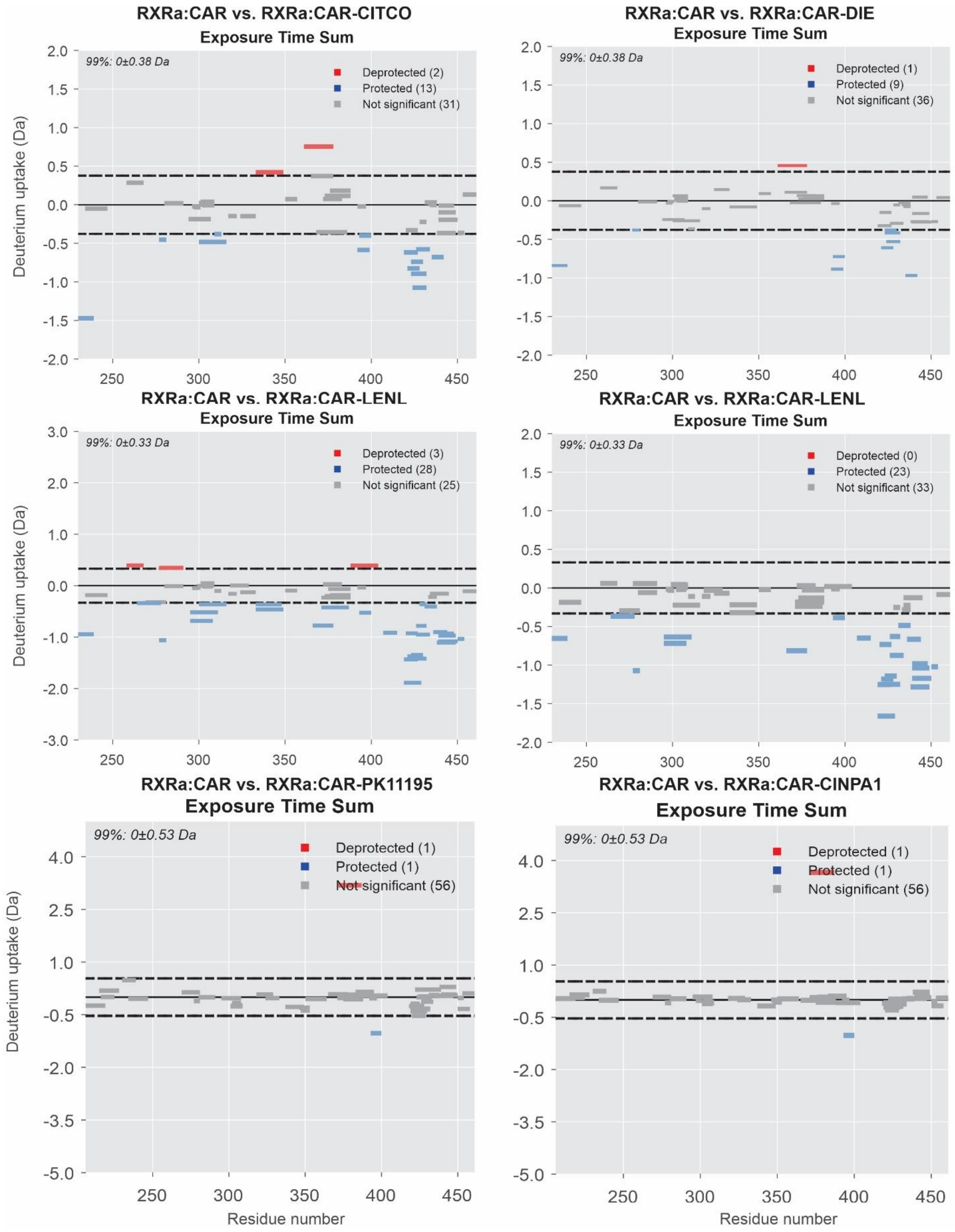

RXRa:CAR vs. RXRa:CAR-CITCO
Exposure Time Sum

RXRa:CAR vs. RXRa:CAR-DIE
Exposure Time Sum

RXRa:CAR vs. RXRa:CAR-LENL
Exposure Time Sum

RXRa:CAR vs. RXRa:CAR-LENL
Exposure Time Sum

RXRa:CAR vs. RXRa:CAR-PK11195
Exposure Time Sum

RXRa:CAR vs. RXRa:CAR-CINPA1
Exposure Time Sum

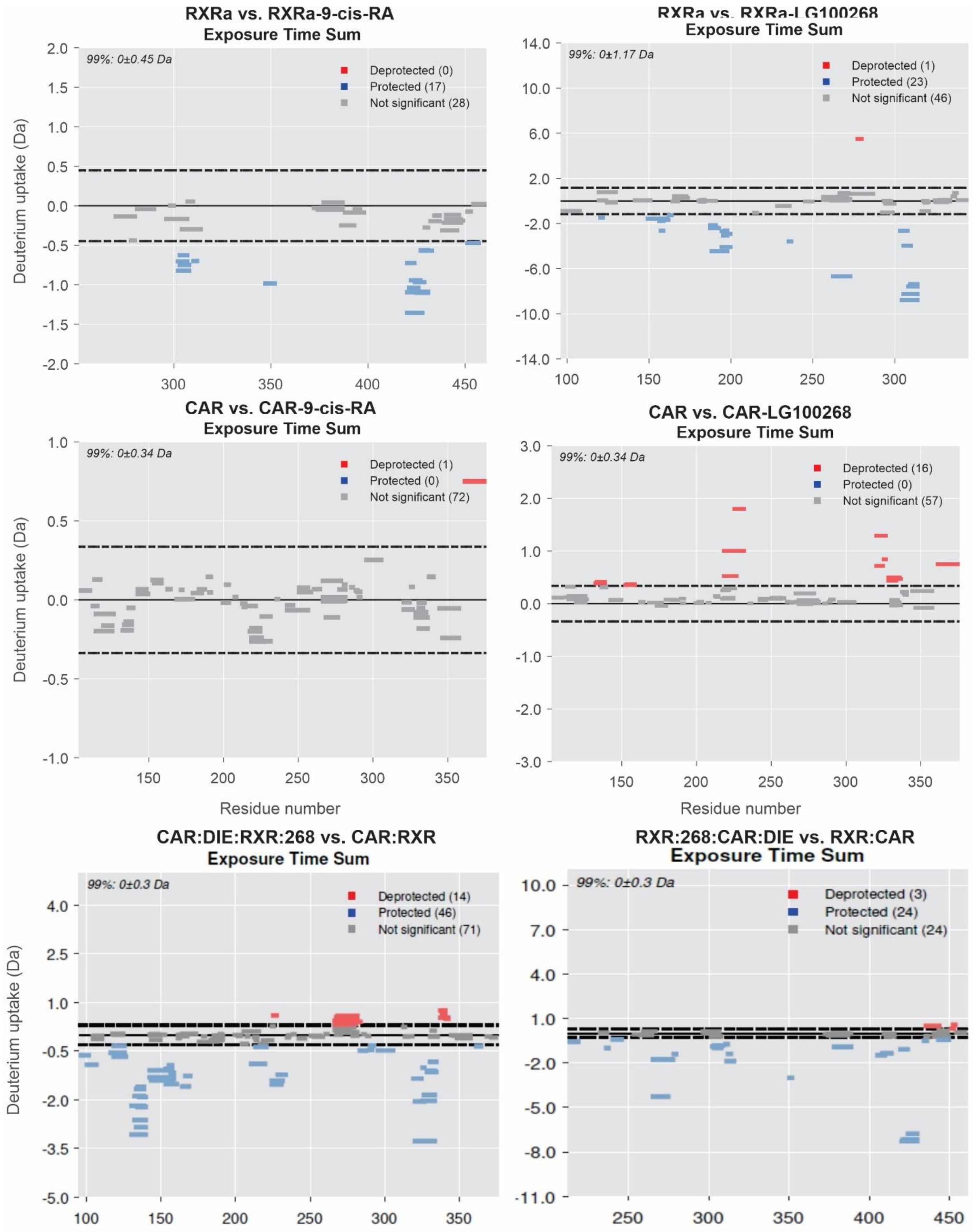
RXRa vs. RXRa-9-cis-RA
Exposure Time Sum
99%: 0±0.45 Da
Deprotected (0)
Protected (17)
Not significant (28)
2.0
1.5
1.0
0.5
0.0
-0.5
-1.0
-1.5
-2.0
300
350
400
450
Deuterium uptake (Da)
RXRa vs. RXRa-LG100268
Exposure Time Sum
99%: 0±1.17 Da
Deprotected (1)
Protected (23)
Not significant (46)
14.0
10.0
6.0
2.0
-2.0
-6.0
-10.0
-14.0
100
150
200
250
300
CAR vs. CAR-9-cis-RA
Exposure Time Sum
99%: 0±0.34 Da
Deprotected (1)
Protected (0)
Not significant (72)
1.0
0.5
0.0
-0.5
-1.0
150
200
250
300
350
Residue number
Deuterium uptake (Da)
CAR vs. CAR-LG100268
Exposure Time Sum
99%: 0±0.34 Da
Deprotected (16)
Protected (0)
Not significant (57)
3.0
2.0
1.0
0.0
-1.0
-2.0
-3.0
150
200
250
300
350
Residue number
CAR:DIE:RXR:268 vs. CAR:RXR
Exposure Time Sum
99%: 0±0.3 Da
Deprotected (14)
Protected (46)
Not significant (71)
4.0
2.5
1.0
-0.5
-2.0
-3.5
-5.0
100
150
200
250
300
350
Deuterium uptake (Da)
RXR:268:CAR:DIE vs. RXR:CAR
Exposure Time Sum
99%: 0±0.3 Da
Deprotected (3)
Protected (24)
Not significant (24)
10.0
7.0
4.0
1.0
-2.0
-5.0
-8.0
-11.0
250
300
350
400
450

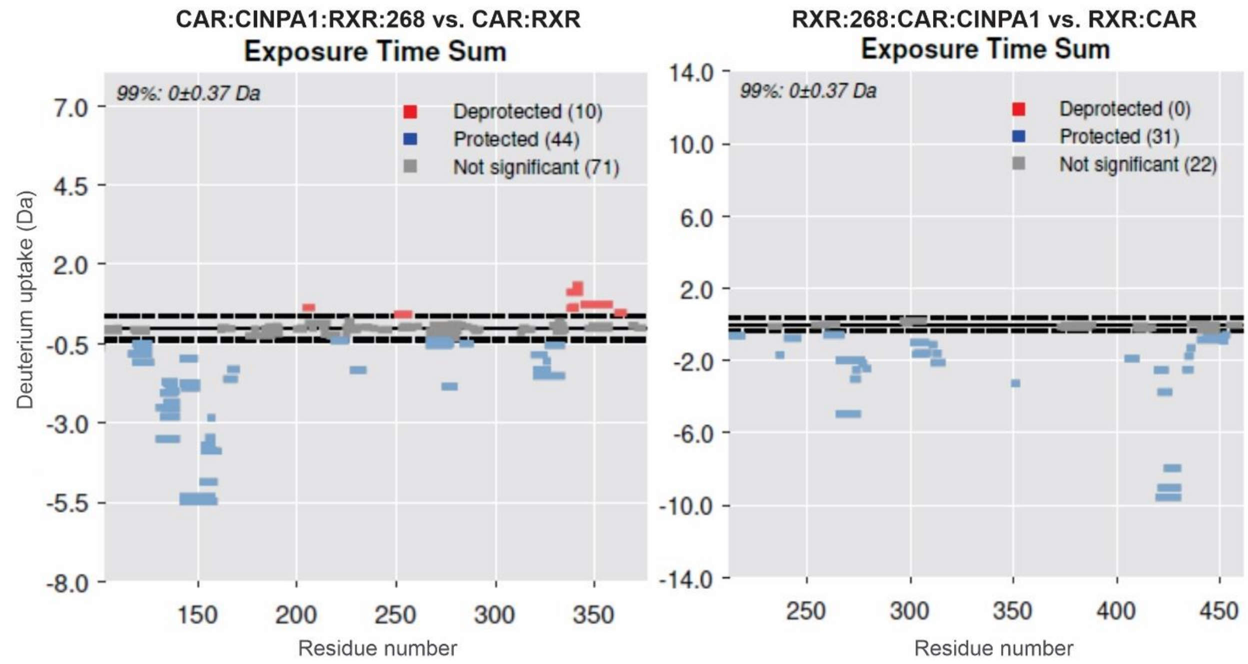

Figure C6. Summed deuterium uptake difference presented in Woods plots for all experiments tested in Chapter 4. Regions highlighted in red, blue or gray represent deprotected, protected and non-statistically significant peptides, respectively. A confidence limit of 99% was applied to each data set to identify peptides that are significant. Presented plots were created using Deuteros software.[198]